Diss. ETH No. 16522

# Self-Illuminating Pressure Sensitive Paints Using Electroluminescent Foils

A dissertation submitted to the
SWISS FEDERAL INSTITUTE OF TECHNOLOGY, ZURICH
for the degree of
DOCTOR OF TECHNICAL SCIENCES

Presented by
STEFANO ANGELO AIRAGHI
Dipl. Masch.-Ing. ETH, Zurich

Born January 10, 1975

citizen of
Brusino Arsizio, Ticino

Accepted on the recommendation of
Prof. Dr. Thomas Rösgen, examiner
Prof. Dr. John P. Sullivan, co-examiner
Prof. Dr. Jürg Wildi, co-examiner

2006

Seite Leer /
Blank leaf

# *Abstract*

Measurements of pressure distributions in wind tunnel testing are used to determine the aerodynamic effectiveness of a design. The classical way of measuring pressure, i.e., pressure taps, has two disadvantages: only discrete points can be acquired and the costs to equip a model are significant. To overcome these problems pressure sensitive paints (PSPs) were developed. This non-intrusive technique allows the measurement of 2-dimensional surface pressure maps with a considerable cost reduction. PSPs have however several intrinsic problems. The emission intensity used to measure pressure does not only depend on pressure variations, but also on homogeneity effects and surface temperature. To reduce the homogeneity problem two techniques were developed: ratio and life-time techniques. Also for the temperature problem many solutions were investigated and proposed in the literature: dual luminophore paints, temperature sensitive paints or the use of IR cameras. However, this increase of complexity results also in an increase of possible problems and measurements errors.

The use of electroluminescent foils as illumination source for pressure sensitive paints was introduced and investigated in this work to simplify the PSP measurements. The feasibility of pre-painting the EL-foils outside the wind tunnel was established. The advantages of the foils are not only confined to a hardware simplification: the errors due to illumination inhomogeneities are reduced and more importantly the possibility of directly measuring surface temperature was demonstrated. As previously explained, the increase in the measurement complexity is accomplained by new problems and difficulties: in particular a reduction of the paint sensitivity could be observed. Some suggestions are given to reduce and possibly eliminate this unwanted effect. Validations in the wind tunnel, showing the capability of measuring pressure and temperature, were successfully performed.

Seite Leer /
Blank leaf

# *Sommario*

Le misurazioni di pressione in galleria del vento sono utilizzate principalmente per migliorare ed ottimizzare il design di un modello. I metodi classici utilizzati, per esempio prese di pressione, hanno principalmente due svantaggi. In primo luogo si possono effettuare unicamente misurazioni in punti distinti e discreti, inoltre i costi per allestire un modello con prese di pressione risultano elevati. L'utilizzo di vernici barosensibili ovvia a questi problemi. Questa tecnica di misurazione non intrusiva permette di visualizzare le pressioni superficiali in modo semplice, riducendo notevolmente i costi.
Tuttavia l'utilizzo di vernici barosensibili implica alcune problematiche. L'intensità delle emissioni fluorescenti dipende non solo dalla pressione parziale in un determinato punto, ma anche dalla omogeneità della vernice/illuminazione e dalla temperatura. Per eliminare, o ridurre, i problemi riguardanti l'omogeneità delle vernici variazioni della tecnica base sono state studiate e sviluppate: *ratio technique* e *life-time PSP*. Per correggere imprecisioni causate dalla temperatura misurazioni addizionali sono state sviluppate e proposte in innumerevoli studi e pubblicazioni: e.s. *dual luminiphore paints*, *temperature sensitive paints* o con l'aiuto di telecamere ad infrarossi. L'aumento in complessità delle tecniche di misurazione causa un inevitabile aumento di problemi correlati alla calibrazione e introduce nuove fonti di errore.
L'utilizzo di fogli elettroluminescenti quale fonte di illuminazione per vernici barosensibili atto a semplificare la tecnica di misurazione é discusso in questa tesi. Le vernici vengono preventivamente spruzzate sui fogli all'esterno della galleria del vento. Altri importanti vantaggi sono chiaramente identificabili: gli errori di misurazione dovuti all' inomogenietà delle vernici e dell'illuminazione sono ridotti e, ancora più importante, la temperatura superficiale può essere misurata direttamente tramite l'emissione dei fogli. Tuttavia, come precedentemente spiegato, aumentando la complessità di una tecnica di misurazione aumentano irrimediabilmente difficoltà, errori e problemi. In particolare, con l'introduzione di fogli elettroluminescenti una riduzione della sensibilità a variazioni di pressione è stata riscontrata. Possibili soluzioni per ridurre o eliminare quest'ultimo problema sono discusse nella tesi. Alcuni esempi di misurazione in galleria del vento sono stati effettuati a dimostrazione della capacità di misurare contemporaneamente pressioni e temperature

superficiali.

# *Acknowledgments*

First of all I would like to thank Prof. Thomas Rösgen. He was an inexhaustible source of interesting ideas and useful hints, but more importantly he was a pleasure to work for on both the professional and the personal level.
Thanks to John Sullivan and Jürg Wildi to serve as co-examiners.
Thanks to Rene Holliger, Pius Stachel and Peter Weber for helping me to design and realize all the hardware components. Their experience was valuable and I take advantage by learning from them.
I would also like to thank RUAG Aerospace, in particular Dr. Jürg Wildi, Marianne Aeschwanden and Dr. Jürg Müller, for supporting this research project.
Thanks to Lumitec AG, in particular Heidi Knechtli and Emil Enz, for supplying special modified and custom made EL-foils.
I would also like to express my gratitude to all the staff of the Institute of Fluid Dynamics and to my colleagues for their help.
I would like to thank the friends of "maja time" and of "nankatsu team" for the friendship.
I also want to thank my family for allowing me to study at ETH, and special thanks go to my wife Leila for her love and patience.

*Zürich, March 30, 2006*

Seite Leer /
Blank leaf

# *Contents*

# Appendices

# Chapter 1

## *Introduction*

## 1.1 Pressure Measurements in Aerodynamic Testing

Technological progress is pushing engineers to continuously improve the performances of final products. The knowledge obtained during testing and development phases is crucial for successful results. From the aerodynamic point of view the detailed knowledge of pressure distribution on a model surface is one the most challenging and important tasks. In particular pressure distributions in wind tunnel testing are used to determine the effectiveness of a design. Since the performance in terms of lift and drag can be evaluated, a possible problem of a specific design can be identified.

The use of discrete pressure transducers is the classical measurement

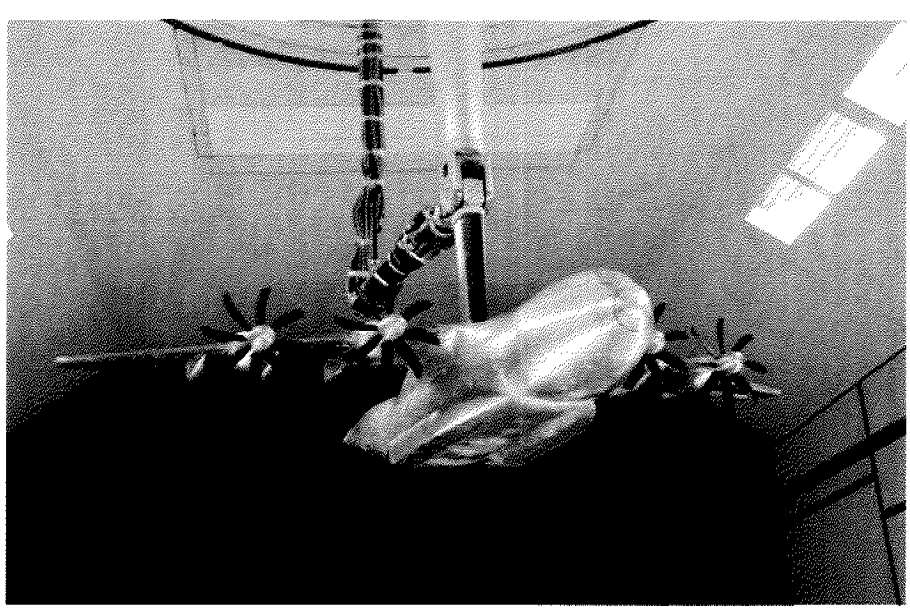

Figure 1.1: A400M model equipped with more than 700 pressure taps.

technique established during the last decades. Highly instrumented mod-

els are carefully prepared with hundreds of pressure taps (Fig. 1.1). The technique is cost intensive and implies weeks of work to prepare a model for a wind tunnel campaign.

## 1.2 Historical Notes

In 1980 J.I. Peterson and R.V. Fitzgerald [24] demonstrated a surface flow visualization technique based on oxygen quenching of fluorescent dyes. The possibility of measuring surface pressures was evident. Two main classes of pressure sensors, so called Pressure Sensitive Paints (PSP), were independently developed by the Central Aero-Hydrodynamic Institute (TsAGI) in Russia [23] and by the University of Washington (USA) [8,14]. PSP offers several advantages compared to traditional techniques: the pressure distribution is recorded over a surface area and not only at discrete points, the spatial resolution is restricted only by the resolution of the CCD camera used and the measurement costs can be reduced. The visualization of dynamic processes is possible and surface flow features like separation, shocks or reattachment points are recognizable. At present several research groups are investigating and optimizing PSP and the related evaluation techniques due to the great advantages compared to traditional pressure measurements techniques.

# Chapter 2

## *PSP Basics*

PSP technology is reaching sufficient accuracy to become a standard technique in wind tunnel measurements. PSP allows measurements of the pressure distribution on a model surface by simply acquiring intensity images with a conventional CCD camera. The acquired images must then be postprocessed to extract the desired pressure maps [18]. This chapter describes the basic functioning principles of PSP, the typical hardware setup and proposes a modified setup.

## 2.1 Photophysical Processes

### 2.1.1 Kinetics of Luminescence

The functioning principle of PSP is based on the oxygen and thermal quenching processes of luminescence. The Jablonsky energy-level diagram (Fig. 2.1) displays the most important photophysical processes involved during PSP measurements. An electronically excited molecule can loose its excitation energy by the emission of radiation: this radiative transition is known as luminescence [17, 22, 25, 27]. There are two main types of luminescence: fluorescence and phosphorescence.

Fluorescence is a spin-allowed radiative transition between two states of the same multiplicity ($S_1 \rightarrow S_0$). The molecules exist in the ground singlet electronic state ($S_0$). In the first step, the excitation, photons of energy level $h\nu_{Ex}$ are supplied by an external light source. The molecules absorb the light and, depending on the excitation energy, reach an excited singlet state. The two absorption maxima $\lambda_1$ and $\lambda_2$ (Fig. 2.2) correspond to the two different excited singlet states $S_2$ and $S_1$. After absorption, vibrational relaxation occurs. The molecules decay to the excited electronic state of energy ($S_1$). A change in electronic state, called Internal Conversion (IC), is achieved without photon emission. From the energy level $S_1$ the molecules return to the ground state $S_0$ by fluorescent emission or by non-radiative relaxation. The emitted fluorescence energy is identical for molecules excited to the $S_2$ or to the $S_1$ energy level, due to the vibrational relaxation. The emission peak,

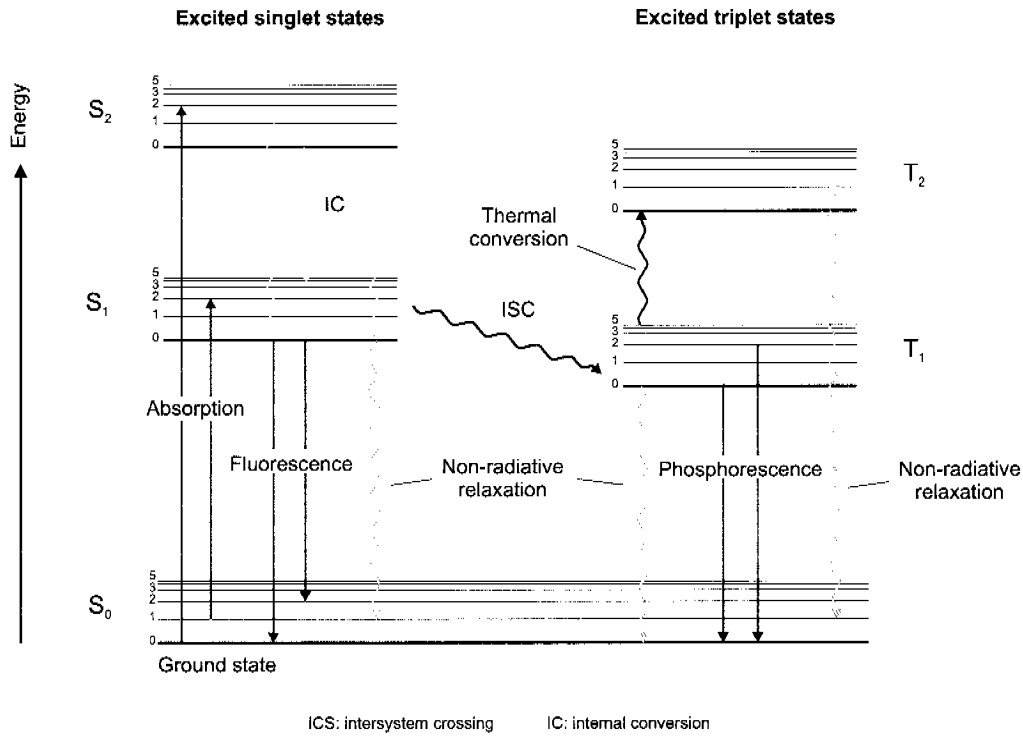


Figure 2.1: Jablonsky energy level diagram.

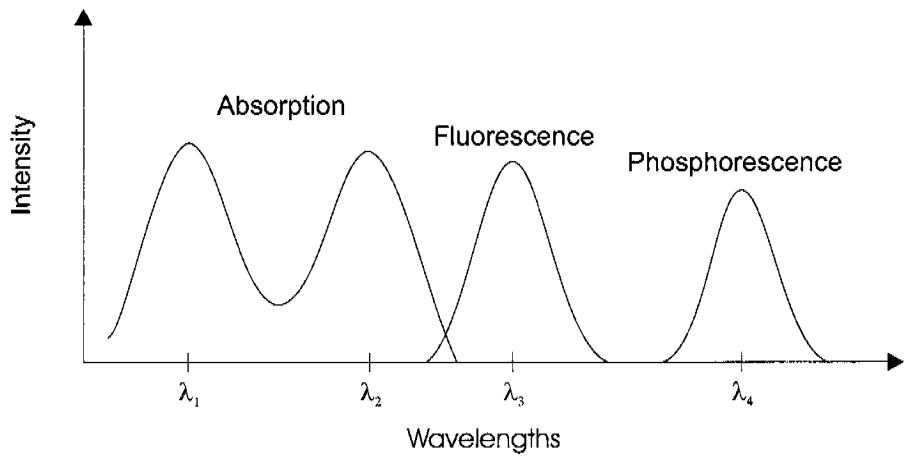


Figure 2.2: Absorption and emission spectra.

or fluorescence wavelength, is represented in Fig. 2.2 by $\lambda_3$. Other processes like collisional quenching and intersystem crossing (ISC) may also depopulate $S_1$. In the case of quenching the presence of another molecular species can lead to an energy transfer from an excited state to the ground state without radiative emission. Intersystem crossing (ISC) is

the spin-forbidden radiationless transition between two states of different multiplicity ($S_1 \rightarrow T_1$). Eq. (2.1) describes the population of the excited singlet state $S_1$:

$$\frac{dS_1}{dt} = I_a - (k_f + k_{ic} + k_{isc(1)} + k_{q(f)}[Q])[S_1], \tag{2.1}$$

where $I_a$ is the light absorption rate (excitation), $k_f$ is the rate constant for fluorescence, $k_{ic}$ is the rate constant for internal conversion, $k_{isc(1)}$ is the rate constant for intersystem crossing ($S1 \rightarrow T_1$), $k_{q(f)}$ is the rate constant for quenching and $[Q]$ is the the population of the quencher. The fluorescence lifetime is defined as:

$$\tau_f = \frac{1}{k_f + k_{ic} + k_{isc(1)} + k_{q(f)}[Q]}. \tag{2.2}$$

Fluorescence is a very short lived process, from $10^{-6}$ to $10^{-11}$ s. The lifetimes and rate constants of the involved processes are summarized in Tab. 2.1 [25].

Phosphorescence is a spin-forbidden radiative transition between two states of different multiplicity ($T_1 \rightarrow S_0$) (Fig. 2.1). Phosphorescence occurs as a delayed emission and at a higher wavelength ($\lambda_4$) than fluorescence due to the lower energy level of the triplet state compared to the singlet states (Fig. 2.2). The direct excitation of a molecule to a triplet state is very improbable. To excite a molecule to the triplet state $T_1$ a process of ISC from $S_1$ to $T_1$ occurs. As the molecule reaches the energy level $T_1$ two different processes can occur. In the first case the molecule looses energy, due to vibrational decay, and reaches the lowest energy level of $T_1$. The transition from from $T_1$ to the ground state $S_0$ occurs, as for the fluorescence, with non-radiative emission or phosphorescence emission. In the second case the molecule, due to thermal conversion, reaches the excited triplet state $T_2$. The relaxation to the the ground state ($S_0$) follows with a non-radiative emission: thermal quenching occurs. The population of the excited triplet state $T_1$ is described as

$$\frac{dT_1}{dt} = k_{isc(1)}[S_1] - (k_p + k_{isc(2)} + k_{q(p)}[Q] + k_{tc})[T_1], \tag{2.3}$$

where $k_p$ is the rate constant for phosphorescence emission, $k_{isc(2)}$ is the rate constant for the intersystem crossing ($T_1 \rightarrow S_0$), $k_{q(p)}$ is the quenching rate for phosphorescence and $k_{tc}$ is the rate constant for

| | Step | Process | Rate | Lifetime (s) |
|---|---|---|---|---|
| 1 | Excitation | $S_0 + h\nu_{Ex} \rightarrow S_1$ | $k_{S_1}[S_0]$ | $10^{-15}$ |
| 2 | Fluorescent emission | $S_1 \rightarrow S_1 + h\nu_F$ | $k_f[S_1]$ | $10^{-6} - 10^{-11}$ |
| 3 | Fluorescent quenching | $S_1 \rightarrow S_0 + \Delta$ | $k_{q(f)}[S_1][Q]$ | - |
| 4 | Internal conversion (IC) | $S_1 \rightarrow S_0 + \Delta$ | $k_{ic}[S_1]$ | $10^{-11} - 10^{-14}$ |
| 5 | Intersystem crossing (ISC) | $S_1 \rightarrow T + \Delta$ | $k_{isc(1)}[S_1]$ | $10^{-8} - 10^{-11}$ |
| 6 | Phosphorescent emission | $T_1 \rightarrow S_0 + h\nu_P$ | $k_p[T_1]$ | $10^{2} - 10^{-3}$ |
| 7 | Phosphorescent quenching | $T_1 \rightarrow S_0 + \Delta$ | $k_{q(p)}[T_1][Q]$ | - |
| 8 | Intersystem crossing (ISC) | $T_1 \rightarrow S_0 + \Delta$ | $k_{isc(2)}[S_1]$ | $10^{-8} - 10^{-11}$ |
| 9 | Thermal conversion (TC) | $T_1 + \Delta \rightarrow T_2$ | $k_{tc}[T_1]$ | - |

Table 2.1: Timescale of photophysical processes.

thermal conversion ($T_1 \rightarrow T_2$). The phosphorescence lifetime can be computed as:

$$\tau_p = \frac{1}{k_p + k_{isc(2)} + k_{q(p)}[Q] + k_{tc}}. \tag{2.4}$$

The lifetime of phosphorescence ($\tau_p$) varies from $10^{-3}$ to $10^{2}$ s.

### 2.1.2 Luminescence Model

#### Stern-Volmer equation

During wind tunnel measurements the detailed study of the involved photophysical processes is not essential. In practical applications a model of luminescence (fluorescence and phosphorescence) is used [17, 20, 25]. The simplified model considers only the quenching process of an excited molecule $D^*$ with a quencher molecule $Q$ (e.g., oxygen). In typical PSP the fluorescent dye is dispersed in an oxygen-permeable binder (e.g.,

polymer, silicone). Diffusion and solubility of the quencher in the binder must be considered. The involved photophysical processes are excitation, radiative emission, non-radiative emission and quenching. The concentration of the excited molecule is given by:

$$\frac{d[D^*]}{dt} = I_a - (k_r + k_q[Q] + k_{nr})[D^*]. \tag{2.5}$$

$I_a$ is the rate of radiation absorption (light absorption), $k_r$ is the rate constant of radiative emission, $k_q$ is the rate constant for quenching and $k_{nr}$ is the rate constant of non-radiative emission. Assuming a steady state excitation (illumination) Eq. (2.5) is simplified to

$$I_a = (k_r + k_q[Q] + k_{nr})[D^*]. \tag{2.6}$$

The quantum yield, or quantum efficiency, of the luminescence is defined with the following ratio

$$\Phi = \frac{rate\,of\,luminescence}{rate\,of\,excitation}. \tag{2.7}$$

The quantum yield in absence of a quencher is

$$\Phi_0 = \frac{k_r[D^*]}{I_a} = \frac{k_r}{k_r + k_{nr}} = \frac{I_0}{I_a}, \tag{2.8}$$

where $I_0$ is the luminescent intensity without quenching. The quantum yield $\Phi$ with quencher is expressed as

$$\Phi = \frac{k_r[D^*]}{I_a} = \frac{k_r}{k_r + k_{nr} + k_q[Q]} = \frac{I}{I_a}, \tag{2.9}$$

where $I$ is the luminescent emission. The Stern-Volmer equation is obtained by computing the ratio between $\Phi_0$ and $\Phi$

$$\frac{\Phi_0}{\Phi} = \frac{I_0}{I} = 1 + \frac{k_q}{k_r + k_{nr}}[Q] = 1 + k_q\tau_0[Q]. \tag{2.10}$$

The luminescent lifetime is expressed as

$$\tau = \frac{1}{k_r + k_{nr} + k_q[Q]}. \tag{2.11}$$

and $\tau_0$ is the quencher-free lifetime, expressed as:

$$\tau_0 = \frac{1}{k_r + k_{nr}} = \tau(Q = 0). \tag{2.12}$$

### Temperature dependence

For typical PSP applications the simple model presented is not satisfying. The luminescent emission of PSP paints depends not only on the presence of a quencher but also on temperature and on the luminophore binder. The diffusion and solubility of the quencher in the binder affect the response of the paint as well. The Stern-Volmer equation with oxygen ($O_2$) as quencher can be expressed as

$$\frac{I_0}{I} = 1 + \frac{k_q}{k_r + k_{nr}}[O_2] = 1 + k_q \tau_0 [O_2]. \tag{2.13}$$

The rate constants $k_{nr}$ and $k_q$ in Eq. (2.13) are temperature dependent. The temperature dependence of the rate constant $k_{nr}$ can be modelled by the Arrhenius relation [5, 30]

$$k_{nr} = k_{nr0} + k_{nr1} e^{(-\frac{E_{nr}}{RT})}, \tag{2.14}$$

where T is the absolute temperature in Kelvin, R is the universal gas constant, $k_{nr0}$ is the non-radiative rate constant at $T = 0°K$, $k_{nr1}$ is the rate constant for the temperature dependent part and $E_{nr}$ is the activation energy for non-radiative emission. The temperature dependence of the $k_q$ rate constant is strictly correlated with the diffusivity of the quencher ($O_2$) in the luminophore binder. The Smoluchowski relation couples $k_q$ with the diffusivity $D$

$$k_q = 4\pi R_{AB} N_0 D, \tag{2.15}$$

where $R_{AB}$ is the interaction distance between luminophore and quencher and $N_0$ is the Avogadro's number. The diffusivity of the quencher depends not only on the structure and density of the binder but also on the temperature. The Arrhenius relation describes the diffusion in the binder

$$D = D_0 e^{(-\frac{E_D}{RT})}, \tag{2.16}$$

where $E_D$ is the activation energy for the quencher diffusion and $D_0$ the theoretical maximum diffusion coefficient at infinite temperature. The concentration of oxygen molecules in the binder is described, according to Henry's law, with the oxygen solubility in the binder $S$ and the partial pressure of oxygen $p_{O_2}$ or with the air pressure $p$ and the mole fraction of oxygen in air $\phi_{O_2}$

$$[O_2]_{polymer} = S p_{O_2} = S \phi_{O_2} p. \tag{2.17}$$

By substituting Eqs. (2.14) to (2.17) into Eq. (2.13) and by taking a reference image $I_{ref}$ at known pressure $p_{ref}$ and temperature $T_{ref}$ instead of an image with zero-quenching $I_0$, the Stern-Volmer equation becomes

$$\frac{I_{ref}}{I} = \frac{\tau_{ref}}{\tau} = A_{polymer}(T) + B_{polymer}(T)\frac{p}{p_{ref}}. \tag{2.18}$$

$A_{polymer}$ and $B_{polymer}$ can be computed as:

$$A_{polymer} = \frac{1}{1 + K_{ref}p_{ref}/k_{aref}} \left[\frac{1 + \xi e^{(-E_{nr}/RT)}}{1 + \xi e^{(-E_{nr}/RT_{ref})}}\right], \tag{2.19}$$

$$B_{polymer} = \frac{p_{ref}}{k_{aref}/K_{ref} + p_{ref}} \left[\frac{E_D}{RT_{ref}}\left(\frac{T_{ref}}{T} - 1\right)\right], \tag{2.20}$$

where $\xi = (k_{nr1})/(k_r + k_{nr0})$ and $K_{ref}$ and $k_{aref}$ are defined as

$$K_{ref} = 4\pi R_{AB} N_0 S D_0 e^{(-\frac{E_D}{RT_{ref}})}\phi_{O_2 ref}, \tag{2.21}$$

$$k_{aref} = k_r + k_{nr0} + k_{knr1} e^{(-\frac{E_{nr}}{RT_{ref}})}. \tag{2.22}$$

This theoretical PSP model involves different material constants that cannot be easily established. The model is primarily used to understand and predict the behavior of the PSP response. For practical wind tunnel measurement and aerodynamic applications the empirical formulation of the Stern-Volmer equation can be of advantage,

$$\frac{I_{ref}}{I} = A(T) + B(T)\frac{p}{p_{ref}} + C(T)\left(\frac{p}{p_{ref}}\right)^2 + \cdots . \tag{2.23}$$

The constants $A(T)$, $B(T)$, ..., of the nonlinear Stern-Volmer equation are determined with calibration measurements in the laboratory.

## 2.2 Standard Setup

### 2.2.1 Setup

A typical PSP setup is illustrated in Fig. 2.3 [6, 28]. The test model is sprayed first with a highly reflective undercoat layer and than with a PSP layer. The paint, a fluorescent dye embedded in a binder, has to be

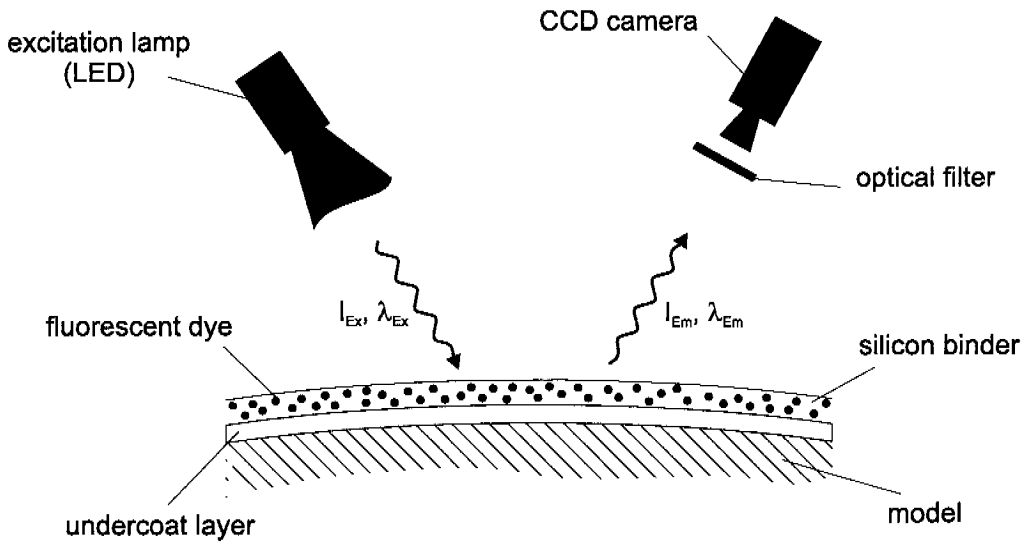


Figure 2.3: Standard PSP setup.

excited with an external light source (e.g., LED lamps, flash lamps or lasers) at a given wavelength $\lambda_{Ex}$ with the intensity $I_{Ex}$ to emit fluorescence (Sec. 2.1). The emitted light intensity $I_{Em}$ at a higher wavelength $\lambda_{Em}$ is proportional to pressure (Eq. (2.23)). Three measurements are necessary due to the fact that the image intensity depends not only on the pressure on the model surface but also on other important factors such as surface temperature, inhomogeneity of the excitation light, inhomogeneity of the fluorescent dye in the paint, paint thickness, angle of view [9]. To overcome these unwanted effects a widely used solution is the ratio technique. The acquired image (wind $ON$) is divided by a reference image taken at known pressure and temperature (wind $OFF$) to eliminate all the inhomogeneities. The result is a picture with the pixel intensity depending on pressure and temperature. With the Stern-Volmer equation (Eq. (2.23)) and a calibration curve the desired pressure can be computed as a function of the temperature. Only the ratio technique will be presented and discussed in this work, although other setup variations are used in engineering applications, e.g., life time PSP.

### 2.2.2 Advantages and Drawbacks

PSP is a non-intrusive optical technique. The main advantage compared to traditional measurement techniques, such as pressure taps, is the capability to obtain global surface measurements. A detailed pres-

sure map of the whole model surface can be measured by simply taking few images, and the measurement costs are substantially reduced. Due to these aspects PSP is becoming more and more attractive as a commercial tool.
One of the main drawbacks of PSP is related to the complex hardware setup and a related increase in time to setup a measurement campaign. The model, for better results, has to be painted directly in the wind tunnel. Special care has to be applied due to the toxicity of the paint and to avoid smearing the wind tunnel. The paint has to cure for some hours and as the model is painted the illumination sources, e.g., LED lamps, have to be positioned very carfully: all illumination inhomogeneities and shadows on the model surface have to be avoided. By modifying the measurement configuration, e.g., by changing the angle of attack of a wing, the illumination should still fullfill the previously described criteria. At the end of the measurement campaign the old paint has to be removed from the model. The adhesion of the paint, or better, of the undercoat layer is high and the removal becomes very tedious. These processes are quite time consuming with an accompanying increase of the measurement costs.
Others drawbacks arise from errors related to the ratio technique and to temperature effects [29, 32]. The accuracy of the pressure measurement is strongly affected by the temperature dependence of PSP. To eliminate the temperature dependence the wind $ON$ and wind $OFF$ images are not sufficient: a third independent measurement is needed. Several techniques were developed, e.g., correction with infrared pictures, dual luminophore paints [7], combined measurements with Temperature Sensitive Paint (TSP) [3] and in-situ calibration [16, 17]. Each of these techniques implies an increase in hardware complexity and involves specific drawbacks. Other errors arise from the illumination sources. For example, when computing the wind $ON$ / wind $OFF$ ratios, the small model displacements between the two pictures yield to inaccuracy. The two images have to be carefully registered. Note that errors in the inhomogeneities' correction can not be avoided: the external light sources do not move with the model causing different illumination conditions between wind $ON$ and wind $OFF$ image. Self illumination, the illumination from one surface to an other, could also create errors. Finally, the illumination of one surface by the other will change with pressure changes and is therefore not constant between measurement and reference image.

## 2.3 Innovative Setup

### 2.3.1 Motivation for a new Setup

For industrial applications time reduction of a measurement campaign in a wind tunnel is very important. For the classical PSP technique a possible solution is a reduction of the hardware complexity. The previous section indicated that the most time expensive processes are the model painting and light source positioning. The painting processes should be faster and possibly outside the wind tunnel facilities. The light source must be homogeneous and avoid producing shadows independently from model position. The new hardware setup presented in the following section is thought to reduce or eliminate those drawbacks.

### 2.3.2 Setup

The new technique, where an electroluminescent foil (EL-foil) as illumination source is used, is presented in Fig. 2.5. This foil emits light upon excitation by an alternating voltage. The EL lamp is essentially a capacitor structure with phosphor sandwiched between the electrodes. As an AC voltage is applied to the electrodes, the electric field causes the phosphor to rapidly charge and discharge, resulting in the emission of light during each cycle. A schematic view of a typical EL-lamp is illustrated in Fig. 2.4. The foil used as excitation source is fixed to the

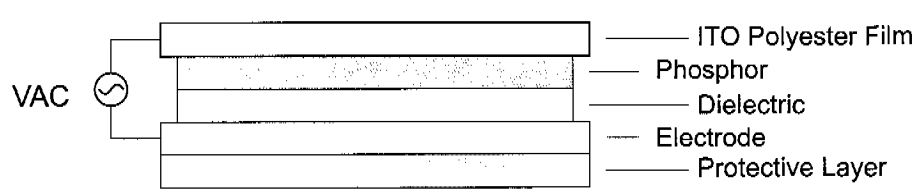


Figure 2.4: Structure of EL-lamp.

model surface with a previously sprayed layer of PSP on it. A CCD camera with a high-pass filter or with a spectrometer is used to acquire the desired paint emission intensity. The main benefit of the setup is the simplified hardware setup and the possibility of painting the EL-Foil outside the wind tunnel. Another important benefit is achieved with the light source on the model surface. The error introduced by the displacement of the model (wind $ON$ / wind $OFF$) is therefore reduced. The inhomogeneities of the illumination moves with the model and no lighting

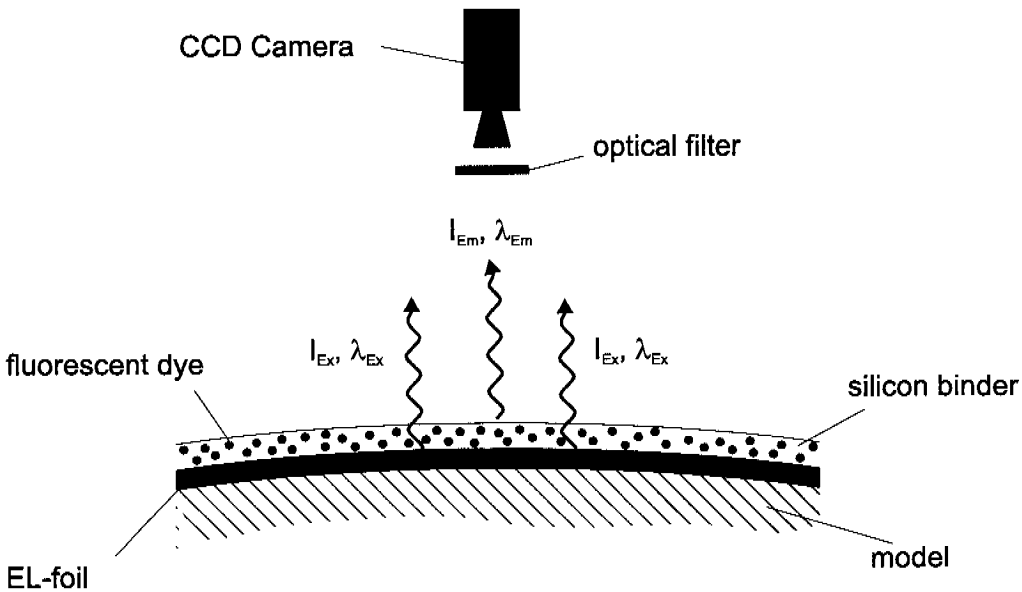


Figure 2.5: Modification of the PSP setup.

shadows are obtained in the measurement region. The self-illumination problem can be alleviated by simply turning ON/OFF the EL-Foils on the different surfaces. A detailed description of the EL-Foil characteristics, properties and benefits will be presented in chapter 4.

# Chapter 3

## *Test Cell Development*

In this chapter the development of an automated PSP calibration tool is described. A Test Cell (TC) was developed to simulate wind tunnel conditions by varying pressure and temperature of PSP samples. A personal computer was used to automatically perform the calibrations by controlling the internal conditions of the TC. Hardware and software solutions adopted are shortly described: more details can be found in appendix A.

## 3.1 Specifications

The TC had to meet some previously agreed specifications. A flexible, fast and automated tool to calibrate or evaluate PSP samples was needed. The TC will be used to simulate PSP pressure measurements in different working conditions, as in a wind tunnel. To allow a wide range of different configurations the possibility to insert test plates with PSP, light filters and illumination foils in a modular way was needed. The most important features of the TC are the changing and setting of the inside pressure and temperature (the inside conditions are monitored with sensors). The ranges vary for the pressure from near vacuum to 2 bar over pressure, and for the temperature, from $10°C$ to $40°C$. The user is able to make standard measurements to calibrate the paint. To obtain qualitative measurements the TC, or better the test plate, must not be under influence of temperature or pressure gradients: that means homogeneous conditions inside the cell. In order to evaluate the dependency of the PSP emission from the angle of view, the test plate can be mounted on a rotating disk.
To summarize, the following specifications were required:

- adjustable pressure: from near vacuum to 2 bar over pressure
- adjustable temperature: from $10°C$ to $40°C$
- homogeneous conditions on the test plate

- modular construction to insert different test plates, luminescent foils, or light filters
- ability to evaluate the angular dependency of the intensity emission
- pressure and temperature sensors to monitor inside conditions

The solutions used to fit the specifications are described in detail in the next sections.

## 3.2 Hardware Description

Fig. 3.1 shows the setup developed according to the required specifications. The main part is the TC, a small aluminum chamber of 10 cm

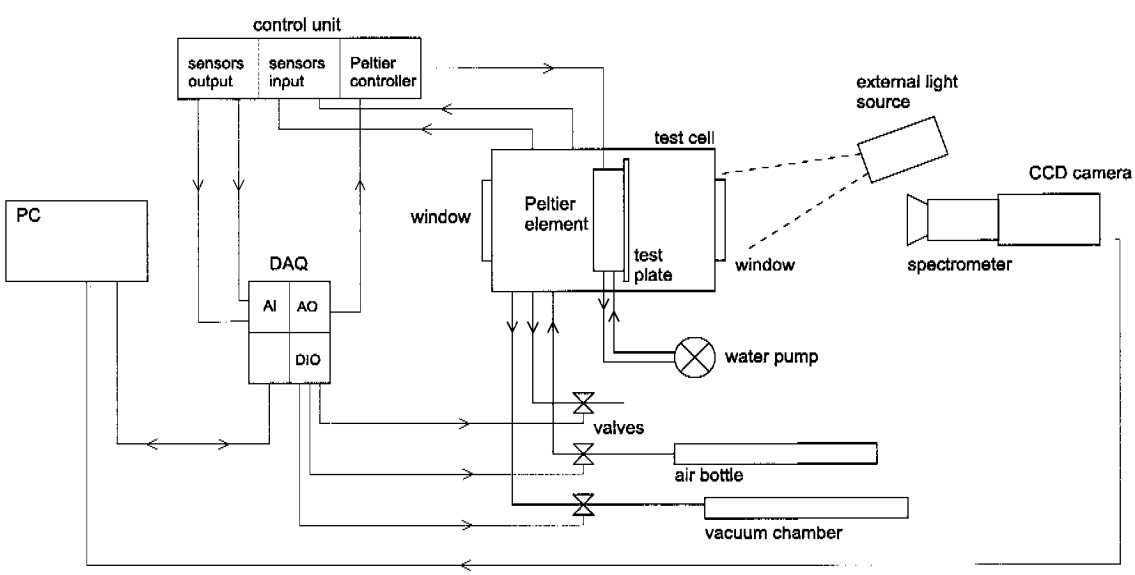


Figure 3.1: Hardware setup.

x 10 cm x 14 cm. Different light sources (external or internal) and different cameras were used. The default camera is a Sensicam[1] from PCO. A Texas Instruments[2] intensified camera was also used during weak light conditions, especially during spectral measurements. To control the electronic devices a PC with a data acquisition card (DAQ) is used. The DAQ is a National Instrument multifunction board (type NI-6036E) with 8

[1] a 1280 x 1024 pixel, 12bit, BW, cooled CCD camera, see appendix A.1.3.
[2] a 656 x 495 pixel, 14bit, BW, cooled CCD camera, see appendix A.1.3.

analog input channels (16 bit), 2 analog output channels (16 bit) and a 8-bit TTL digital input/output (DIO) line (App. A.1.3). The maximum acquisition rate is $200kS/s$. The TC has a top, a bottom and a side window allowing multiple visual access (used by external light sources or by the cameras). A picture of the TC is shown in Fig. 3.2. The aluminum walls of the chamber, milled with a CNC machine, have a grid shape (Fig. 3.2 ❸) to allow the insertion of different plates (with filters, PSP samples or illumination foils) and to avoid unwanted light reflections. A rotating stage (Fig. 3.2 ❹) onto which the plates are mounted, allows the study of the angular dependency of PSP readout on illumination sources or on light emission. This modularity gives the TC a large flexibility to investigate different configurations. The holes (Fig. 3.2 ❶) are used to control and measure the pressure inside the test cell or to introduce another medium than air (e.g., helium) in order to reduce the oxygen partial pressure (simulated vacuum). The feedthroughs (Fig. 3.2 ❷) are used to insert electric cables or thermocouples. To simplify the change of PSP samples a fast opening system was incorporated. The specifications of the hardware are given in appendix A.

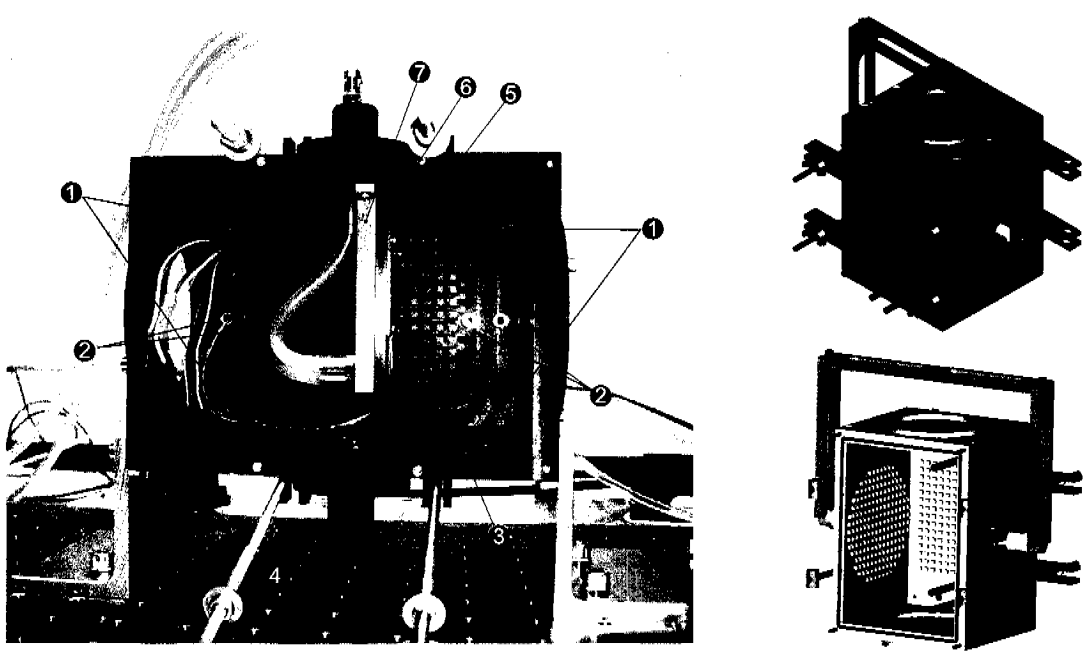


Figure 3.2: Test Cell (TC).

### 3.2.1 Pressure Control

To set and control the pressure inside the cell a very simple solution is applied. Fig. 3.3 shows a schematic view of hardware setup. The inlet and outlet holes (Fig. 3.2 ❶) are used to control the pressure inside the TC. The inlet hole is connected through a pipe to a bottle of compressed air (5 bar): a solenoid valve is placed in-between to control the in-flow rate to increase the pressure. To decrease the inside pressure below the atmospheric pressure an outlet hole is connected to a vacuum camber. A second solenoid valve is used to control the depressurization. A third solenoid valve is used to release the air contained in the TC. The DAQ connected to the PC is used to control the valves and to set the desired inside pressure. A pressure sensor[3] is used to monitor the inside pressure during the setup and measurement phase. The pressure transducer, placed in the control unit, is differential and temperature compensated. It measures the pressure difference $\Delta p = p_{TC} - p_{\infty}$, where $p_{TC}$ is the pressure inside the TC and $p_{\infty}$ is the ambient pressure. The calibration process is described in appendix. A.2.1. The output voltage, proportional to the pressure, is read by the DAQ. The software written to control the pressure is described later.

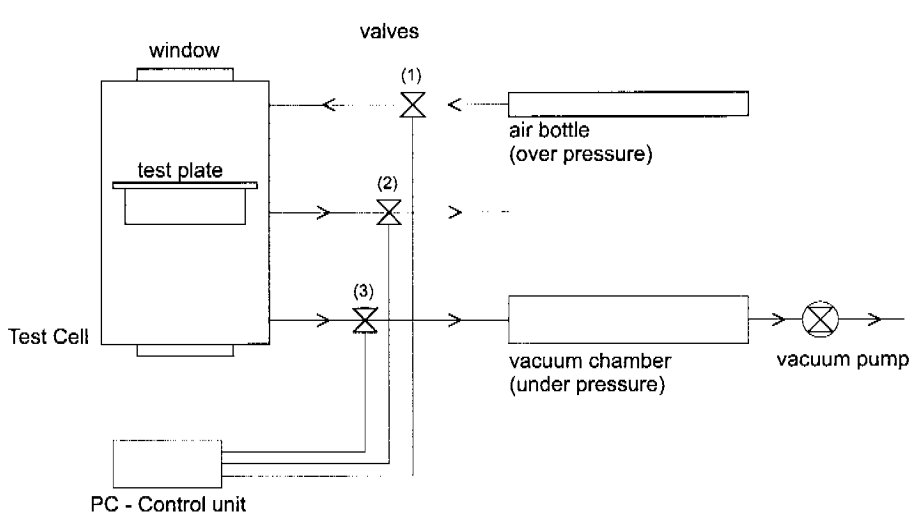


Figure 3.3: Pressure control setup.

[3]see appendix A.1.2.

### 3.2.2 Temperature Control

To control the temperature on the test plate a Peltier element is used. A schematic overview is given in Fig. 3.4. Changing the current

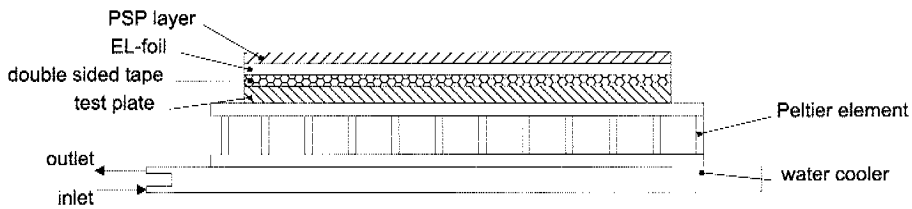


Figure 3.4: Peltier system for TC.

applied to the Peltier element makes it possible to transfer heat from one side of the Peltier to the other one, heating or cooling the aluminum plate (Fig. 3.2 ❺) used as test plate for the PSP samples. To set the required temperature on the test plate a control loop in the control unit is used. The system compares a reference voltage, $V_{ref}$, given by the DAQ with the voltage of a thermocouple, $V_{is}$, placed on the test plate and minimizes the difference $\Delta V$. By changing $V_{ref}$ it is possible to vary the temperature of the test plate. A calibration with an IR camera was performed to correlate $V_{is}$ with the temperature of the test plate (App. A.2.2). A water cooled plate (Fig. 3.2 ❼) is used to remove the heat produced by the Peltier out of the TC. A picture of the Peltier system in the TC is shown in Fig. 3.5. With this setup the temperature range can be varied from $0°C$ to $36°C$ (specifications: $10°C$ to $40°C$).

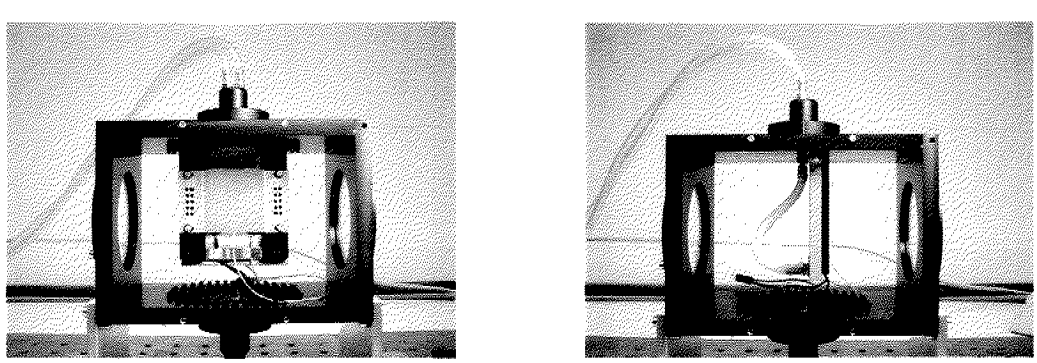

Figure 3.5: Peltier system mounted inside the TC.

An important goal in developing the temperature control was to avoid

temperature gradients on the test plate: a homogeneous temperature distribution is desired. The water channel in the cooling plate was designed to keep the distribution as homogeneous as possible. A problem arising from the first measurements was the complicated way of fixing the PSP sample to the test plate. The PSP was painted directly on the EL-foil and then fixed with a thermally conductive compound to the test plate (Fig. 3.4). To obtain a homogeneous temperature distribution on the test plate the thermal compound had to be applied very carefully yielding not always an acceptable data quality. Better results were obtained by simply using double sided tape. To validate the quality of the Peltier cooling system images with an infrared camera were acquired. A measurement example is illustrated in Fig. 3.6. The temperature distributions on the test plate at $14°C$ and $34°C$ are shown: a good homogeneity is clearly recognizable.

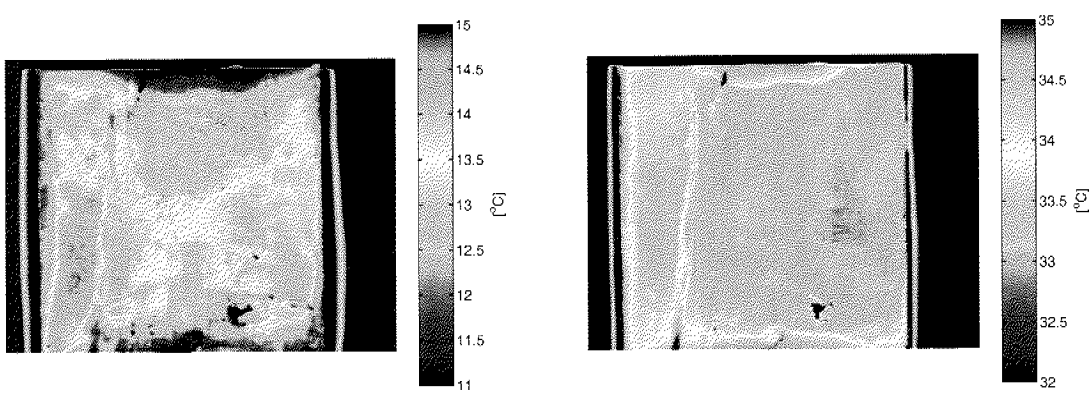


Figure 3.6: IR images of the test plate taken at $14°C$ and $34°C$.

The spatial standard deviation of the temperature (for 8 measurements from $10°C$ to $40°C$) has an average value of $0.4°C$ confirming the good homogeneity. With the aid of the IR pictures it is also possible to correctly position the thermocouple in order to read a representative temperature as accurately as possible.

### 3.2.3 Spectrometer

A good PSP setup is obtained by choosing the correct light source that excites the fluorescent molecules at the right wavelength, and a filter that allows only the red emitted light to reach the camera. To investi-

gate the emission, excitation and absorption wavelengths a spectrometer, Specim ImSpectorV7[4], was used. The basic functional principle is shown in Fig. 3.7: the light entering through a slit is deflected by a prism in dependence of the wavelength. A CCD camera is used to collect the light intensity. The result is an image with spectral resolution on the y-axis and spatial resolution on the x-axis. This allows the measurement of the spectrum on a line with a single picture.

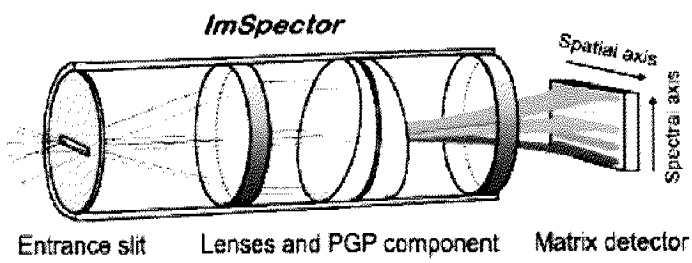


Figure 3.7: ImSpector, Prism-Grating-Prism (PGP) technique.

The spectrometer is simply mounted between camera and lens (Fig. 3.8). The measurable wavelength range goes from 400 nm to 710 nm with a spectral resolution of $\pm 2$ nm. The calibration process is described in App. A.2.3.

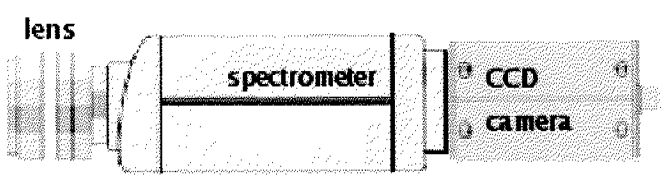


Figure 3.8: ImSpector.

## 3.3 Software Description

The software to control the TC environment, acquire data and automate the calibration and measurement of PSP emission was developed in a modular way for a better flexibility. Fig. 3.9 shows a schematic view of the program. The most important part for the user is the Graphical

[4]see appendix A.1.3.

User Interface (GUI) which gives the user the control over the TC and monitors the inside TC conditions by using five different modules:

1. data acquisition
2. pressure control
3. temperature control
4. image acquisition
5. data evaluation.

The main part of the software was developed using MATLAB 6.5.1 and MATLAB 7.1[5]. Some libraries were written in C++ to increase the execution speed or for a better compatibility with the different hardware devices (e.g., CCD cameras).

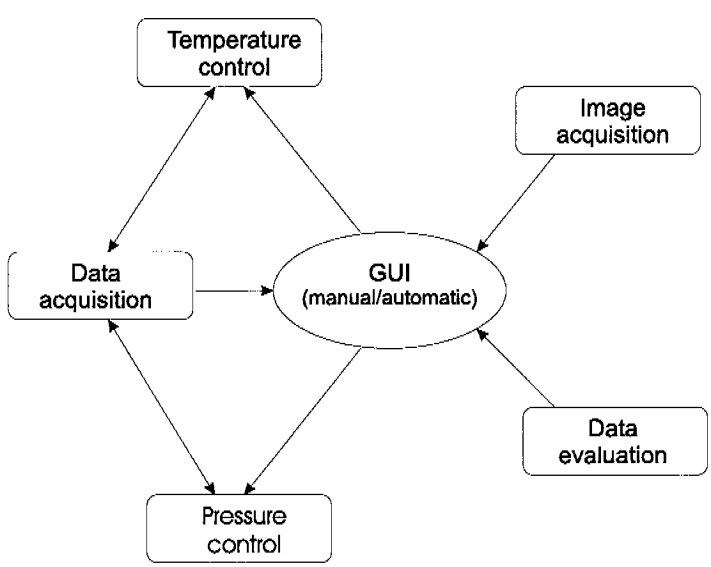


Figure 3.9: Schematic software description.

**Graphical user interface** A simple GUI including basic functions that gives the user full control of the TC was developed. The main features included are:

[5]MATLAB is a product from MathWorks Inc. (www.mathworks.com)

- *Automated measurement settings*: perform an automated calibration process by automatically varying pressure and temperature with customizable ranges (Fig. 3.10 ❶).
- *Camera settings*: settings for the CCD camera (Fig. 3.10 ❷) especially developed for the Sensicam.
- *Data monitor*: monitor all the input data. Read and display voltages of the input channels acquired with the DAQ board, especially temperatures of the thermocouples and the pressure inside TC (Fig. 3.10 ❸). Display a live picture or a snap shot image of the camera in a separate window.
- *Manual settings*: manual setting of test plate temperature and pressure (Fig. 3.10 ❹).
- *Visualization window*: display a fast evaluation of the acquired data: intensity plot, spectral response, or acquired images (Fig. 3.10 ❺).

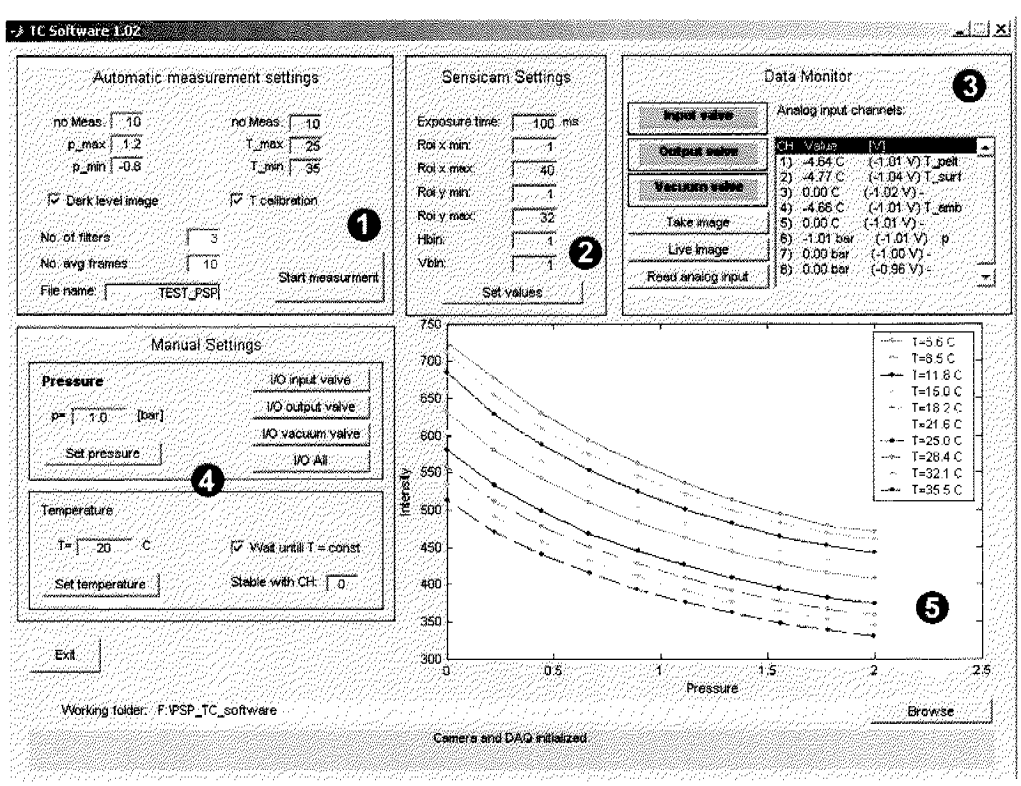


Figure 3.10: TC Control GUI.

### 3.3.1 Module Description

**Data acquisition** This first module acquires data from the NI-DAQ. Channel 1 is used to acquire the temperature on the Peltier element, channel 2 for the temperature on the test plate (thermocouple directly applied to the PSP sample) and channel 3 for the ambient temperature. The pressure inside the TC is monitored using channel 6.

**Pressure control** The pressure inside the TC is controlled by opening the input/output valves. This module is used to set the pressure inside the TC. The algorithm (setPressure.m) used to control the solenoid valves, and therefore the pressure, is described in Fig. 3.11. The function

**Require:** $-0.8\ bar < p < 2.5\ bar$
  **if** $p = 0$ **then**
    **while** $p \neq 0$ **do**
      open release valve
    **end while**
  **else**
    **for** i:=1 to number of refinements **do**
      **if** $p > p_{actual}$ **then**
        **while** $p > p_{actual}$ **do**
          open input valve (air bottle)
        **end while**
      **end if**
      **if** $p < p_{actual}$ **then**
        **while** $p < p_{actual}$ **do**
          open output valve (vacuum chamber)
        **end while**
      **end if**
    **end for**
  **end if**

Figure 3.11: Function *setPressure(p)*.

compares the desired final pressure $p$ with the actual pressure $p_{actual}$ and correnspondigly opens the correct valve. This process is repeated n-times to refine the pressure value (usually n=3). The pressure can be set very quickly (1 to 4 s) with a good accuracy (0.001 bar).

**Temperature control** The temperature control is the most complex module of the TC software. It compares a reference voltage with a voltage coming from a thermocouple applied on the PSP sample. The difference multiplied by a factor (given in the hardware controller) returns the current intensity that must be applied to the Peltier to cool or heat the test plate. The heat produced by the EL-foil slightly changes the paint temperature and therefore a continuous temperature correction is performed. For this reason it is very difficult to exactly set the temperature of the paint. Nevertheless it is possible to exactly measure the temperature with the aid of the thermocouple. Fig. 3.12 shows the calibration curve to compute the required voltage as a function of the desired test plate temperature. Several minutes are necessary to obtain a stable and

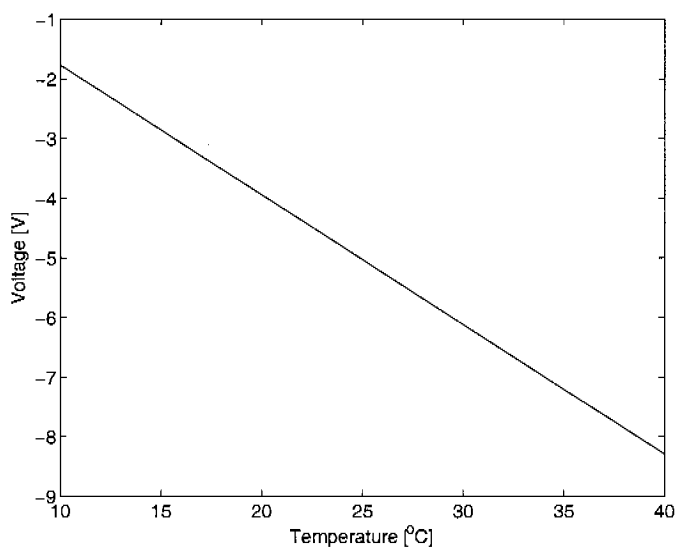


Figure 3.12: Calibration curve.

homogeneous temperature distribution on the test plate. Therefore for an automatic measurement the temperature is held constant during a pressure ramp to save time. The algorithm used to control and set the temperature is described in detail in appendix A.3.

**Image acquisition** The code for the different CCD cameras was developed by using the manufacturer-provided C++ libraries. The basic functions written in C++ are compiled as a run-time library (DLL) and differ slightly from one camera the other. A parameter in the GUI MATLAB code allows the user to select the desired camera type depending

on the measurement requirements.

**Data evaluation** For the data evaluation various functions were developed. Two different functions included in the GUI compute and display the results of the measurements. The first is used for typical PSP response curves (intensity measurements). The intensity is plotted against pressure for different temperatures. The possibility of plotting the ratio with a reference image taken at ambient pressure and temperature is also included.
The second functionality is used during spectral measurements. The code takes a picture from the camera and converts it to a plot with intensity as a function of wavelength for different pressures and temperature steps.

### 3.3.2 Automated measurements

This part of the code combines the previously described modules in order to automatically calibrate or measure PSP responses. A schematic overview of the algorithm is illustrated in Fig. 3.13. The routine initializes the CCD camera and reads from the GUI the ranges for pressure, temperature and the number of steps. The initial temperature ($T_{min}$) is set and a pressure ramp from $p_{min}$ to $p_{max}$ is executed. The algorithm is then repeated with $T_{new} := T_{previous} + T_{step}$ until $T_{max}$ is reached. During the automatic measurement session the acquired data are saved in the "working folder". For every temperature and pressure step a file is saved in MATLAB format with the name "FILENAME_%X_%Y.mat". The indices %X and %Y refer to the temperature and pressure steps. A reference file, taken at ambient pressure and temperature, is saved as "reference_FILENAME.mat". Every file contains the image acquired with the CCD camera and the values of the NI-DAQ input channels (in volts). The settings of the whole measurement (camera setup, pressure range, number of pressure steps,...) are stored in a file named "settings_FILENAME.mat". At the beginning of each measurement a dark level image (without excitation light) is stored in "FILENAME_DL.mat".

A detailed description of the software, algorithms and a user manual is given in appendix A.3.

**Require:** $p_{min}, p_{max}, \Delta p, T_{min}, T_{max}, \Delta T$
initialize DAQ board and CCD camera
**while** $T < T_{max}$ **do**
$T = T_{min}$
$p = p_{min}$
**while** $p < p_{max}$ **do**
setPressure(p)
setTemperature(T)
read CCD image
read values
save data to file
$p := p + \Delta p$
**end while**
$T := T + \Delta T$
**end while**
deinitialize DAQ and CCD camera

Figure 3.13: Automated measurement algorithm.

# Chapter 4

## *Laboratory Measurements*

## 4.1 Preliminary Tests

In this chapter some preliminary tests are presented. The properties of fluorescent molecules and of light sources were investigated in order to choose the optimal paint-excitation light system for subsequent development and wind tunnel tests.

### 4.1.1 Emission Properties of Different PSPs

Different PSPs formulations were studied. For this purpose three different fluorescent molecules were used (an overview is given in Tab. 4.1).

| | | |
|---|---|---|
| 1 | Name: | Bathophenanthroline Ruthenium Chloride |
| | | **Ru(dpp)** |
| | Formula: | $(C_{24}H_{16}N_2)_3RuC_{12}$ |
| 2 | Name: | Pt(II)meso-Tetra(pentafluorophenyl) Porphine |
| | | **PtTFPP** |
| | Formula: | $C_{44}H_8F_{20}N_4Pt$ |
| 3 | Name: | Pt(II) Octaethylporphine |
| | | **PtOEP** |
| | Formula: | $PtC_{36}H_{44}N_4$ |

Table 4.1: Investigated fluorescent molecules.

The first investigated PSP is a Ruthenium-based paint. Ruthenium molecules are widely used as oxygen sensors. The main advantages of this metal are high emission intensity, low photobleaching and the capability to be exited by a large wavelength band. The are different types of Ruthenium molecules used for PSP techniques. In the following section the behavior of bathophenanthroline ruthenium chloride is shown. The

Ru molecules are embedded in a silicone binder. RTV 118 silicone from General Electric is used due to its good oxygen permeability. Both, Ru and RTV 118, are dissolved in dichloromethane. The formulations of the different PSPs are described in appendix B.
The absorption and emission spectrum of the paints were investigated. To measure the absorption a reference spectrum, white card, was taken. The absorption rate was computed with:

$$\text{absorption} = \frac{I_{white_{ref}} - I_{PSP}}{I_{white_{ref}}}$$

Due to possible non-uniformities of the "white" spectrum the measured absorption has to be considered as a qualitative result only. The measurements were done at atmospheric pressure and at room temperature.

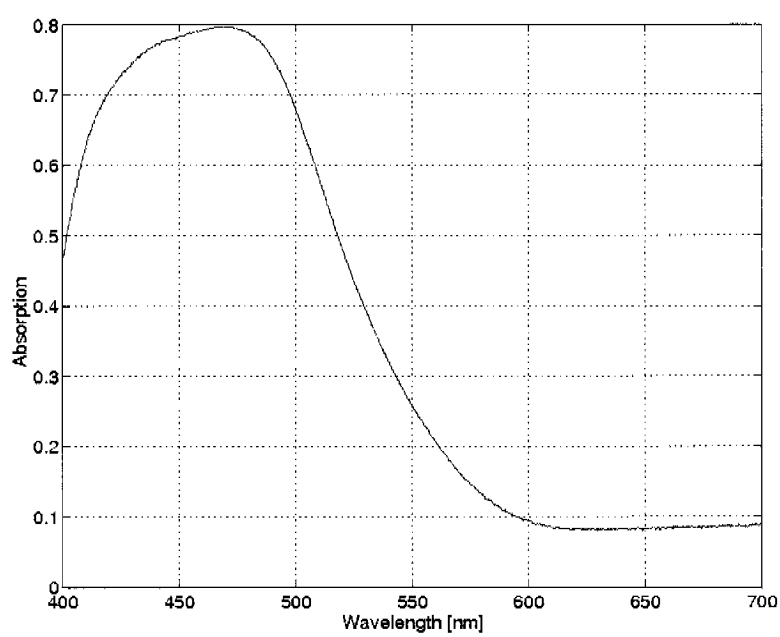


Figure 4.1: Absorption of Ru(dpp) in RTV 118.

**Ru - based PSP:** As shown in Fig. 4.1 Ruthenium absorbs light of wavelengths ranging from ultraviolet to blue-green (measurable from 400 nm to 550 nm). The maximum absorption is located at 470 nm

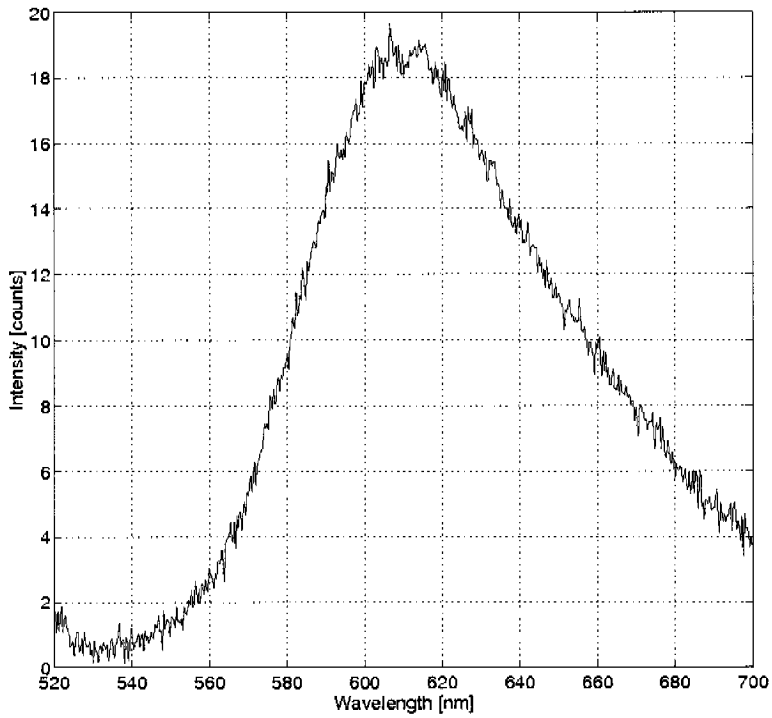


Figure 4.2: Emission of Ru(dpp) in RTV 118.

with an absorption value of about 80%. This property allows the use of a wide range of illumination light sources. In Fig. 4.2 the Ru sample is excited with a blue LED lamp. The emission is located in the red region and extends from 560 nm to 700 nm. The emission peak is at about 610 nm. This value is slightly higher than those found in the literature: 605 nm in [19] and 600 nm in [16].

**Pt-based PSP:** The second type of PSP investigated are platinum (Pt) based paints. The main advantages of Pt based fluorescent molecules are a good sensitivity to oxygen changes and a high emission intensity. Compared to Ru, Pt molecules are more affected by photobleaching. Two different types of Pt molecules were investigated: PtTFPP and PtOEP. As for Ru, the Pt molecules are dissolved in dichloromethane and embedded in RTV 118. Figs. 4.3 and 4.4 show the absorption spectra of both Pt paints. The excitation of the paint occurs between 400 nm and

560 ÷ 570 nm. Different local maxima are visible, due to the different excitation levels (Sec. 2.1.1), with a maximum absorption of about 70%. Compared to Ru paint, Pt absorbs in a similar wavelength range in a less efficient way: maximum absorption is 67% at 540 nm for PtTFPP and 69% at 542 nm for PtOEP. PtTFPP shows two absorption leaks at about 480 nm and 520 nm.

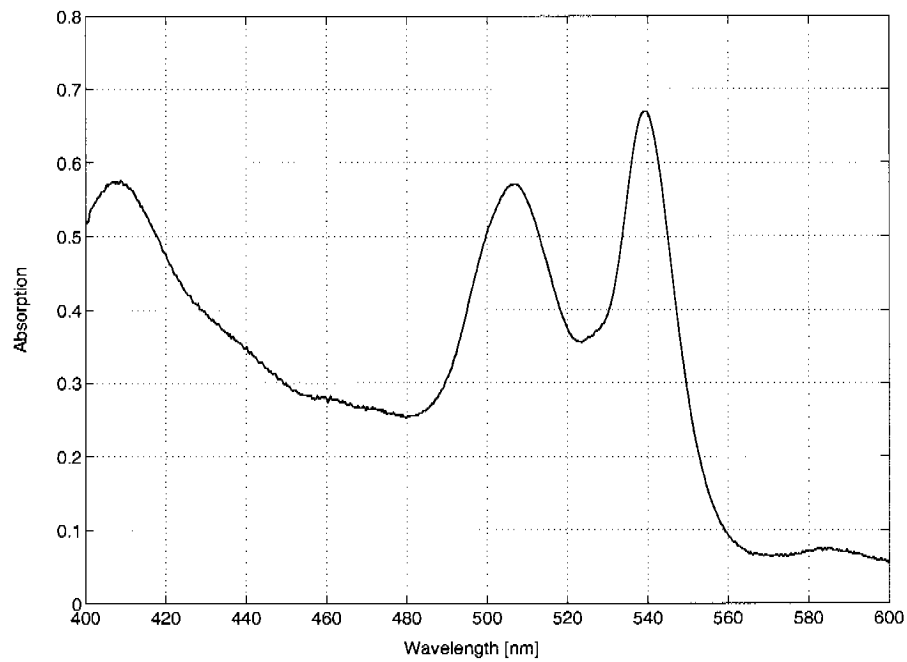


Figure 4.3: Absorption of PtTFPP in RTV 118.

Figs. 4.5 and 4.6 show the emission spectrum of PtTFPP and PtOEP samples illuminated with the blue LED lamp. The emission peak for PtTFPP is located at 650 nm. For PtOEP the maximum of intensity is reached at 646 nm. Notice that the emission intensity is lower compared to the Ru-based PSP. A summary of the absorption and emission of the different luminophores and a comparison with the literature is given in Tab. 4.2. The measured emission peaks are in good agreement with the values measured by Mebarki [19] and Sullivan et all. [16]. The absorption properties differ slightly from the published measurements: a possible explanation is the more qualitative measurement of the absorption rate presented in the this work. Another factor affecting the absorption of the Pt-based paints is the different binder used: RTV 118 instead of silica gel.

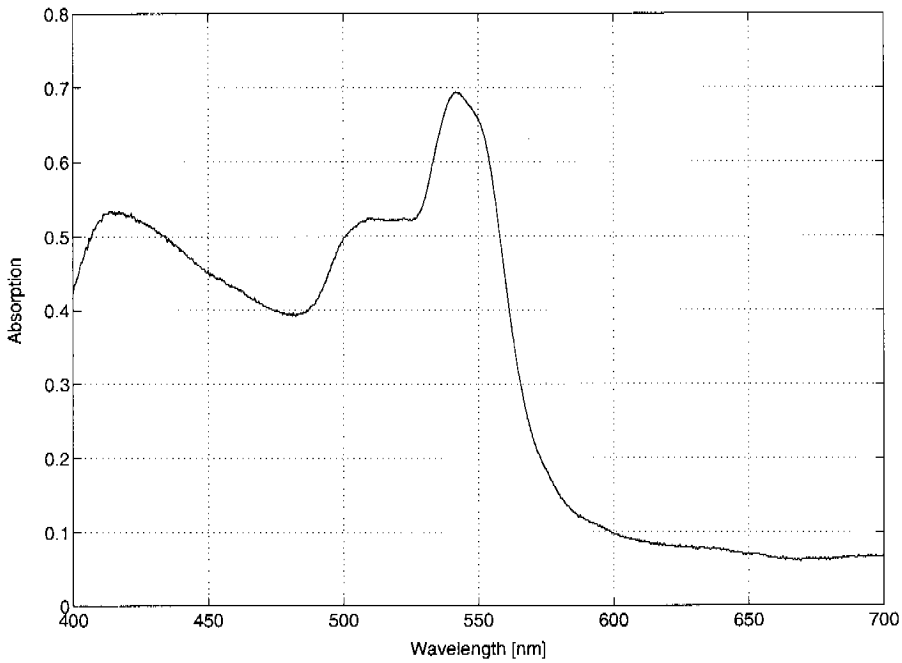


Figure 4.4: Absorption of PtOEP in RTV 118.

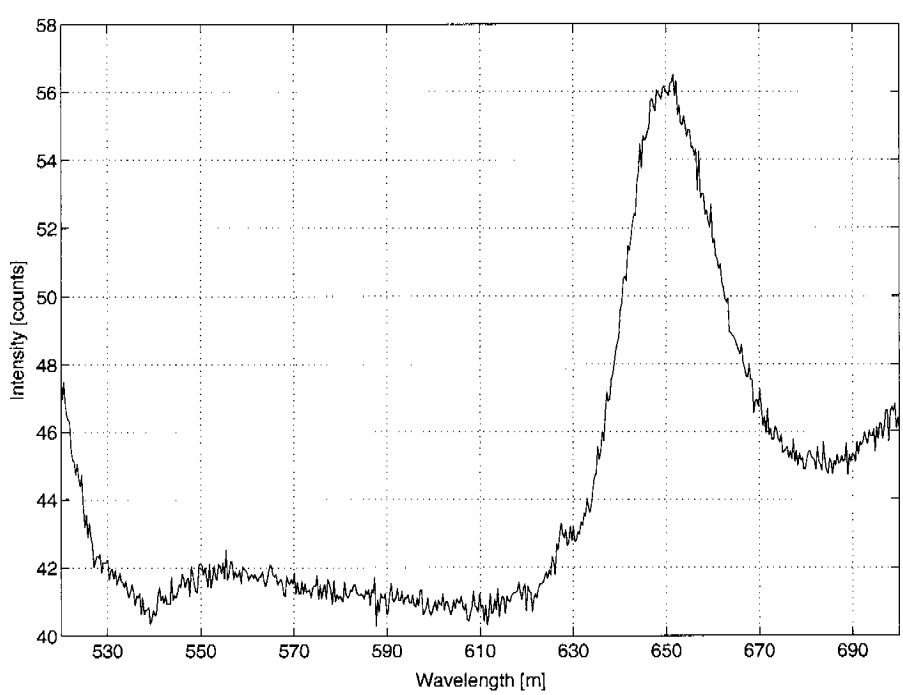


Figure 4.5: Emission of PtTFPP in RTV 118.

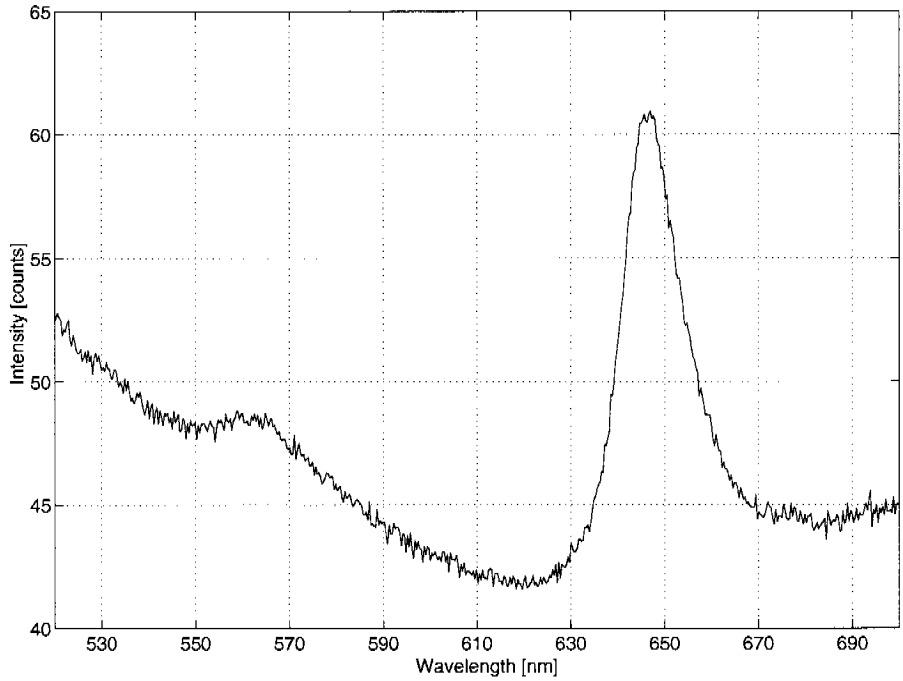


Figure 4.6: Emission of PtOEP in RTV 118.

| Luminophore | Measured | | In [19] | | In [16] | |
|---|---|---|---|---|---|---|
| | $\lambda_{ems}$ | $\lambda_{abs}$ | $\lambda_{ems}$ | $\lambda_{abs}$ | $\lambda_{ems}$ | $\lambda_{abs}$ |
| Ru(dpp) | 610 | 470 | 605 | 450 | 600 | 337, 457 |
| PtOEP | 646 | 416, 542 | 650 * | 380-530 * | 650 * | 366, 543 * |
| PtTFPP | 650 | 408, 506, 540 | 650 * | 390-530 * | 650 * | 390 * |

* Embedded in silica gel and not in RTV 118.

Table 4.2: Emission and absorption properties comparison.

### 4.1.2 Emission Properties of Illumination Sources

To find the optimal illumination source, spectral measurements were performed. The comparison between light sources was done by simply measuring the emission spectrum at room temperature and atmospheric pressure using no camera filters. Tab. 4.3 summarizes the different illumination sources used during the tests. The blue LED lamp ❶ was used

as reference and as comparison for the light emission of the different EL-foils.

| No. | Illumination source | Type | Em. peak [nm] |
|---|---|---|---|
| ❶ | blue LED lamp | - | 460 |
| ❷ | blue EL-foil (A) | Lumitec ELF2007 | 452 |
| ❸ | green EL-foil | Lumitec ELF1659 | 506 |
| ❹ | green EL-foil with filter | Lumitec ELF1659 | 500 |
| ❺ | blue EL-foil (B) | Lumitec ELF1655 | 452 |

Table 4.3: Investigated illumination sources.

Fig. 4.7 shows the emission spectrum of the blue LED lamp ❶. The emission intensity is plotted against the wavelength with the emission peak located at about 460 nm. Compared to the light emission of an EL-foil (Fig. 4.8 or Fig. 4.9) the emission band is very narrow and there is no emission above 520 nm. The spectral characteristics of the LED lamp fit very well the excitation criteria for the Ru based PSP, while the Pt-based paint is not optimally excited.

The EL-foils excite the fluorescent molecules over a wider wavelength range due to their larger emission band. Figs. 4.8 to 4.9 show a peak at about 452 nm for the blue EL-foils ❷ and ❺, 506 nm for the green ❸ and 500 nm for the green EL-foil with filter ❹. The main disadvantages of the EL-foils compared to the LED light sources are two. First the emission intensity is lower, meaning a lower excitation of the paint. Further investigations have shown a doubled emission intensity of the green EL-foil compared to the blue one. The second drawback is an overlap of the emission with the red emission of the paint. By looking at the Stern-Volmer equation (Eq. (2.23)) it is clear that an offset in the intensity emission of the paint causes a loss of sensitivity of the PSP response. A possible solution to this problem seems to be the use of a filter applied directly to the foil (Fig. 4.9). This particular EL-foil, specially built by Lumitec for this test series, has an optical filter that cuts the emission in the red region. The filter decreases the emission intensity by a factor 2 but decreases the overlap of the emission of foil and paint. The green EL-foils show a higher emission intensity compared to the blue ones, but with higher leakage. The choice of the EL-foil is a compromise be-

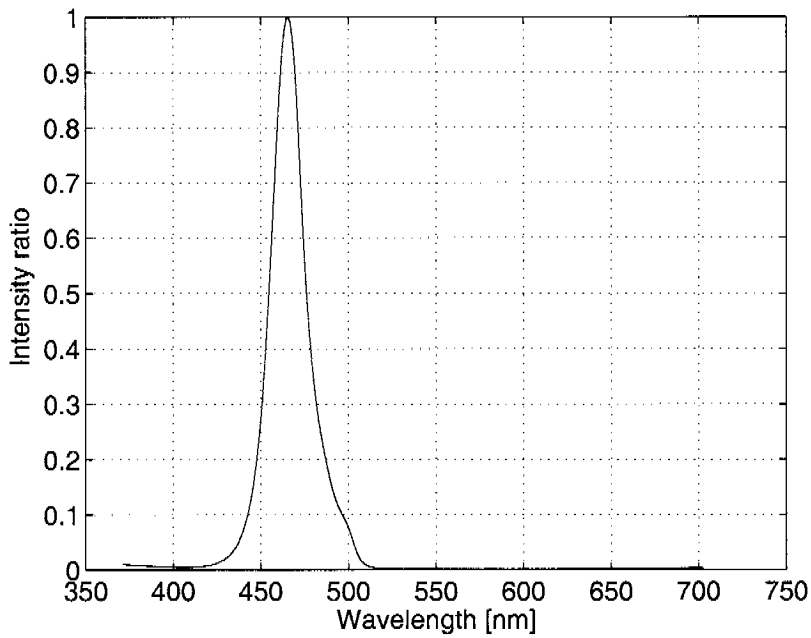


Figure 4.7: LED lamp emission spectrum ❶.

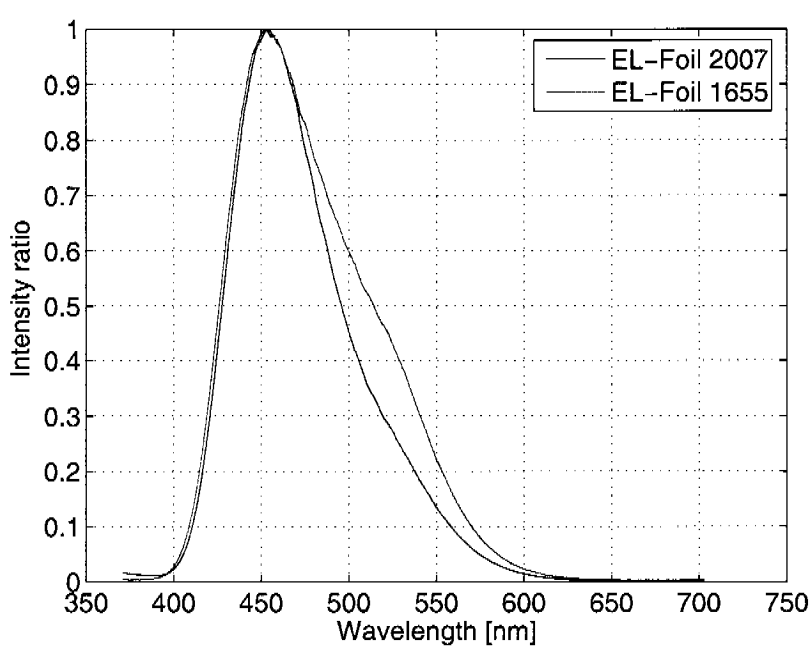


Figure 4.8: Blue light foil emission spectrum ❷+❺.

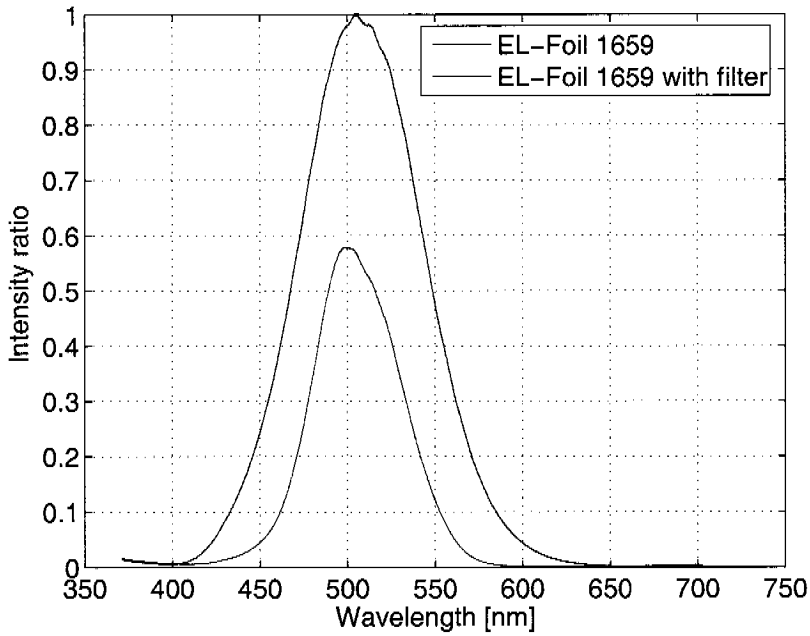


Figure 4.9: Green light foil emission spectrum ❸+❹.

tween required illumination intensity and paint sensitivity. Laboratory measurements with the different illumination sources are illustrated and discussed in Sec. 4.2.

## 4.2 PSP Systems Characterization

This section gives an overview of the response to pressure and temperature changes of EL-foils alone and of EL-foils with PSP. Results with the classical intensity measurement technique are illustrated. For a better understanding of the behavior at different wavelengths spectral measurements are also presented and a comparison of the PSP-System sensitivity with the classical PSP (LED) is performed. The list of the presented laboratory measurements is summarized in Tab. 4.4. The complete measurement list is given in appendix E.1.

Measurements number 1 to 3 were performed in order to characterize the response of the EL-foils to pressure and temperature changes. Sec. 4.2.2 illustrates the properties of Ru-based PSPs (meas. 4 to 9). Pt-based PSP are investigated in Sec. 4.2.3 (meas. 10 to 11).

| No. | Illumination source | Paint | p range [bar] | T range [$^{\circ}C$] | Filter |
|---|---|---|---|---|---|
| 1 | blue EL-foil ❺ | - | $0 \div 2$ | $0 \div 40$ | - |
| 2 | green EL-foil ❸ | - | $0 \div 2$ | $0 \div 40$ | - |
| 3 | green EL-foil ❹ | - | $0 \div 2$ | $0 \div 40$ | Spectrometer |
| 4 | LED | Ru(dpp) | $-0.8 \div 1.2$ | $20 \div 30$ | OG 610 |
| 5 | LED | Ru(dpp) | $-0.6 \div 1.2$ | $10 \div 30$ | Spectrometer |
| 6 | green EL-foil ❸ | Ru(dpp) | $-0.8 \div 1.2$ | $20 \div 30$ | OG 610 |
| 7 | green EL-foil ❸ | Ru(dpp) | $-0.6 \div 1.2$ | $10 \div 30$ | Spectrometer |
| 8 | blue EL-foil ❺ | Ru(dpp) | $-0.8 \div 1.2$ | $20 \div 30$ | OG 610 |
| 9 | blue EL-foil ❺ | Ru(dpp) | $-0.8 \div 1.2$ | $20 \div 30$ | Spectrometer |
| 10 | green EL-foil ❸ | PtOEP | $-0.8 \div 1.2$ | $20 \div 30$ | OG 630 |
| 11 | blue EL-foil ❺ | PtOEP | $-0.8 \div 1.2$ | $20 \div 30$ | OG 630 |

Table 4.4: Laboratory measurements.

### 4.2.1 Temperature Dependence of EL-foil(s)

In this section the light emission of the EL foils is investigated by measuring the emission intensity as function of temperature and pressure. The EL-foil samples were placed in the TC and the intensity response was measured (1 to 3) varying the temperature from about $0^{\circ}C$ to $40^{\circ}C$ and the pressure ranging from 0 to 2 bar over-pressure. The Sensicam with a Nikon Nikkor 60 mm lens and without any filter was used to acquire the images. The measurements were performed on two different EL-foils: the blue (❺) and the green EL-foil (❸).

The result of the measurement for the blue EL-foil is shown in Fig. 4.10. The intensity emission of the EL-foil alone shows only a temperature dependence [1,2]: a property that can be used to compute the calibration variables A(T),B(T),... of the Stern-Volmer equation (Eq. (2.23)). The pressure maps can then be computed (the temperatures shown in the plot legend are mean values). The intensity changes for the same mean temperature value are caused by temperature fluctuations on the test

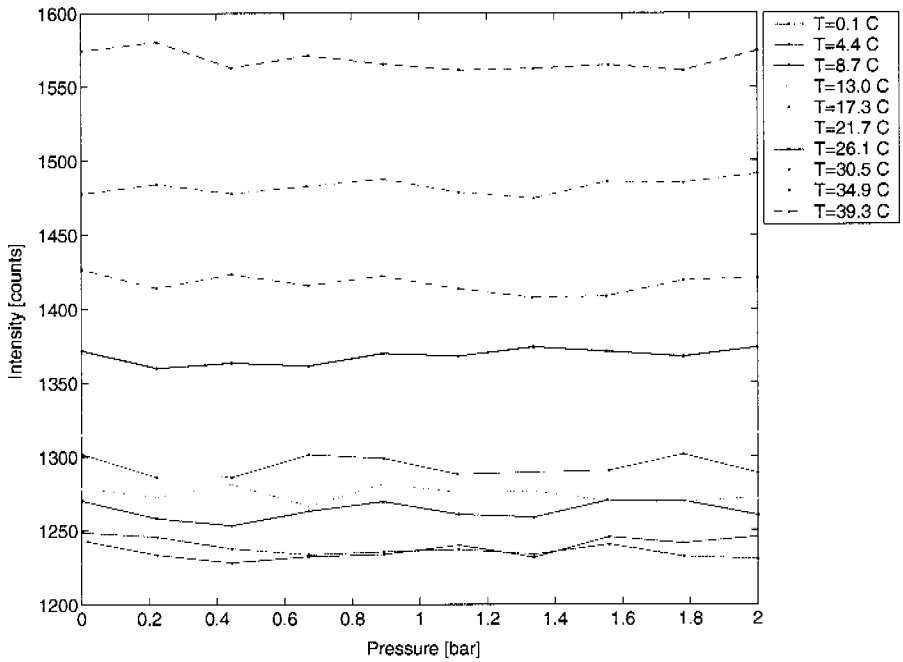


Figure 4.10: Blue EL-foil ❺ emission.

plate and from noise in the measurement. For a better visualization of the temperature dependence a mean value of the intensity for all pressure steps was computed. The results are illustrated in Fig. 4.11 for the blue EL-foil and in Fig. 4.12 for the green EL-foil.

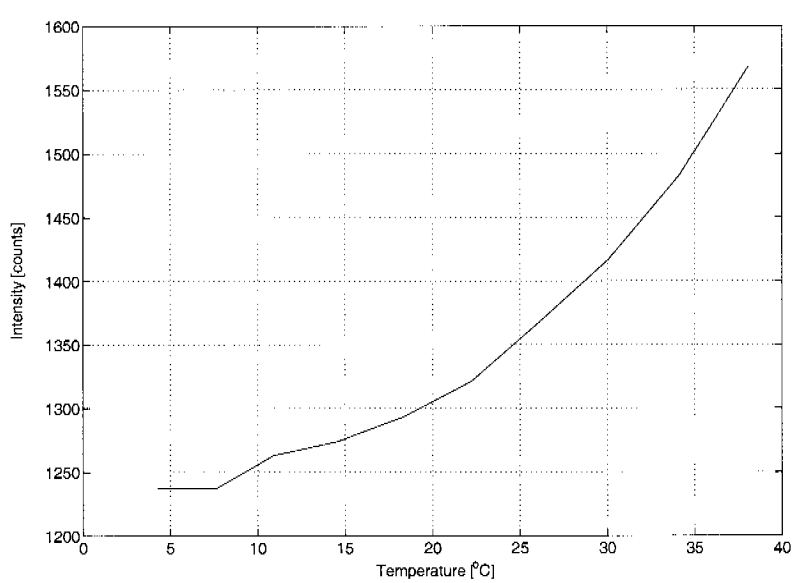


Figure 4.11: Blue EL-foil ❺ temperature dependence.

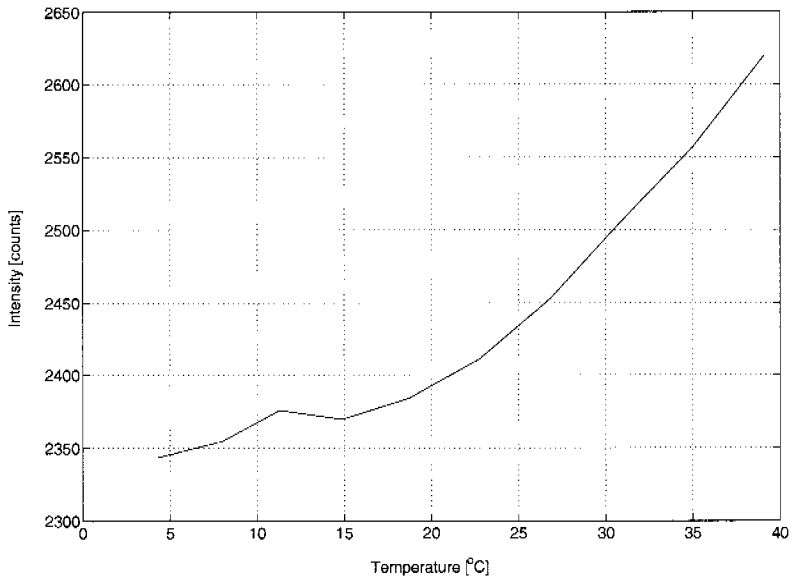


Figure 4.12: Green EL-foil ❸ temperature dependence.

The plots show a clear and similar temperature dependence with a small local maximum located at about $12°C$. As expected the green foil emits with a higher intensity (2300/2600 counts) compared to the blue one (1200/1500 counts). Due to the local maximum good temperature measurements using the EL-foil emission intensity can only be performed for temperatures higher than $15°C$.
For a better understanding of the emission properties, in particular the local maxima, spectral measurements were performed. Fig. 4.13 shows the spectral response of the green EL-foil (❹) at different wavelengths. The spectral response is normalized with a reference spectrum taken at $3.4°C$ and ambient pressure.

Below $450 - 470$ nm the emission intensity decreases with increasing temperatures. Between 470 nm and 640 nm the intensity increases with increasing temperature. Measuring the intensity changes with a CCD camera without a spectrometer is the same as collecting the integral of the curve. For this reason in the previous plots (Fig. 4.11 and Fig. 4.12) there was a local maximum located at about $12°C$. Notice that spectral measurements on the blue EL-foils show a reduced intensity decrease with an increasing temperature below 470 nm. Fig. 4.11 confirms this behavior by showing a less prominent peak.

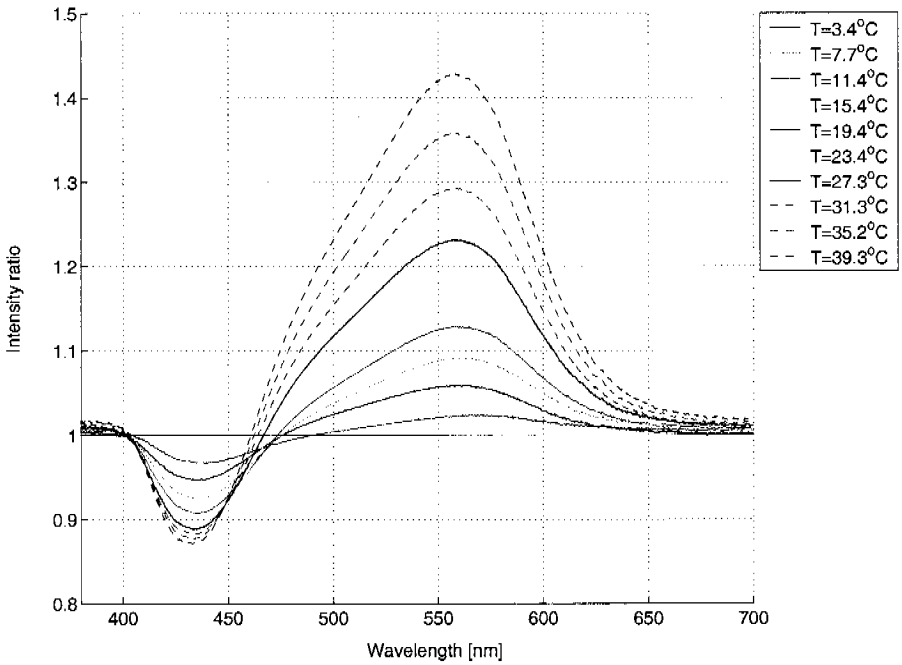


Figure 4.13: Spectral response of green foil with filter ❹.

### 4.2.2 Ru(dpp)-based PSP System

In this section measurements done with the Ru-based PSP are presented. The aim of the tests is to identify the quality, characteristics and properties of the new PSP setup. A first measurement of the PSP response with a traditional setup (LED lamp) was performed and is used as comparison with the new setup. Two different configurations, namely with blue EL-foil ❺ and with green EL-foil ❷, are presented. Intensity responses and spectral characteristics are investigated.

**LED** An intensity response measurement was performed. The CCD camera[1] was equipped with a Nikon 60 mm lens and a Schott OG 610 filter and an external LED lamp was used. The pressure was varied from $-0.8$ to 1.2 bar over-pressure and the temperature from $\approx 20°C$ to $\approx 30°C$. The result is shown in Fig. 4.14. The plot shows a typical PSP response to pressure and temperature variations.

The pressure sensitivity is computed by taking the slope in Fig. 4.14 at $p = p_{atm}$ and $T = 19.7°C$. A sensitivity of 67% is obtained and used as reference to evaluate the quality of the EL-foil setup. The measure-

[1] PCO, Sensicam.

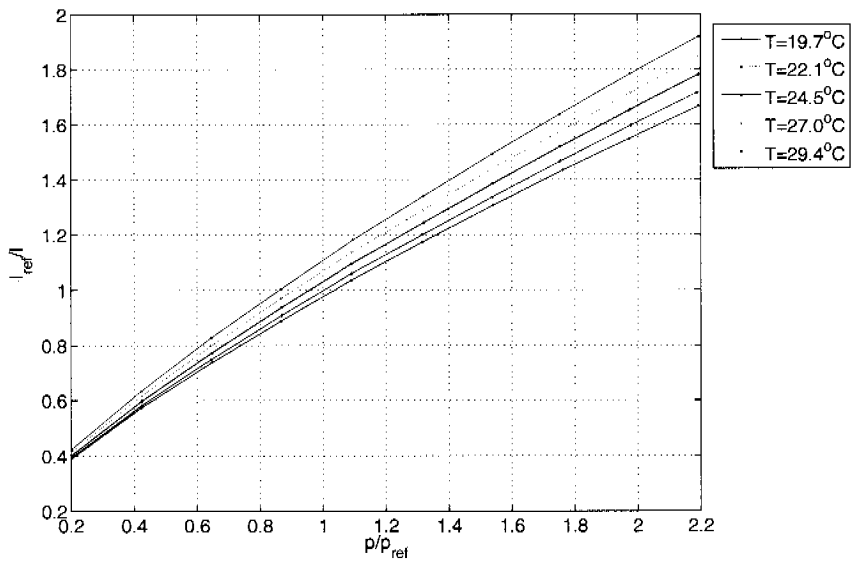


Figure 4.14: Ru based PSP, LED light source.

ment was repeated with the spectrometer. The spectral responses for a pressure range from 0.4 bar to 2.2 bar (10 steps) at $T = 14.5°C$ and $T = 29.2°C$ are illustrated in Figs. 4.15 and 4.16.

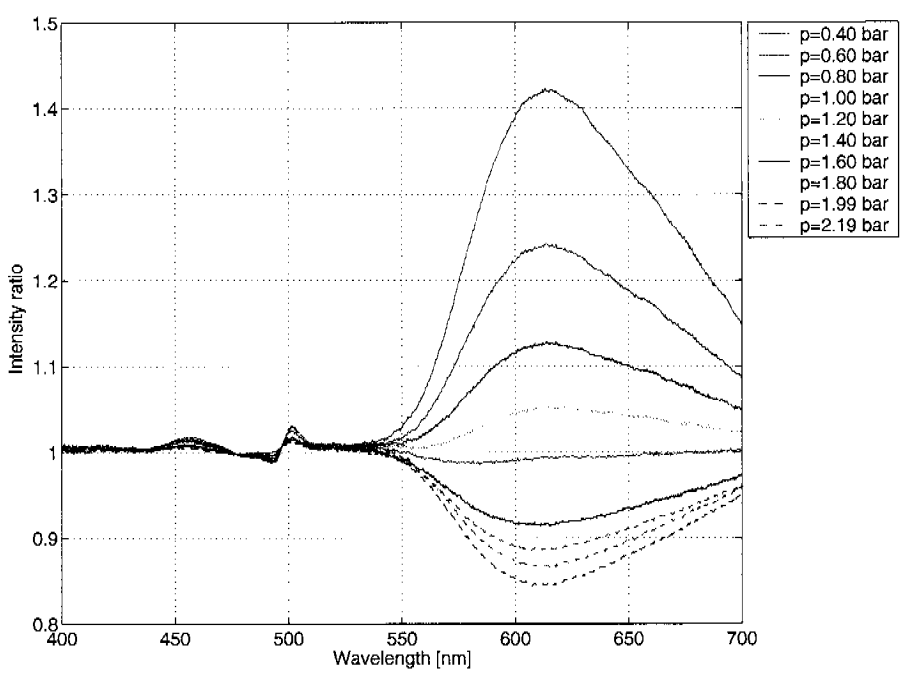


Figure 4.15: PSP response with LED ($T = 14.5°C$).

As expected the pressure and temperature dependencies of the PSP are clearly visible. An interesting response to temperature changes is visible in the emission region of the LED lamp ($430 \div 530$ nm).

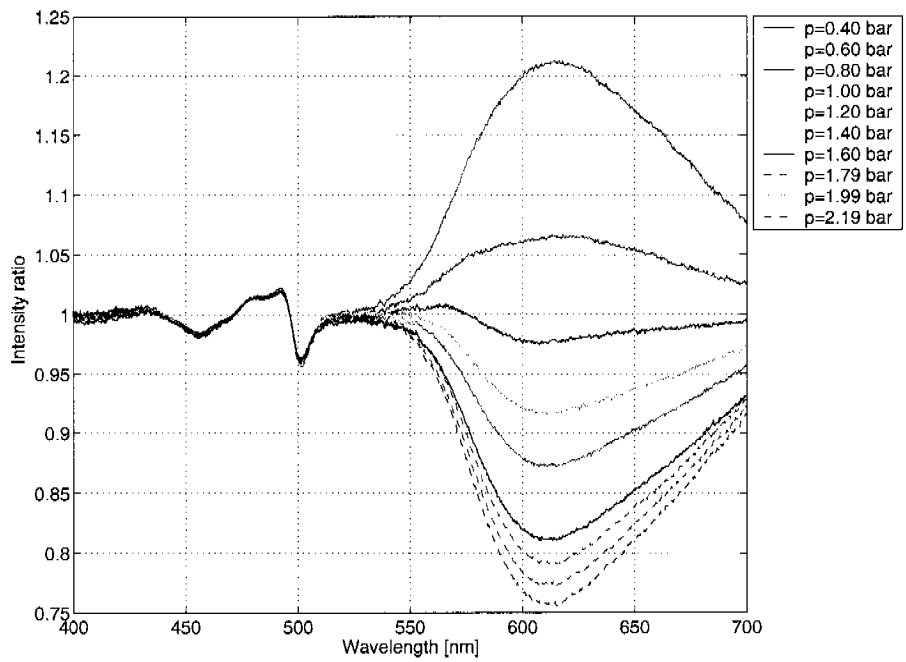


Figure 4.16: PSP response with LED ($T = 29.2°C$).

For this test the Ru paint was sprayed on the EL-foil and illuminated with an external LED light. A more detailed investigation could be very interesting in order to understand if the temperature dependence in the blue region depends on absorption changes of the Ru or of the phosphor contained in the EL-foil substrate.

**Green EL-foil** The intensity response with the green EL-foil is shown in Fig. 4.17. The response of the PSP to changes in pressure and temperature is similar to the one shown in Fig. 4.14. The main difference is the less regular separation between isothermal lines with a corresponding reduction of the temperature dependence. The pressure sensitivity is decreased from 67.0% to 45.0%. For a better understanding of the irregularities the measurement was repeated using the spectrometer.

The results of the spectral response measurement, normalized with data at $T = 20.0°C$ and $p = p_{atm}$, are shown in Figs. 4.18 and 4.19. Some interesting observations can be made: as in Fig. 4.13 it is possible to see the dependency of the EL-foil emission on the temperature.

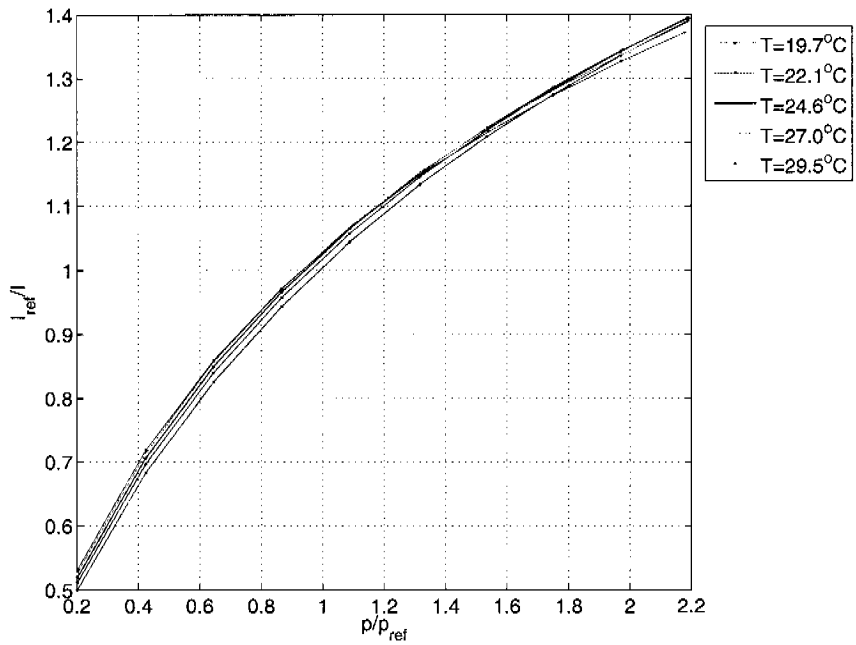


Figure 4.17: Ru based PSP, green EL Foil ❸.

The main difference from the previous plot is that a pressure dependence is visible. In Fig. 4.19 three different spectral regions are clearly recognizable. Below 470 nm the intensity emission increases with decreasing temperature. Between 470 nm and 600 nm the intensity decreases with decreasing temperature. In both regions the intensity is primarily a function of the temperature. The region where intensity changes due to pressure variations are predominant is above 600 nm (Fig. 4.18). The three different regions could be used to directly measure pressure and temperature. Since the effects of temperature and pressure on the intensity are very complex and non-linear, the use of special algorithms to perform the evaluation process is necessary (Sec. 5.2).

**Blue EL-foil** The intensity response with the blue EL-foil ❺ is shown in Fig. 4.20.

The blue EL-foil, compared to the green one, reduces the leakage and the intensity response becomes very similar to the LED reference measurement. The sensitivity of the system to pressure changes is increased to 60.3%. The measurement was repeated with the aid of the spectrometer. The results are shown in Fig. 4.21 and 4.22.

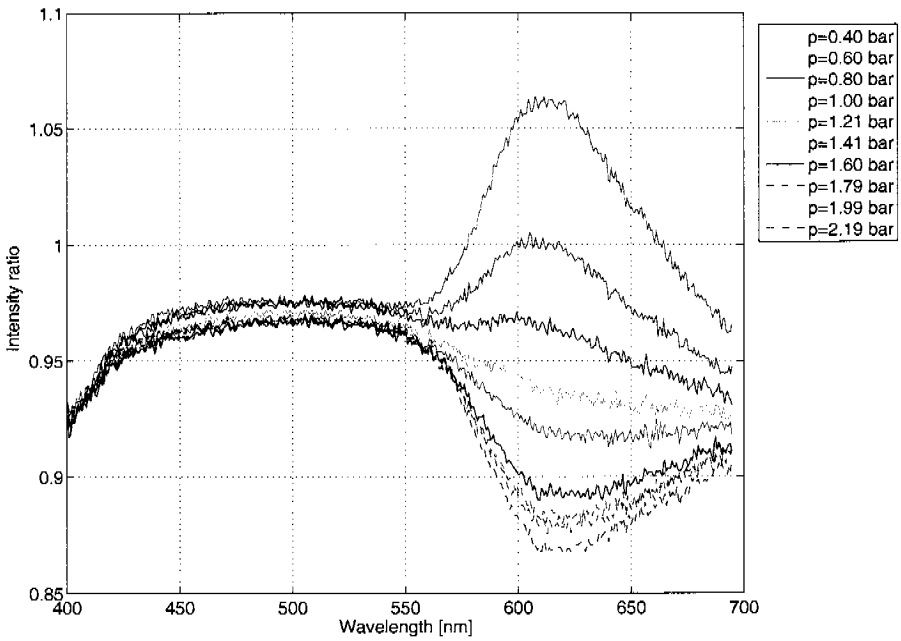


Figure 4.18: Ru based PSP, green EL-foil ❸ ($T = 19.6°C$).

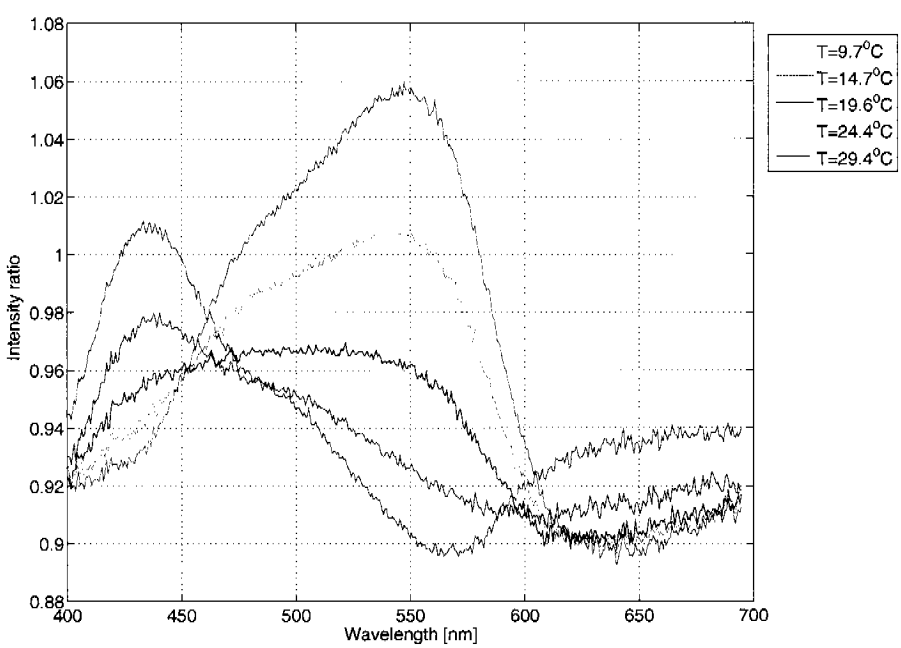


Figure 4.19: Ru based PSP, green EL-foil ❸ ($p = 1.4$ bar).

The three spectral regions described in the previous paragraph are not easily recognizable with the blue EL-foil. A possible explanation is the different phosphor mixtures used in the EL-foils. The intensity

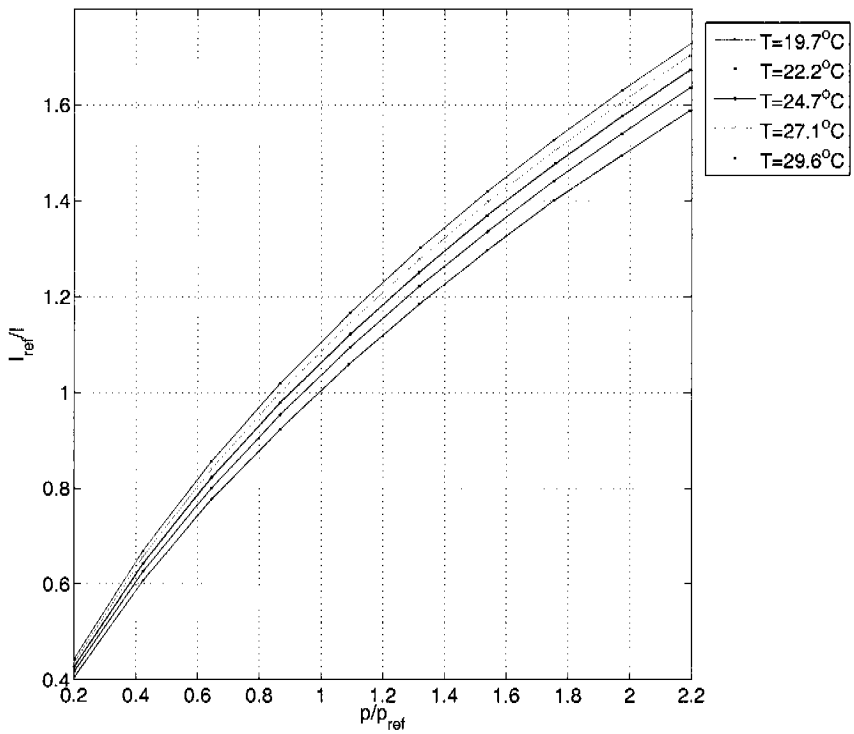


Figure 4.20: Ru based PSP, blue EL Foil ❺.

emission of the blue EL-foil (450 nm) could be used, as with the green EL-foils, to compute the surface temperature.

### 4.2.3 Pt-based PSP System

Measurements were performed with the Pt-based paints. The aim was to reduce the leakage of the EL-foils by using a paint with an emission peak located above 640 nm. Two different paint formulations were investigated: PtOEP and PtTFPP. Due to the low emission intensities of the EL-foil the paint was not properly excited. Fig. 4.23 and Fig. 4.24 show the intensity measurement results obtained with PtOEP-based PSP.

The quality of the measurements is poor. The paint emission is weak and the noise affects the acquired data. To compute the intensity response a strong frame averaging has to be performed. Altough the results in Fig. 4.23 seem to be reasonably, the values of the absolute signals are very low and the slope of the curves is strongly affected by noise signals. Pressure maps can not be computed with an adequate accuracy.

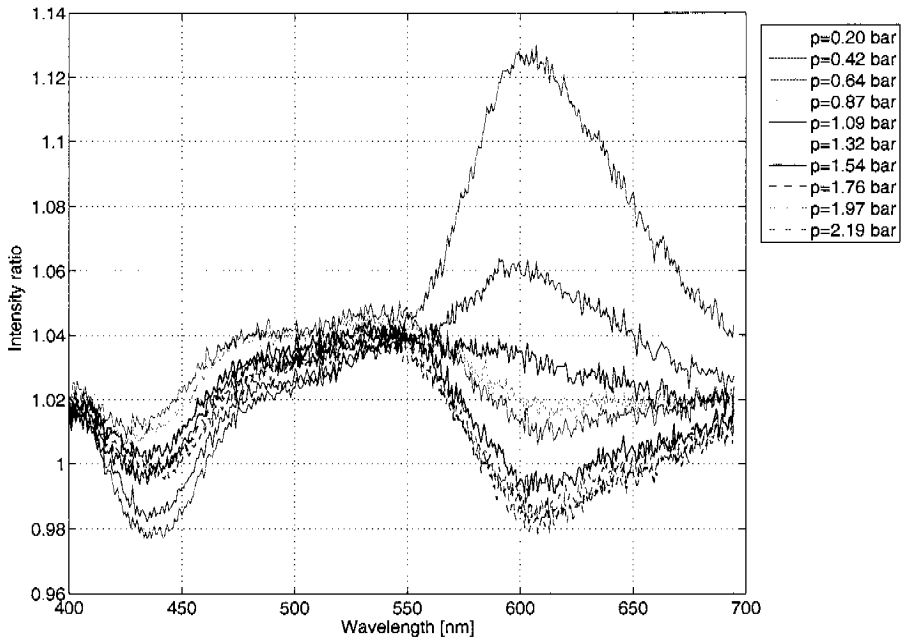


Figure 4.21: Ru based PSP, blue EL Foil ❺ ($T = 30°C$).

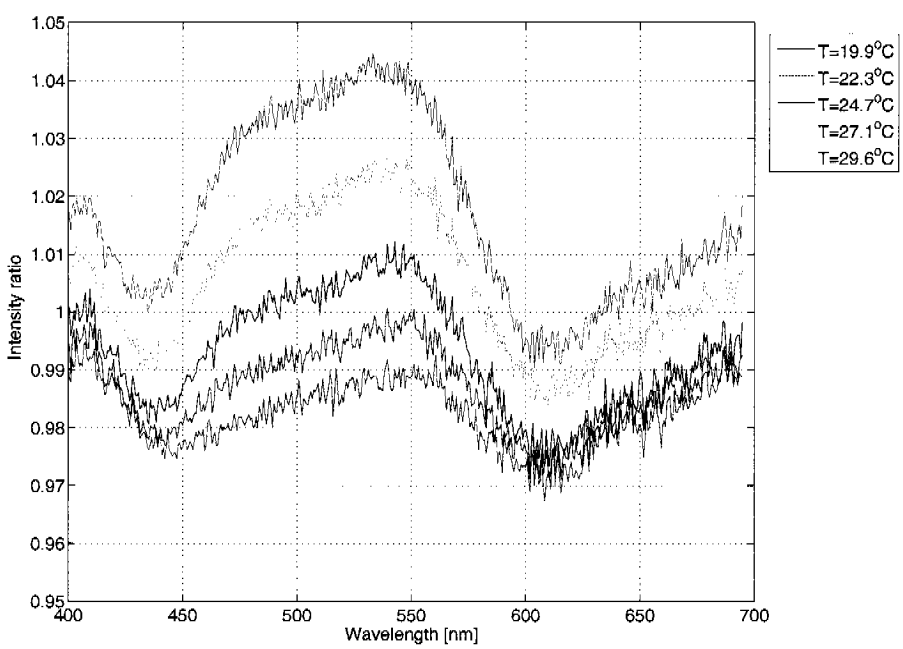


Figure 4.22: Ru based PSP, blue EL Foil ❺ ($p = 0.54$ bar).

## 4.3 Discussion

The measurements show that the Pt-based paints are not correctly excited with the available foils and therefore for further measurements

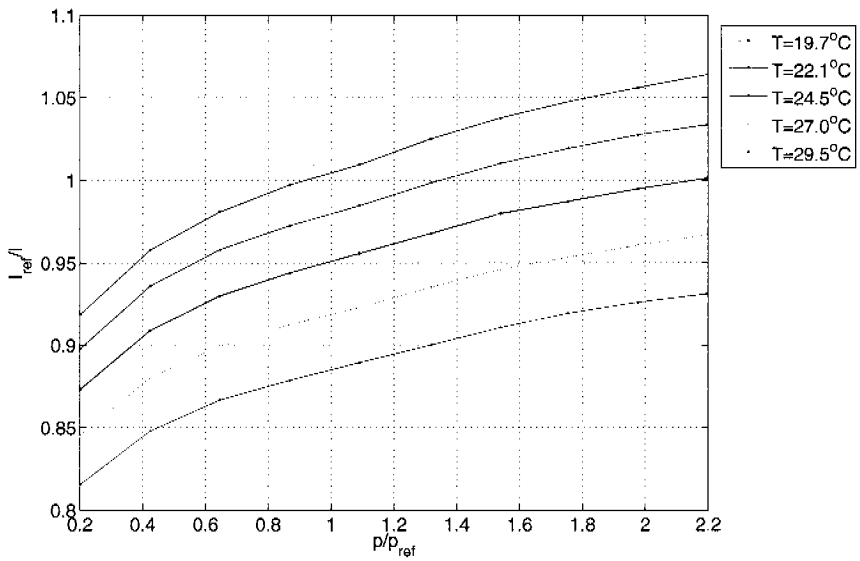


Figure 4.23: PtOEP, green EL-foil (Schott OG 630).

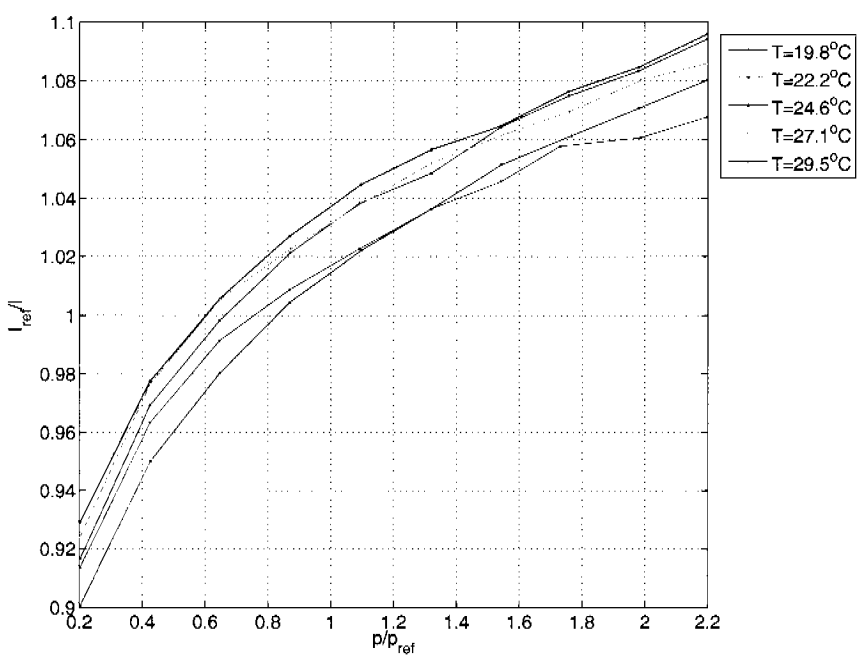


Figure 4.24: PtOEP, blue EL-foil (Schott OG 630).

and discussions Ru-based paints were preferred. The choice of the EL-foil affects the emission peak position, the emission intensity and the amount

of leakage in the red region. The LED illumination source has, compared to EL-foils, a higher emission intensity and no leakage in the emission region of the paint. The green EL-foil ❸ has a higher emission intensity compared to the blue one ❺, but due to lower leakage the sensitivity is higher with the blue EL-foil ❺. Tab. 4.5 summarizes the sensitivities of the most important configurations.

| Illumination | Type | p sensitivity [%] | T sensitivity [%] |
|---|---|---|---|
| LED | - | 67.0 (75*) | 11 |
| EL-foil | 1659 ❸ | 45.0 | 2.5 |
| El-Foil | 1655 ❺ | 60.3 | 9.7 |

* from [16]

Table 4.5: Comparison of PSP systems sensitivity.

To compare data acquired with EL-foil illumination the sensitivity values of the LED setup are used as a reference. The classical LED setup shows a pressure sensitivity of 67.0%, a value slightly lower compared to literature (75%) [16]. A visual comparison between LED and EL-foil sensitivities is shown in Fig. 4.25.

The measurements are performed at $20°C$ by varying the pressure from $-0.8$ to 1.2 bar over-pressure. The CCD camera (Sensicam) was equipped with a Nikkor 60 mm and a Schott OG 610. The sensitivity with the green EL-foil ❸ is only 45%, that means 33% lower than with the classical technique. With the use of a blue EL-foil the sensitivity is increased to a value of 60.3% (10% lower).

Not only is the pressure sensitivity coupled with the amount of leakage involved, but also the unwanted temperature sensitivity. Temperature sensitivity is computed by taking the relative change in intensity with an increase of the temperature from $20°C$ to $30°C$. Fig. 4.26 shows the temperature sensitivity at different pressures. The reference measurement, LED without leakage, has a mean temperature sensitivity of 11%. With the use of the EL-foils leakage is involved and the temperature sensitivity is decreased to 9.7% with the blue EL-foil and to 2.5% with the green EL-foil. The leakage has therefore a negative influence on the pressure sensitivity but reduces the temperature dependence of PSPs. Different evaluation techniques were developed in order to exploit

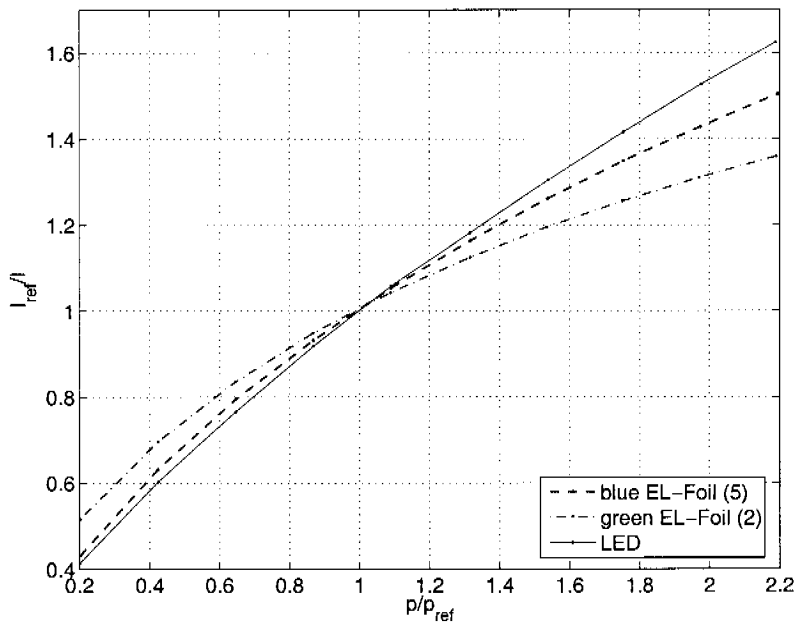


Figure 4.25: Pressure sensitivity comparison.

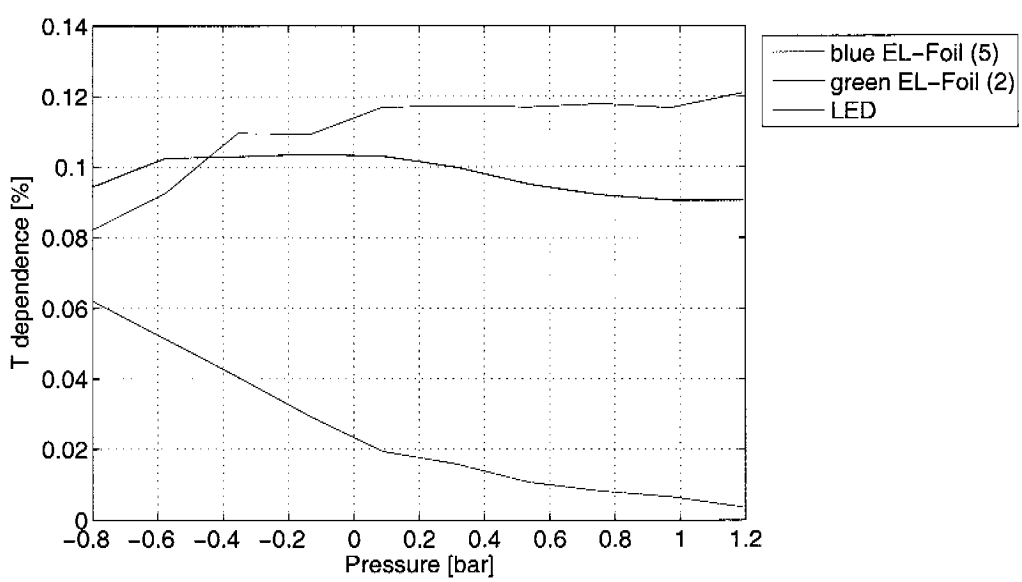


Figure 4.26: Temperature dependence of Ru-based PSP.

the capability of the new setup to reduce or, with the use of the EL-foil emission, measure temperature effects (chapter 5).
In wind tunnel measurements the choice between blue and green EL-foils

is a tradeoff between higher excitation intensity, temperature sensitivity and measurement accuracy. In the first measurement campaign at RUAG Aerospace (chapter 6) the higher intensity was preferred. In the second validation test a comparison between green and blue illumination is presented (chapter 7).

# Chapter 5

## *Data Evaluation Techniques*

## 5.1 PSP Measurement Techniques

In chapter 4.2 the dependence of the EL-foil/PSP system on temperature and pressure was presented. As explained in chapter 2 the intensity response of the PSP depends not only on the mentioned quantities but also on the excitation intensity. To compute the pressure distribution at least three measurements are necessary. For this purpose different techniques for the new PSP setup were developed and investigated. The spectral measurement, temperature compensated PSP and multifilter measurement techniques are described in detail in sections 5.1.1 to 5.1.3. The chapter is focused on the data evaluation and not on the measurement with different hardware configurations. All the presented results and examples were taken by using a green EL-foil (Tab. 4.3 ❸) and Ru-based paint. Advantages and drawbacks are summarized in a comparison chart (Sec. 5.1.4). The second part of the chapter analyzes in more detail different ways of evaluating pressure and temperature with the multifilter technique (Sec. 5.2).

### 5.1.1 Spectral Measurement

This technique is based on the intensity measurement with the aid of the spectrometer [15], an example is given in Fig. 5.1. The emission intensity at different wavelengths is acquired with the spectrometer as a function of pressure and temperature. Fig. 5.2 shows the spectral response of the paint-foil system at $19.4°C$ for a pressure ranging from $-0.5$ bar under-pressure to 0.83 bar over-pressure. Below 570 nm there is no intensity dependence to pressure changes. By increasing the temperature from $19.4°C$ to $28.1°C$ the temperature effects on the whole spectrum are clearly visible. Fig. 5.3 shows this temperature dependence at ambient pressure. A strong temperature dependence is clearly visible above 500 nm. Below 470 nm a weaker temperature dependence is also noticeable.

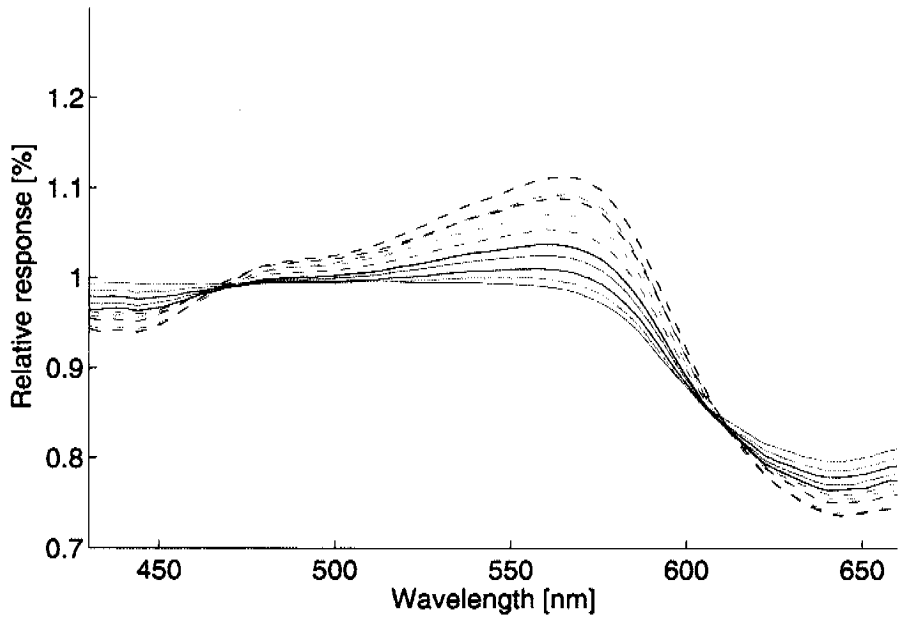


Figure 5.1: Spectral response example.

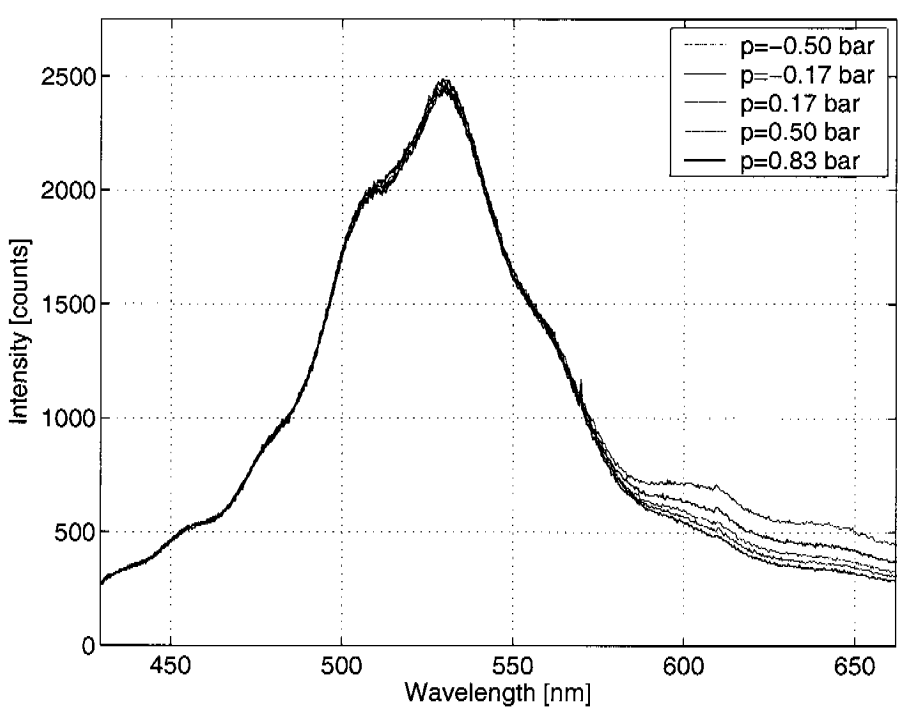


Figure 5.2: Spectral response at 19.4°$C$.

Due to the different absolute emission intensities in the different spectral regions the intensity changes are not always clearly visible or recog-

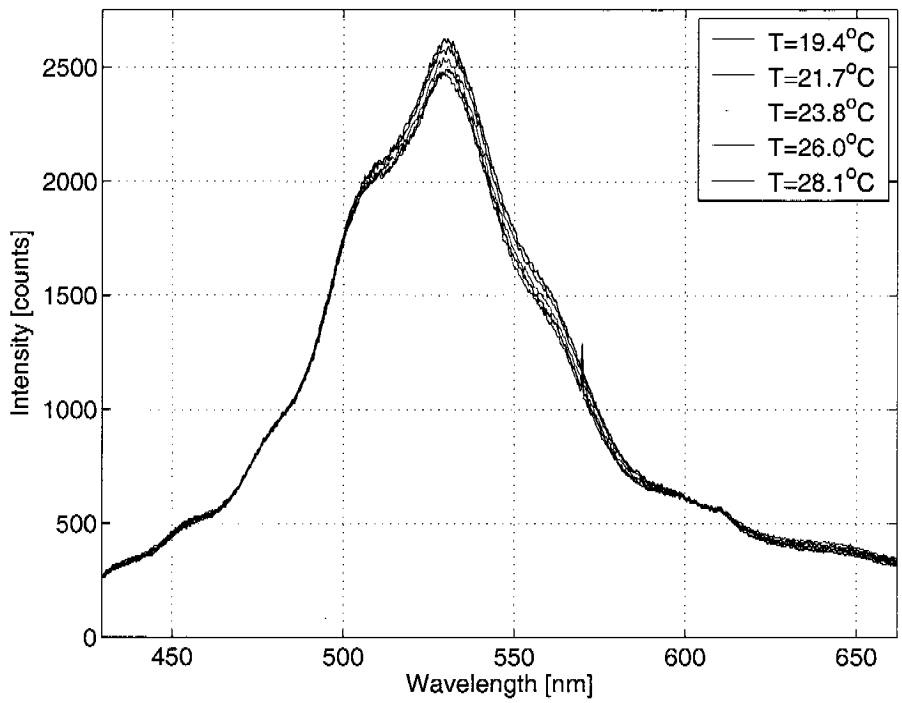


Figure 5.3: Spectral response at $p = p_{atm}$.

nizable. For this purpose ratios with a spectral emission taken at $20°C$ and at $p = p_{atm}$ are computed. The resulting normalized plots are shown in Figs. 5.4 and 5.5. Fig. 5.4 shows the response to pressure changes at $19.4°C$: an intensity variation is clearly visible in the red emission region ($> 570$ nm). Below 570 nm the pressure does not influence the emission intensity.

Fig. 5.5 shows the temperature influence on the normalized spectral response at $p = p_{atm}$.

The intensity behaves, as already explained in Sec. 4.2.2, differently in three distinct regions. Below 570 nm the emission intensity is primarily a function of the surface temperature. The emission intensity decreases with increasing temperature in the first region (below 470 nm) and increases with increasing temperature between 470 nm and 600 nm. Above 570 nm the emission intensity becomes a function of pressure and temperature as in a typical PSP paint. Due to the different behavior to pressure and temperature changes of the spectral regions a single measurement can be used to compute more than one unknown parameter. Every intensity at a given wavelength can be considered as a measurement. The simultaneous measurement of pressure and temperature is

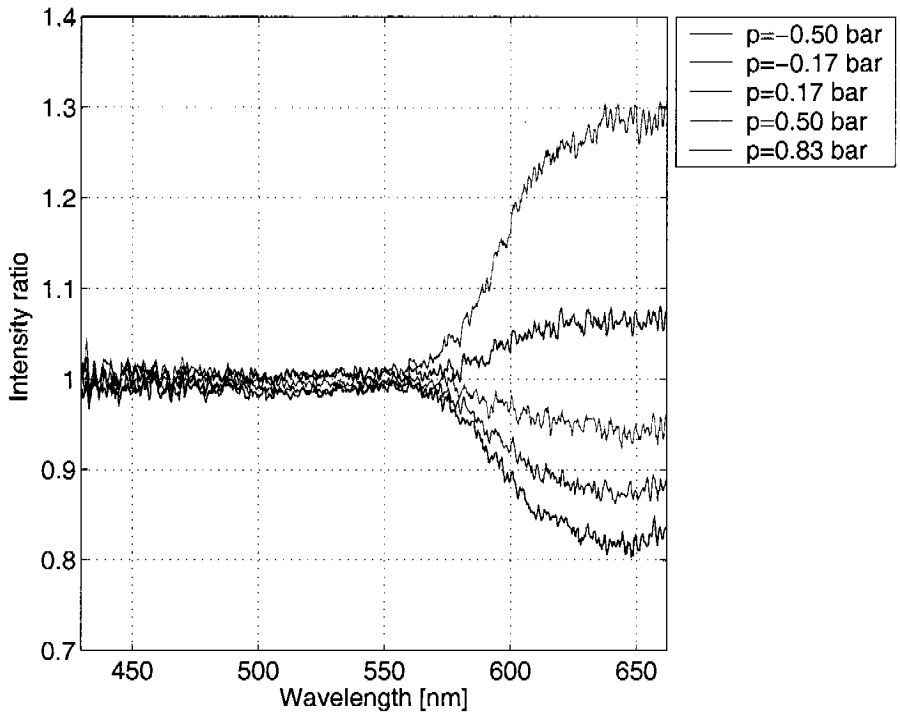


Figure 5.4: Spectral response at 19.4°$C$ (normalized).

therefore possible, still some detailed investigations with different intensities and conditions (e.g., paint thickness) have to be made in order to identify the possibility of eliminating the reference image. Several drawbacks are associated to this technique: the most significant is the capability of the spectrometer of measuring on a line (1-dimensional): scans of the model surface are needed to compute the 2-dimensional pressure map. The hardware setup for spectral measurements is quite complex and the emission intensity observed by the CCD camera is strongly reduced.

### 5.1.2 Temperature Compensated PSP

The basic idea of temperature compensated PSP is to use the EL-foil leakage in the emission region of the paint to reduce or eliminate the temperature dependence of the paint. As previously explained, by decreasing the temperature the paint emission decreases and the EL-foil emission above 500 nm increases. By acquiring the light emission with a specifically chosen optical filter it is theoretically possible to compensate the intensity changes due to temperature variations. An example is given

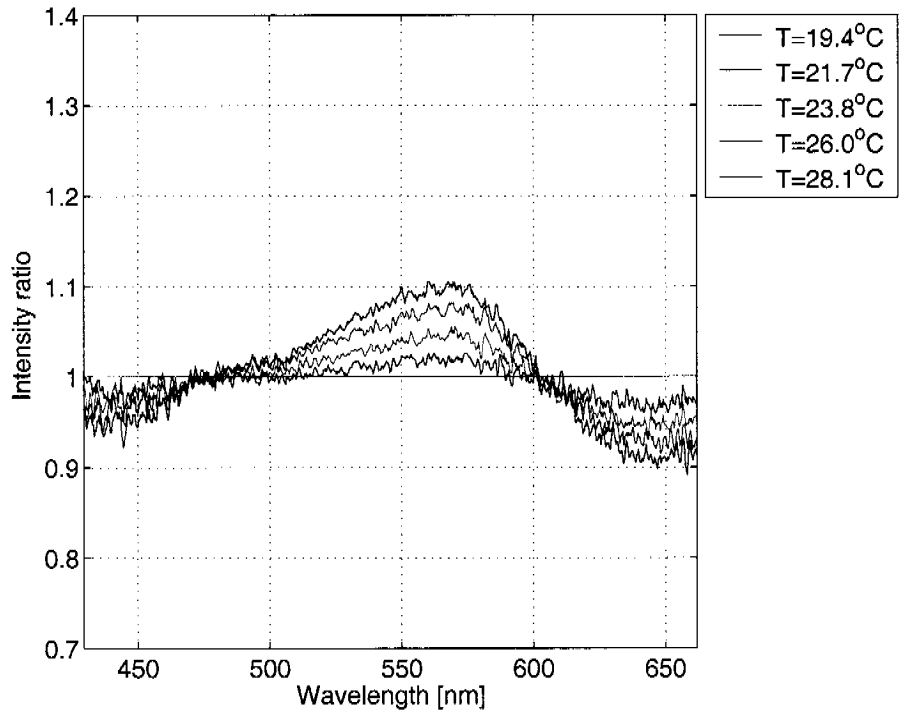


Figure 5.5: Spectral response at $p = p_{atm}$ (normalized).

in Fig. 5.6. Figs. 5.7, 5.8 and 5.9 show the intensity measurements taken

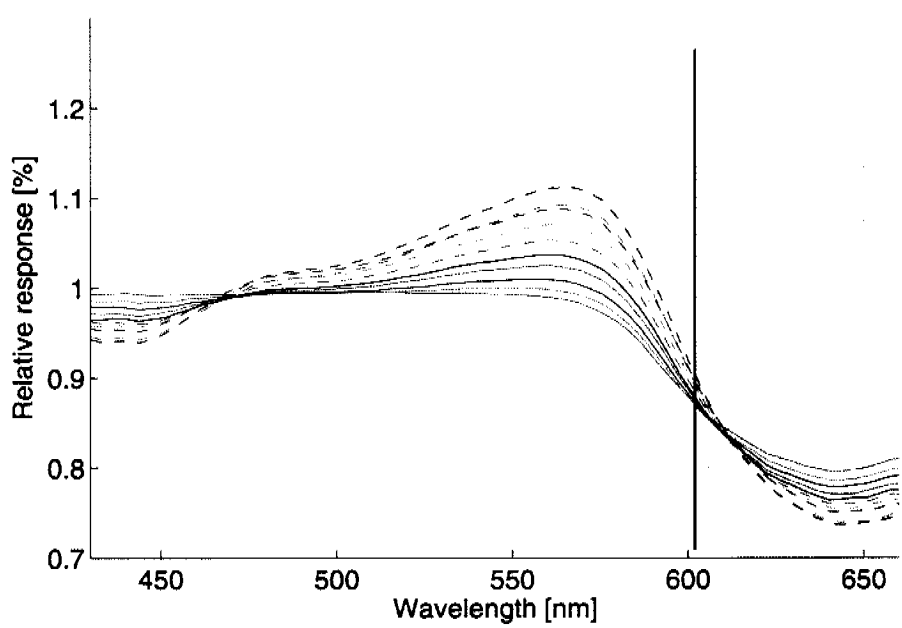


Figure 5.6: Temperature compensated PSP example.

with the green EL-foil. Three different optical filters were used, namely the OG 610, OG 590 and OG 570[1]. The pressure varied from $-0.6$ bar under-pressure to 1.2 bar over-pressure and the temperature from $10°C$ to $30°C$.

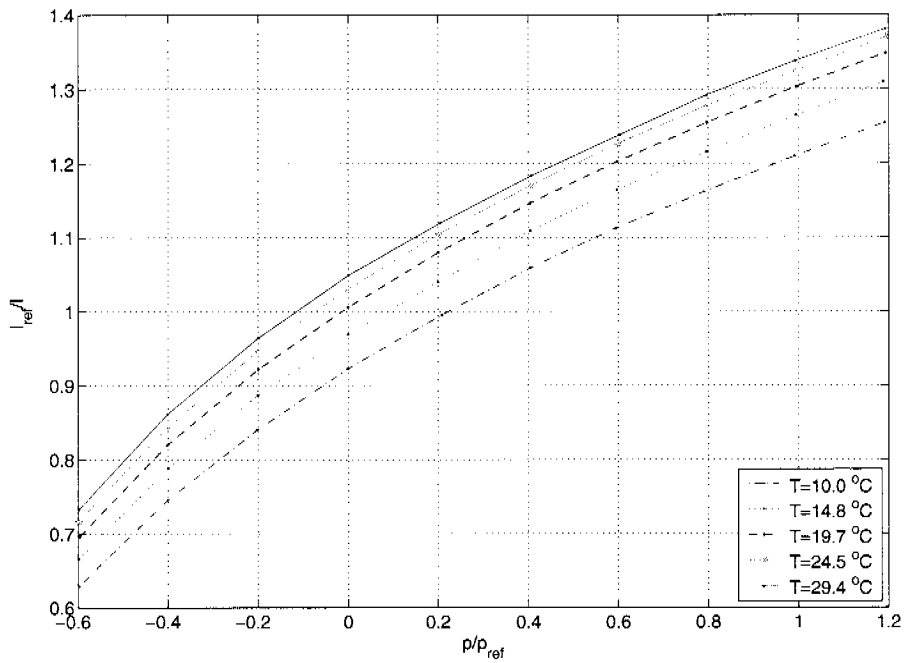


Figure 5.7: T-compensated PSP, with OG 610, EL-foil.

A comparison with a traditional LED setup is performed and illustrated in Figs. 5.10, 5.11 and 5.12.

By using the OG 610 only the emission intensity above 610 nm is acquired. The emission of the EL-foil above 610 nm is weak and therefore the intensity response is similar to the one taken with a standard PSP setup (compare Fig. 5.7 with Fig. 5.10). The leakage problem is nevertheless clearly visible. The response to pressure changes is, as expected, weaker with the EL-foil (40.3%) than with an LED lamp (52.8%). Notice that the sensitivity results differ from the results obtained in Sec. 4.2.2, since the dark level image was not subtracted with a corresponding reduction of the sensitivity. By looking at the effect of temperature at atmospheric pressure it is possible to see that temperature sensitivity is 13.6% for the LED and only 3.7% for the EL-foil system. A summary of the response data is given in Tab. 5.1.

[1]see appendix D

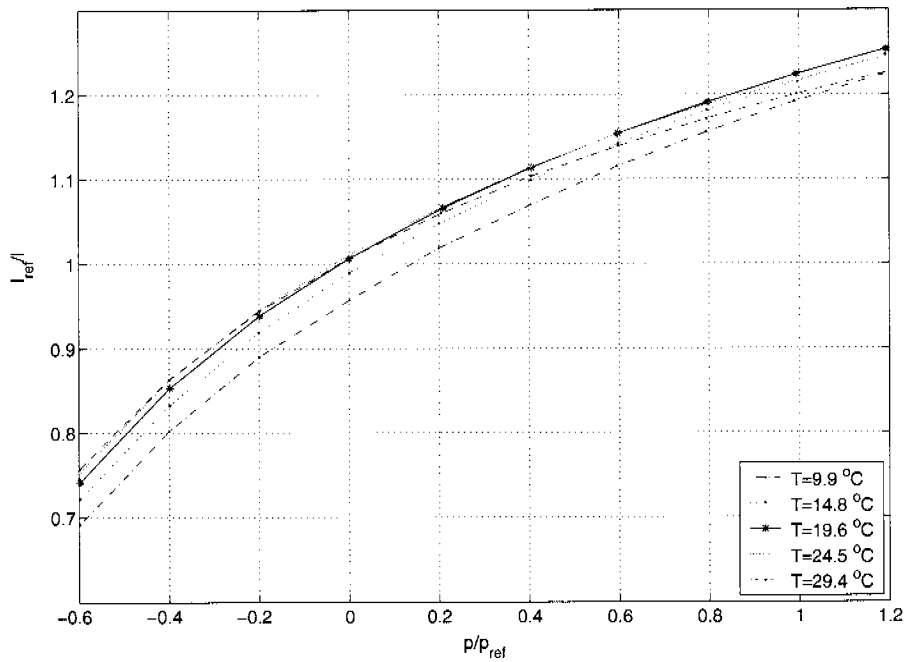


Figure 5.8: T-compensated PSP, with OG 590, EL-foil.

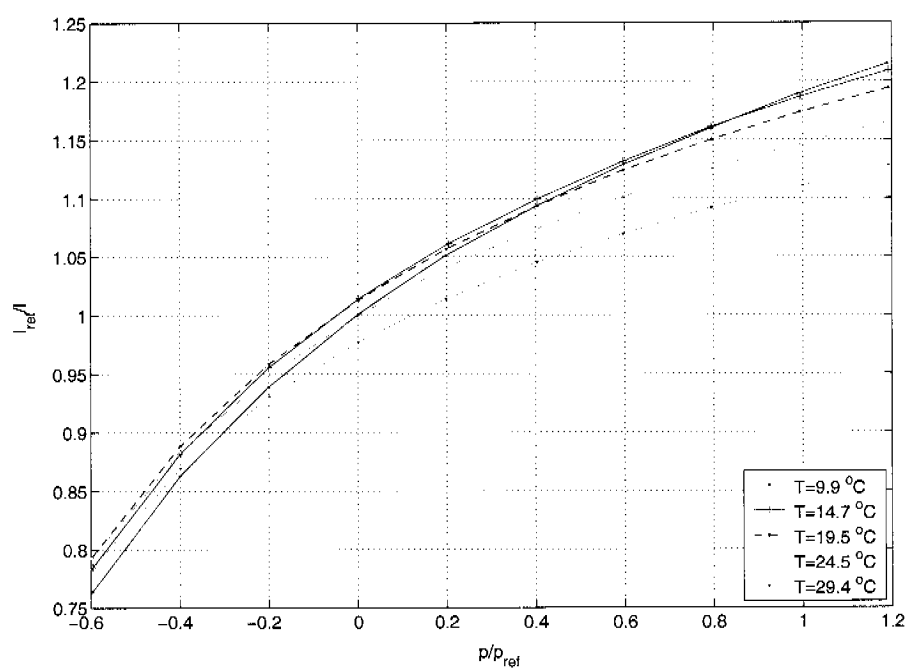


Figure 5.9: T-compensated PSP, with OG 570, EL-foil.

The OG 590 increases the leakage of the EL-foil and consequently the temperature compensation. Figs. 5.8 and 5.11 show the comparison

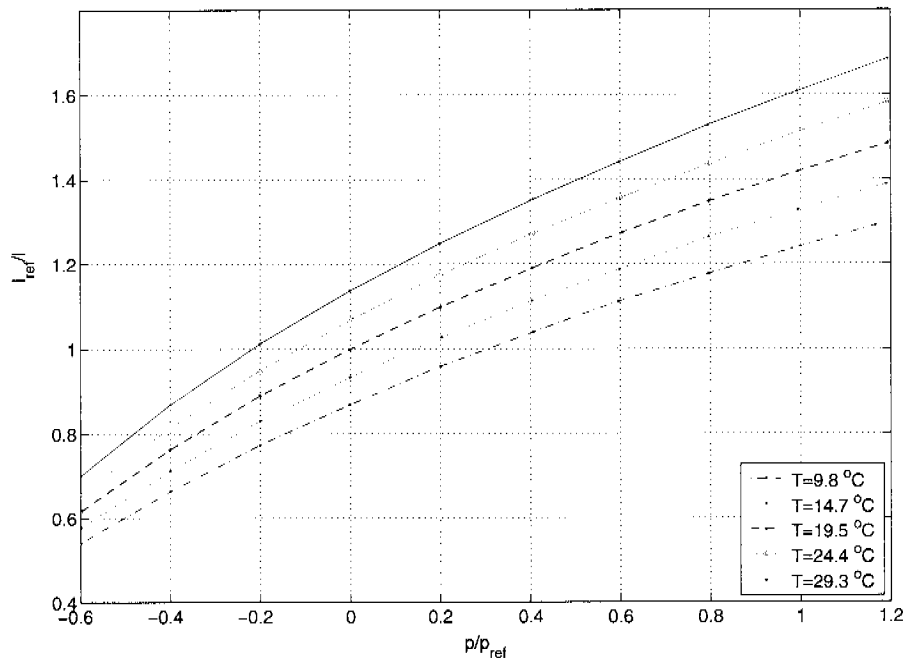


Figure 5.10: T-compensated PSP, with OG 610, LED.

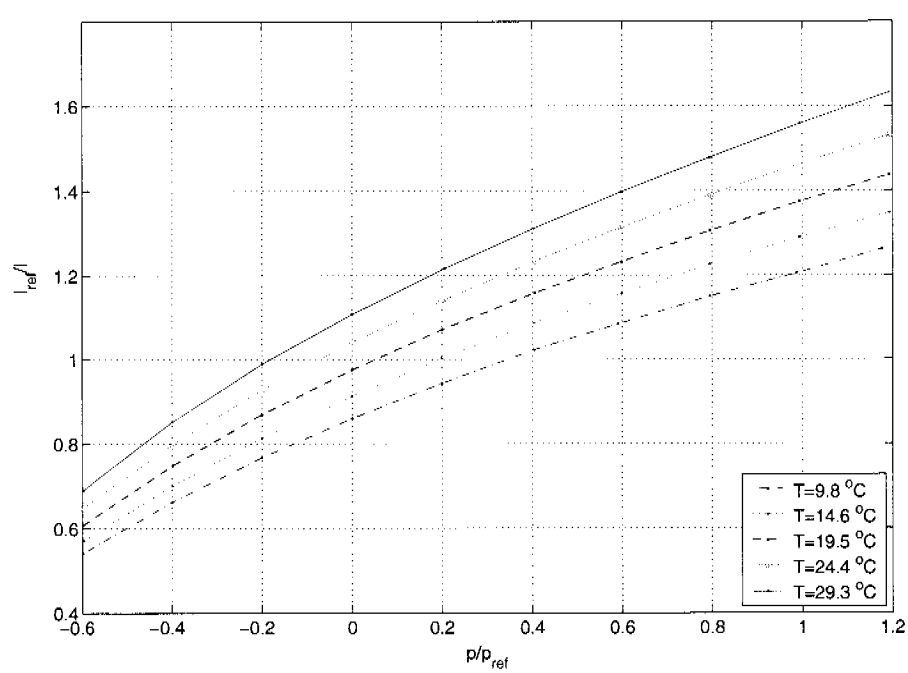


Figure 5.11: T-compensated PSP, with OG 590, LED.

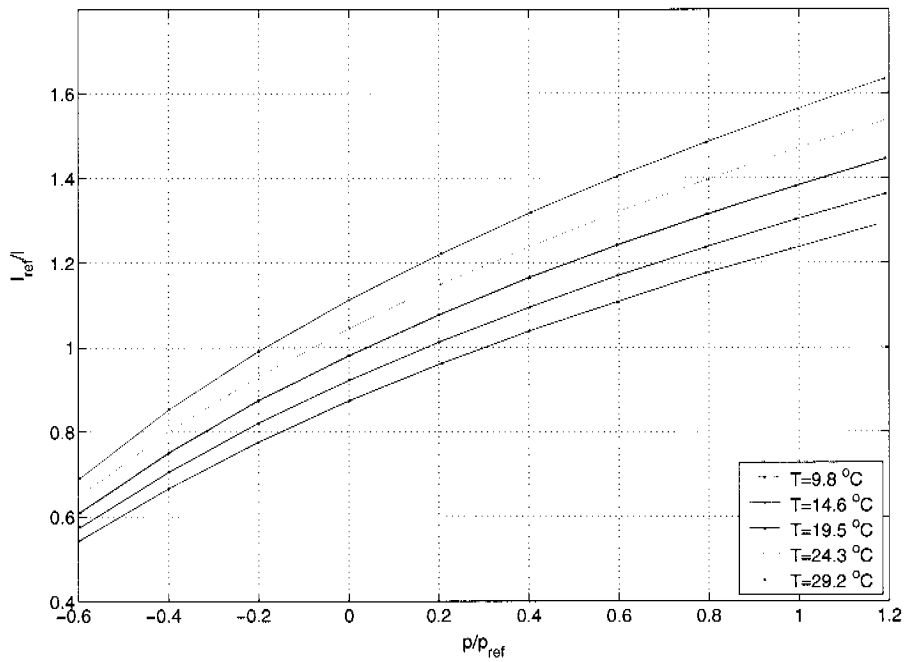


Figure 5.12: T-compensated PSP, with OG 570, LED.

| Illumination | Filter | p sens. [%]* | T sens.[%]† |
|---|---|---|---|
| LED | OG 610 | 52.8 | 13.6 |
| LED | OG 590 | 50.7 | 13.5 |
| LED | OG 570 | 51.5 | 13.3 |
| EL-foil | OG 610 | 40.3 | 3.7 |
| EL-foil | OG 590 | 32.3 | -0.4 |
| EL-foil | OG 570 | 25.6 | -3.8 |

* slope of $I_{ref}/I$ at $p = p_{atm}$ and $T = 20°C$
† mean relative intensity change from $20°C$ to $30°C$

Table 5.1: Summary for pressure and temperature sensitivity.

EL-foil/LED illumination. As expected the temperature dependence for the EL-foil system is decreased to $-0.4\%$. By having larger leakage the sensitivity of the PSP is also decreased to 32.3%. The filter does not have, as expected, a large influence on the LED/PSP system.

The third filter used is the OG 570. With this configuration the leakage becomes very high and the response of the PSP is decreased to 25.6%. The emission intensity is increased with the increase of temperature. The EL-foil affects the intensity too much and the PSP-system is over compensated. The temperature sensitivity has a value of $-3.8\%$.
This technique has the advantage of being very simple and the hardware used does not differ from the hardware used for standard PSP measurements. The contradictory part of the technique is the need to eliminate the leakage in order to increase the pressure sensitivity and simultaneously the need of a sufficient large leakage in order to compensate the temperature effects. The technique can be very useful in measurements with large pressure and temperature variations. Notice that the surface temperature is not computed but only auto-compensated with an important loss of useful temperature information. A third technique was developed to avoid this shortcoming.

### 5.1.3 Multifilter Measurement

The basic idea of this technique is to use the properties shown in the spectral measurements to compute pressure and temperature on the model surface. As explained in Sec. 4.2.2 there are different regions of the spectrum were the PSP system behaves differently. With the aid of different optical filters the emission is acquired at different wavelengths in a two-dimensional image. An example is given in Fig. 5.13. The filters used during multifilter measurements are listed in Tab. 5.2 with the spectral transmission curves summarized in appendix D.

| No. | Filter | Emission peak [nm] | HBW [nm] | Type |
|---|---|---|---|---|
| 1 | 400FS70-50 | $400 \pm 25$ | $70 \pm 16$ | band pass |
| 2 | 470FS10-50 | $470 \pm 3$ | $10 \pm 2$ | band pass |
| 3 | 500FS40-50 | $500 \pm 10$ | $40 \pm 8$ | band pass |
| 4 | 600FS10-50 | $600 + 3 - 0$ | $10 \pm 2$ | band pass |
| 5 | OG 610 | $> 610$ | - | high pass |
| 6 | RG 630 | $> 630$ | - | high pass |

Table 5.2: List of filters used.

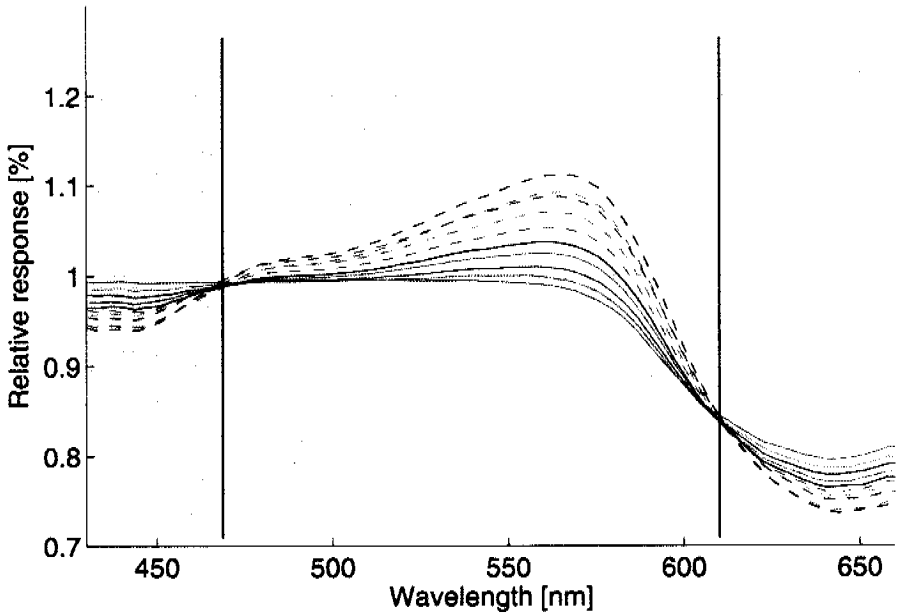


Figure 5.13: Temperature compensated PSP example.

Measurements were performed with different setups: blue and green EL-foils were tested combined with filters [1] to [6]. The complete measurement list is summarized in appendix E.1. In this section, for the presented results, three optical filters (1,3,5) were used for each measurement point. The pressure was varied from 0.2 bar to 2.2 bar in 10 steps and the temperature was set from $20°C$ to $30°C$ in 5 steps.

Fig. 5.14 shows the response of the PSP multifilter calibration. In this specific case the filter used in Fig. 5.14 ❸ is very selective and the acquired intensities are quite weak. The temperature dependence is present but is very noisy. Fig. 5.14 ❷ shows the emission properties at $500 \pm 10$ nm. The temperature dependence is clearly identifiable. A very weak pressure dependence is noticeable. The last filter (Fig. 5.14 ❶) shows a typical PSP response. With the aid of a reference image and the temperature computed from the images taken with filters (2) and (3) it is possible to extract the pressure on the model surface.
Different measurements with other configurations were performed and investigated in [31]. The possibility of measuring pressure and temperature was clearly demonstrated. Attempts to eliminate the reference image (wind $OFF$) were performed. Due to the difficulty and time needed to investigate different reference images (e.g., by changing paint thickness, paint homogeneity, ...) the possibility of eliminating the wind $OFF$

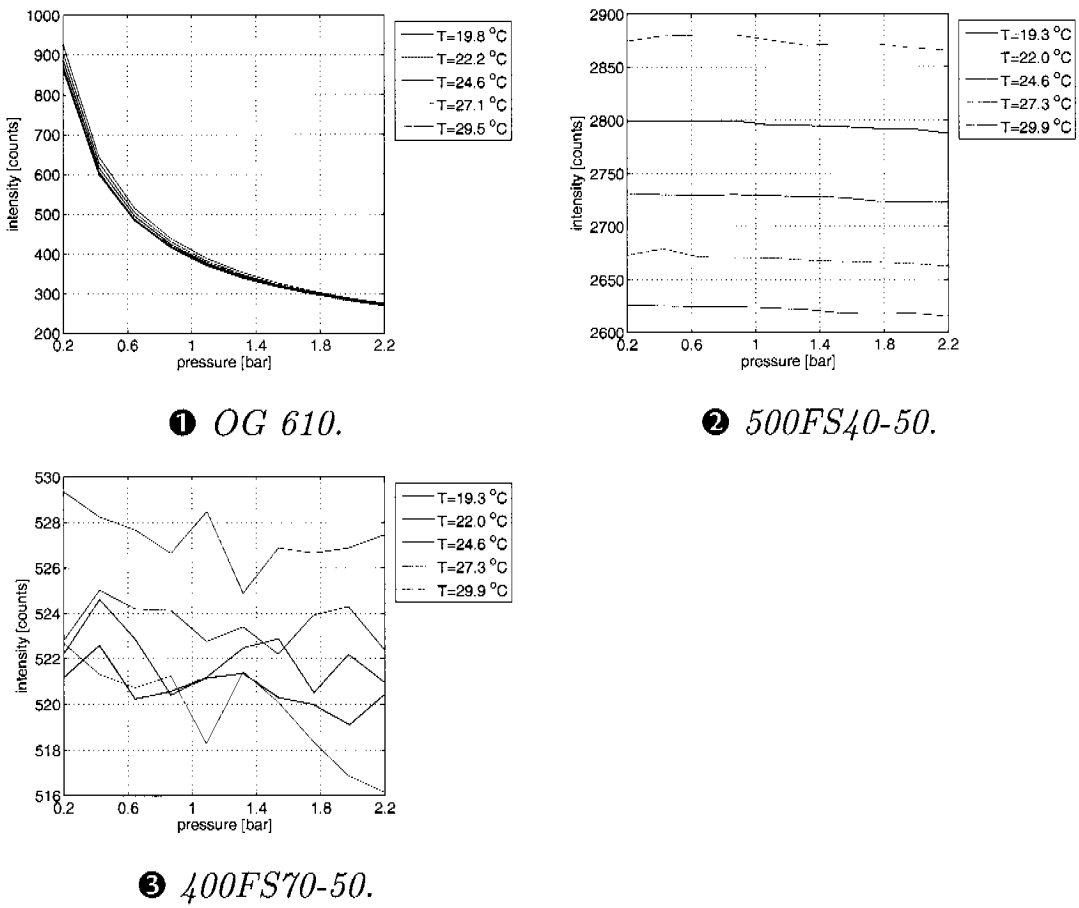


❶ *OG 610.*

❷ *500FS40-50.*

❸ *400FS70-50.*

Figure 5.14: Intensity response with different filters.

image could not fully be demonstrated. The use of special algorithms (Sec. 5.2) to decompose the signals coming from the measured intensities has to be investigated in more detail. This decomposition should take the mixed signals and decompose them into three distinct signals depending on pressure, temperature and reference intensity. Sec. 5.2.2 illustrates some examples.

### 5.1.4 Measurement Techniques Comparison

Tab. 5.3 summarizes the properties of the different PSP acquisition techniques.

The multifilter measurement has several advantages compared to the other techniques. Temperature and pressure maps can be computed with two or three pictures by simply changing the optical filter in front of the

| Technique | | Advantages (+) and drawbacks (−) |
|---|---|---|
| Spectral measurement | (+) | Acquisition of the whole spectral range (no information loss) |
| | (+) | Possibility of measuring $p$, $T$ and $I_{ref}$ (without wind $OFF$ image) |
| | (−) | Only 1D measurement possible |
| | (−) | Complex hardware setup |
| | (−) | High emission intensity needed (weak signal) |
| Temperature compensated PSP | (+) | very simple (standard) hardware setup |
| | (+) | 2D pressure maps |
| | (+) | reduction of temperature sensitivity |
| | (−) | temperature not measurable |
| | (−) | unavoidable reduction of pressure sensitivity |
| | (−) | choice of correct filter |
| Multifilter measurement | (+) | simple hardware setup |
| | (+) | 2D pressure maps |
| | (+) | measure $p$, $T$ |
| | (+) | possibility of eliminating $I_{ref}$ |
| | (−) | complex algorithm to compute / extract p and T |

Table 5.3: Measurement techniques summary.

camera. A reference picture (wind $OFF$) is at the present still needed. The possibility of substituting this image with a third measurement should be investigated in more detail in the future. The hardware does not require substantial changes compared to the standard one and any CCD camera can be used.

## 5.2 Data Analysis

The intensity changes measured with the spectral or multifilter methods are the results of different influencing factors. The computation of pressure and temperature from these mixed signals is, as explained, very difficult. Different algorithms are available in order to decompose the signals into separate signal contributions. In Sec. 5.2.1 a simple solution to compute pressure and temperature maps is presented. Sec. 5.2.2 introduces a series of advanced techniques to decompose the measured signals into pressure and temperature signals.

### 5.2.1 Simple Multifilter Technique

The basic idea of this algorithm is to use two filters to compute pressure and temperature maps with an "a-priori calibration". Reference images, or wind $OFF$ images, at known pressure ($p = p_{atm}$) and temperature ($T = T_{atm}$) for both filters are needed. The first filter acquires the emission of the EL-foil (below 570 nm) with the assumption that the acquired emission intensity depends only on temperature variations. The second filter acquires, as for a standard PSP measurement, the emission intensity of the paint for $\lambda > 610$ nm. The computed temperature (filter 1) is used to correct the pressure measurements. The algorithm can be summarized in three main steps. In the first step the reference intensities for both filters are computed. From the calibration measurement $(I_{ref1})_{cal}$ and $(I_{ref2})_{cal}$ are extracted for the given reference pressure $p_{ref} = p_{atm}$ and reference temperature $T_{ref} = T_{windOFF} = T_{atm}$ (Fig. 5.15). The calibration curve, or $(I_{ref}/I)_{cal1}$ as a function of temperature, for filter (1) is computed. In the second step, summarized in Fig. 5.16, the ratio $(I_{ref}/I)_{meas1}$ is computed with the measured wind $ON$ and wind $OFF$ images. From the calibration curve it is possible to obtain the temperature on the model surface $T_{meas}$. In the third step, see Fig. 5.17, the pressure map is computed. With the ratio $(I_{ref}/I)_{meas2}$ measured with filter (2) and the calibration curve $(I_{ref}/I)_{cal2}$ the pressure can be computed as a function of the previously measured temperature $T_{meas}$. This technique is very simple: it needs only two filters and the pressure can be computed with a good accuracy (an example is given in Sec. 7.4.2). There are however some problems that cause a decrease in accuracy. The first is the assumption of no pressure dependence in the emission region located below 570 nm. Measurements have shown a

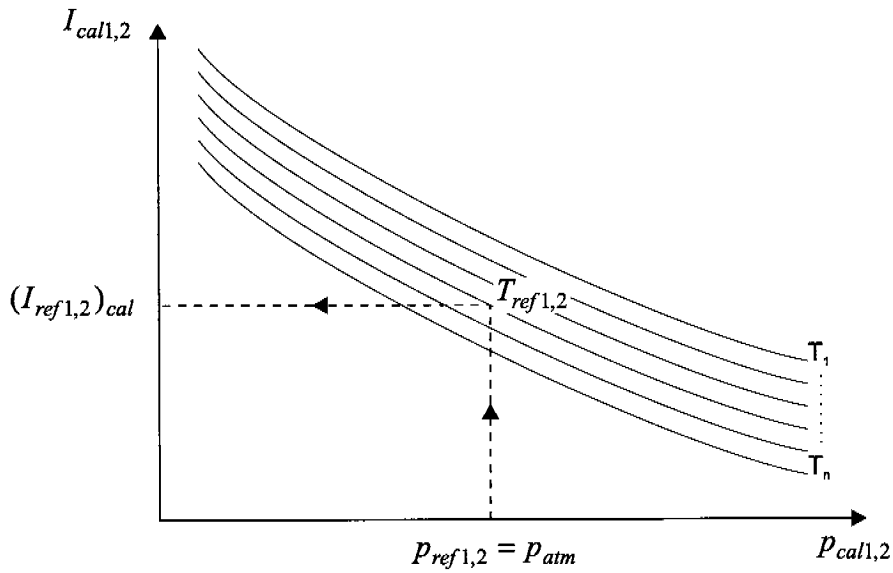


Figure 5.15: Step 1: $I_{ref}$ computation.

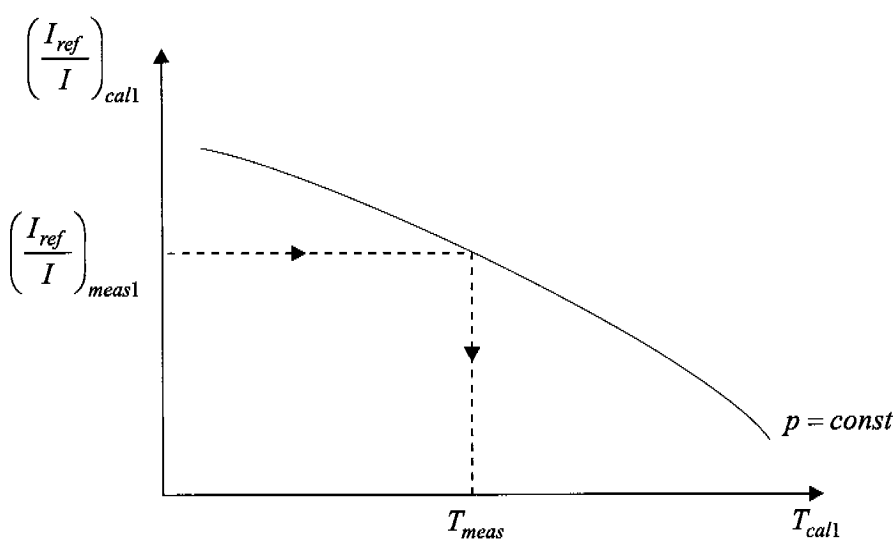


Figure 5.16: Step 2: measurement of surface temperature.

weak pressure dependence that will not be corrected. The second problem is the loss of the data contained in the third spectral region (below 470 nm). The use of different and more complex algorithms can solve or reduce the above mentioned problems, e.g., with the advanced multifilter

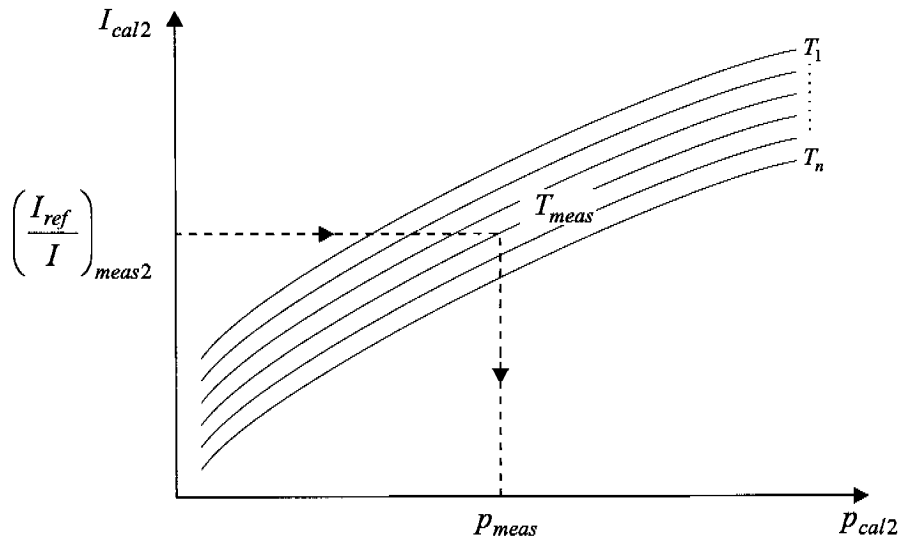


Figure 5.17: Step 3: pressure map computation.

technique.

## 5.2.2 Advanced Multifilter Techniques

With the simple multifilter technique it is not possible to completely eliminate the pressure dependence from the EL-foil emission region. To reduce this dependence and to optimize the use of all the acquired information several algorithms are available. In this section a brief introduction is given to the investigated techniques, namely Proper Orthogonal Decomposition (POD), Independent Component Analysis (ICA) and Neural Network (NN). The basic idea is to convert the input signals (measured intensities with different filters) and transform them into two new signals: one representing temperature, the other representing pressure.

### Proper Orthogonal Decomposition (POD)

POD is a widely used linear transform that exactly decorrelates the data in terms of the covariance matrix. The method generates a new set of variables, called principal components. Each principal component is a linear combination of the original variables. The decorrelated data $s$ can

be than expressed as

$$\mathbf{s} = T\ \mathbf{x}, \tag{5.1}$$

where $x$ are the measured signals and $T$ is the result of the diagonalization / eigenvector decomposition of the covariance matrix $R = T\ \Lambda\ T^{-1}$. T is a matrix containing the three eigenvectors (principal axes) of the covariance matrix. All the principal components are orthogonal to each other, so there is no redundant information left. In this way the response to pressure and temperature changes may be isolated and extracted from the set of original, mixed signals. As demonstrated by [4] the algorithm can be applied in the PSP field. An example, with the use of EL-Foils, is given at the end of the section. A detailed description of the algorithm can be found in [11, 26, 27].

### FastICA

Independent Component Analysis, or ICA, is a statistical technique that represents a multidimensional random vector as a linear combination of non-gaussian random variables ("independent components") that are as independent as possible. ICA is a non-gaussian version of factor analysis, and somewhat similar to principal component analysis. As for the previous algorithm the measured signals $x$ are a linear mixture of the decorelated signals $s$:

$$\mathbf{x} = A\ \mathbf{s}. \tag{5.2}$$

The matrix $A$ is a matrix with the weight coefficients. By computing the inverse matrix $W = A^{-1}$ the decorrelated signals can be expressed as

$$\mathbf{s} = W\ \mathbf{x}. \tag{5.3}$$

The ICA assumes that the observations $x$ are statistically independent. In order to fulfill this assumption, as demonstrated in [11], the independent components must have non-gaussian distributions. In order to compute the $W$ matrix ICA is based on the central limit theorem which says that the distribution of a sum of independent random variables tends towards a gaussian distribution. It follows that the coefficients $w_i$ can be computed by maximizing the non-gaussianity of the signals $s$. Different ways are available to measure the "non-gaussianity": the most significant for the ICA algorithm, namely kurtois and negentropy, are described in detail in [11].

The FastICA algorithm is a computationally highly efficient method for performing the estimation of ICA and it can be considered as an evolution of the classical POD. For our PSP application the resulting outputs are two signals encoding pressure and temperature. This algorithm was used and tested in [21]. An example is given at the end of the section.

### Neural network

An artificial Neural Network (NN) is an algorithm that is inspired by the way biological nervous systems, such as the brain, process information. The property of this algorithm is the structure of the information processing system. It is composed of a large number of interconnected neurons working together to solve specific problems. NNs, like people, learn by examples. Neural networks, with their ability to derive meaning from complicated or imprecise data, can be used to extract patterns and detect trends that are very complex to be noticed.

The different techniques were tested with several datasets, in particular with measurements performed with the aid of a spectrometer. Attempts were made to extract pressure and temperature. The dataset computed with POD gives two signals: the first one represents the surface temperature with a slight pressure dependence and the second a classical PSP measurement (with pressure and temperature dependence). The FastICA algorithm, which can be considered an evolution of POD, returns the best results: the temperature can be computed and used to correct the pressure measurements.
The quality of the results obtained with the NN is very difficult to evaluate. NN is a very simple algorithm but the results strongly depend on the training, or learning, phase. Since NNs are "black box" in terms of algorithmic performance the results are not always reliable. Measurements with different intensities have to be performed in order to evaluate the capability of eliminating the reference image. An example of POD and FastICA computation, extracted from [21], is given in the next paragraph.

### Measurement example

An example is given with the use of the multifilter technique. A calibration measurement with a blue EL-Foil and three different optical

filters was performed in the test cell. The acquired intensities in dependence of pressure and temperature are shown in Fig. 5.18.

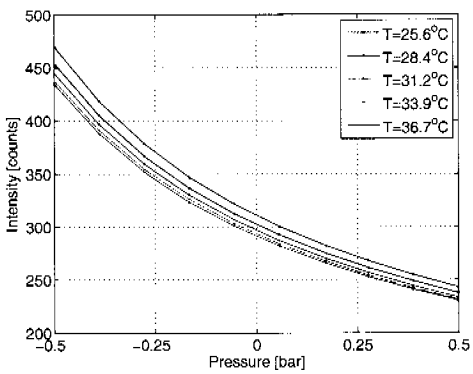


❶ *Filter OG 610.*

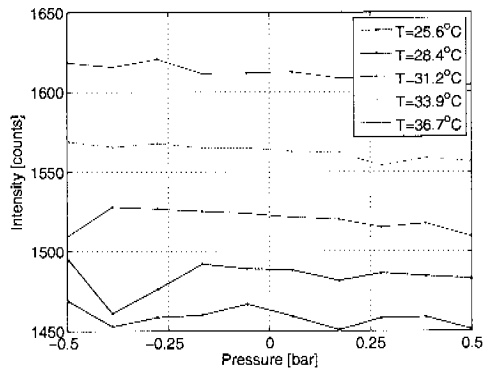


❷ *Filter 500FS40-50.*

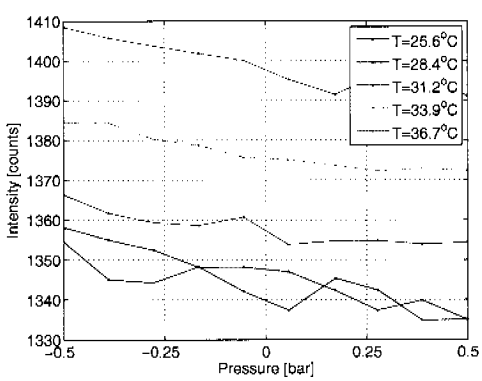


❸ *Filter 400FS70-50.*

Figure 5.18: Intensity response with different filters.

As previously explained the possibility of measuring pressure and temperature is present, but an algorithm to separate both signals is needed. In this section a signal decorrelation with POD and FastICA is presented and compared.
The temperature dependencies at different pressures are shown in Fig. 5.19. The normalized intensity is given as comparison (Fig. 5.19 ❶). By applying the POD the temperature dependence, contrary to expectation, is increased (Fig. 5.19 ❷). In fact the POD seems not to separate temperature from pressure signals as in [4], but EL-foil intensity emission from PSP intensity emission. The effect of the POD on the measured data should be investigated in more detail. The use of the FastICA algorithm produces as expected a reduction of the temperature dependence

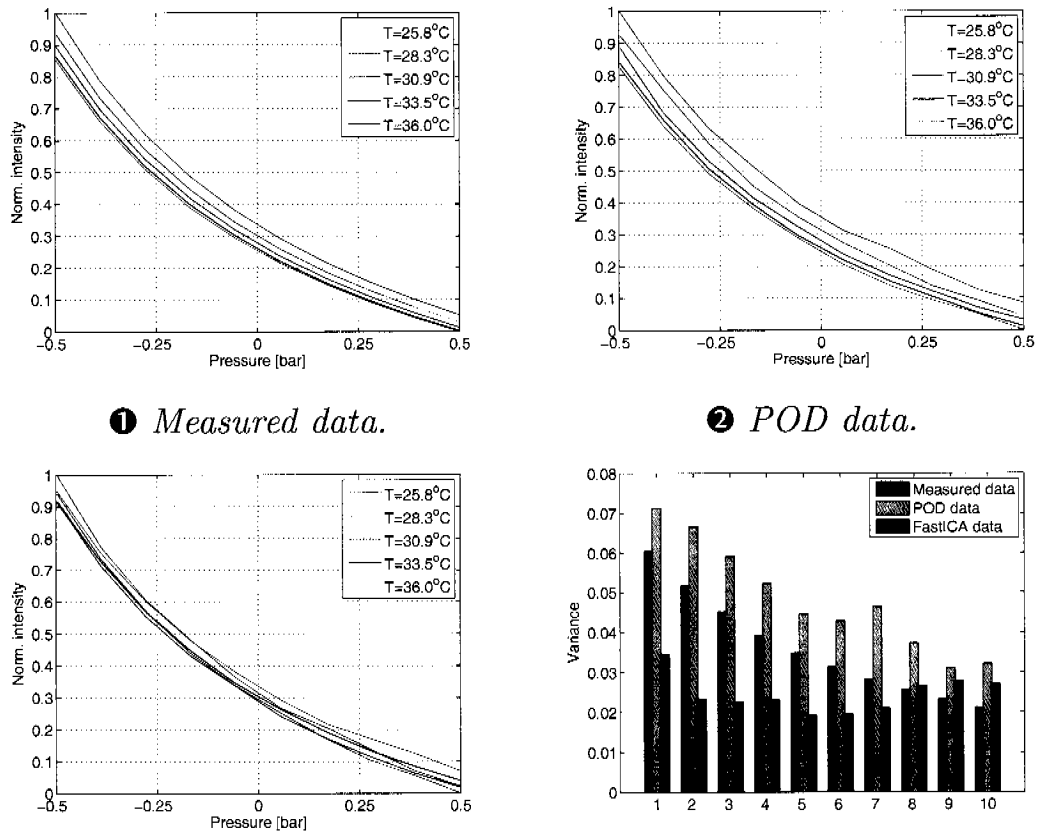


❶ *Measured data.* ❷ *POD data.*

❸ *FastICA data.* ❹ *Variance comparison.*

Figure 5.19: Temperature dependence reduction.

(Fig. 5.19 ❸). To simplify the comparison of the results a bar plot of the temperature variance at ten different pressures (from $-0.5$ to 0.5 bar) is presented in Fig. 5.19 ❹. The mean values of the computed variances are given in Tab. 5.4. The mean variance of the measured data for a temperature difference of about $10°C$ and a pressure raging from $-0.5$ to 0.5 bar is 0.0381. With the use of FastICA the dependence is reduced to 0.0245. Further improvements can be achieved by preprocessing the acquired data. An example is given in Fig. 5.20.

The results obtained with the traditional FastICA, used as comparison, are illustrated in Fig. 5.20 ❶. The "logarithmic" ICA, Fig. 5.20 ❷, is obtained by preprocessing the intensity measurement taken with the OG 610 filter with a logarithmic function: $I_{OG610new} = log(I_{OG610})$. The "inverse" ICA, Fig. 5.20 ❸, is computed by simply inverting the pressure response: $I_{OG610new} = 1/I_{OG610}$. The improvements are clearly visible

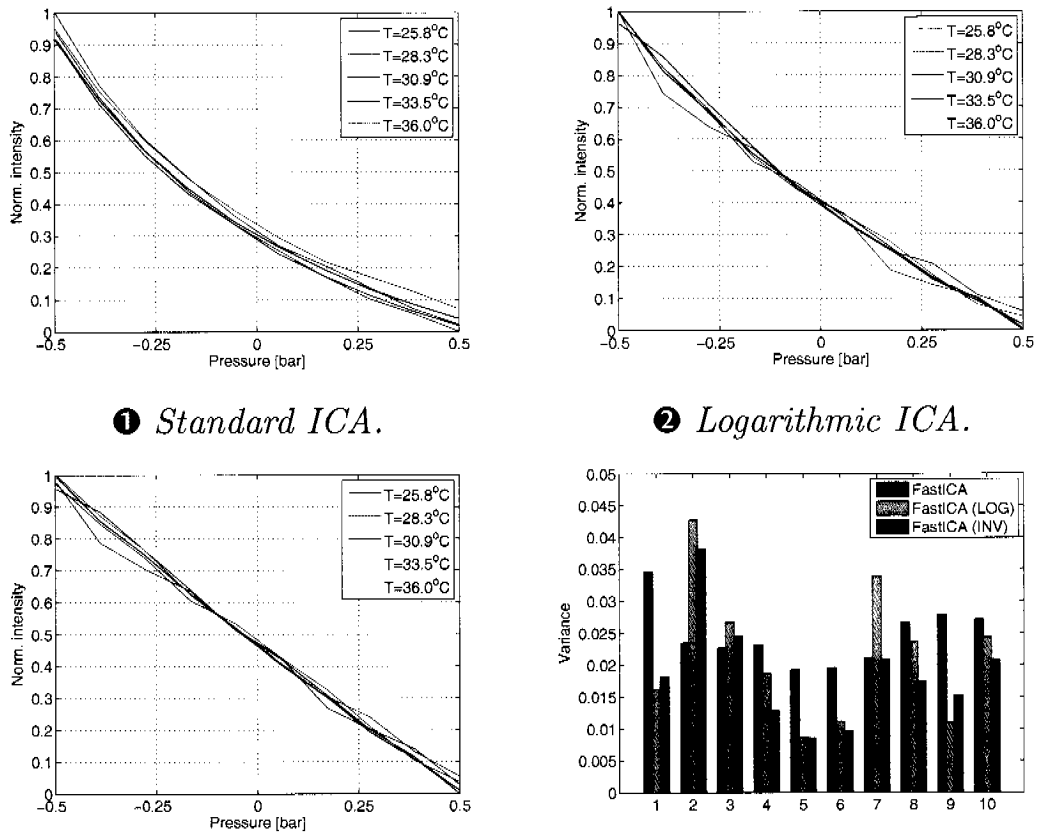


❶ *Standard ICA.* ❷ *Logarithmic ICA.*

❸ *Inverse ICA.* ❹ *Variance comparison.*

Figure 5.20: Comparison different FastICA techniques.

in Fig. 5.20 ❹. The variance mean value is reduced from 0.0245 to 0.0217 with the logarithmic method and to 0.0186 with the inverse ICA.

The FastICA algorithm, as demonstrated, reduces the temperature dependence of the pressure signal. Still, the unwanted temperature effects can not be completely avoided. A possible explanation is the restriction of the FastICA to separate only signals in a linear way. With the coupling of the measured signals being non-linear an optimal signal separation can not be achieved. The use of special preprocessing methods helps to improve the results.

| | Pressure | | Temperature | |
|---|---|---|---|---|
| | POD | FastICA | POD | FastICA |
| Standard ICA | 0.0484 | 0.0245 | 0.0516 | 0.0361 |
| Logarithmic ICA | 0.0505 | 0.0217 | 0.0523 | 0.0355 |
| Inverse ICA | 0.0517 | 0.0186 | 0.0525 | 0.0348 |

Mean variance of measured data: $< p >= 0.0361, < T >= 0.0381$.

Table 5.4: Variance comparison

# Chapter 6

# *RUAG Aerospace Measurement Campaign*

The aim of this test campaign was to validate the characteristics, properties and response of the EL-foil / PSP system developed in the laboratory. The hardware setup and the problems encountered in the small test environment (test cell) differ from those of a large environment like a wind tunnel. The effects of dark level correction, frame averaging and filter choice were investigated. A comparison between LED, and green and blue EL-foil techniques is presented. Due to higher emission intensity and setup problems with the blue EL-foil, the green one was preferred.

## 6.1 Hardware Facilities and Setup

The measurements were performed in the large subsonic wind tunnel at RUAG Aerospace[1]. The tunnel is of the atmospheric, closed single return type with a test section area of 7 $x$ 5 $m^2$. A schematic view is given in Fig. 6.1. An F-18 airplane model was used during the whole test campaign. The model was chosen because of measurements previously done at RUAG Aerospace with "standard" Ru-based PSPs. A comparison of the measurement results could thus be performed. For every measured configuration a comparison between the standard technique and the EL-foil is presented. For this purpose a standard hardware setup with LED lamps was installed. The external blue LED light sources were placed outside the wind tunnel to illuminate one wing of the airplane model (Fig. 6.2).

Two different digital cameras were used. To acquire the PSP fluorescent emission the intensified Texas Instrument[2] CCD camera was used. Three different optical filters, namely Schott 570 nm, Schott 590 nm and Schott 610 nm, were used to collect the red fluorescent emissions of the paint. To study in more detail the effects of the temperature on the PSP measurements the IR camera was employed[3]. The measurements were

[1] RUAG Aerospace, 6032 Emmen, Switzerland

[2] see appendix A.1.3

[3] see appendix A.1.3

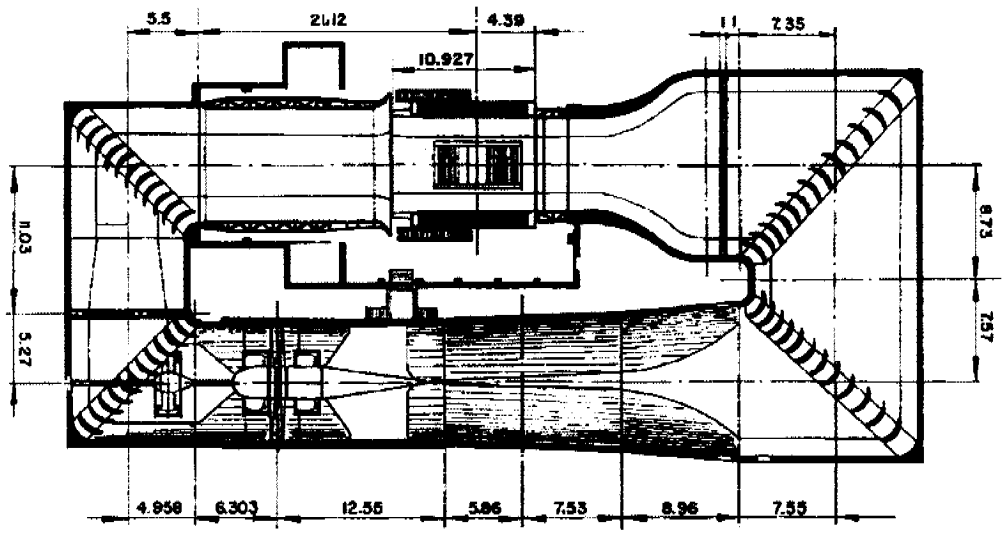


Figure 6.1: Schematic view of the large wind tunnel.

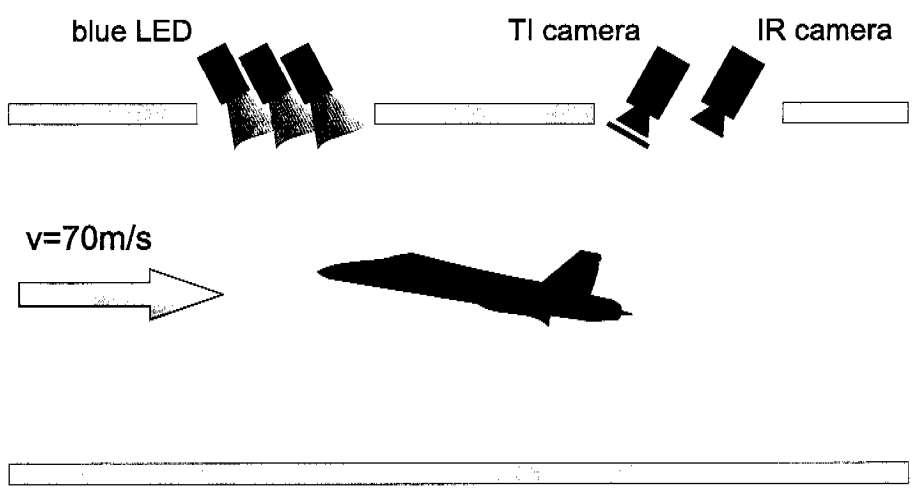


Figure 6.2: Setup of the PSP measurements.

performed using the following procedure:

1. Acquisition of data without any illumination in the tunnel (dark level image (DL))
2. Acquisition of data without wind (wind $OFF_1$ image)
3. Wind tunnel power on

4. Acquisition of data (wind $ON$ image)

5. Wind tunnel power off

6. Acquisition of data without wind (wind $OFF_2$ image)

For every data acquisition step a Matlab file containing all images and the acquisition time was saved. The DL image is used to reduce the errors due to the dark level noise of the CCD camera. The wind $OFF_1$ or wind $OFF_2$ images are used in the PSP image ratio technique to eliminate the inhomogeneities of the fluorescent illumination. A detailed description of the choice of the proper reference image is presented in Sec. 6.3.2. The wind $ON$ image is used to compute the pressure map. A Matlab program was witten to align the wind $ON$ images with the reference images, compute the intensity ratios and evaluate the data. For every measurement the acquired images were postprocessed and different evaluation images were created (Tab. 6.1).

| $n^o$ | | Description | Image name [a] |
|---|---|---|---|
| 1 | Ratio 1 | $\frac{wind\ OFF_1-DL}{wind\ ON-DL}$ | $Ratio\ XXX_1$ |
| 2 | Ratio 2 | $\frac{wind\ OFF_2-DL}{wind\ ON-DL}$ | $Ratio\ XXX_2$ |
| 3 | IR 1 | wind $ON$ | $IR\ XXX_1$ |
| 4 | IR 2 | wind $OFF_1$ | $IR\ XXX_2$ |
| 5 | IR 3 | wind $OFF_2$ | $IR\ XXX_3$ |

[a] XXX refers to the run number (see appendix E.2)

Table 6.1: Computed images.

Ratios 1 and 2 are computed taking the pictures of the CCD camera and IR 1 to 3 by taking the pictures of the IR camera. Comparisons between the different ratio techniques are described in Sec. 6.3.2. Notice that the PSP/EL-foil system was not calibrated. The absolute pressure on the model surface will therefore not computed: the measurements refers only to a relative change in intensity [%].

## 6.2 Measurements

As first step the behavior of the different hardware configurations was investigated. Two different EL-foils were attached to the right airplane wing. Fig. 6.3 shows a detail of the the measurement setup: the blue EL-foil[4] ❶ and the green EL-foil[5] ❷ were painted with Ru-based PSP embedded in RTV 118.

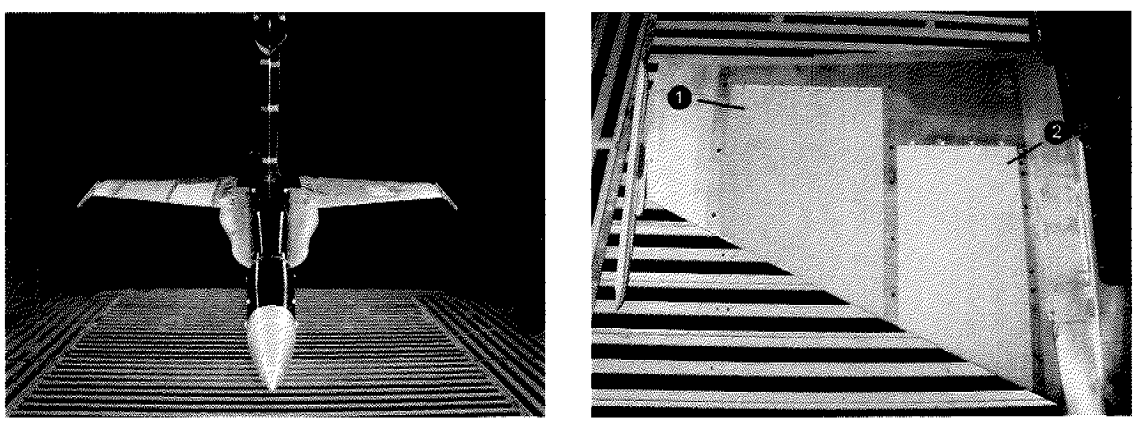


Figure 6.3: F-18 model in the large wind tunnel with EL-foils.

The influence of parameters, such as integration time of CCD and choice of color filters, on the measurement quality was evaluated. The results are shown and discussed in Sec. 6.2.1. A comparison of the pressure maps taken with the standard and new technique at different angles of attack is performed (Sec. 6.3.2). Some preliminary measurements were also performed to investigate the dependence of the EL-foil emission intensity on temperature changes (Sec. 6.3.3).

### 6.2.1 Setup Optimization

The aim of these test runs was to optimize the hardware setup. For a direct and simple comparison every measurement was done with a wind speed of 70 $m/s$ and an angle of attack of 10°. The complete list of tests is summarized in Tab. 6.2. Measurements numbered 161 to 169 were focused on the behavior of the green EL-foil. Three different filters were tested by using as illumination source the EL-foil (161-163) and as comparison the LED lamps (164-166). The tests numbered 167 to

[4]Type: Lumitec 1655, see appendix C
[5]Type: Lumitec 1659, see appendix C

169 were focused on the influence of the number of averaged frames on measurement quality and noise. The effects of filters and of frame averaging were also investigated with the blue EL-foil configuration (170-173). As comparison two measurements (174-175) were performed with the standard technique.

| Meas. | AoA | Avg. frames | EL-foil | Illumination | Filter |
|---|---|---|---|---|---|
| 161 | 10° | 20 | green | EL-foil | OG 590 |
| 162 | 10° | 20 | green | EL-foil | OG 610 |
| 163 | 10° | 20 | green | EL-foil | OG 570 |
| 164 | 10° | 20 | green | LED | OG 570 |
| 165 | 10° | 20 | green | LED | OG 590 |
| 166 | 10° | 20 | green | LED | OG 610 |
| 167 | 10° | 60 | green | LED | OG 610 |
| 168 | 10° | 60 | green | EL-foil | OG 610 |
| 169 | 10° | 180 | green | EL-foil | OG 610 |
| 170 | 10° | 20 | blue | EL-foil | OG 610 |
| 171 | 10° | 20 | blue | EL-foil | OG 590 |
| 172 | 10° | 20 | blue | EL-foil | OG 570 |
| 173 | 10° | 180 | blue | EL-foil | OG 610 |
| 174 | 10° | 20 | blue | LED | OG 610 |
| 175 | 10° | 180 | blue | LED | OG 610 |

Table 6.2: Setup optimization, runs list.

### 6.2.2 Measurements at Different Angles of Attack

The second part of the work was focused on measuring pressure and temperature maps at different angles of attack. The wind speed was set for every run to 70 $m/s$. The measurements were taken using the green EL-foil, which shows higher emission intensity compared to the blue one (Sec. 6.3.1). Both LED and EL-foil light sources were used to directly compare the results. An OG 610 filter was used to acquire the emission

intensity of the paint. Four different angles of attack were investigated: 10°, 5°, 0° and −10°. The effects of temperature on the reference images wind $OFF_1$ and wind $OFF_2$ were investigated as well.

| Meas. | AoA | Avg. frames | EL-foil | Illumination | Filter |
|---|---|---|---|---|---|
| 167 | 10° | 60 | green | LED | OG 610 |
| 169 | 10° | 180 | green | EL-foil | OG 610 |
| 177 | 0° | 180 | green | EL-foil | OG 610 |
| 178 | 0° | 180 | green | LED | OG 610 |
| 179 | −10° | 180 | green | EL-foil | OG 610 |
| 180 | −10° | 180 | green | LED | OG 610 |
| 181 | 5° | 180 | green | EL-foil | OG 610 |
| 182 | 5° | 180 | green | LED | OG 610 |

Table 6.3: Angle of attack, runs list.

The list of the runs is summarized in Tab. 6.3. The results are shown and discussed in Sec. 6.3.2.

### 6.2.3 Temperature Measurements

This set of measurements was performed to demonstrate the capability of measuring temperature using the emission intensity of the EL-foils. A green EL-foil without PSP to avoid unwanted pressure dependencies in the red light emission intensity was applied to the model surface. The pictures were taken without any filter in order to acquire the EL-foil emission in the whole blue/green light spectrum. The intensity changes related to temperature variations are computed as.

$$[\%] = \frac{wind\ ON}{wind\ OFF_1}. \tag{6.1}$$

The measurements were done at three different angles of attack with a wind speed of 70 $m/s$ (Tab. 6.4). A comparison with IR images is performed.

| Meas. | AoA | Avg. frames | EL-foil | Illumination | Filter |
|---|---|---|---|---|---|
| 183 | 5° | 180 | green | EL-foil | OG 610 |
| 184 | 5° | 180 | green [a] | EL-foil | - |
| 185 | 10° | 180 | green [a] | EL-foil | - |
| 186 | 0° | 180 | green [a] | EL-foil | - |

[a] without PSP

Table 6.4: Temperature measurement, list of test runs.

## 6.3 Results

### 6.3.1 Setup Optimization

To obtain an optimal measurement setup with high responsivity, low noise and high excitation intensity different aspects have to be taken into account. In this section the influence on the results of EL-foil type, filters and number of frames averaged is presented.

**EL-foils** The choice of the EL-foil is crucial to obtain a good, sensitive PSP system. As explained before green EL-foils compared to blue ones have the advantage of a higher emission intensity with a consequently higher paint excitation. The main disadvantage of the green EL-foils is the leakage: the sensitivity of the paint/foil system is strongly affected. Figs. 6.4 and 6.5 show the percentage of change in intensity with the two EL-foils by self-illumination and LED illumination with an angle of attack of 10°.

A first comparison for both EL-foils shows a reduced sensitivity response. The pressure maps are noisy and the intensity variations lower. For an easier interpretation and direct comparison of the different ratio images mean values and standard deviations of the pixel values in the measurement domain were computed. A summary is given in Tab. 6.5. The standard deviation of the EL-foil divided by the standard deviation of the LED measurement is used to roughly evaluate the quality of the EL-foil measurements. The setup with the green EL-foil has a ratio of 0.56. The blue foil shows a higher value of the ratio (0.64) and therefore a higher sensitivity. In Figs. 6.5 ❶ and ❷ it is possible to see that the

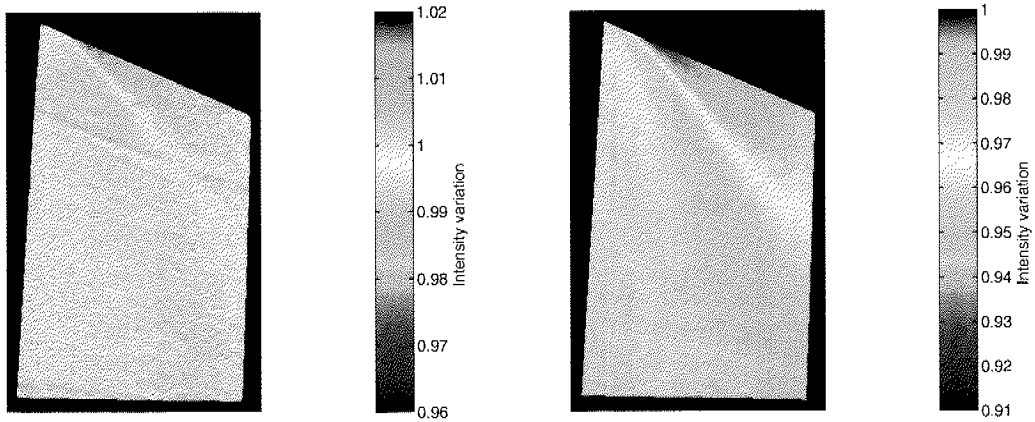


❶ *Ratio* $168_2$, *green EL-foil.* ❷ *Ratio* $167_2$, *LED.*

Figure 6.4: Comparison with green EL-foil at 10° AoA.

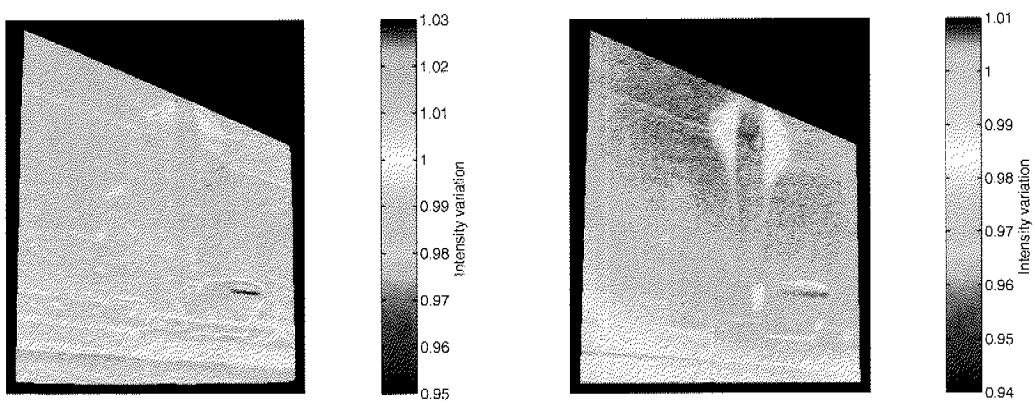


❶ *Ratio* $173_2$, *blue EL-foil.* ❷ *Ratio* $175_2$, *LED.*

Figure 6.5: Comparison with blue EL-foil at 10° AoA.

blue EL-foil has some difficulties to adhere to the complex shape of the airplane wing. The quality of the performed measurements is therefore poor and not usable. For this reason all the results presented in the following sections are computed using the green EL-foils, relying them on a lower response to pressure changes.

**Filter comparison** As shown in the laboratory tests the choice of the optical filter is very important to obtain quantitative results. The emission peak of Ru paint is located at 610 nm. An overlap of the emissions EL-foil / PSP occurs. Three different filters were available during the measurements: OG 570, OG 590 and OG 610. To investigate in more

| Meas. | Illum. source | EL-foil type | $I_{mean}$ | $I_{rms}$ | $\frac{I_{rms}(Foil)}{I_{rms}(LED)}$ |
|---|---|---|---|---|---|
| $168_2$ | EL-foil | green | 0.9997 | 0.0051 | 0.56 |
| $167_2$ | LED | green | 0.9718 | 0.0090 | |
| $173_2$ | EL-foil | blue | 0.9907 | 0.0057 | 0.64 |
| $175_2$ | LED | blue | 0.9694 | 0.0088 | |

Table 6.5: Statistical comparison of PSP response.

detail the system response, measurements with all three filters were performed. As comparison an image with the standard LED setup was acquired as well. The filters do not affect the LED measuremens, therefore only ratios with the OG 610 are presented in this case.

Fig. 6.6 shows measurements taken on the green EL-foil with an angle of attack of 10°. With the OG 570 filter the difference between EL-foil and LED measurement (Fig. 6.6 ❶ and ❷) is quite large. The leakage is very high and the paint responsivity very low. The computed ratio for the EL-foil setup does not reflect the pressure acting on the model surface. By increasing the cut-off wavelength the leakage problem becomes less important and the quality of the measurement with EL-foil increases. Fig. 6.6 ❸ and ❹ shows a similar trend compared to Fig. 6.6 ❶. Tab. 6.6 summarizes the mean and standard deviation values for the discussed measurements. As in the previous section a ratio of the standard deviations is computed. With the OG 590 the value is about 0.62: it means 38% less response than the LED illumination. By decreasing the the leakage the ratio is increased to about 0.87 with a loss of 13%. For this reason in the following the OG 610 will be preferred to the other filters.

| Meas. | Filter | Illum. source | $I_{mean}$ | $I_{rms}$ | $\frac{I_{rms}(Foil)}{I_{rms}(LED)}$ |
|---|---|---|---|---|---|
| $163_2$ | OG 570 | EL-foil | 0.9974 | 0.0076 | 0.75 |
| $161_2$ | OG 590 | EL-foil | 1.0015 | 0.0063 | 0.62 |
| $162_2$ | OG 610 | EL-foil | 0.9970 | 0.0088 | 0.87 |
| $166_2$ | OG 610 | LED | 0.9913 | 0.0101 | - |

Table 6.6: Statistical comparison of PSP response with different filters.

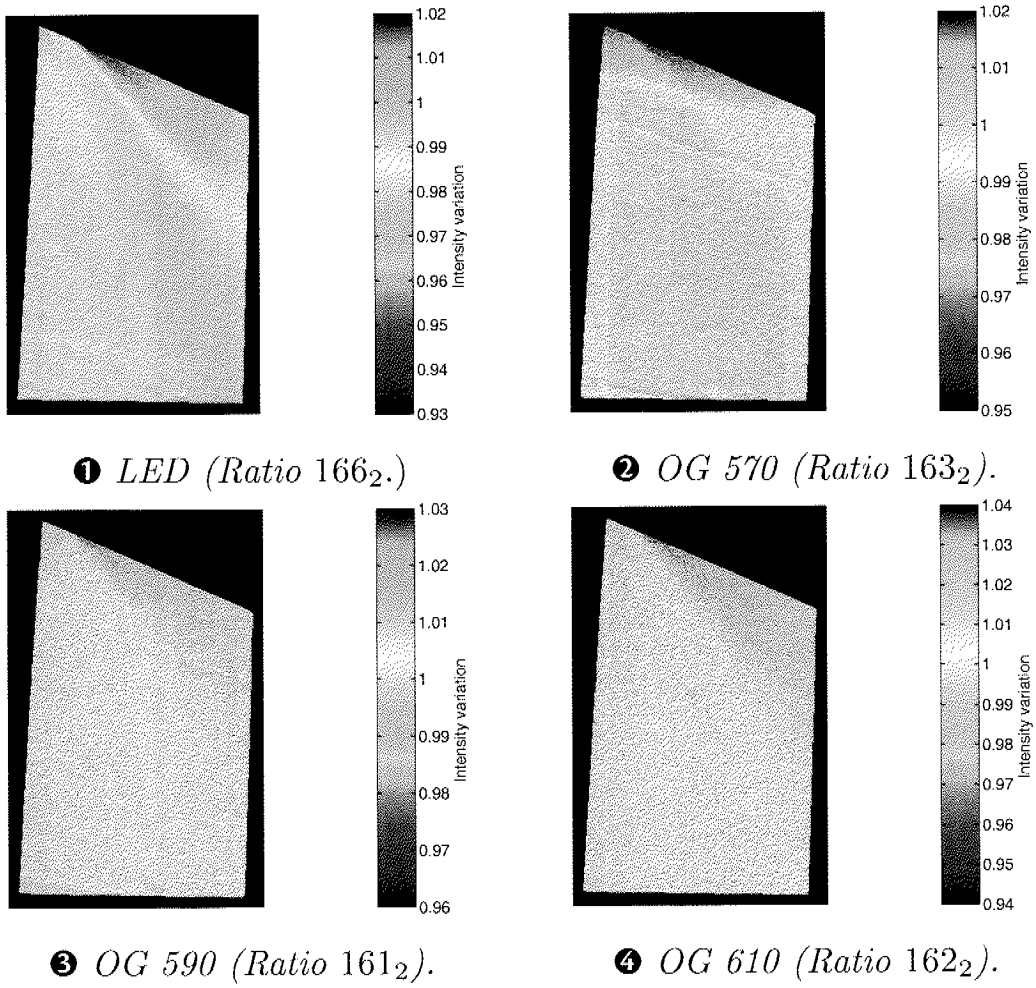


❶ *LED (Ratio* $166_2$*.)*

❷ *OG 570 (Ratio* $163_2$*).*

❸ *OG 590 (Ratio* $161_2$*).*

❹ *OG 610 (Ratio* $162_2$*).*

Figure 6.6: Filters comparison.

**Frame averaging** In this section the importance of frame averaging on the image quality is illustrated. The ratio images were computed using the measurements taken at 10° angle of attack with the green EL-foil. To compute the ratio in Fig. 6.7 ❶ an average of 20 frames was computed for both wind *OFF* and wind *ON* images. A quite large amount of noise is present. By comparing this picture with Fig. 6.7 ❷ (60 frames) and Fig. 6.7 ❸ (180 frames) the improvements are clearly visible. The flow pattern becomes much more visible and the images are smoother. The acquisition time for every measurement dataset is 50 s with a CCD integration time of 260 ms per frame. Being an acceptable time, the average of 180 frames was chosen as default for all measurements.

As for the previous sections a statistical analysis was performed and is summarized in Tab. 6.7. The noise reduction is represented by the

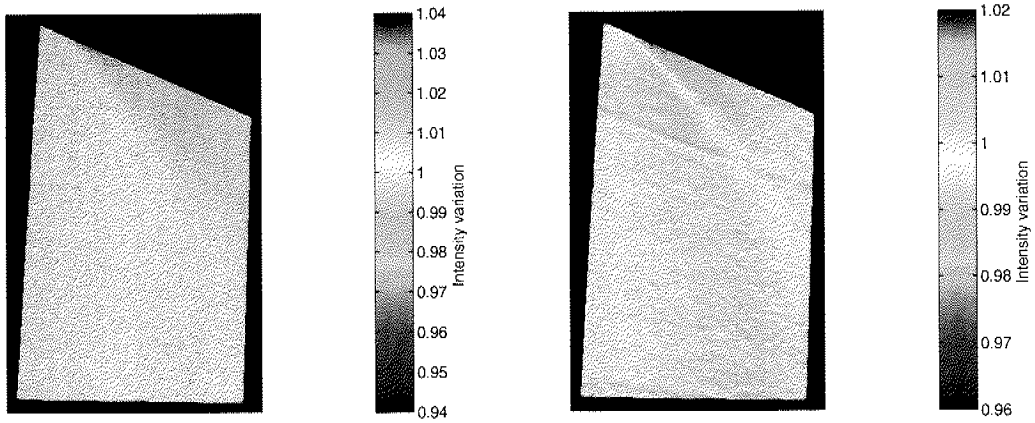


❶ *20 frames (Ratio* $162_2$*.)* ❷ *60 frames (Ratio* $168_2$*.)*

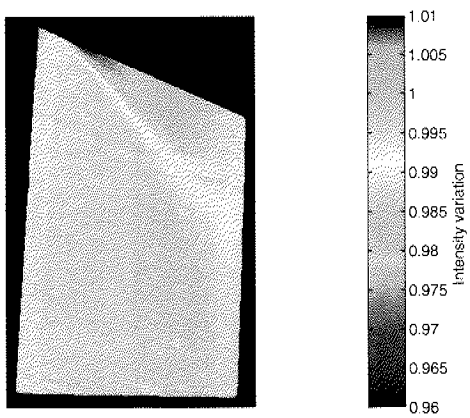


❸ *180 frames (Ratio* $169_2$*).*

Figure 6.7: Frame averaging.

decrease of the standard deviation from 0.0088 (20 frames) to 0.0049 (180 frames).

| Meas. | Avg. frames | $I_{mean}$ | $I_{rms}$ |
|---|---|---|---|
| $162_2$ | 20 | 0.9970 | 0.0088 |
| $168_2$ | 60 | 0.9997 | 0.0051 |
| $169_2$ | 180 | 0.9942 | 0.0049 |

Table 6.7: Frame averaging.

**Dark level correction** As expected the correction of the acquired images with a dark level image reduces the noise in the measurements. The ratio images do not differ optically very much with or without dark level correction. The increase in sensitivity is visible by looking at the standard deviation of the computed ratio images. Tab. 6.8 summarizes the values for measurements taken with both illumination sources. The standard deviation with dark level correction is always a bit higher compared to the one without DL correction for both setups. The sensitivity of the paint system is also increased. The ratio images shown in the next sections are always computed using dark level correction.

| | | | without DL | | with DL | |
|---|---|---|---|---|---|---|
| Meas. | AoA | Illum. source | $I_{mean}$ | $I_{rms}$ | $I_{mean}$ | $I_{rms}$ |
| $169_2$ | 10° | EL-foil | 0.9945 | 0.0046 | 0.9942 | 0.0049 |
| $167_2$ | 10° | LED | 0.9736 | 0.0085 | 0.9718 | 0.0090 |
| $181_2$ | 5° | EL-foil | 1.0012 | 0.0024 | 1.0013 | 0.0026 |
| $182_2$ | 5° | LED | 0.9923 | 0.0039 | 0.9917 | 0.0042 |
| $177_2$ | 0° | EL-foil | 1.0035 | 0.0035 | 1.0037 | 0.0037 |
| $178_2$ | 0° | LED | 0.9850 | 0.0068 | 0.9841 | 0.0072 |
| $179_2$ | −10° | EL-foil | 1.0086 | 0.0074 | 1.0090 | 0.0077 |
| $180_2$ | −10° | LED | 0.9979 | 0.0069 | 0.9978 | 0.0073 |

Table 6.8: Influence of dark level correction.

**Hardware selection summary** An optimal setup for the next series of measurements was established. Every test was performed using the green EL-foil (Fig. 6.3 ❶) with the OG 610 filter. The images acquired with the TI camera are averaged over 180 frames and the ratios are computed after applying the dark level correction. The images taken with the IR camera are not averaged.

### 6.3.2 Measurements at Different Angles of Attack

In this section measurements at different angles of attack: 10°, 5°, 0° and −10° are presented. The ratios are computed by using the wind

$OFF_2$ reference image. A comparison with the standard LED illumination source is always performed.

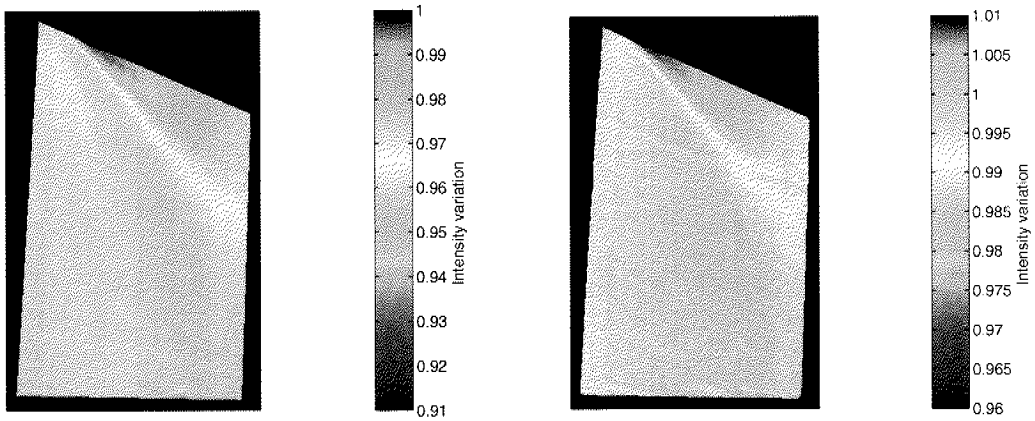


❶ *Ratio* $167_2$, *LED.* ❷ *Ratio* $169_2$, *EL-foil.*

Figure 6.8: Comparison at 10° AoA.

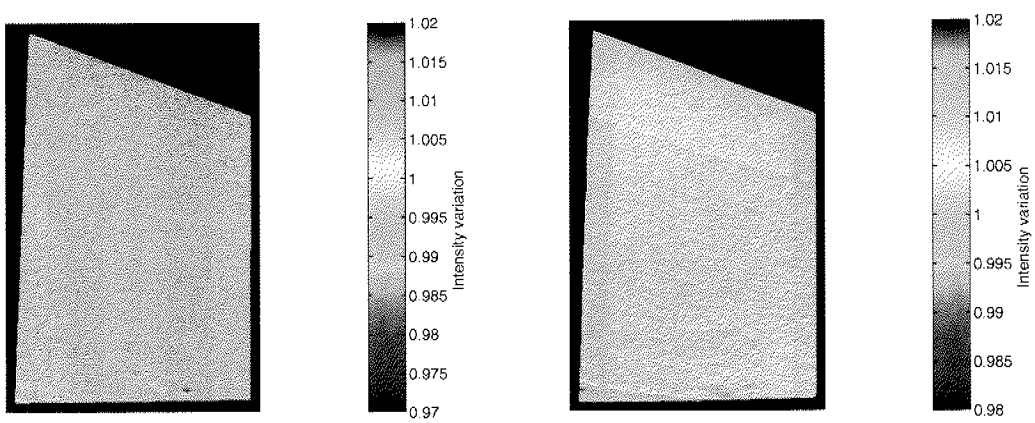


❶ *Ratio* $182_2$, *LED.* ❷ *Ratio* $181_2$, *EL-foil.*

Figure 6.9: Comparison at 5° AoA.

At 10° the flow signature is very strong and therefore in Fig. 6.8 pictures ❶ and ❷ are very similar. A vortex is crossing the whole measurement domain and is clearly visible. The picture taken with external illumination has many more identifiable details and as previously demonstrated the response is stronger. By changing the angle of attack to 5° (Fig. 6.9) and to −10° (Fig. 6.11) the flow pattern becomes very weak. The visual comparison of the images is much more difficult and no direct

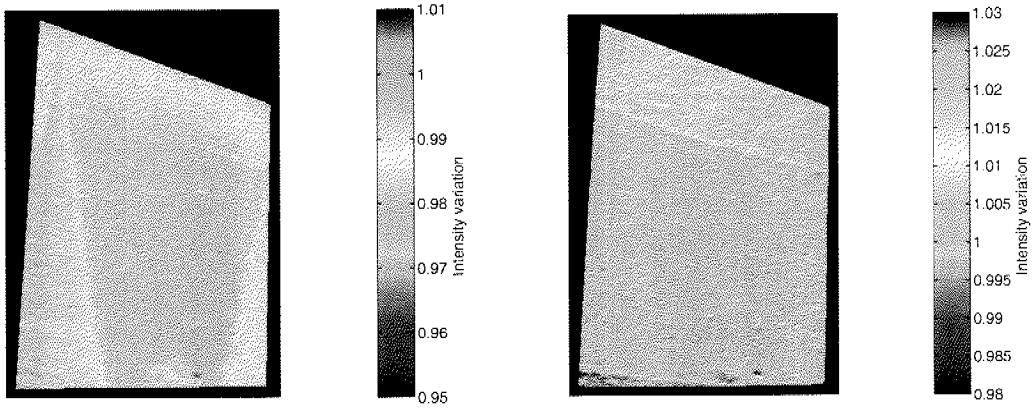


❶ *Ratio* $178_2$, *LED.* ❷ *Ratio* $177_2$, *EL-foil.*

Figure 6.10: Comparison at 0° AoA.

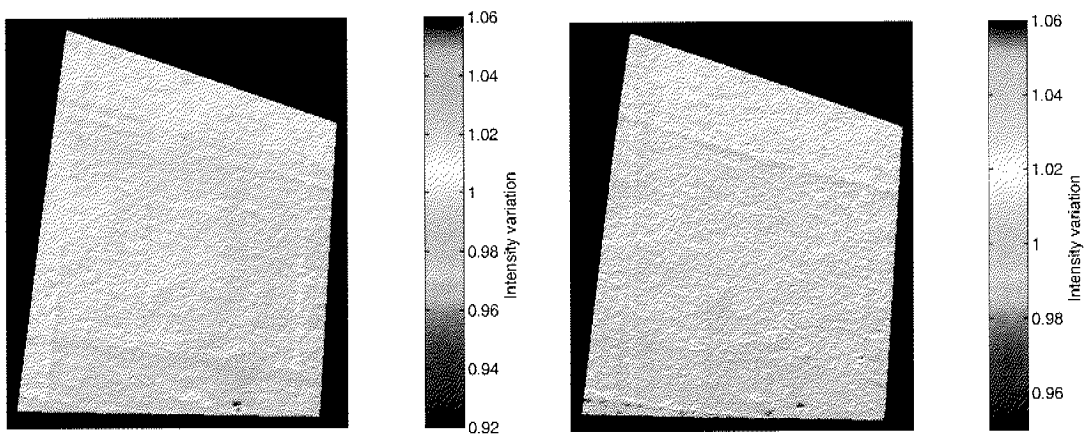


❶ *Ratio* $180_2$, *LED.* ❷ *Ratio* $179_2$, *EL-foil.*

Figure 6.11: Comparison at −10° AoA.

conclusions can be deduced. The influence of the wing structure on the temperature distribution is clearly visible in both images. In Fig. 6.10 (at 0°) the flow pattern is recognizable for LED (❶) and EL-foil (❷) illumination. The pressure maps are similar despite the lower response of the EL-foil setup. An optical comparison with PSP measurements performed at RUAG Aerospace is illustrated in Fig. 6.12. The measurements were performed with Ru-based PSP paint, LED illumination, DL correction, wind $OFF_2$ as reference and a wind speed of 70 m/s.

Fig. 6.12 ❶ shows the pressure distribution with an AoA of 10°. The vortex arising from the wing root seen in Fig. 6.8 is clearly visible. At 0°

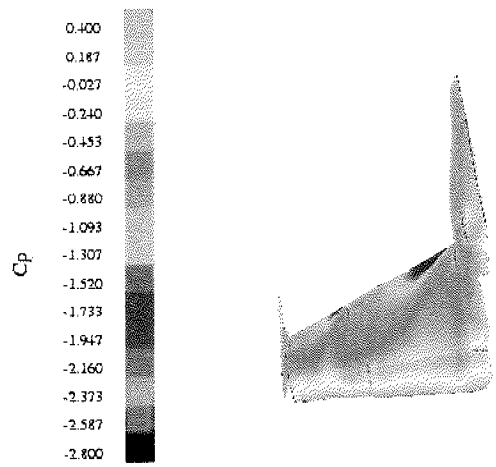


❶ *RUAG AoA*=10°.

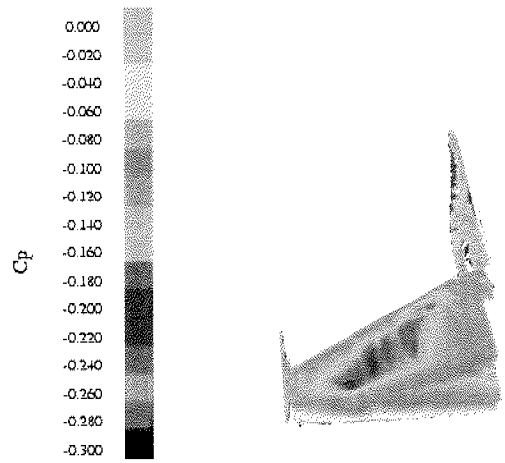


❷ *RUAG AoA*=0°.

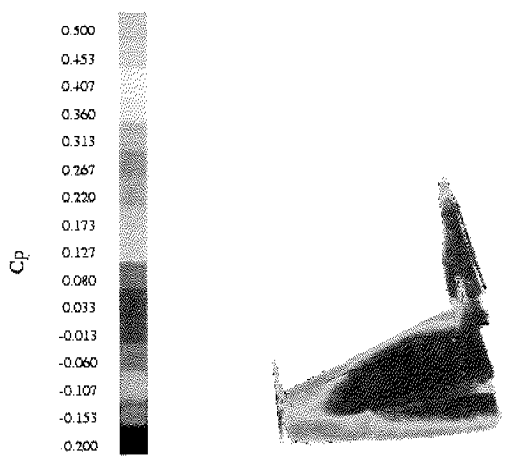


❸ *RUAG AoA*=−10°.

Figure 6.12: RUAG Aerospace measured $c_p$ maps.

AoA (Fig. 6.12 ❷) a region of under-pressure is recognizable. Fig. 6.10 shows a similar behavior. At −10° AoA (Fig. 6.12 ❸ and Fig. 6.11) no clear statement about the flow structure can be derived due to a quite homogeneous pressure distribution. The comparison shows similar results with the EL-foil/PSP data.

Another important aspect of these PSP measurements is that the EL-foil measurements are simple ratios and therefore only relative changes of the intensity emission are identifiable. The quality and results of the pressure maps strongly depend on the choice of the reference image and on the temperature distribution on the model surface. In the next section

the choice of the reference image between wind $OFF_1$ and wind $OFF_2$ images is discussed.

**Temperature effects on the reference image** The reference image taken after the run should reduce the unwanted temperature effect on the PSP measurements. In the wind $OFF_1$ image the temperature distribution on the model surface is assumed to be homogeneous and equal to the ambient temperature. In the wind $OFF_2$ image the temperature distribution is assumed to be similar to the wind $ON$ image. For this reason the errors due to temperature changes should be reduced. The EL-foil technique introduces two new important factors that affect the measurements compared to the traditional setup. First, the EL-foil produces heat and the temperature increases in the whole measurement domain. Second, the EL-foil acts as insulation between paint and model surface (metallic surface). The heat transfer characteristics and properties of the new model surface are affected and therefore the temperature distribution could be different. In Fig. 6.13 a comparison for the LED setup at 10° AoA between wind $OFF_1$ and wind $OFF_2$ is shown. It is very difficult to evaluate the results by simply looking at the intensity variation maps. An offset in the computed intensity ratios is noticeable.

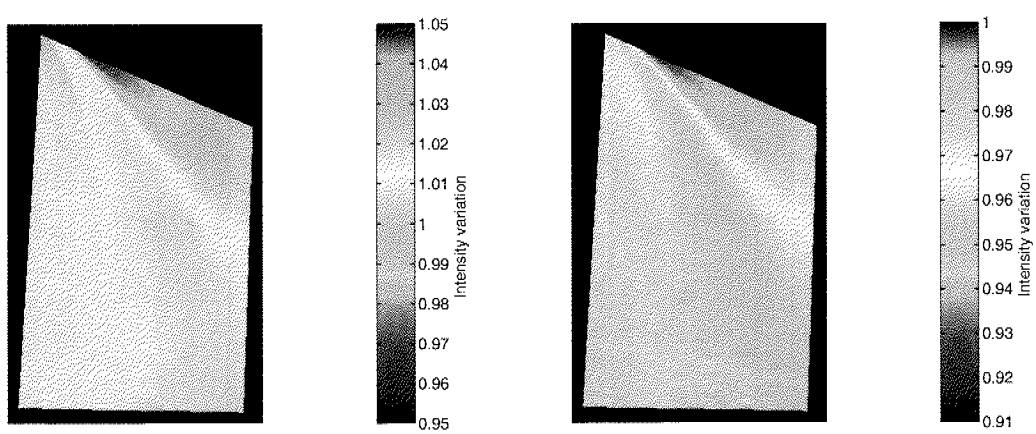


❶ *Ratio* $167_1$, *wind* $OFF_1$. ❷ *Ratio* $167_2$, *wind* $OFF_2$.

Figure 6.13: Comparison of ratios computed with wind $OFF_1$ and wind $OFF_2$.

For an easier comparison between different ratios, the statistical values of the ratio images at different angles of attack for both illumination sources are computed. A summary is given in Tab. 6.9.

| | | | wind $OFF_1$ | | wind $OFF_2$ | |
|---|---|---|---|---|---|---|
| Meas. | AoA | Illum. source | $I_{mean}$ | $I_{rms}$ | $I_{mean}$ | $I_{rms}$ |
| 169 | 10° | EL-foil | 0.9956 | 0.0052 | 0.9942 | 0.0049 |
| 181 | 5° | EL-foil | 0.9968 | 0.0035 | 1.0013 | 0.0026 |
| 177 | 0° | EL-foil | 0.9971 | 0.0042 | 1.0037 | 0.0037 |
| 179 | −10° | EL-foil | 0.9992 | 0.0081 | 1.009 | 0.0077 |
| 167 | 10° | LED | 1.0118 | 0.009 | 0.9718 | 0.009 |
| 182 | 5° | LED | 0.9879 | 0.0041 | 0.9917 | 0.0042 |
| 178 | 0° | LED | 1.0085 | 0.0075 | 0.9841 | 0.0072 |
| 180 | −10° | LED | 0.9991 | 0.0076 | 0.9978 | 0.0073 |

Table 6.9: AoA tests list.

The values of the standard deviation decrease between wind $OFF_1$ and wind $OFF_2$ for both illumination sources. A possible explanation is a lower temperature influence on the measured ratios. The mean value sometimes considerably differs between reference image (1) and (2). The values for the EL-foil tend to increase. A possible explanation is an increase of the EL-foil temperature. For the LED illumination source the mean value is usually decreasing, in some cases dramatically. The illumination intensity of the LED lamps used decreases with time and causes a decrease of the paint emission.
A further investigation is performed by comparing the histograms of the intensity ratio images. A comparison between LED and EL-foil at 10° and 0° is presented (Fig. 6.14 and 6.15).

Previous considerations about mean and standard deviation values are confirmed with the analysis of the histograms. In general with EL-foil the shape of the histograms does not change very much between taking wind $OFF_1$ or wind $OFF_2$ as reference image. An offset of the curve is present. For the measurements with LED the shapes change sometimes in a noticeable way, see for example data with an AoA of 10° (Fig. 6.14) and AoA of 0° (Fig. 6.15). This effect can be explained by a change of the model surface temperature.

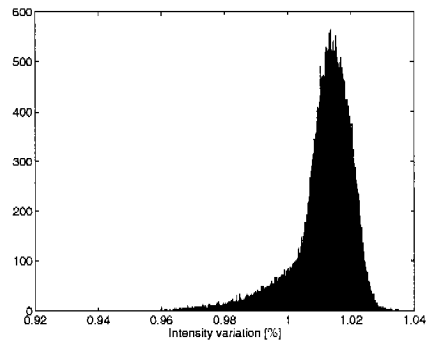


❶ $167_1$, *LED, wind* $OFF_1$.

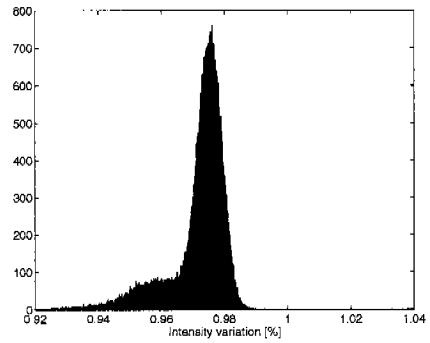


❷ $167_2$, *LED, wind* $OFF_2$.

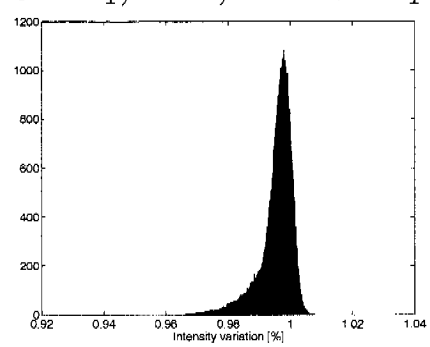


❸ $169_1$, *EL-foil, wind* $OFF_1$.

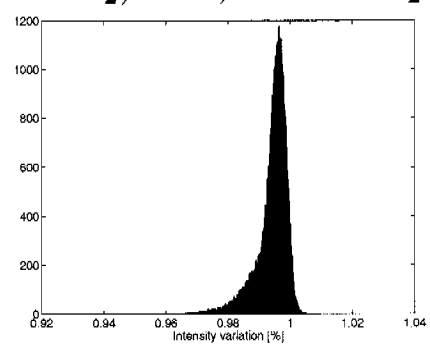


❹ $169_2$, *EL-foil, wind* $OFF_2$.

Figure 6.14: Histograms comparison at 10° AoA.

**Temperature effects on measurements** Temperature effects on PSP measurements have a great influence on the quality of the results. In the previous section differences due to the choice of different reference images were illustrated. As already explained wind $OFF_2$ images are usually preferred for higher accuracy of the measurements ratios due to the assumption of a more similar temperature distribution between wind $ON$ and wind $OFF_2$ images. Fig. 6.16 and Fig. 6.17 show the temperature distributions of the wind $OFF_1$, wind $ON$ and wind $OFF_2$ images for an AoA of 10° and 0° using the IR camera. By comparing Fig. 6.14 with Fig. 6.16 it is possible to see that with the LED illumination the temperature distribution between wind $OFF_1$ and wind $OFF_2$ changes slightly. This is explained by a different shape of the histograms in Fig. 6.14 (❶ and ❷). For the same AoA, but with EL-foil illumination, the temperature distribution does not considerably change between wind $OFF_1$ and wind $OFF_2$ and the histogram confirms this trend (Fig. 6.14 ❸). The offset in the histograms is explained with a higher surface temperature in the wind $OFF_2$ image. In general the IR

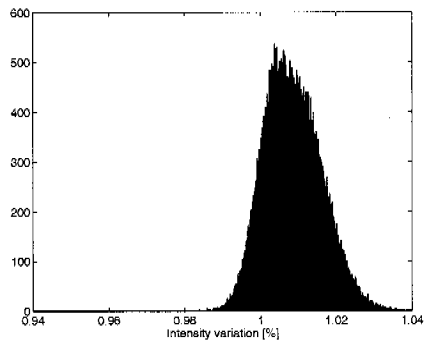


❶ $178_1$, *LED, wind* $OFF_1$.

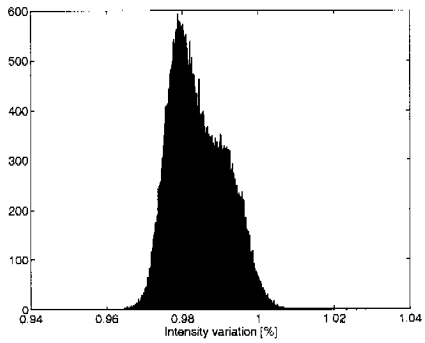


❷ $178_2$, *LED, wind* $OFF_2$.

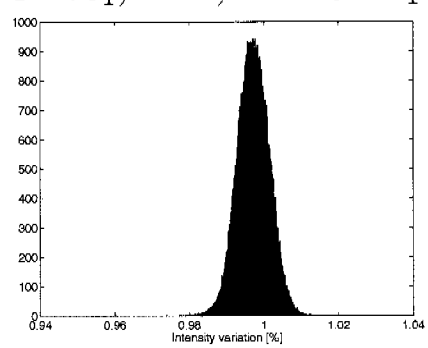


❸ $177_1$, *EL-foil, wind* $OFF_1$.

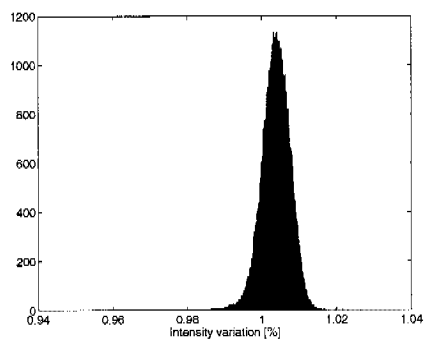


❹ $177_2$, *EL-foil, wind* $OFF_2$.

Figure 6.15: Histograms comparison at 0° AoA.

pictures (wind $OFF$) taken with the EL-foil illumination source tend to be very similar and more stable in time, probably due to a constant heat production of the foil. The structure of the model wing is clearly visible in all measurements. With the LED illumination the temperature distribution of the wind $OFF$ images changes in some cases significantly affecting the results of the computed ratio images. With both illumination sources the correlation between the wind $OFF_2$ and wind $ON$ temperature distribution is very weak. For this reason the temperature dependence of PSP can not be efficiently corrected or reduced by simply taking the wind $OFF_2$ image as a reference.

### 6.3.3 Temperature Measurements

In this section the capability of the EL-foils to measure temperature is investigated. The absolute value of the temperature was not computed. The relative change of intensity is used as indicator for temperature variations. The green EL-foil without any paint and without using any filter

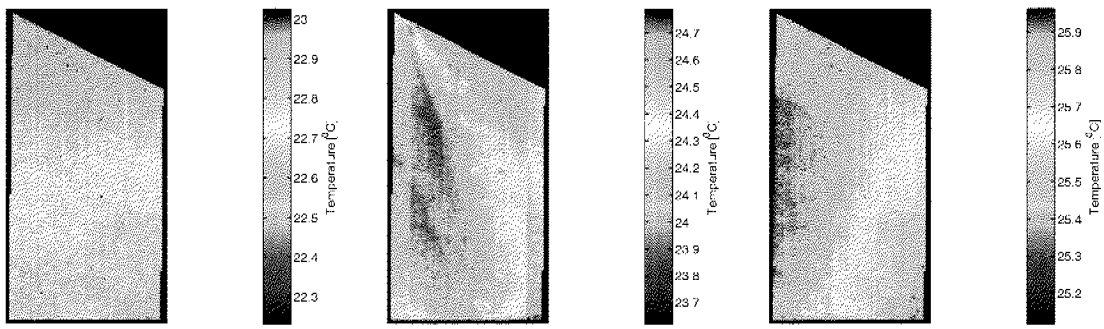


❶ 167, LED - IR: wind $OFF_1$,wind $ON$,wind $OFF_2$

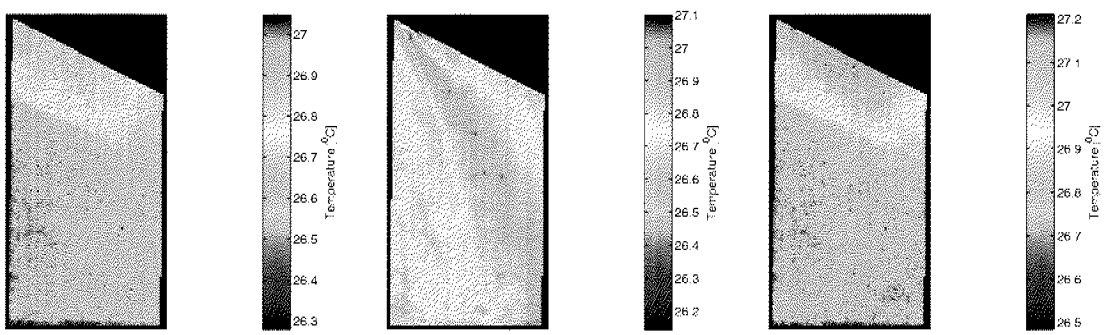


❷ 169, EL-foil - IR: wind $OFF_1$,wind $ON$,wind $OFF_2$

Figure 6.16: IR pictures comparison at 10° AoA.

in front of the camera was used. Figures 6.18 to 6.20 show a comparison of IR pictures with ratio images at 10°, 5° and 0° AoA. The ratios (❶) are computed applying the dark level correction and using the wind $OFF_1$ image as a reference. The pictures (❷) are the absolute value of the temperature on the model surface measured with the IR camera. At every AoA it is possible to see some similarities between IR and ratio images. Where the flow pattern is very pronounced (e.g., in Fig. 6.18) the structure of the flow on the wing is clearly visible. Notice that the temperature variations on the surface are very small ($1°C \div 1.5°C$). Further, more detailed investigations of these EL-foil properties have to be performed in the laboratory to quantify the accuracy of the measurement technique. Measurements with filters to acquire the EL-foil emission at a given wavelength have to be performed. An example of a full temperature measurement with EL-foil is given in chapter 7.

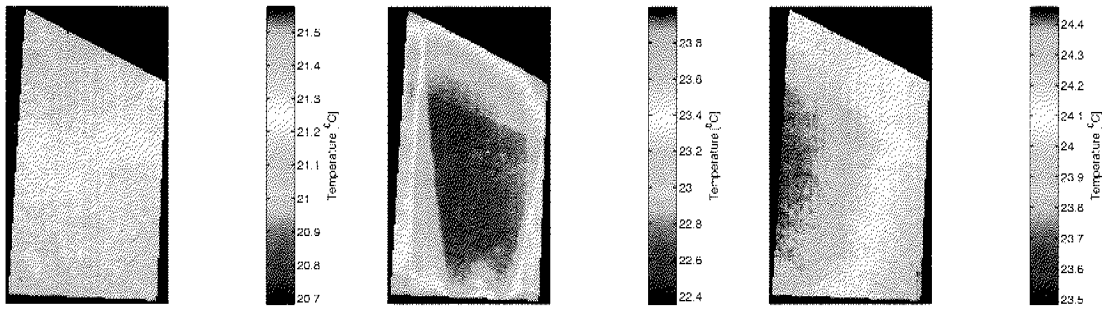


❶ 178, LED - IR: wind $OFF_1$,wind $ON$,wind $OFF_2$

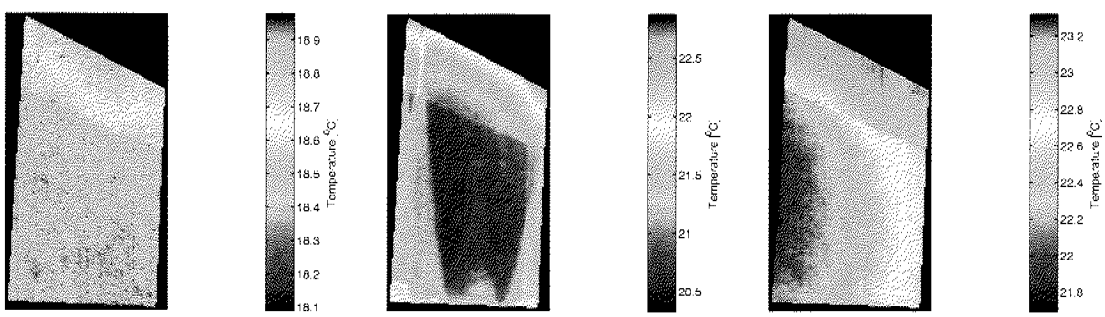


❷ 177, EL-foil - IR: wind $OFF_1$,wind $ON$,wind $OFF_2$

Figure 6.17: IR pictures comparison at 0° AoA.

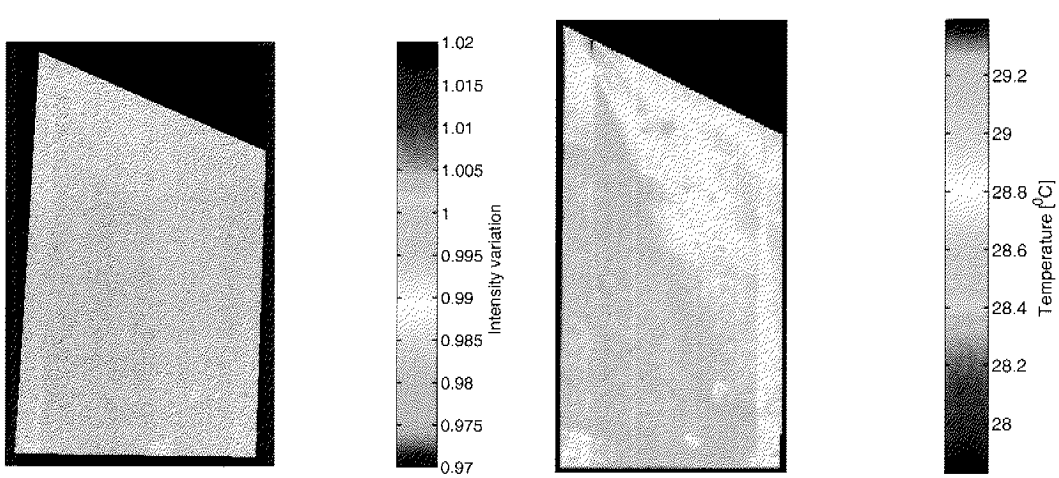


❶ $185_1$, *EL-foil, ratio image.* ❷ 185, *EL-foil, IR image.*

Figure 6.18: Temperature distribution at 10° AoA.

## 6.4 Discussion

During the measurement campaign several hardware configurations were investigated. Only the most interesting plots and ratio images are

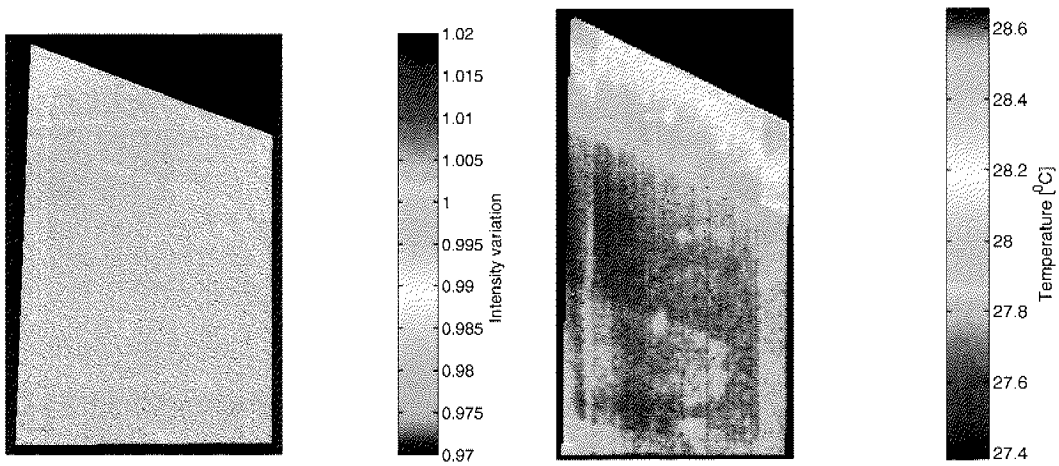


❶ $184_1$, *EL-foil, ratio image.* ❷ 184, *EL-foil, IR image.*

Figure 6.19: Temperature distribution at 5° AoA.

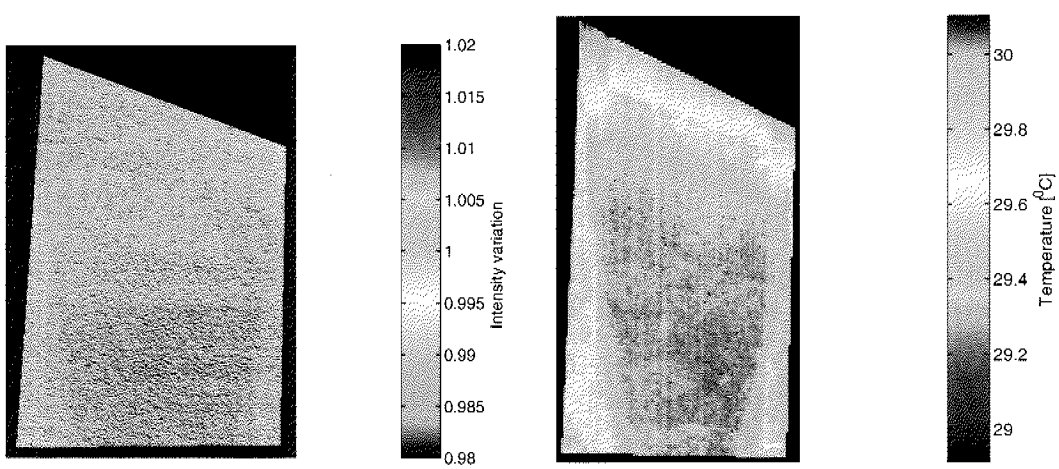


❶ $186_1$, *EL-foil, ratio image.* ❷ 186, *EL-foil, IR image.*

Figure 6.20: Temperature distribution at 0° AoA.

illustrated and discussed in this chapter. A complete list of tests and images can be found in appendix E.3. The green EL-foil was preferred to the blue one due to higher emission intensity although the acquired images have not shown particular problems with the intensity levels. In fact the emission intensity of the LED light source is higher, but with the EL-foils located directly under the paint a correct and sufficient excitation of the paint was always assured. For future measurements the blue EL-foil should be preferred because of its increase of the sensitivity.

The negative effects of temperature variations on the measurement accuracy were illustrated (Sec. 6.3.2 and Sec. 6.3.2). The choice of the reference image can be problematic and in weak pressure conditions the temperature has a dramatic influence on the results' quality. The possibility of measuring the surface temperature, and consequently the possibility of correcting the pressure maps, with the acquisition of the EL-foil emission was demonstrated. Therefore investigations in the laboratory, in particular with the multifilter technique, were performed (Sec. 5.1.3). Chapter 7 reports on the validation measurement performed on a NACA 0012 wing using the multifilter technique and the blue EL-foil: an "a-priori calibration" is used to compute both temperature and pressure maps.

# Chapter 7

# *Wind Tunnel Measurements (NACA0012)*

The aim of this measurement campaign was to demonstrate the capability of the blue EL-foils to increase the accuracy of PSP measurements and to measure surface temperature. The multifilter technique (Sec. 5.1.3) to measure surface temperature and pressure was applied to a wind tunnel test case. "A-priori calibration" is used to convert intensity variations into absolute pressure and temperature values.

## 7.1 Hardware Facilities and Setup

The measurement campaign was performed in the IFD wind tunnel. The overall dimensions can be seen in Fig. 7.1. The test section has a length of approximately 4 $m$ and a cross section of 3.0 $x$ 2.1 $m^2$. The maximum attainable dynamic pressure is about 230 $mmH_2O$, which corresponds to about 60 $m/s$, depending on the ambient conditions. A piezoresistive 6-component balance allows to measure aerodynamic forces and torques acting on the model.

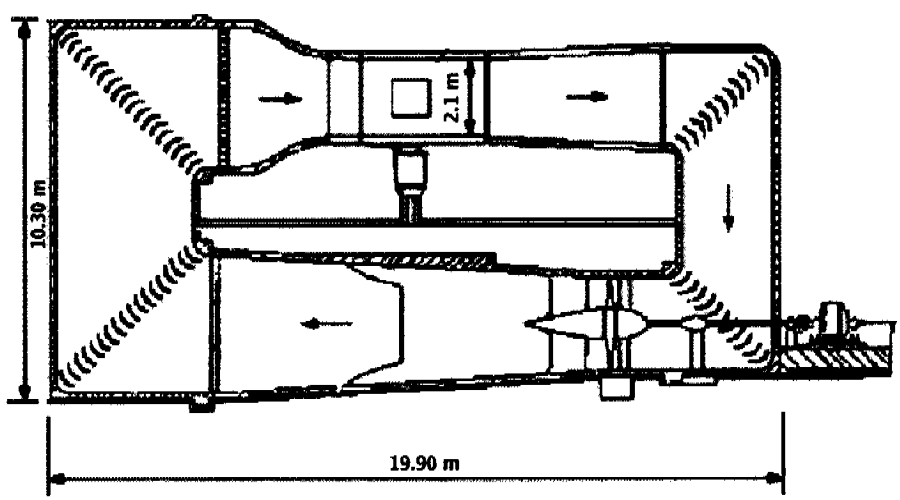


Figure 7.1: Schematic view of the IFD wind tunnel.

A rectangular wing section was chosen for the PSP measurements.

Due to the detailed documentation of its aerodynamic behavior [10, 12, 13] and model availability a NACA 0012 wing was chosen.

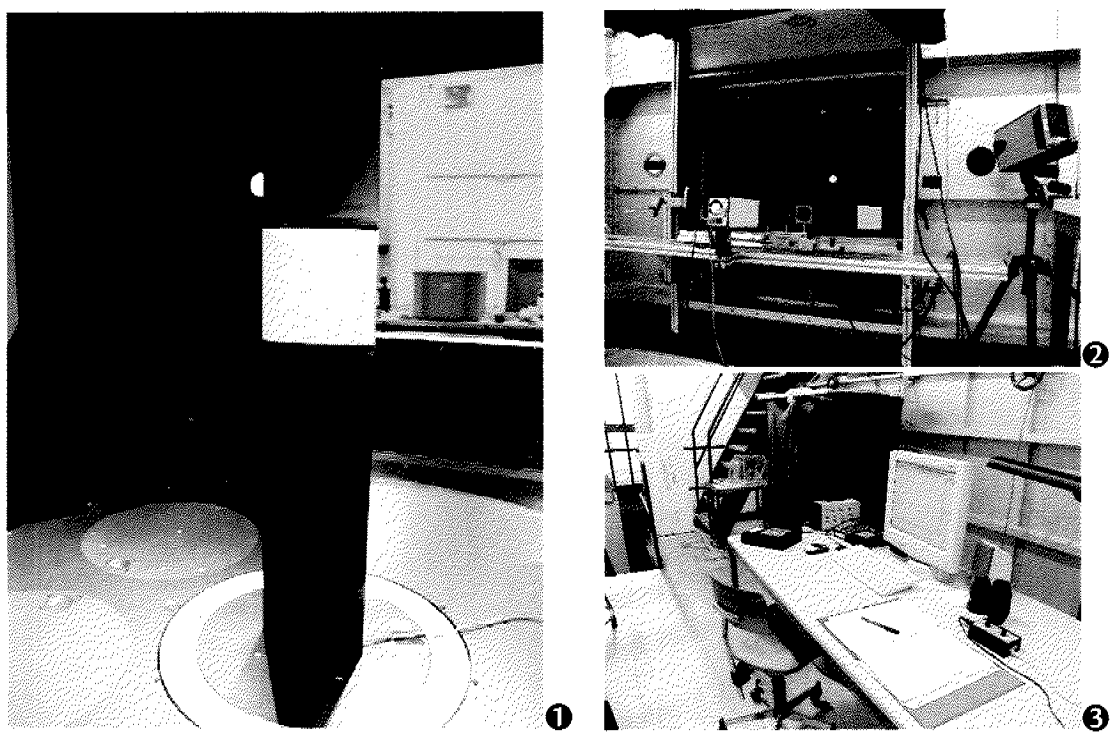

Figure 7.2: Overview of the measurement setup.

Fig. 7.2 ❶ shows the wing in the wind tunnel with a blue EL-foil and Ru paint applied. The wing was equipped with pressure taps in order to compare and evaluate the quality of the PSP measurements. The distribution of the pressure taps along the wing cord is summarized in Tab. 7.1.

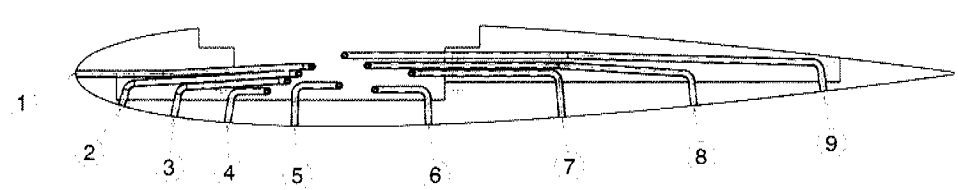


| PT $n°$ | 1 | 2 | 3 | 4 | 5 | 6 | 7 | 8 | 9 |
|---|---|---|---|---|---|---|---|---|---|
| $x/c$ [%] | 0 | 5.5 | 11.5 | 17.5 | 25.5 | 40.5 | 56.0 | 71.0 | 85.5 |

Table 7.1: Pressure tap distribution.

A Scannivalve system was used to scan the pressure taps. The measured values were acquired with a PC equipped with a data acquisition card[1] (Fig. 7.2 ❸). Two cameras (Fig. 7.2 ❷) were used during the measurement campaign. The first, the Sensicam[2], was used to acquire the intensity images (e.g., wind $ON/OFF$). Three optical filters were used to acquire the emission intensity at different wavelengths (Fig. 7.3): a list is given in Tab. 7.2.

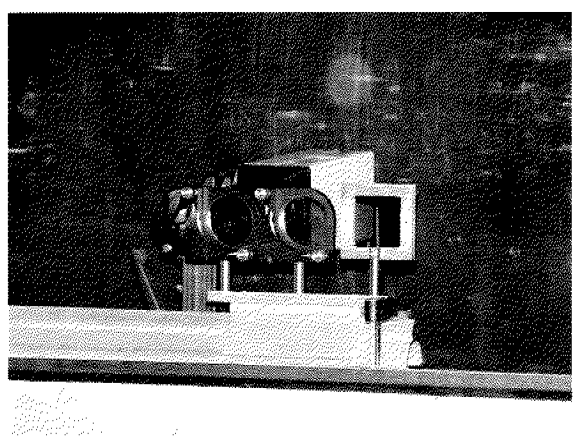

Figure 7.3: Sensicam with filters.

| No. | Type | Wavelength range |
|---|---|---|
| 1 | OG 610 | $> 610$ nm |
| 2 | 500 FS40-50 | $500 \pm 10$ nm |
| 3 | 400 FS70-50 | $400 \pm 25$ nm |

Table 7.2: Optical filters.

Filter [1] is used, as for the standard technique, to acquire the PSP emission. Filters [2] and [3] are used during the multifilter measurements (Sec. 7.3.2) in order to extract the surface temperature. In fact, by applying the simple multifilter technique, only filter [2] will be used to compute temperature maps. The second camera, the Cedip IR camera[3],

[1] NI 6036, see appendix A.1.3
[2] Lens Nikon Nikkor 60mm
[3] Appendix A.1.3

was used to directly acquire the surface temperature used as a reference. Fig. 7.4 ❶ shows the EL-foil with a layer of Ru based PSP after a measurement. Two different illumination, or excitation, sources were used: internal illumination (Fig. 7.4 ❷) with green[4] or blue[5] EL-foil and external illumination (Fig. 7.4 ❸) with four LED lamps.

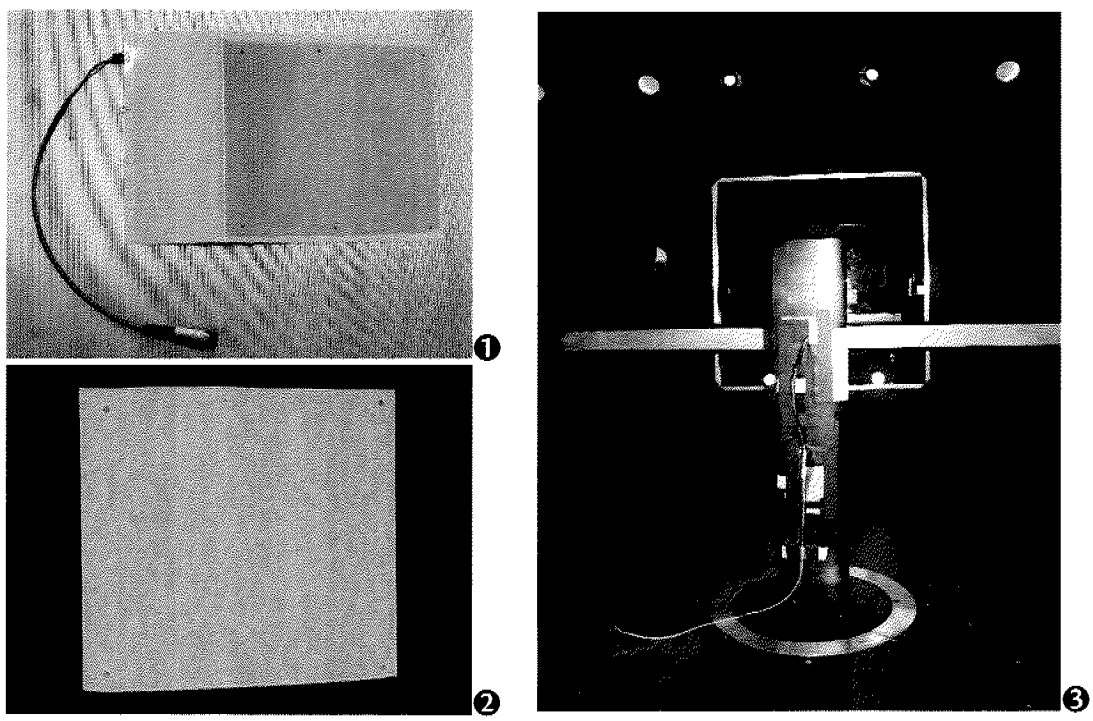


Figure 7.4: Illumination sources.

To correlate the measurements of the pressure taps with the measurements of the PSP / EL-foil system four markers were printed on the EL-foils (Fig. 7.4 ❷). Fig. 7.5 summarizes the position of the EL-foil, pressure taps and reference markers on the wing surface.

## 7.2 Preliminary Tests

This section is primarily focused on the properties of the NACA 0012 wing. The aim is to correctly plan the PSP measurements in dependence on the wing characteristics. Measurements in the wind tunnel were per-

[4]Type: Lumitec ELF 1659, see appendix C
[5]Type: Lumitec ELF 1655, see appendix C

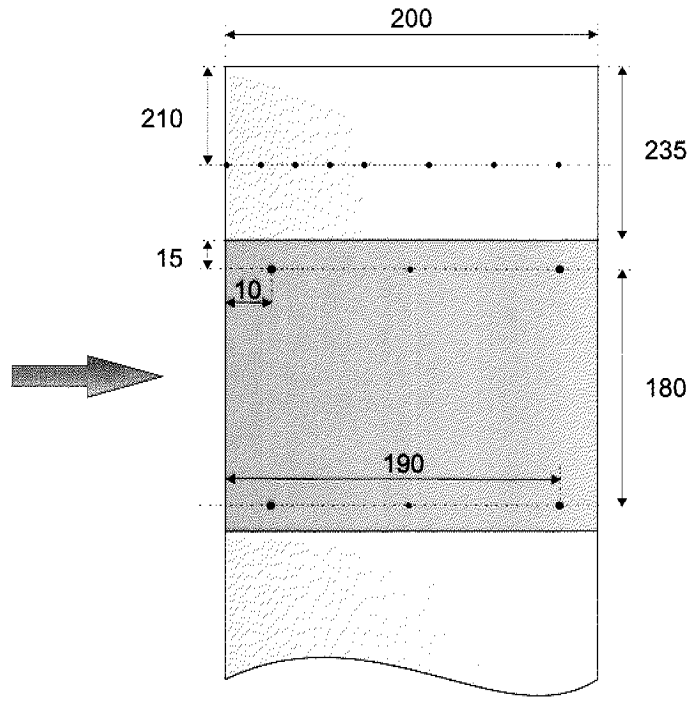


Figure 7.5: Position of EL-foil, PT and markers.

formed accordingly. In the second part a multifilter calibration of the PSP / EL-foil system is presented. An "a-priori calibration" can thus be performed to evaluate the acquired intensity data.

### 7.2.1 NACA 0012 Properties

The wing polar was measured with an angle of attack (AoA) continuously varying from $-18°$ to $18°$. Lift and drag forces were determined. The wind tunnel speed during the measurement was set to 58 m/s. With $T_{atm} = 25.5°C$ and $p_{atm} = 723.6\ mmHg$ a Re-number of $7.1 \cdot 10^5$ is obtained. The $C_L - \alpha$ and $C_D - \alpha$ diagrams were computed. From these measurements the angle with maximum lift, and therefore with highest pressure excursions, can be extracted. The flow separation angle can also be determined. In Fig. 7.6 the polar of the NACA 0012 wing is illustrated. As expected the zero lift angle for a symmetrical airfoil is located at $0°$ degrees. The asymmetry visible in both the $C_L - \alpha$ and $C_D - \alpha$ diagrams is due to a hysteresis effect. The measurement starts at $-18°$ with a fully stalled wing. Therefore the separation point at a negative angle of attack differs from the one at a positive angle of attack. The

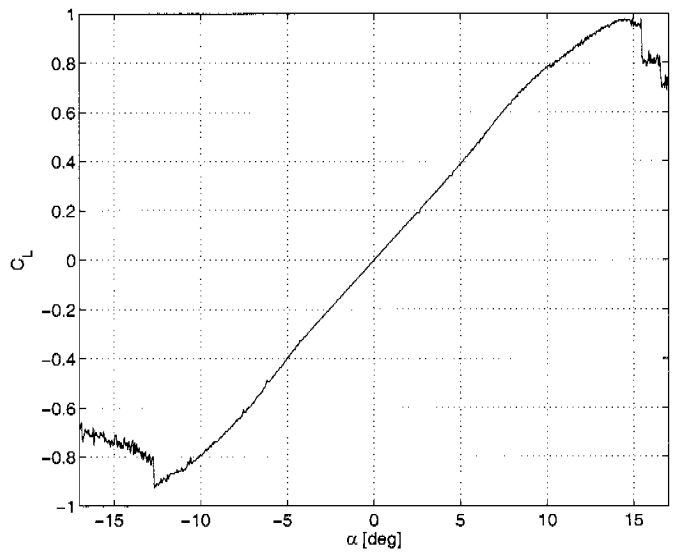


❶ $C_L$-$\alpha$ *diagram*

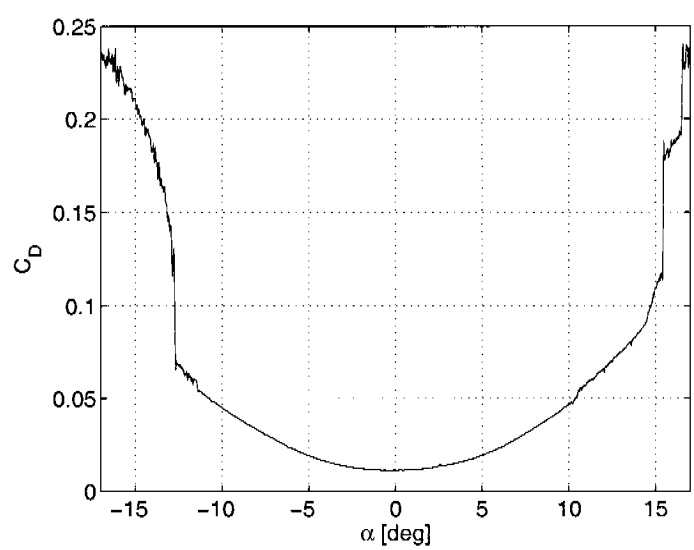


❷ $C_D$-$\alpha$ *diagram*

Figure 7.6: Polar of the NACA 0012 wing.

maximum lift coefficient is reached at 14.8° ($C_{Lmax}$ = 0.98). The flow separation occurs at about 15° with a positive AoA. With a negative AoA the reattachment occurs at 13°. The minimal drag coefficient ($C_{Dmin}$) is 0.011. The pressure distribution at four different angles of attack was

then measured using the pressure taps (PT). The wind tunnel speed was set, as for the previous measurement, to 58 m/s ($Re = 7.1 \cdot 10^5$). The measured pressures at $-10°$, $0°$, $10°$ and $12°$ degrees are intended to give an overview of the maximum pressure acting on the model surface. The pressure distributions are presented in Fig. 7.7. The pressure peaks,

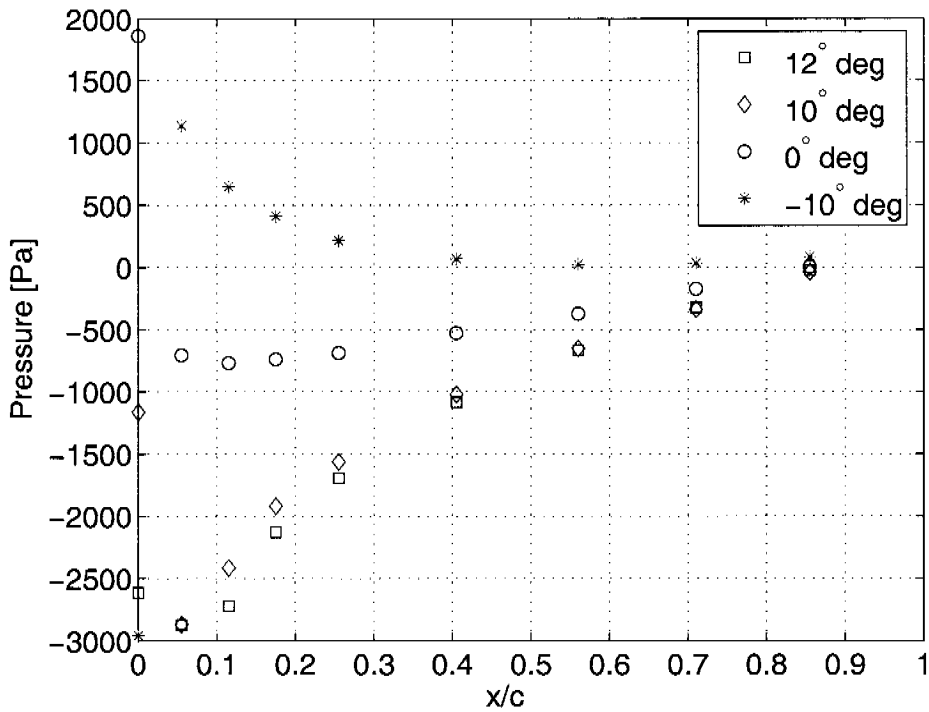


Figure 7.7: NACA 0012 - pressure distribution.

depending on the AoA, are located at about $5\% \div 10\%$ from the leading edge with a maximum value of 3000 Pa (AoA=12°). The pressures acting on the model surface are therefore quite weak. An estimation of the PSP response in order to choose interesting measurement configurations can thus be performed. By looking at the PSP calibration data (Sec. 7.2.2) with a pressure variation of 3000 Pa the expected PSP intensity changes are on the order of a few percent. With the analysis of the presented data the chosen AoAs are $-10°$, $5°$, $10°$ and $18°$. $-10°$ and $10°$ have high $C_L$ values (high pressures) and are not affected by flow separation. An angle of $5°$ was chosen to test the sensitivity of the paint in weaker pressure conditions. The AoA $18°$ is used as example of separated flow.

### 7.2.2 PSP Calibration

To compute pressure and temperature maps with an "a-priori calibration" a multifilter measurement in the TC is needed. The behavior of the blue EL-foil with Ru-based PSP was investigated. The calibration was performed with the Sensicam and a Nikkor 60 mm lens. The pressure was varied from $-0.5$ bar under-pressure to 0.5 bar over-pressure and the temperature from $25°C$ to $35°C$. For every measurement point images were acquired with all filters listed in Tab. 7.2. The intensity responses,

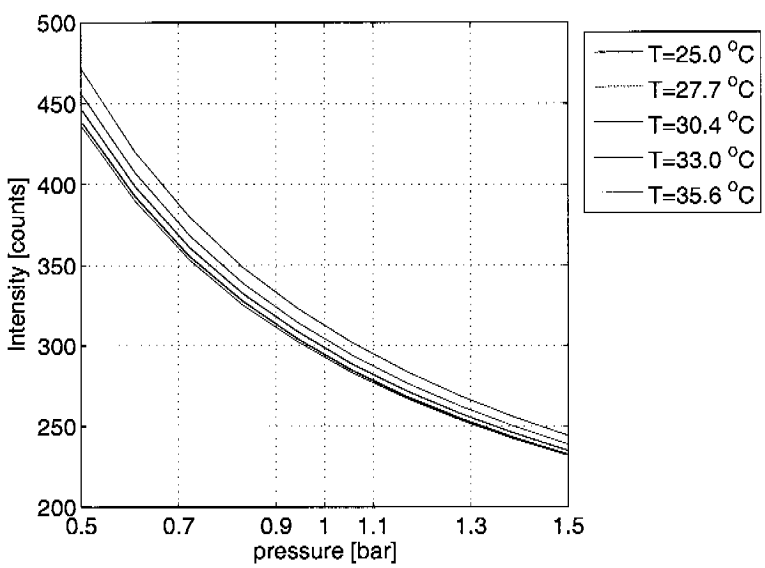


Figure 7.8: Multifilter calibration filter [1].

shown in Figs. 7.8 to Fig. 7.10, are computed by averaging 40 frames and by subtracting the dark level image. In Fig. 7.8 the classical PSP response is visible. With a pressure variation of $\pm 5000$ Pa the intensity variation is about 5%. With the use of the filters [2] and [3] (Fig. 7.9 and Fig. 7.10) the temperature distribution can be computed. With filter [2] the mean intensity variation at $p = p_{atm}$ is about 1 % per degree. The variations are very small and an adequate amount of frame averaging is needed.

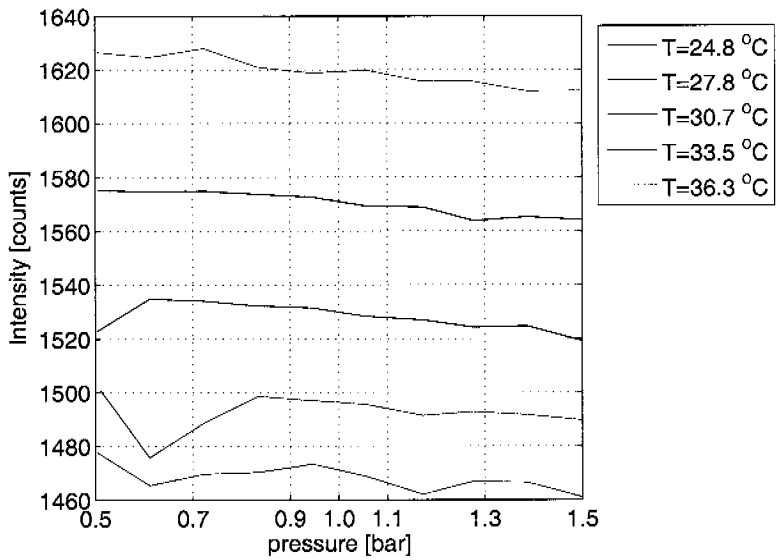


Figure 7.9: Multifilter calibration filter [2].

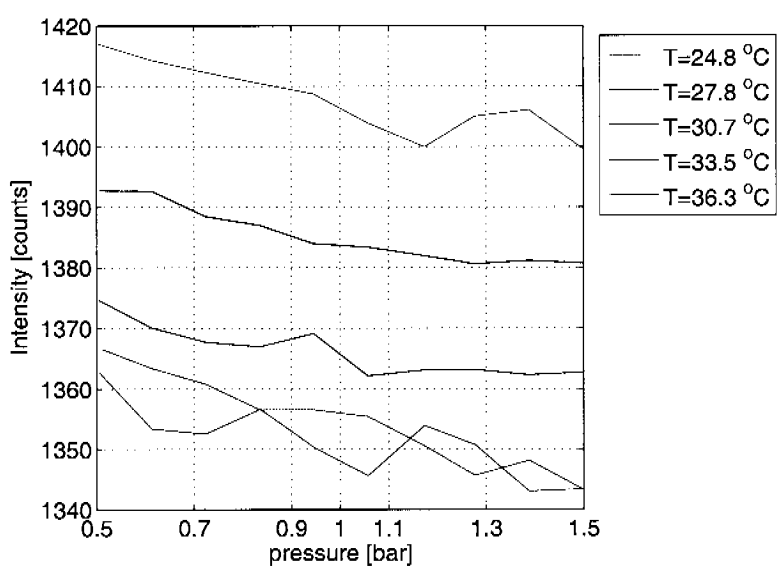


Figure 7.10: Multifilter calibration filter [3].

## 7.3 PSP Measurements

This section is divided in two parts. In Sec. 7.3.1 the sensitivity of the PSP using two different EL-foils (blue/green) was investigated to confirm

the laboratory measurements. In Sec. 7.3.2 pressure and temperature distributions are measured with the multifilter measurement technique. As explained in the previous section the measurements were performed at $-10°$, $5°$, $10°$ and $18°$ AoA. The wind tunnel speed was set to 59 m/s, corresponding to a Re-Number of $7.1 \cdot 10^5$ ($p_{atm} = 725.1 mmHg$, $T = 29°C$). At $18°$ AoA the wind tunnel speed was decreased to 50 m/s, due to strong vibration of the stalled wing ($Re = 6.0 \cdot 10^5$). The complete list of measured configurations is summarized in Tab. 7.3. The field "EL-foil" refers to the EL-foil onto which the PSP was painted on. For the LED measurements the paint was not painted directly onto the aluminum surface of the wing but onto an a EL-foil.

For all the measurements, data with the IR camera, CCD camera and PT were recorded. The following acquisition procedure was applied:

1. Acquisition of intensity images without any illumination in the tunnel (dark level (DL) images) with all optical filters[6].

2. Acquisition of intensity images without wind (wind OFF images) with all optical filters.

3. Acquisition of IR image without wind (reference temperature).

4. Wind tunnel power on.

5. Acquisition of intensity images (wind ON images) with all optical filters[7].

6. Acquisition of IR image (surface temperature).

7. Acquisition of pressure distribution data (pressure taps).

8. Wind tunnel power off.

9. Save data files.

A Matlab file containing all the images and pressure data was saved. Different algorithms were developed to evaluate the images and compute the pressure and temperature distributions.

[6] 1 for LED measurements and 3 for EL-foil measurements
[7] 1 for LED measurements and 3 for EL-foil measurements

| $n°$ | $\alpha$ [°] | EL-foil | Illumination | Run $n°$ | Re number |
|---|---|---|---|---|---|
| 1 | -10 | blue | EL-foil | 05 | $7.1 \cdot 10^5$ |
| 2 | -10 | blue | LED | 06 | $7.1 \cdot 10^5$ |
| 3 | -10 | green | EL-foil | 13 | $7.1 \cdot 10^5$ |
| 4 | -10 | green | LED | 14 | $7.1 \cdot 10^5$ |
| 5 | +5 | blue | EL-foil | 07 | $7.1 \cdot 10^5$ |
| 6 | +5 | blue | LED | 08 | $7.1 \cdot 10^5$ |
| 7 | +5 | green | EL-foil | 15 | $7.1 \cdot 10^5$ |
| 8 | +5 | green | LED | 16 | $7.1 \cdot 10^5$ |
| 9 | +10 | blue | EL-foil | 03 | $7.1 \cdot 10^5$ |
| 10 | +10 | blue | LED | 04 | $7.1 \cdot 10^5$ |
| 11 | +10 | green | EL-foil | 11 | $7.1 \cdot 10^5$ |
| 12 | +10 | green | LED | 12 | $7.1 \cdot 10^5$ |
| 13 | +18 | blue | EL-foil | 09 | $6.0 \cdot 10^5$ |
| 14 | +18 | blue | LED | 10 | $6.0 \cdot 10^5$ |
| 15 | +18 | green | EL-foil | 17 | $6.0 \cdot 10^5$ |
| 16 | +18 | green | LED | 18 | $6.0 \cdot 10^5$ |

Table 7.3: Measured configurations.

### 7.3.1 Comparison blue - green EL-foils

In this section the PSP sensitivity is investigated. As demonstrated in the laboratory test the sensitivity of the PSP can be substantially increased by substituting the green EL-foil with the blue one. A comparison of intensity responses is performed for all investigated AoA. As reference measurements with the standard LED setup are used. To eval-

uate the results the classical ratio technique is applied. The OG 610 filter is used to acquire only the paint emission. Effects of temperature variations on the model surface are not evaluated here. The ratios are computed by using the wind $ON$, wind $OFF$ and $DL$ images with the following equation:

$$I[\%] = \frac{windOFF - DL}{windON - DL}. \tag{7.1}$$

The ratio images are converted to false color images with color coded in relative intensity variations. A visual comparison is performed between pictures with different illumination sources. For a better evaluation of the results the intensity distribution profile along the wing chord is computed. A region with constant (2D) pressure distribution is extracted from the intensity ratio image (Fig. 7.11). The mean value of the in-

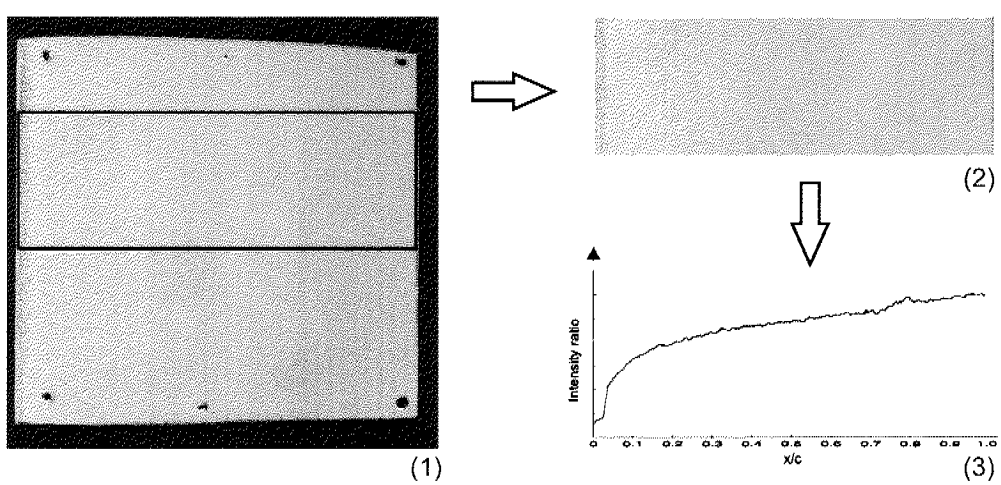


Figure 7.11: Computation of the pressure distribution.

tensity along the wing span is computed. The resulting intensity ratio distribution is plotted as a function of the wing cord $[x/c]$. The results are presented in Sec. 7.4.1.

### 7.3.2 Multifilter Measurements

The basic idea of the multifilter measurements is to directly measure temperature and pressure maps. The intensity measurements performed in the wind tunnel are calibrated with the data presented in Sec. 7.2.2.

The simple MF-technique presented in Sec. 5.2.1 is used to evaluate the data.
In the first part, temperature maps are computed. A comparison between IR and EL-foil measurements is performed. The temperature profile along the wing chord is extracted: leading and trailing edge are used as alignment reference.
In the second part of the section pressure maps are computed. A comparison between EL-foil, LED and PT is performed. The temperature on the model surface in wind $OFF$ conditions is assumed to be constant. The pressure values computed with the MF-technique are corrected by using the previously computed temperature maps. As for the previous measurements the pressure profile along the wing cord is computed. Notice that $x/c = 0$ for the PT corresponds to the wing stagnation point and differs slightly with the $x/c = 0$ of the PSP measurements, where the leading edge is used as a reference. A comparison with non-temperature corrected pressure maps is also performed.
Tab. 7.4 summarizes the measurements discussed in Sec. 7.4.2. The investigated AoA are $-10°$, $5°$, $10°$ and $18°$.

| | blue EL-foil | LED | IR | PT |
|---|---|---|---|---|
| Temperature | x | - | x | - |
| Pressure (with T corr.) | x | - | - | x |
| Pressure (without T corr.) | x | x | - | - |

Table 7.4: Performed measurements.

## 7.4 PSP Results

In the following sections the results of the EL-foil comparison and MF measurements are analyzed and discussed. Only the most significant plots and pressure maps are presented. The complete list of results and plots is given in Appendix E.3.

### 7.4.1 Comparison blue - green EL-foil

Before showing the results of the comparisons some general problems related to the measurements are discussed. Fig. 7.12 shows the intensity ratios at AoA=−10° with all three illumination sources. The results obtained with the LED illumination on a green or on a blue EL-foil are similar and therefore only one picture is shown, namely with the blue EL-foil. The flow on the wing is not always 2-dimensional. Small perturbations or dirt can affect the flow behavior. In the upper part of the image (Fig. 7.12 ❶) a transition is clearly visible from laminar to turbulent flow, probably due to a small particle of dirt sticking on the surface. Some flow disturbances are also present at the lateral edges of the EL-foils. The thickness of the standard EL-foils used is about 100 $\mu m$. Despite the use of tape to smooth the step between EL-foil and wing surface some edge effects on the flow characteristics remain visible. The regions of interest to compute pressure distributions must therefore be carefully chosen.
Another problem arising during the measurements is well illustrated in Fig. 7.13. The four LED lamps were carefully positioned with the wing at an angle of attack of 0°. A homogeneous illumination intensity was obtained and no light reflections were visible. After changing the angle of attack the LED lamps were not rearranged. With high AoA some reflections arise and are clearly visible, e.g., in Fig. 7.13 ❶. This unwanted effect occurs especially with the LED illumination due to the fact that the illumination sources are not rotating with the wing. The use of EL-foils is in this situation of a great advantage: the reflection problem is strongly reduced (Fig. 7.13 ❷ and ❸).
In Figs. 7.12 and 7.13 different sensitivities between the blue and green EL-foil setups are visible. In weak pressure conditions (e.g., Fig. 7.12, AoA=−10°) the response to pressure changes with the green EL-foil can hardly be identified. To carefully evaluate the sensitivity of the paint the mean values of the intensity along the wing cord are computed (Sec. 7.3.1). The results at different AoAs are shown in Figs. 7.14 to 7.17.

Fig. 7.14 shows the results at an angle of attack of 10°. At the leading edge, where the pressure is maximum, the change in intensity with the standard LED technique is about 5.5 %. The sensitivity reduction with the use of a green EL-foil is clearly visible. The intensity variation at $x/c = 0$ is only 2 %. With the blue EL-foil the value is increased to

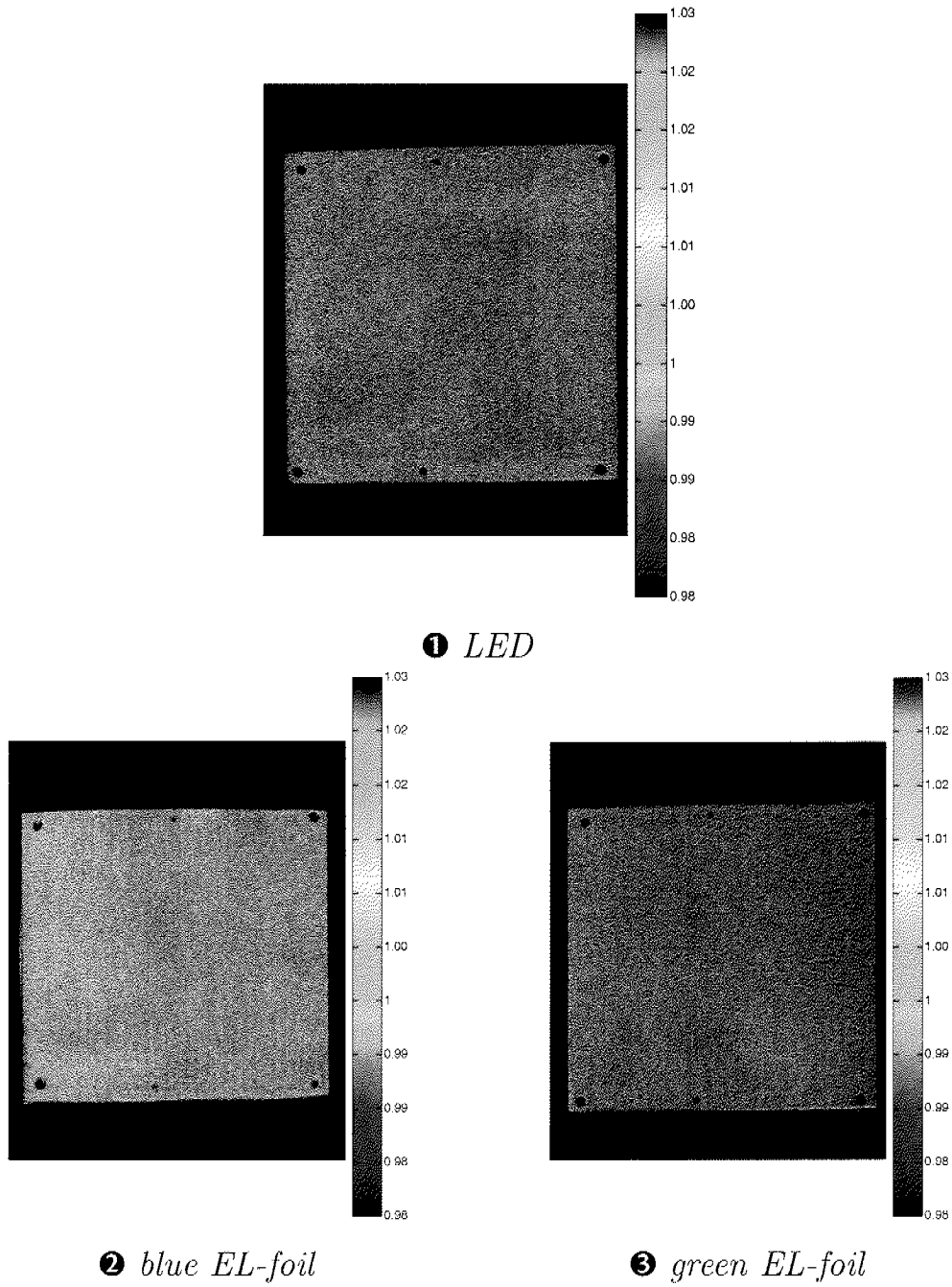


Figure 7.12: Intensity response at $-10^0$ AoA.

3.9 %. The increase of sensitivity is visible along the whole wing cord. The different behavior of the intensity distribution between LED and EL-foils at about $x/c = 0.8$ is caused by a small reflection present in the LED image.

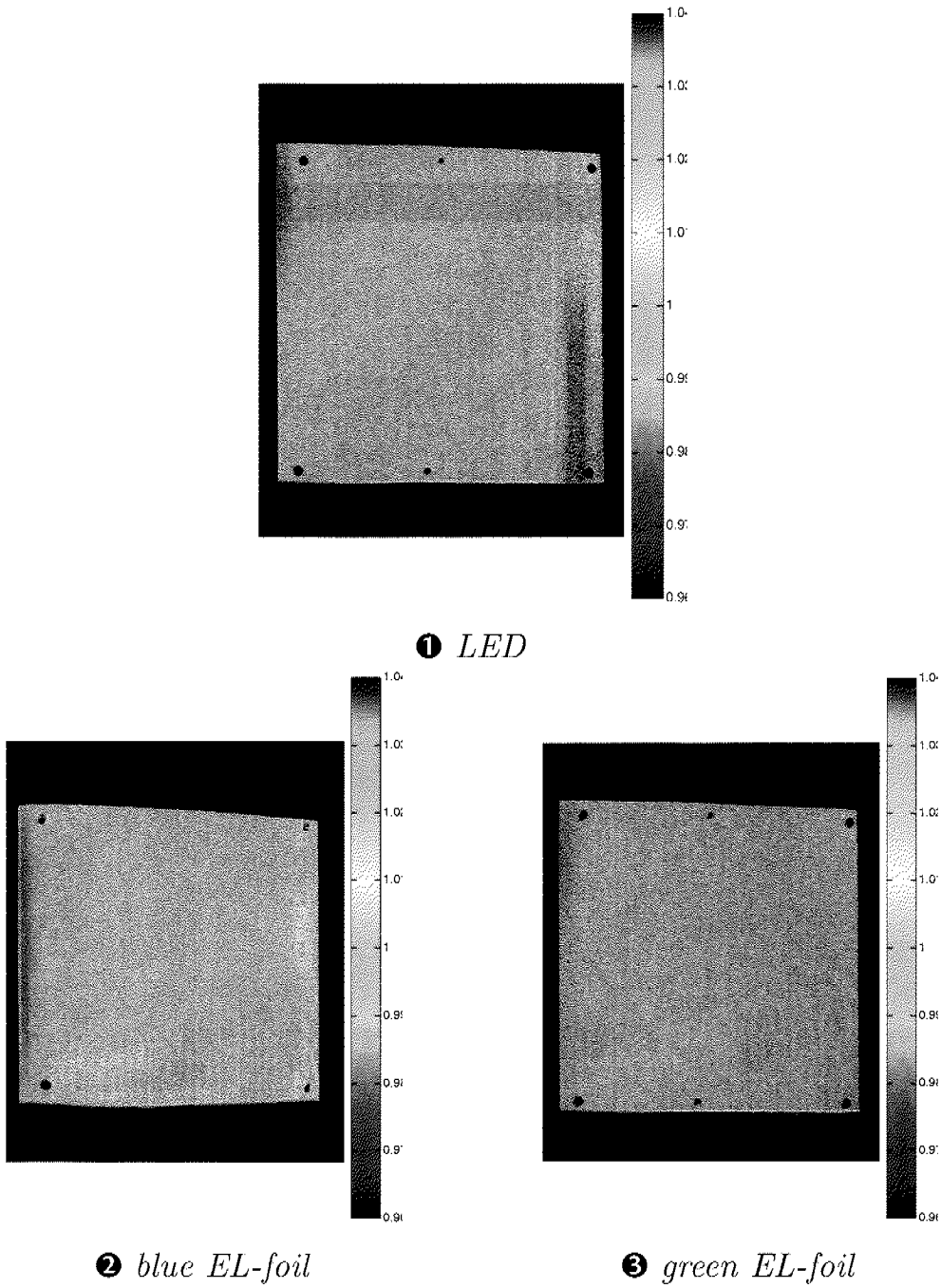

❶ *LED*

❷ *blue EL-foil*

❸ *green EL-foil*

Figure 7.13: Intensity response at $18^0$ AoA.

By decreasing the angle of attack to 5°, with a consequently lower pressure variation, the difference between green and blue sensitivities remains noticeable (Fig. 7.15). At $x/c = 0.1$ occurs, for both the LED and blue EL-foil, a change in the intensity ratio slope. This effect is not

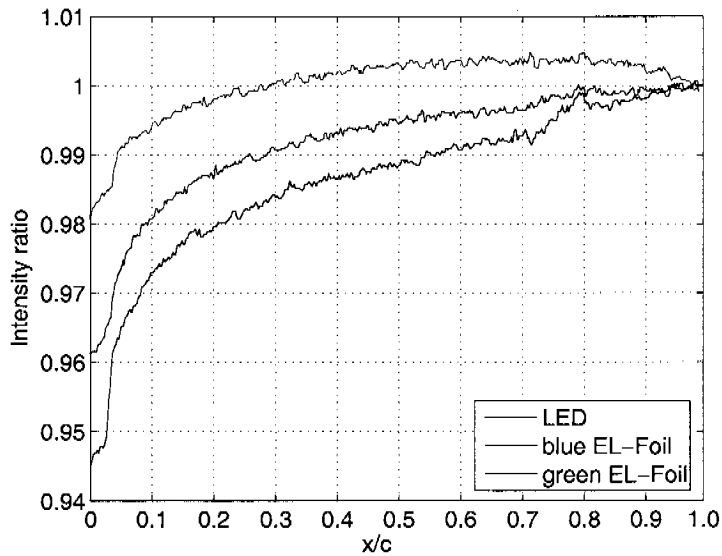


Figure 7.14: Intensity ratio distribution at 10° AoA.

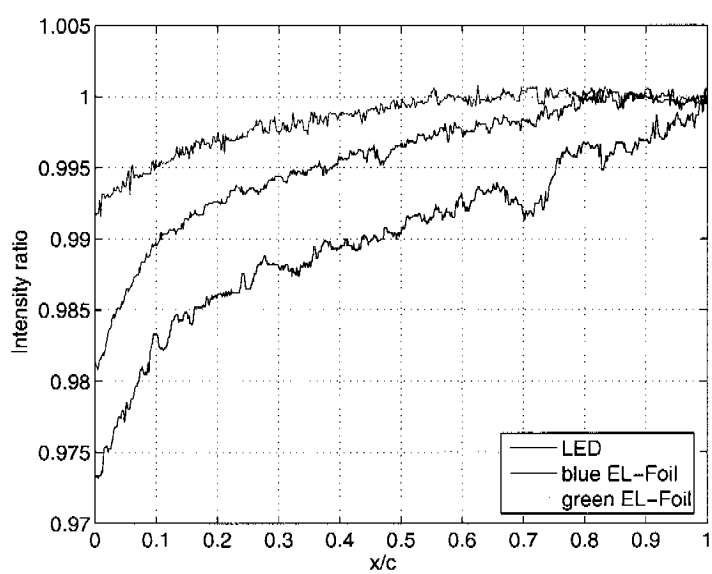


Figure 7.15: Intensity ratio distribution at 5° AoA.

visible with the green EL-foil. Not only the sensitivity is reduced but also the shape of the intensity distribution is different, due do weak and noisy signal. As for the previous measurement a reflection occurs in the

LED measurement at $x/c = 0.7$.

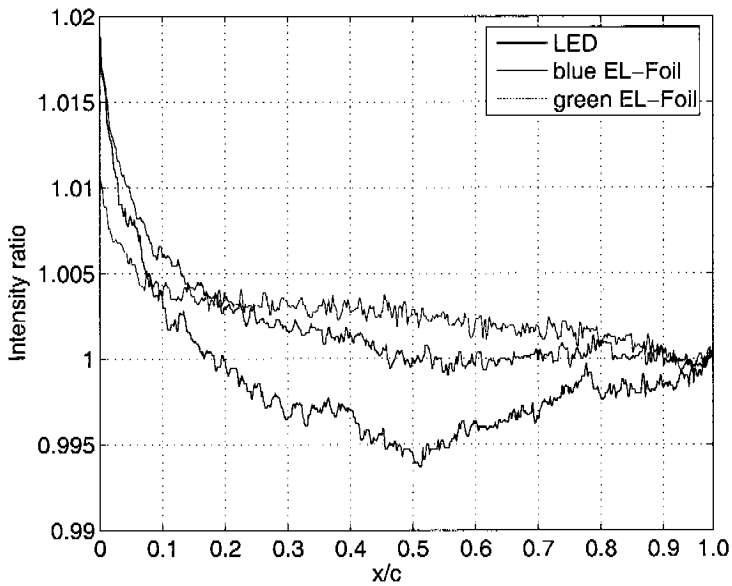


Figure 7.16: Intensity ratio distribution at $-10°$ AoA.

In Figs. 7.16 (AoA=$-10°$) and 7.17 (AoA=18°) the differences between blue and green foils are reduced, especially in the region of lower pressure variations ($x/c = 0.2 \div 0.8$). A possible explanation is a different temperature distribution between EL-foils and LED. These two special cases, in particular with blue EL-foil and LED, are analyzed in more detail with pressure calibration and temperature correction in Sec. 7.4.2.

The higher sensitivity of the blue EL-foil setup is demonstrated not only in the laboratory tests but also during wind tunnel measurements. In the following section PSP measurements, i.e., pressure and temperature maps, are computed and compared with PT and IR measurements.

### 7.4.2 Multifilter Measurements

The presented comparisons are focused on measurements with blue EL-foil and LED illumination. Pressure and temperature maps are computed with "a-priori calibration" and a simple MF technique (Sec. 5.2.1). The effects of temperature corrections on PSP measurements are investigated.

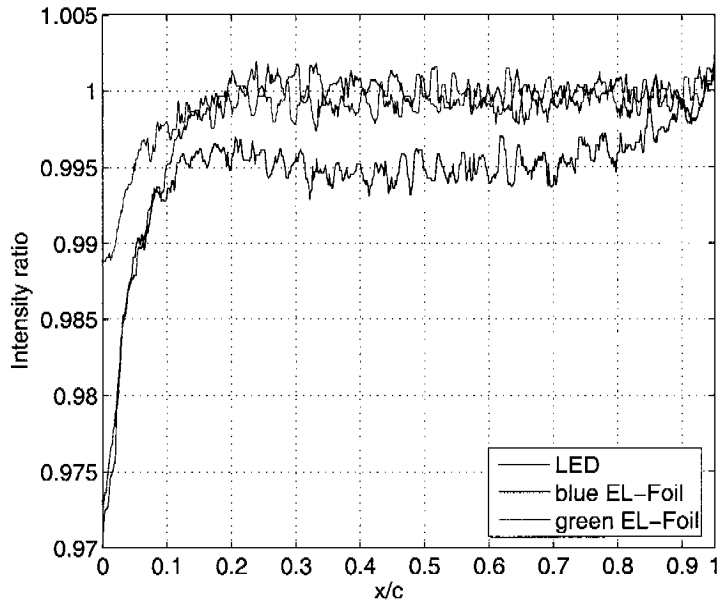


Figure 7.17: Intensity ratio distribution at 18° AoA.

### Temperature measurements

Figs. 7.18 to 7.21 show a comparison between surface temperature profiles measured with the IR technique and with the blue EL-foil at different AoAs.

The measurements performed with the IR camera show temperature variations from $0.2°C$ at AoA=10° to $0.6°C$ at AoA=−10°. The temperature variations along the wing cord are therefore reasonably small. A general review of the results shows that the measurements with the EL-foil have a similar temperature distribution but with an offset. This offset varies from $1°C$ for angles of attack of −10°, 5° and 10° to $0.6°C$ for an angle of attack of 18°. A possible explanation of the offset is a calibration problem related with the simple multifilter technique. More detailed measurements, possibly with higher temperature gradients, have to be performed in order to identify the origin of the temperature offset. Another important consideration concerns the quality the EL-foil measurements: with small temperature variations the noise present in the measurements becomes important. To overcome the problem, the number of averaged frames could be increased or optimized optical filters could be used.

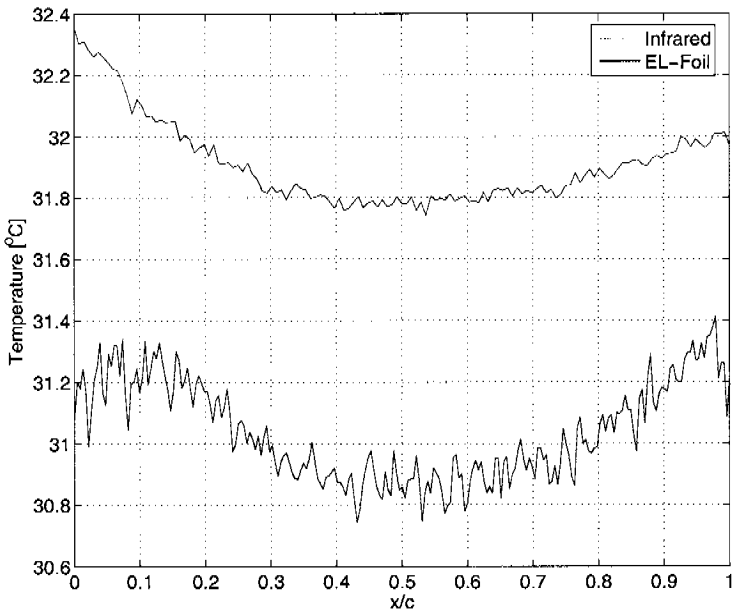


Figure 7.18: Temperature distribution at AoA=−10°.

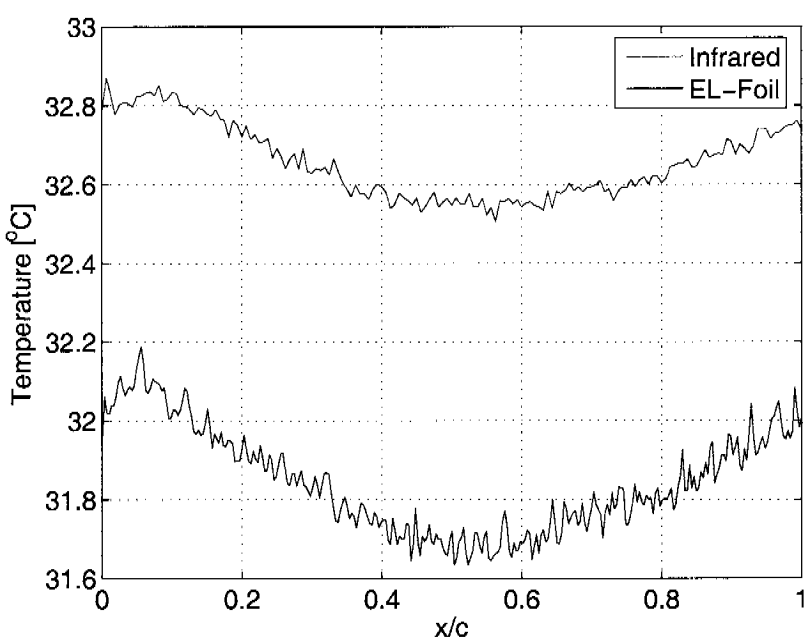


Figure 7.19: Temperature distribution at AoA=5°.

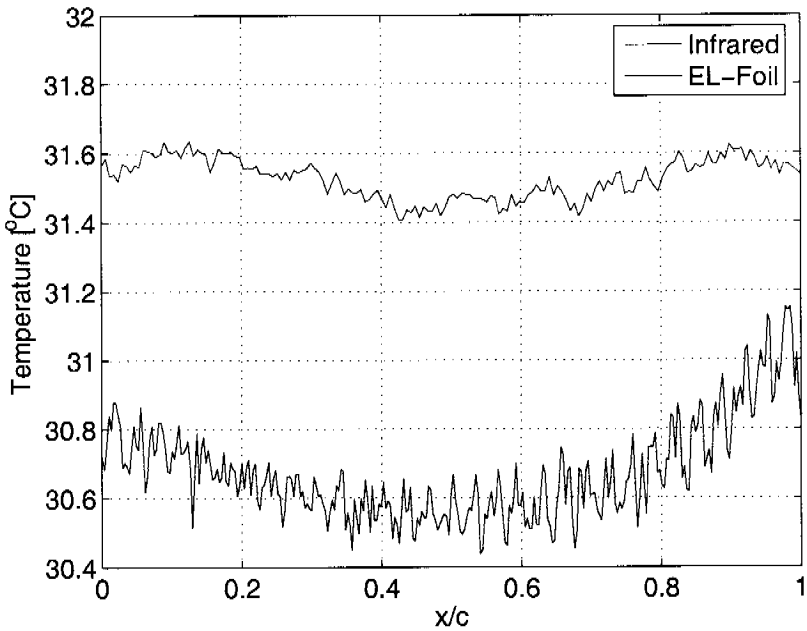


Figure 7.20: Temperature distribution at AoA=10°.

Despite the above mentioned problems, or inaccuracies, temperature maps are computed and used to correct the pressure measurements.

### Pressure measurements

The pressure distribution along the wing cord is measured with PT and PSP. A comparison is always performed. Notice that the pressures computed with the traditional LED technique are not temperature corrected. A mean value of the temperature on the model surface is used as a reference for the "a-priori calibration". Fig. 7.22 shows the comparison at an angle of attack of $-10°$. The pressure distribution obtained with PT and PSP/EL-foil are in good agreement. The pressure is increasing towards the leading edge. Notice that the values at $x/c = 0$ differ slightly between PSP and PT measurements. The first PT is located at the stagnation point of the wing. With an angle of attack of $-10°$ the measurement point does not correspond to the leading edge visible by the camera. For this reason the pressure measured at $x/c = 0$ has a positive value with the PSP techniques and a negative one with PT. By increasing the angle of attack to 5° the good agreement between EL-foil and PT

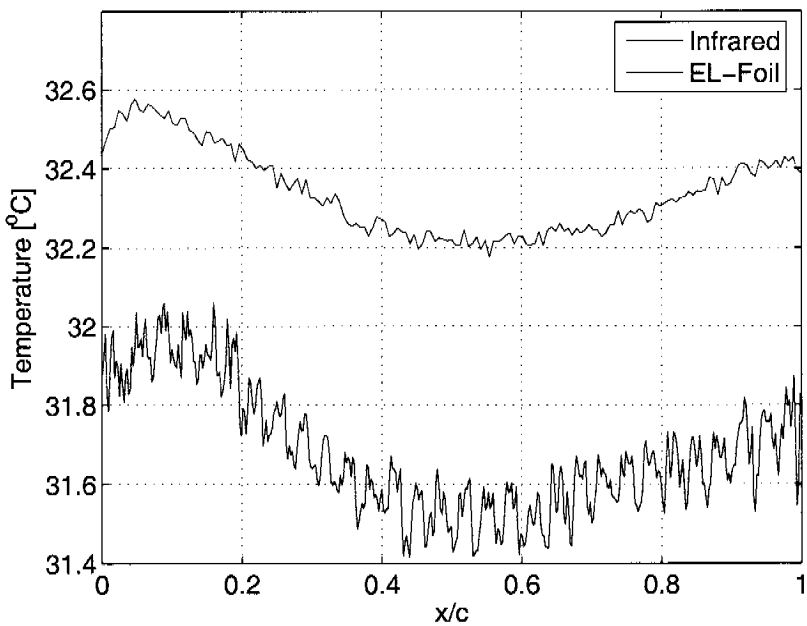


Figure 7.21: Temperature distribution at AoA=18°.

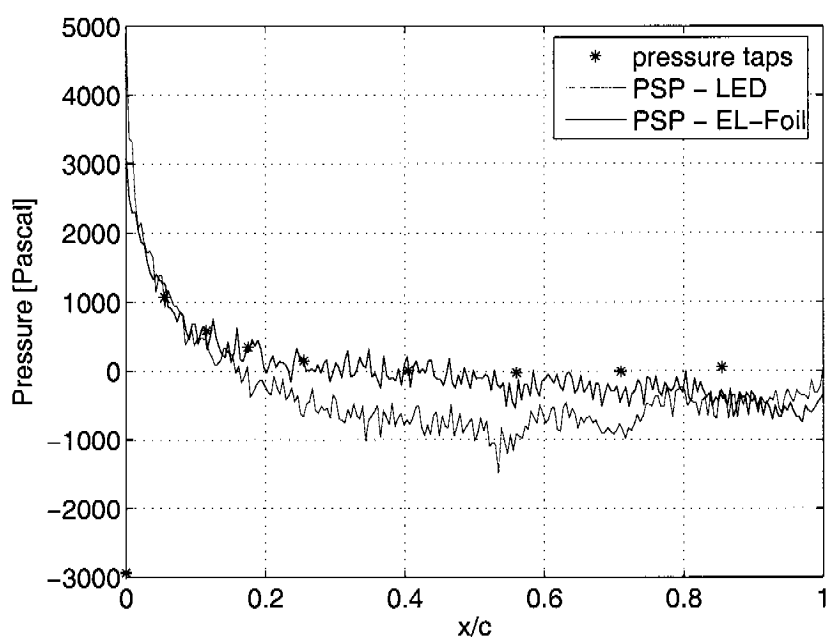


Figure 7.22: Pressure distribution at AoA=−10°.

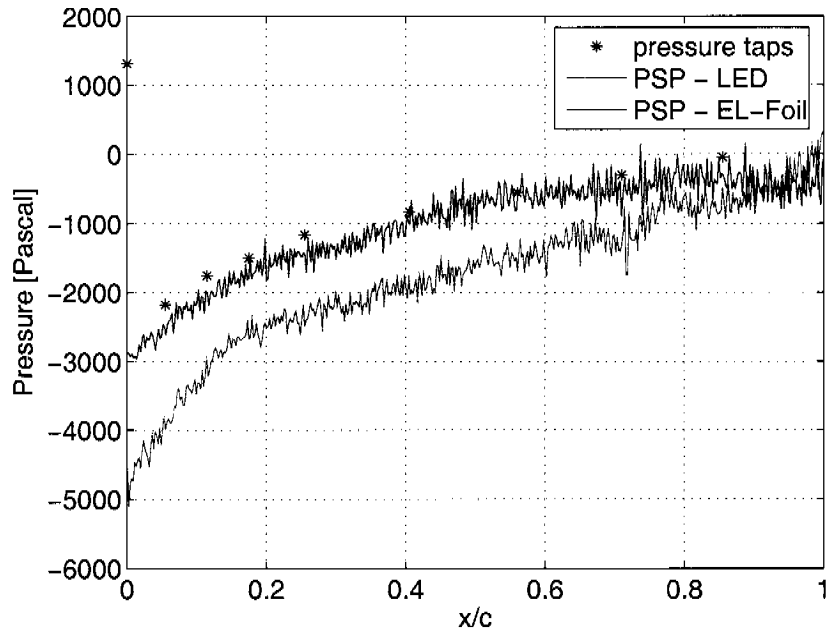


Figure 7.23: Pressure distribution at AoA=5°.

is preserved. The different results between EL-foil and LED techniques are due to temperature effects: a detailed discussion of the temperature effects on PSP measurements is given in the next paragraph.

At 10° the PT taps show a similar trend, but lower pressure compared to the PSP techniques. The reason for the different behavior is not yet understood. Further laboratory tests have to be performed in order to fully understand the problem.

The results are quite different at 18°. Theoretically the wing is stalled and the measurement with the PT confirm the expectations. The pressure distribution along the wing cord remains between 0 and −1000 Pa. The measurements performed with the EL-foil show a pressure distribution that does not correspond to those of a stalled wing. For a better understanding of the flow characteristics the IR picture is investigated. Fig. 7.26 shows the temperature distribution on the wing. The different flow characteristics between wing with EL-foil and wing without EL-foil are clearly visible. The PT are located above the EL-foil (Fig. 7.5), above which the flow is not separated: the IR picture confirms this fact. The thickness of the EL-foil or some dirt on the leading edge have probably a negative influence to the flow behavior. Small scale turbulence is

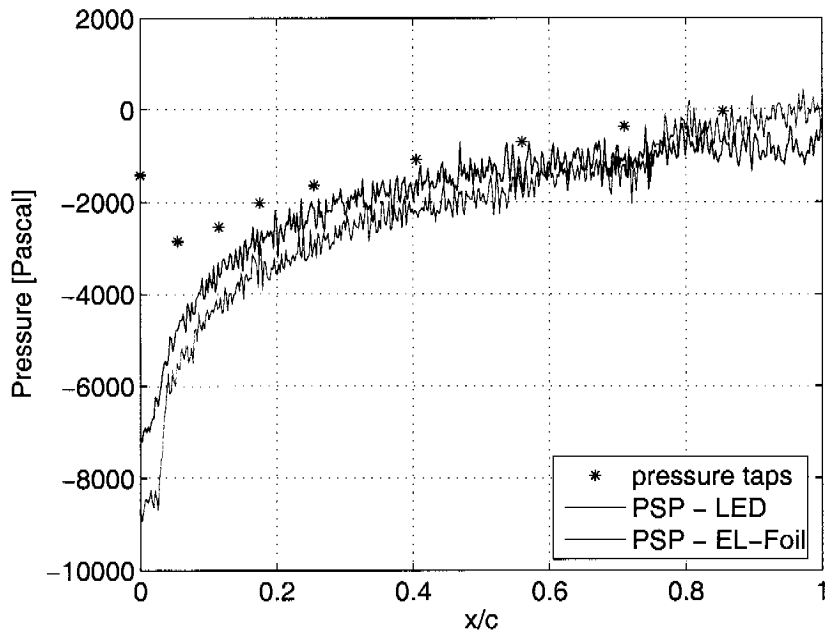


Figure 7.24: Pressure distribution at AoA=10°.

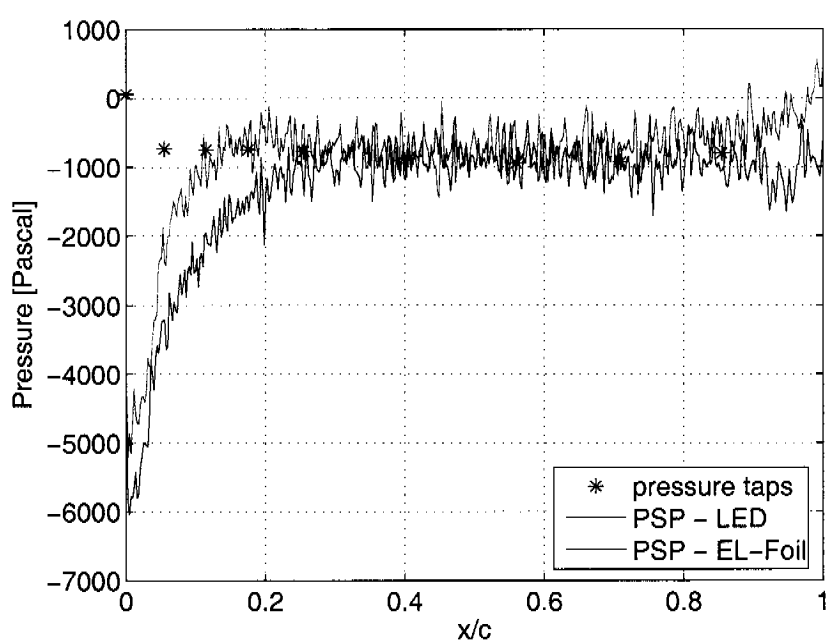


Figure 7.25: Pressure distribution at AoA=18°.

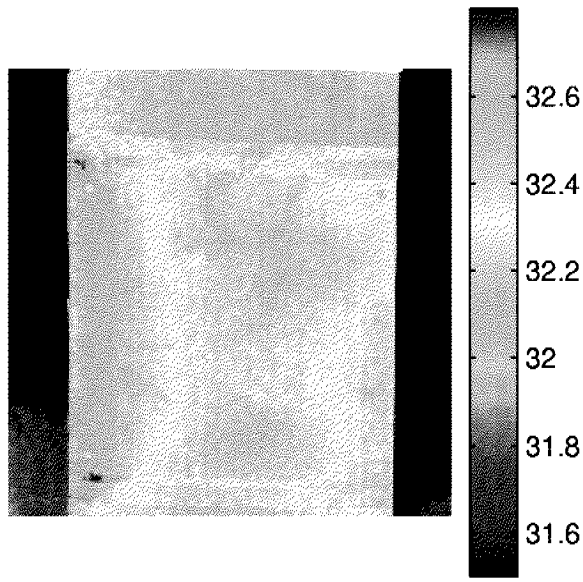


Figure 7.26: IR picture at AoA=18°.

generated and flow separation does not occur.

### Effects of temperature correction on PSP data

The effects of the temperature correction at angles of attack of 18° and 5° are illustrated in Fig. 7.27 and Fig. 7.28. A comparison of the EL-foil technique with the standard LED measurement is performed with and without temperature correction. The mean wind $OFF$ temperature is used as a reference for the "a-priori calibration". In Fig. 7.27 the mean temperatures, measured with the IR camera in wind $OFF$ condition are for both techniques $T_{OFF} = 31.5°$. The difference in pressure distribution between EL-foil and LED is primarily given by the temperature correction. The pressure changes are quite small and small temperature differences can yield large errors in the pressure calibration. Another example is given with an angle of attack of 5°. The previously performed comparison shows a similar pressure distribution between PT and EL-foil. The different pressure profile obtained with the traditional LED technique is explained in Fig. 7.28. The offset involved in the three

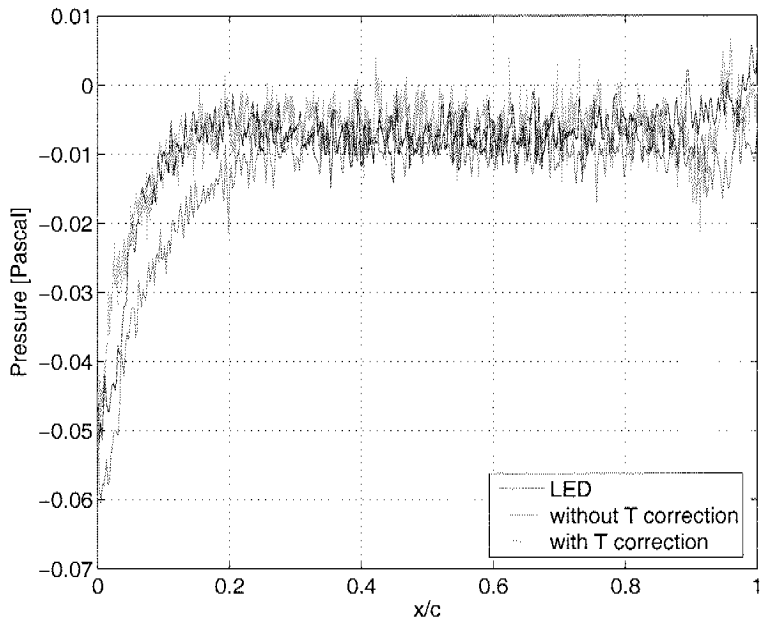


Figure 7.27: Pressure distribution comparison at AoA=18°.

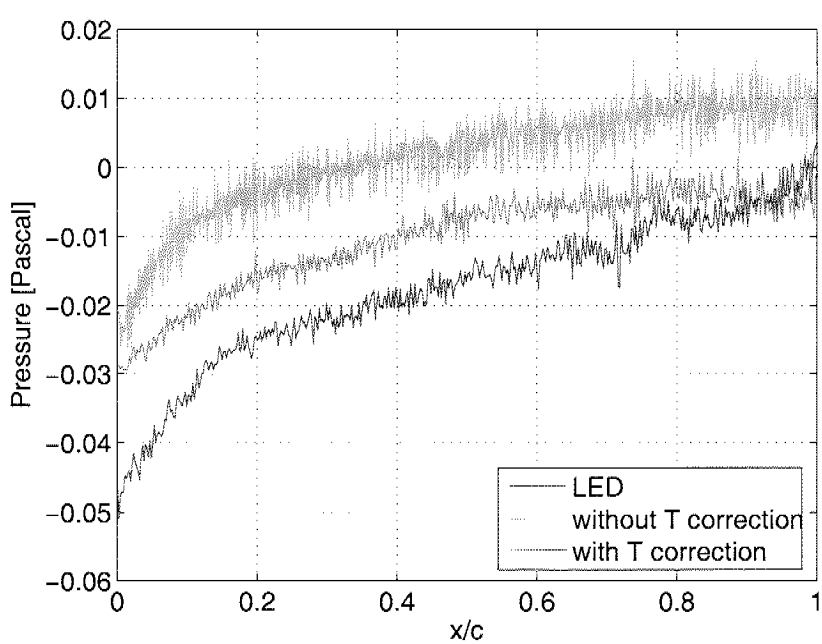


Figure 7.28: Pressure distribution comparison at AoA=5°.

measurements is due to the different wind $OFF$ surface temperatures: $T_{OFF} = 31.87°C$ for the LED measurements and $T_{OFF} = 30.75°C$ for the EL-foil measurements. The shape of the pressure distribution is similar for the non-corrected dataset. Between $x/c = 0$ and $x/c = 0.2$ the slopes are more pronounced than with the MF technique. An explanation comes from the fact that the surface temperature at the leading edge is higher compared to the rest of the wing. The PSP emission intensity decreases and without correcting temperature effects the computed pressure becomes higher than the real pressure. This behavior is also visible in Fig. 7.23.

## 7.5 Discussion

The test model, a NACA 0012 wing, at low wind tunnel speed is somewhat problematic due to weak pressure and temperature variations. PSP measurements, especially with reduced sensitivity like the PSP/EL-foil system, become noisy and small temperature effects can dramatically affect the results. Despite the mentioned disadvantages several interesting observations can be made. The increase of sensitivity by using the blue EL-foil is clearly demonstrated: the non temperature corrected intensity profiles show a very similar pressure distribution between LED and the blue EL-foil. In the second part the MF technique is successfully applied for the first time in a wind tunnel test case. For simplicity, although being less accurate, the simple MF algorithm is used. Temperature distributions are computed with a similar accuracy compared to the IR images. Some problems, e.g., temperature drift and noise, remain. A detailed study would be of interest in order to understand the source of the temperature drift and the possibility of reducing the noise level. The temperature maps are then used to compute the pressure distribution with "a-priori calibration". The EL-foil / PSP measurements are in good agreement with the PT data. Compared to the LED technique the pressure profiles computed with the EL-foils are more noisy. The comparison with PT data demonstrated a good agreement and the importance of temperature corrections in weak pressure conditions. The expectations from laboratory measurements are therefore confirmed. In addition two practical considerations can be extracted. The time consuming LED light positioning, with all the intrinsic problems (e.g., surface reflections), is reduced or eliminated through the use of EL-foils. Furthermore, the foils

used influence the wing flow in a very important and significant way, affecting the non-intrusivity of the PSP technique. A clear example is given in the measurement performed at an angle of attack of 18°, where the expected flow separation does not occur. The thickness of the EL-foil must be therefore decreased by developing special EL-foils for wind tunnel applications.
The obtained results are very promising. The PSP / EL-foil technique has some clear advantages compared to the traditional method. Further development is needed in order to increase the accuracy and optimize the emission/absorption properties of the system. Chapter 8 summarizes the properties, advantages and disadvantages of the new technique and suggest some possible directions for future developments.

# Chapter 8

## *Summary and Conclusions*

## 8.1 Achievements

An improvement of the standard PSP technique is presented. Using an EL-foil instead of the classical LED illumination source the PSP setup is simplified. In fact the illumination, or excitation light source, is directly embedded with the paint. The advantages are evident: homogeneous illumination intensity, reduction of the wind $ON/OFF$ errors, decrease of unwanted shadows and possibility of pre-painting the EL-foils outside the wind tunnel. Other advantages but also drawbacks, are related to the new hardware configuration. To evaluate in more detail the characteristics of the new PSP setup, a tool to simulate wind tunnel conditions in the laboratory is needed. As a result, a test cell (TC) was developed.
The TC allows the measurement of the intensity and spectral responses to pressure and temperature changes with different PSP configurations. By controlling and monitoring the internal conditions with a PC the possibility of performing automated calibrations by simply selecting a pressure range (p=$-0.8 \div 2$ bar) and a temperature range (T=$10°C \div 40°C$) is achieved. The number of steps to increase pressure and temperature during a measurement is selected by the user. The TC fullfills a number of important requirements: automated calibrations, modular construction with different optical accesses, ability to evaluate angular dependency and homogeneous conditions on the test plate. Different CCD cameras can be chosen to optimally and selectively measure intensity or spectral variations of the PSP emissions.
In the laboratory, with the use of the TC, different industrial EL-foils and different paint formulations were investigated. By looking at the emission spectrum of the EL-foil/PSP system the possibility of measuring not only pressure but also temperature was noticeable. The blue emission of the phosphor contained in the EL-foil is proportional to the surface temperature. With the temperature dependence of PSPs being a major source of errors, the possibility of eliminating it is of great interest. A detailed

study of the new setup was performed. Different measurement techniques were developed to exploit this peculiarity: spectral measurements, temperature compensated PSP and multifilter measurements. Because of a simple hardware setup (similar to the traditional one) and the capability of measuring 2-dimensional pressure and temperature maps the multifilter measurements technique was ultimately preferred. An associated drawback of the technique is a reduction of PSP system sensitivity: a leakage of the EL-foil emission occurs in the red emission region of the paint. A validation of the acquired laboratory data was performed in the wind tunnel during two different measurements campaign.
The first test was performed on a F-18 airplane model at RUAG Aerospace. The primary objective was to utilize the new technique in a wind tunnel measurement to increase the know-how of PSP measurements, discover advantages and drawbacks of the new technique and to validate the laboratory measurements. Different hardware configurations were tested. The influence of dark level correction, frame averaging and temperature variations were investigated. Green EL-foil was preferred to the blue one due to higher emission intensity. This choice, as demonstrated later, was not optimal in other respects. In fact the leakage of the green EL-foil decreases so much the sensitivity of the paint that the results become unusable for industrial applications. The quality is poor and comparisons with standard PSP measurements are not always possible. Nevertheless some interesting considerations arise from the measurement campaign. The intensity emission of the EL-foil was not so weak as expected from the laboratory measurements and the possibility of using the blue EL-foil to reduce the leakage problem was evident. Some preliminary tests were performed to identify the possibility of measuring surface temperature: an intensity variation, corresponding to variations in the IR images, was clearly visible. The need of a second wind tunnel campaign to investigate possible hardware improvements become evident.
The aim of the second measurement campaign was to increase the PSP system accuracy by using a blue EL-foil, and to perform a temperature measurement using the multifilter technique: a NACA 0012 wing was used. The pressure distribution, or better pressure variation, with this configuration was quite weak: it become extremely important to measure with a sufficiently sensitive paint. A comparison between green and blue EL-foils clearly showed the advantages of the blue EL-foil: the leakage is reduced with a subsequent increase in accuracy. The simple multifilter technique was than applied to compute pressure and temperature maps.

Despite the simplicity of the algorithm the agreement with pressure tap readings and IR pictures was evident. The temperature correction influences the results in an important way as demonstrated by comparing LED measurements with pressure taps and EL-foil data. The new technique developed so far may still not be usable for commercial purposes but compared to the first measurement campaign significant improvements could be implemented.

## 8.2 Future developments

Further improvements may be obtained by modifying the existing hardware, by developing more sophisticated evaluation algorithms and by additional research.
From the hardware point of view the possibility of manufacturing customized EL-foils for PSP measurements will be advantageous. The improvement should primarily be focused on increasing the sensitivity by reducing the leakage, by simplifying the application procedure of the foils and by decreasing the temperature dependency. A simple and easy improvement is the reduction of the foil thickness: commercial EL-foils are built by using different plastic layers, e.g., water vapor barriers and insulating layers, that are not needed for PSP applications. Investigations to reduce the leakage problem should be performed: by choosing other phosphor compounds the emission peak could be shifted while maintaining the useful temperature dependence of the EL-foil emissions. The rapid development of new plastic materials, e.g. conductive polymers, opens up new possible hardware scenarios: the ruthenium molecules could be embedded directly into the EL-foil by substituting the conductive layer with an oxygen permeable conductive membrane. Another improvement could be the use of EL-foils with increased flexibility for a better adhesion on complex surface shapes. A more futuristic vision is the use of the foil not only as excitation light source, but also as detector. Organic light emitting diodes (OLEDs) are similar to the EL-foils but can also be used as an organic sensor. Altough the technique is still in a development stage some companies are introducing it into the marked (e.g., Nanoident Technologies AG[1]).
The software used to decompose the measured signals, in particular POD, FastICA and neural network, do not always give satisfactory re-

[1] http://www.nanoident.com

sults. These evaluation algorithms, in particular for the simple MF technique, were discussed and investigated at the basic level only. More accurate and advanced techniques have to be developed to fully exploit the measured information, that is, all three optical filter images or spectral data. The origin of the temperature offset discussed in Sec. 7.4.2 has also to be identified with more clarity.
Research should be performed to evaluate the possibility of eliminating the wind $OFF$ image and to develop auto-compensated PSPs. The wind $OFF$ image can be eliminated by performing three measurements. Spectral measurements show three different emission regions: theoretically the simultaneous measurement of reference intensity, temperature and pressure should be possible. Measurements in the laboratory have to be performed by changing the emission intensity of the foil, paint thickness and paint homogeneity in order to fully investigate the influence on the spectral data. Another concept of auto-compensated PSP can also be investigated. Instead of using the leakage of the EL-foil in the red emission zone of the paint, the increase/decrease of the EL-foil emission due to temperature changes could be used. The paint could be therefore be differently excited depending on the surface temperature resulting in a reduction of the PSP temperature dependence.

## 8.3 Conclusions

The possibility of using EL-foils as illumination sources for pressure sensitive paint measurements and as surface temperature indicators was established. The developed technique is however not yet ready for being used in industrial applications: several drawbacks must be corrected or reduced. Finding better EL-foils and optimizing the measurement techniques could further improve the sensitivity of the system and establish thus a new PSP measurement method.

# Appendix A

## *Automated PSP System Description*

In this appendix, with the PSP system already described in Chap. 3, a short description and the technical specifications of the automated PSP measurement system are given. As first, the used hardware is listed: electronic controller, pressure sensors, DAQ card, CCD cameras, etc.. App. A.2 explains the procedures adopted to calibrate the measurement system. In App. A.3 the developed Matlab software is listed and a user manual is given.

## A.1 Hardware Specifications

A scheme of the complete hardware setup is given in Fig. A.1. As

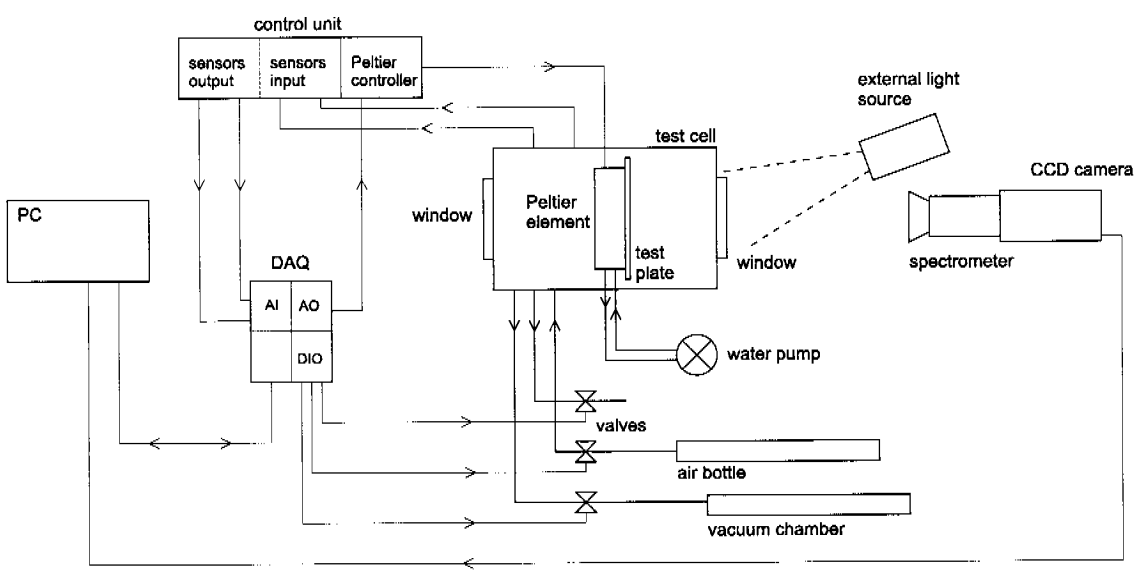


Figure A.1: Hardware setup

explained in Chap. 3 the PSP calibration is performed by using a TC. An electronic controller unit (ECU) is used to connect the PC with the TC. The ECU not only allows the user to read/set pressure and temperature, but also supplies the required power to connect LED lamps, EL-Foils and solenoid valves. The PC, with a NI-6036E DAQ card, collects the measurements and send the signals to control the TC interior conditions.

### A.1.1 Test Cell Specifications

An overview of the TC overall dimensions is given in Fig. A.2.

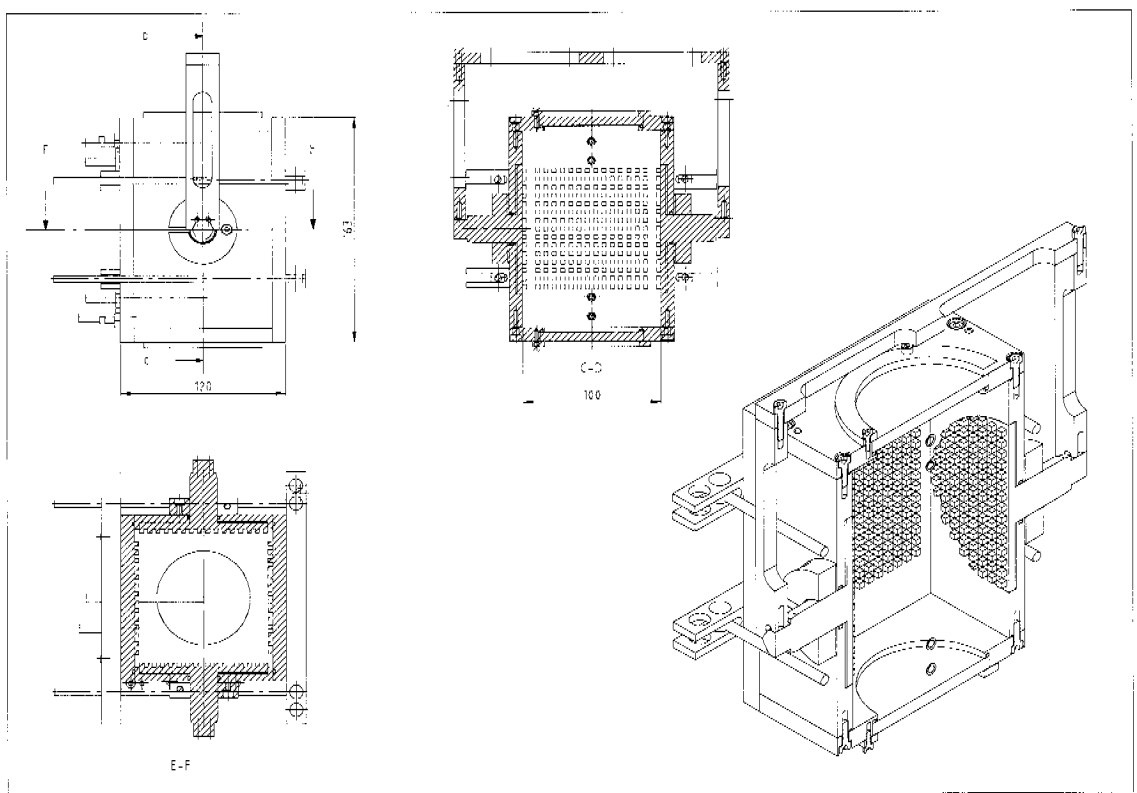


Figure A.2: Test Cell overall dimensions

The following specifications are met:

- adjustable pressure: from $-0.8$ bar under pressure to 2 bar over pressure
- adjustable temperature: from $10°C$ to $40°C$
- uniform conditions on the test plate
- modular construction to insert different test plates, luminescent foils, or light filters
- ability to evaluate the angular dependency of the intensity emission
- pressure (Honeywell 26PCDFA6D) and temperature (K-type thermocouple) sensors to monitor interior conditions

A further design iteration was performed to allow a faster open/closing of the TC and define a simplified hardware without unwanted/unused features (e.g., milling grid). Fig. A.3 shows the second version of the TC.

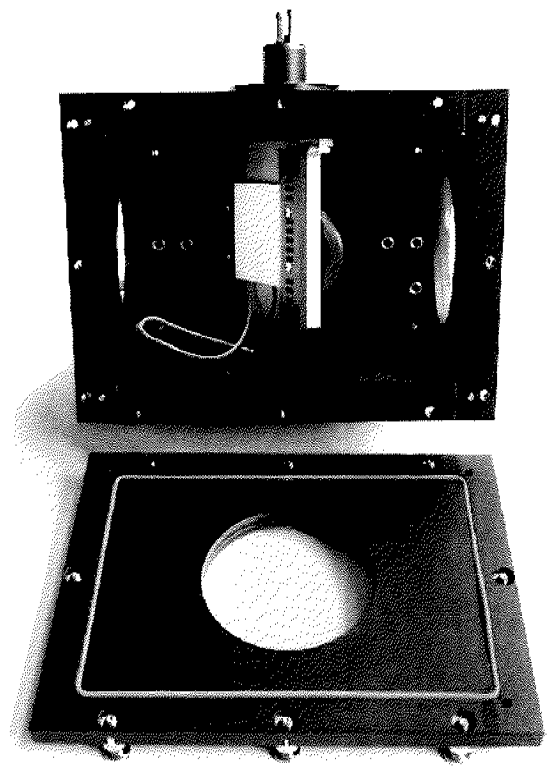

Figure A.3: Modified Test Cell

## A.1.2 Electronic Controller Unit (ECU)

The ECU, show in Fig. A.4, is divided in 7 modules: power supply, auxiliary power supply, TC power supply, peltier controller, voltmeter, output signals and pressure/temperature sensors amplifier unit.

### Power supply (❶)

This first module contains the internal power supply for all the ECU modules.

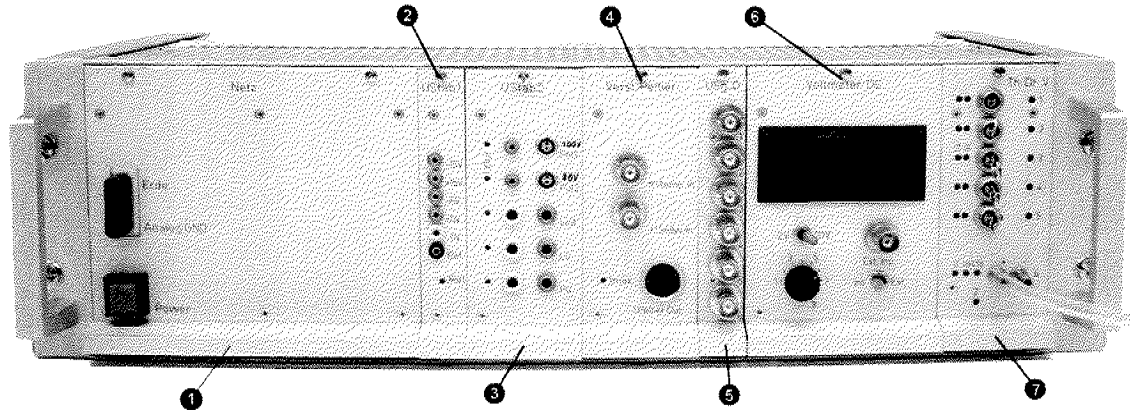


Figure A.4: Electronic controller unit

### Auxiliary power supply (❷)

The second module is an auxiliary power supply. Several external devices can be powered without the need for an additional external power supply. Different voltages are available: 0 V, +5 V, +10 V and +15 V.

### TC power supply (❸)

Different electronic devices can be connected to this module: e.g., EL-foils, LED lamps and a small fan. The EL-foil emission is controlled by applying an alternating voltage to the foil. The drivers contained in this module are from Enz Electronic type 3085 0110 and type 3085 0210. The technical specifications are given in Fig. A.5 and Fig. A.6.

### Peltier controller (❹)

The peltier controller module was developed at IFD. An external voltage is supplied (−10/10 V) as a reference. The controller compares the supplied voltage with a measured voltage (thermocouple) to set the desired temperature. A calibration, described in Sec. A.2.2, was performed.

### Output signals (❺)

The ECU is connected to the PC with this module: the output channels are the voltages of the temperature and pressure signals. The outputs range from −10 to +10 Volts.

**Spezifikationen** **3085 0110** ENZ electronic

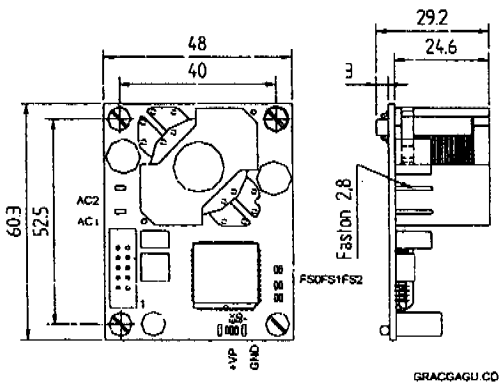


| Nr. | Name | Bemerkung |
|---|---|---|
| 1 | +VP | Versorgung + 36VDC |
| 2 | GND | Versorgung-, Ground |
| 3 | SD | Sollwerteingang PWM (VCC/GND) Lötpunkt von *INT* auf *EX* |
| 4 | INH | Eingang Inhibit (VCC = Aus) |
| 5 | FL | Blinken wenn FL = VCC |
| 6 | VCC | Out = 5V, max 5mA |
| 7 | SW | Speisung Pot (Max) |
| 8 | NINV | Mittelabgriff Pot |
| 9 | ALN | Übertemperat. (akt low) |
| 10 | GND | GND Pot (Min) |

| | | | |
|---|---|---|---|
| Nenn-Eingangsspannung | 36VDC | Max. Leuchtfläche | 850cm$^2$ |
| Typ. Ausgangsspannung | 80VAC | Lagertemperatur | -30°C - +80°C |
| Typ. Frequenz | 2800Hz | Betriebstemperatur | -10°C - +70°C |

Figure A.5: EL-driver, Lumitec 3085 0110

**Spezifikationen** **3085 0210** ENZ electronic

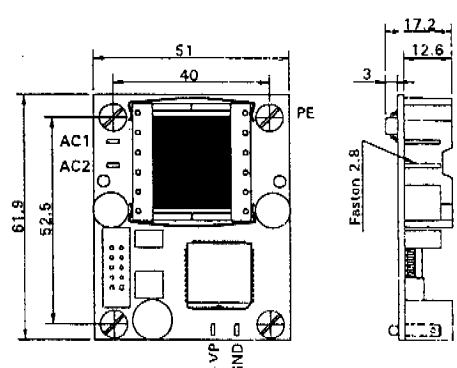


**Pinbelegung 10polige Stiftleiste**

| Nr. | Name | Bemerkung |
|---|---|---|
| 1 | +VP | Versorgung + 12VDC |
| 2 | GND | Versorgung-, Ground |
| 3 | SD | Sollwerteingang PWM (VCC/GND) Lötpunkt von *INT* auf *EX* |
| 4 | INH | Eingang Inhibit (VCC = Aus) |
| 5 | FL | Blinken wenn FL = VCC |
| 6 | VCC | Out = 5V, max 5mA |
| 7 | SW | Speisung Pot (Max) |
| 8 | NINV | Mittelabgriff Pot |
| 9 | ALN | Übertemperat. (akt low) |
| 10 | GND | GND Pot (Min) |

**Statusanzeige**
LED grün = OK

| | | | |
|---|---|---|---|
| Nenn-Eingangsspannung | 12VDC | Max. Leuchtfläche | 400cm$^2$ |
| Max. Eingangsleistung | 3 W @ 13 VDC | Lagertemperatur | -30°C - +80°C |
| Typ. Ausgangsspannung | 100VAC | Betriebstemperatur | -10°C - +70°C |
| Typ. Frequenz | 1600Hz | Gewicht | 65 g |

Figure A.6: EL-driver, Lumitec 3085 0210

## Voltmeter (❻)

This module displays the voltages read by the 6 thermocouples, pressure sensor and an external source. It allows a fast evaluation of the

**26PC Series Performance Characteristics at 10.0 ± 0.01 Vdc Excitation, 25°C**

| | Min. | Typ. | Max. | Units |
|---|---|---|---|---|
| Excitation | — | 10 | 16 | Vdc |
| Response Time | — | — | 1.0 | ms |
| Input Resistance | 5.5 k | 7.5 k | 11.5 k | Ohm |
| Output Resistance | 1.5 k | 2.5 k | 3.0 k | Ohm |
| Weight | | 2 | | gram |

**Environmental Specifications**

| | |
|---|---|
| Operating Temperature | -40°C to +85°C (-40°F to +185°F) |
| Storage Temperature | -55°C to +100°C (-67°F to +212°F) |
| Compensated Temperature | 0°C to +50°C (32°F to +122°F) |
| Shock | Qualification tested to 150 g |
| Vibration | MIL-STD-202, Method 213 (0 to 2 kHz, 20 G sine) |

NOTE: For media compatibility specifications, refer to catalog or web site: www.honeywell.com/sensing

**26PC CIRCUIT TERMINATION**

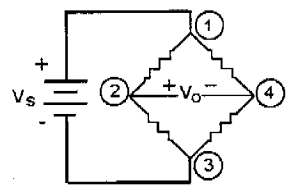


Pin 1 = Vs (+)
Pin 2 = Output (+)
Pin 3 = Ground (-)
Pin 4 = Output (-)

Pin 1 is notched
Pin 2 is next to Pin 1, etc.

Figure A.7: Honeywell 26PC DFA6D

interior conditions without the need for the PC.

### Pressure/temperature sensors and amplifier unit (❼)

This module contains six voltage amplifiers connected to the thermocouples and a differential gauge pressure sensor. The thermocouples are standard K-types. The pressure sensor is a Honeywell type 26PCDFA6D. The specification for the pressure sensor is given in Fig. A.7. The amplified pressure signal corresponds roughly to 1 Volt per bar.
Further information, electronic scheme and details can be found in the IFD workshop documentation.

## A.1.3 Data Acquisition and Controlling

The PC used was a PIII 800 MHz with SCSI hard disk (6 GB) and 512 MB RAM. A National Instruments (NI) card was used to acquire and send data from/to the ECU.
The NI-DAQ card used is a 6036E type. The specifications are summarized in Fig. A.8. To connect the card to the ECU with BNC cables a NI - BNC 2110 interface module was used (Fig. A.9). To control the pressure, as illustrated in Fig. A.1, three solenoid valves were used (Fig. A.10). The valves were controlled with relays, in particular with

the NI - ER8 (Fig. A.11). Three different cameras were used during the measurement campaign: a PCO Sensicam CCD, a Texas Instrument MC681SPD-ROBO EMCCD and a Cedip Jade III infrared camera.

### 1 - PCO Sensicam

The CCD camera most frequently used during the measurement campaign was the PCO Sensicam (http://www.pco.de). The camera is a 12 bit cooled CCD camera with good signal to noise ratio. The specifications (super VGA Sensicam) are summarized in Fig. A.12.

### 2 - Texas Instrument MC681SPD-ROBO

An intensified CCD camera, Texas Instruments type MC681SPD-ROBO, was also used in weak light conditions. The camera has a resolution of 656x480 pixels with 12 bit. The datasheet is shown in Fig. A.13.

### 3 - Cedip Jade III Infrared

A Cedip Infrared camera, model Jade III MWIR, was used to measure surface temperature or calibrate the TC thermocouples. The camera has a resolution of 320x240 pixels with a gray level resolution of 14 bit. Further information can be found in Tab. A.1.3.

### Specim ImSpector (V7)

The Specim ImSpector V7 is a 1-D spectrometer. The functioning principle is quite simple: the light entering through a slit is deflected by a prism in dependence of the wavelength. A CCD camera is used to collect the light intensity. The spectrometer measures light from 400 to 710 nm with a spectral resolution of about 2 nm (with a slit of $25\mu m$). To achieve the mentioned accuracy an image correction is performed during the calibration. The specifications are summarized in Fig. A.14.

| Camera | |
|---|---|
| Model | JADE III MWIR |
| Sensor | InSb (FPA-construction) |
| Resolution | 320 x 240 |
| Sensitivity spectrum | 3 - 5.2$\mu m$ |
| Measurable temperature range | $-20°C$ to $1300°C$ |
| Cooling | Stirling (77 K) |
| Dynamic range | 14 Bit |
| Integration time | 1$\mu s$ to 10$ms$ |
| Frame rate | 1$Hz$ to 170$Hz$ |
| NETD | 18.59mK @ $25°C$ |
| **Optics** | |
| Focal length | 25 mm |
| FOV | $21^o x 16^o$ |
| IFOV | 1mrad |

Table A.1: IR camera specifications

**E Series – Low-Cost**

- 16 analog inputs at up to 200 kS/s, 12 or 16-bit resolution
- Up to 2 analog outputs at 10 kS/s, 12 or 16-bit resolution
- 8 digital I/O lines (TTL/CMOS); two 24-bit counter/timers
- Digital triggering
- 4 analog input signal ranges
- NI-DAQ driver simplifies configuration and measurements

**Families**

- NI 6036E
- NI 6034E
- NI 6025E
- NI 6024E
- NI 6023E

**Operating Systems**

- Windows 2000/NT/XP
- Real-time performance with LabVIEW
- Others such as Linux and Mac OS X

**Recommended Software**

- LabVIEW
- LabWindows/CVI
- Measurement Studio
- VI Logger

**Other Compatible Software**

- Visual Basic, C/C++, and C#

**Driver Software (included)**

- NI-DAQ 7

Calibration Certificate Included

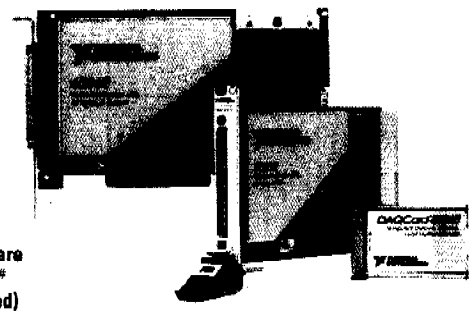

| Family | Bus | Analog Inputs | Input Resolution | Max Sampling Rate | Input Range | Analog Outputs | Output Resolution | Output Rate | Output Range | Digital I/O | Counter/Timers | Triggers |
|---|---|---|---|---|---|---|---|---|---|---|---|---|
| NI 6036E | PCI, PCMCIA | 16 SE/8 DI | 16 bits | 200 kS/s | ±0.05 to ±10 V | 2 | 16 bits | 10 kS/s[1] | ±10 V | 8 | 2, 24-bit | Digital |
| NI 6034E | PCI | 16 SE/8 DI | 16 bits | 200 kS/s | ±0.05 to ±10 V | 0 | - | - | - | 8 | 2, 24-bit | Digital |
| NI 6025E | PCI, PXI | 16 SE/8 DI | 12 bits | 200 kS/s | ±0.05 to ±10 V | 2 | 12 bits | 10 kS/s[1] | ±10 V | 8 | 2, 24-bit | Digital |
| NI 6024E | PCI, PCMCIA | 16 SE/8 DI | 12 bits | 200 kS/s | ±0.05 to ±10 V | 2 | 12 bits | 10 kS/s[1] | ±10 V | 8 | 2, 24-bit | Digital |
| NI 6023E | PCI | 16 SE/8 DI | 12 bits | 200 kS/s | ±0.05 to ±10 V | 0 | - | - | - | 8 | 2, 24-bit | Digital |

[1] 10 kS/s typical when using the single DMA channel for analog out put. 1kS/s maximum when using the single DMA channel for either analog input or counter/timer operations. 1 kS/s maximum for PCMCIA DAQCards in all cases.

Figure A.8: Specifications NI - PCI 6036 E

## Connector Blocks

### BNC-2100 Series Connector Blocks (See Figure 3)

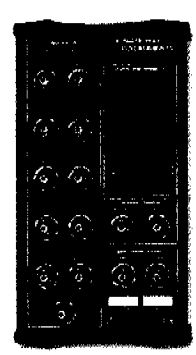

The BNC-2100 Series are shielded connector blocks with signal-labeled BNC connectors for easy connectivity of your analog input, analog output, digital I/O and counter/timer signals to your multifunction DAQ device, including analog output devices. The BNC-2110 and BNC-2120 work with all E Series and Basic multifunction DAQ devices. The BNC-2120 also provides a function generator, quadrature encoder, temperature reference, thermocouple connector, and LED so that you can test the functionality of your hardware. The BNC-2115 has 24 BNC inputs for connecting to the extended I/O channels of our 100-pin E Series DAQ devices.

BNC-2110 .....777643-01

Figure A.9: NI - BNC 2110

Microsol 2/2 ways NC direct acting - PPS body - Subbase

| Orifice size [mm] | kv flow factor | Freq. [Hz] | Pressure (bar) | Vacuum [Torr] | Power [W] |
|---|---|---|---|---|---|
| 0.50 - 1.50 | 0.12 - 0.55 | DC | 0 ... 10 | 25 | 1 - 2 |
| | | 50 | 0 ... 10 | 25 | 1 |
| | | 60 | 0 ... 10 | 25 | 0.9 |

more information: http://www.fas.ch

Figure A.10: Solenoid valve (http://www.fas.ch)

**NI ER-8, NI ER-16**

- 8 or 16 independent SPDT nonlatching relays
- Switching capacity
  - 3 A at 250 $V_{rms}$
  - 3 A at 30 VDC
- Expandable to 32 channels
- Switch motors, lamps, small fans, or solenoids

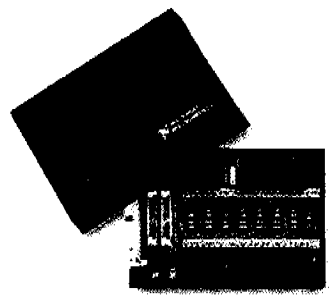

Figure A.11: NI - ER-8

| SensiCam | VGA | SuperVGA |
|---|---|---|
| Sensor Type | CCD-Interline Progressive Scan with "lens-on-chip" | |
| Number of Pixels | 640(H) x 480(V) | 1280(H) x 1024(V) |
| Pixel Size | 9.9µm x 9.9µm | 6.7µm x 6.7µm |
| Sensor Format | 1/2" | 2/3" |
| Scan Area | 6.3mm x 4.8mm | 8.6mm x 6.9mm |
| Cooling Type | 2-stage peltier cooler with forced air cooling | |
| CCD Temperature | -15°C | -12°C |
| Full Well Capacity | 35.000 e⁻ | 25.000 e⁻ |
| Scan Rate | 12.5 MHz | 12.5 MHz |
| Readout Noise @12.5 MHz | 13 ... 14 e⁻ | 7 ... 8 e⁻ |
| A/D-Converter | 12 Bit @12.5MHz | |
| A/D Conversion Factor | 7.5 e⁻/count | 5 e⁻/count |
| Max. Quantum Efficiency monochrome, @ 520nm | ≥ 40% | |
| Spectral Response (monochrome) | 280 ... 1000nm | |
| Spectral Response (color) | RGB primary colors | |
| Average Dark Charge [7] | < 0.1 e⁻/pixel·sec | < 0.1 e⁻/pixel·sec |
| Extinction Ratio [1] | 1:2000 | 1:2000 |
| Smear [2] | < 0.005% | < 0.005% |
| Anti Blooming [3] | > 1000 | > 1000 |
| CCD Quality | grade 0 | grade 0 |
| Non-Linearity | < 1% | < 1% |
| Readout Time (Full Frame) | 30 fps | 8 fps |
| Binning Horizontal | 1...8 | |
| Binning Vertical | 1...128 | |
| **Blemishes** | | |
| Point Defects [4] | 0 | 0 |
| Cluster Defects [5] | 0 | 0 |
| Column Defects [6] | 0 | 0 |
| **Warm Pixels** [7] typ. | | |
| # pixels > 100 e⁻ | 0 | 0 |
| # pixels > 5 e⁻ | 0 - 2 | 0 - 2 |
| # pixels > 1 e⁻ | 250 - 1000 | 500 - 2000 |
| **Non-Uniformity in darkness** [8] typ. | 1 count | 1 count |
| **Non-Uniformity in brightness** [9] typ. | 0.2% | 0.6% |
| # pixels > 12% | 0 | 0 |
| # pixels 8 ... 12% | 0 | 0 - 2 |
| # pixels 4 ... 8% | 0 | 10 - 50 |
| # pixels 2 ... 4% | 0 - 5 | n.a. |
| Optical Input | C-Mount with adjustable focus length | |
| Dimension | Head: 93(W) x 78(H) x 210(L) mm | |
| Weight | 1.6 kg | |
| Operating Temperature | 0...40°C | |
| Storage Temperature | -20...+70°C | |
| Humidity | 10...90% non condensing | |

Figure A.12: PCO - Sensicam

| | | |
|---|---|---|
| 1) Imager | TEXAS INSTRUMENTS Frame Transfer CCD | |
| | 1/3-inch TC253 | |
| 2) Pixel | Total Pixels | 680(H)*500(V) |
| | Active Pixels | 656(H)*480(V) |
| 3) Optical Dimension | Active Area | 4.87mm(H)*3.60mm(V) |
| | Pixel Size | 7.4 x 7.4 microns (square format) |
| 4) Sensor Readout | Progressive scan | |
| 5) Video Format | Digital video (LVDS) 12 bit | |
| | Analog Composite Head unit : Progressive Non-interlace | |
| | Analog Composite Control unit : EIA-170 2:1interlace | |
| 6) Synchronization | Internal | |
| 7) Exposure Mode | Internal / VI mode | |
| 8) Exposure Settings | 16 steps by 4 bit rotary switch | |
| 9) Dark S/N ratio | > 48 dB (without CM gain) | |
| | > 40 dB (with 100 times CM gain) | |
| 10) S/N ratio | > 40 dB (at 100% video out without CM gain) | |
| | > 20 dB (at 100% video out with 100 times CM gain) | |
| 11) Resolution | 500(H) x 380(V) TV Lines | |
| 12) MTF | 5MHz: > 35%, 6MHz: > 23% (without CM gain) | |
| 13) Anti Blooming | > 100 times for 100% video output level | |
| 14) CM gain | From 0 dB to +40 dB (Manual volume control) | |
| 15) Pixel Clock Rate | 12.2718 MHz(digital) | |
| | 12.2718 MHz(analog) | |
| 16) Lens Mount | CS/C-mount | |
| 17) Power Voltage | 100/240VAC | |
| 18) Power Consumption | 38W | |
| 19) Defect | TBD | |
| 20) Shading | Horizontal: < 30mV at 100% video out, <10mV at 0% video out (without CM gain) | |
| | Vertical: < 30mV at 100% video out, <10mV at 0% video out (without CM gain) | |
| 21) Gamma | 1.0 | |
| 22) Recommended Temperature | 0 degree C to +40 degree C | |
| 23) Storage Temperature - | -25 degree C to +80 degree C | |
| 24) Vibration | 4.4g, sinusoidal from 700 to 6000 per minute | |
| 25) Weight | Camara head | 300 g |
| | Camera control unit(CCU) | 1350 g |
| | Accessories(Refer to 2-8) | 375 g |
| 26) Dimensions | Camara head | 60(W) x 50(H) x 83.5(D) mm |
| | Camera control unit(CCU) | 200(W) x 66(H) x 140(D)mm |
| 27) Housing | All metal enclosure | |

Figure A.13: TI datasheet

## 4. *ImSpector* SPECIFICATIONS

| | Standard products | Notes for OEM/custom products |
|---|---|---|
| Optical characteristics | | |
| Spectral ranges[1] and dispersions | | |
| ImSpector V7 | 400 - 710 nm ±5nm, 47 nm/mm | |
| ImSpector V8 | 380 - 780 nm ±5 nm, | Custom dispersions and ranges available in the region of 380 - 2400 nm. |
| ImSpector V9 | 430 - 900 nm[3] ±5 nm, 71.2 nm/mm | |
| ImSpector N10 | 700 - 1000 nm ±5 nm, 45.5 nm/mm | |
| Spectral resolution[2] (with 60 µm slit) | | |
| ImSpector V7, V8, N10 | 5 nm | Resolution can be changed to start at 1.5 nm by narrowing the slit. |
| ImSpector V9 | 7 nm | |
| Image size[1] | 6.6 mm x 8.8 mm (corresponding to standard 2/3" CCD) | Custom image sizes available to match customer's detector |
| Spatial resolution[2] | 15 line-pairs/mm | |
| Aberrations | Insignificant astigmatism<br>Bending of spectral lines across spatial axis <±2 nm | |
| Numerical aperture | 0.18 (F/2.8) | |
| Slit width | 13, 25, 50, 80, 150 µm | Custom slit sizes available. |
| Effective slit length | 8.8 mm | |
| Total efficiency (typical) | > 50%, independent of polarization | |
| Stray light | < 0.5 % (halogen lamp, 633 nm notch filter) | |
| Mechanical characteristics | | |
| Size (L x W x H) | 135 x 70 x 60 mm | Basic spectrograph tube of size 35 x 110 mm (D x L) without the outer housing readily available for OEM use[4]. |
| Body | Anodized aluminum with thread for standard camera tripod | |
| Lens and camera mount | Standard C-mount | Other mounts available |
| User adjustments | Image axis relative to CCD row<br>Back focal length adjustable ±1mm | |
| Environmental characteristics | | |
| Storage | -20 ... +85 °C | |
| Operating | +5 ... +40 °C, non-condensing | |

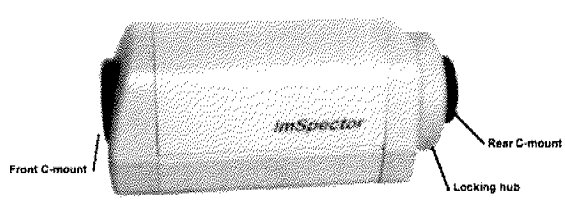


Figure A.14: Specim ImSpector V7

## A.2 Calibration Procedures

In this section the calibration procedures for pressure, temperature and spectral measurement are briefly described.

### A.2.1 Pressure Calibration

To calibrate the pressure sensors a mechanical pressure gauge was used. Pressure was varied from 0 to 2 bar and the readout of the mechanical pressure gauge was compared with the measured pressure sensor voltage. The linearity of the sensor was demonstrated: 1 Volt change corresponds to 1 bar pressure change. The calibration curve is then used during the measurements to convert voltages into pressures [bar].

### A.2.2 Temperature Calibration

To calibrate the temperature response the IR camera was used. Different images of the test plate were acquired with temperatures varying from $10°C$ to $40°C$. The IR pictures, or measured temperatures, were compared with the thermocouple readouts. A polynomial fit was performed and the coefficients were used during the data evaluation steps to compute the test plate temperature.

### A.2.3 Spectrometer Calibration

The calibration of the spectrometer is described in detail in the Specim ImSpector user manual. The calibration procedure can be summarized in the following steps:

- Alignment of the spectrometer with respect to the CCD camera chip
- Focusing the spectrometer onto the measurement surface
- Acquisition of two reference measurements at known wavelength
- Correction of the "smile" effect

To correctly focus and align the spectrometer a test target is used. A template of black stripes is printed on white paper, see Fig. A.15.

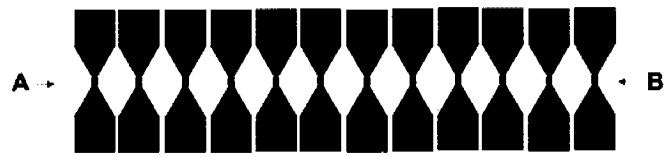


Figure A.15: Test target for alignment

### Alignment

The spectrometer has to be aligned by rotating it with respect to the CCD camera. As result the x-axis represents the spatial resolution and the y-axis represents the spectral resolution. Fig. A.16 shows spectral images before and after the alignment.

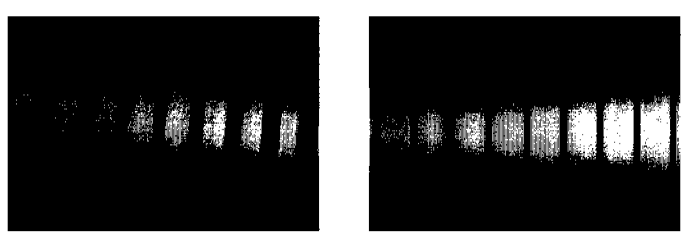

Figure A.16: Image alignment

### Focusing

The spectrometer, or better the lens used, has to be correctly focused on the measurement surface. The procedure is the same as with a conventional CCD camera. Fig. A.17 shows the images before and after focusing.

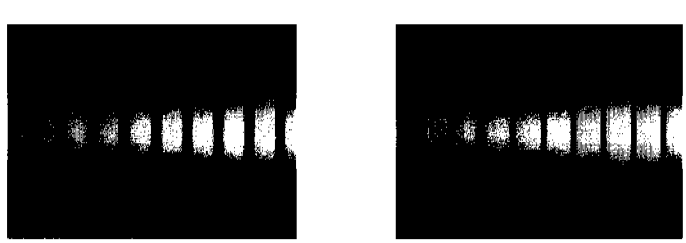

Figure A.17: Out of focus - Focus OK

### Acquisition of reference images

Two images at known and small bandwith wavelengths are used as a reference. A green LED laser (532 nm) and a red LED laser (679 nm) were used. The two peaks in the spectral response were used as a reference by assuming a linear response between the two points to compute the wavelength calibration.

### "Smile effect"

The acquired images have a small (few pixel) distortion of the spectral image in the x-axis direction (center of the image), see Fig. A.18. To overcome this problem and increase the accuracy a correction function was developed and applied to all measurements.
After these preliminary steps the acquired images can be converted into

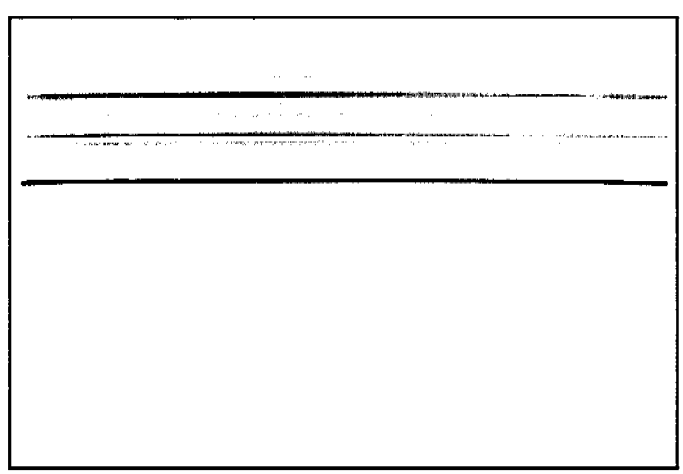

Figure A.18: "Smile" effect

1-D spectral measurements.

## A.3 Software Specifications

The software functions were originally written in Matlab 6.1 and then converted to Matlab 7. Some functions, to increase speed and portability, were written in C++, and converted to MEX-files[1]. The main advantage of Matlab 7 compared to Matlab 6.1 is the capability of compiling m-files and obtain a stand-alone application. This manual is intended to give the user an overview of the main features of the PSP calibration software. The description of the Matlab code is thought to help a possible further improvement or development of the code.

### A.3.1 User Manual

To start the calibration program the main function in Matlab is "controlTC.m", or "controlTC.exe" for the compiled version. The GUI, appearing on the screen, is illustrated in Fig. A.19. The features available

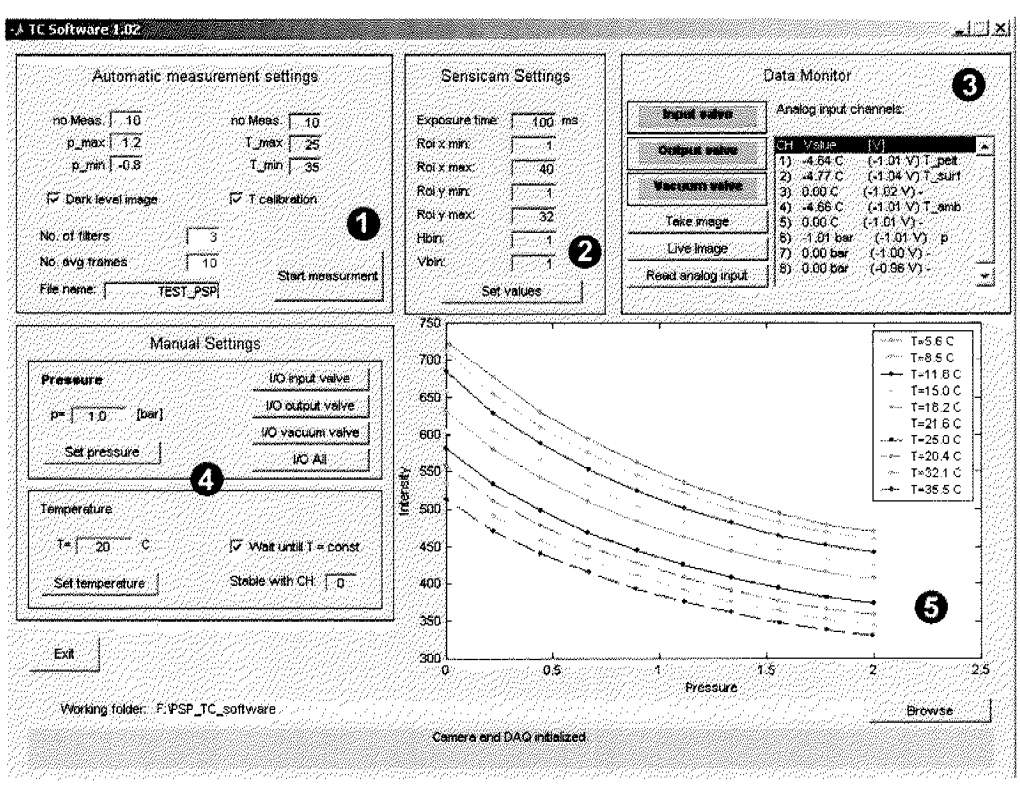


Figure A.19: TC Control GUI.

[1] Matlab MEX-files, see Matlab documentation (http://www.mathworks.com).

are listed in the following.

- *Automated measurement settings*: perform an automated calibration process by automatically varying pressure and temperature with customizable ranges (Fig. A.19 ❶). The pressure range varies from *p_min* to *p_max* in noMeas. steps. The temperature calibration can be activated with the checkbox "T calibration" and it varies from *T_min* to *T_max* in noMeas. steps. The "Dark level image" checkbox is used to store an image without illumination source: the user is asked to shutdown the illumination before the calibration procedure starts. The acquired images are saved with the file name suffix "DL". The number of optical filters used (e.g., for multifilter measurements) is set in "No. of filters" and the images taken with different filters are saved with the suffix "_FX", where X is the filter number. The number of frames averaged can be changed in the "No. avg frames" box. The root filename for all the images is defined in the "File name:" field. The automated measurement is started with the "Start measurement" button.

- *Camera settings*: settings for the CCD camera (Fig. A.19 ❷), especially developed for the Sensicam. The parameters are self explanatory: exposure time, ROI (region of interest) in x and y directions and vertical/horizontal binning. Some parameters are disabled with the use of different CCD cameras.

- *Data monitor*: monitor all the input data. Reads and displays voltages of the input channels acquired with the DAQ board, in particular temperatures of the thermocouples and pressure inside TC (Fig. A.19 ❸). The status of the three valves is monitored with the valve boxes: red, valve is closed, green, valve is open. The sensors signals are monitored in the "Analog input channels" box. Readouts 1 to 5 are related to the thermocouples (peltier (1), surface (2) and ambient (4) temperature). Pressure is associated with the sixth field. Channels 3, 5, 7 and 8 are not used. A live picture ("Live image" button), or a snap shot image, ("Take image") of the camera can be displayed in a separate window.

- *Manual settings*: manual setting of test plate temperature and pressure (Fig. A.19 ❹). The pressure can be set by putting the end value in the "p=" box and by pressing the "Set pressure" button.

A manual control of the individual valves is also possible (I/O input, output, vacuum valve). At the end of a measurement cycle the button "I/O All" is used before opening the TC to open all the valves and empty pipes and the vacuum chamber. Temperature can be set in the same way as pressure. Notice that the algorithm implements a temperature stabilization function: the program waits until the temperature of channel "Stable with CH" is stable. The function can be activated with the "Wait until T=const." checkbox.

- *Visualization window*: display a fast evaluation of the acquired data: intensity plot, spectral response, or acquired images (Fig. A.19 ❺). As default (setable in the matlab code) the acquired image is displayed.

The "Working folder" box shows the location where the measured images/file are saved. The dark gray box shows the user useful information during the measurement.

### A.3.2 Matlab Code

The main program is "controlTC.m" with the graphical interface "controlTC.fig". This software, as already described in Sec. 3.3, is divided in 5 modules:

1. data acquisition
2. pressure control
3. temperature control
4. image acquisition
5. data evaluation.

For every module different functions were developed. A list of all functions, divided in subcategories, is given with a short description. Note that the description of the input/output parameters for each function is contained in the header of the m-file.

### Data acquisition

- *initBoard.m*: initializes the NI-6036E card and sets all predefined acquisition parameters (e.g. sample rate, samples per trigger, channels names and ranges, output channels, ...).

- *deinitBoard.m*: deinitailizes the NI card and clears all the related variables.

### Pressure control

- *openValve.m*: this function is used to control the solenoid valves. A specific valve can be opened/closed for a specific time period or continuously left opened/closed.

- *setPressure.m*: this function is used to set the pressure inside the test cell. The software controls the valves in order to obtain the desired pressure.

- *pressure_ramp*: this function is used during a calibration procedure to change the pressure from a minimum value ($p_{min}$) to a maximum value ($p_{max}$) with a given number of steps. Images at every pressure point are saved.

### Temperature control

- *VtoT.m*: the thermocouples readout is converted into temperatures with the VtoT function. The calibration is performed with the IR camera.

- *setTemperature.m*: to set the test plate temperature the function setTemperature is used. The desired temperature is given and the software sends the required signals to the ECU. Since the temperature is not immediately stable the function WaitIsStable is called to avoid temperature fluctuations during a measurement.

- *WaitIsStable.m*: this function reads the temperature of the test plate for several seconds. It computes the maximal and minimal values and if the fluctuations are smaller than a given value the main program can continue with the data acquisition, if not the, readout is repeated.

### Image acquisition

- *initSensicam.dll*: function to initialize the PCO Sensicam.
- *stopSensicam.dll*: function to deinitialize the PCO Sensicam.
- *readImgSensicam.dll*: images from the PCO Sensicam are acquired and stored in a Matlab variable. As parameter the number of frames averaged can be given.
- *settingsSensicam.dll*: sets the acquisition parameters of the PCO Sensicam (integration time, ROI, trigger (external/internal), ...).
- *Live.exe*: this program opens a window with a live preview of the PCO Sensicam camera. It is very useful during spectrometer calibrations or to properly focus the camera.
- *snapTI.dll*: images with the Texas Instrument camera are acquired and stored in a Matlab variable. As parameter the number of frames averaged can be given.
- *hlgrab.exe*: this program opens a window with a live preview of the Texas Instrument camera. It is very useful during spectrometer calibration or to properly focus the camera.

### Data evaluation

- *brodir.m*: this function is used to select the working folder, or the folder where all measured data/images are stored.
- *display_DAQ.m*: this function displays the actual voltages of the different channels in the data monitor window.
- *compSpectrum.m*: this function converts the images taken with the spectrometer into emission intensity as function of wavelength.

The code of the functions can be found on the CD-ROM provided with the thesis or at the Institute of Fluid Dynamics (IFD), ETH Zurich.

# Appendix B

## *Pressure Sensitive Paint Formulation*

The receipt for the Ru - based PSP was taken from [9] (Purdue University). The Pt-based PSP the receipt was simply adapted.

### Ru - Based

Ingredients: 1/3 level scoops (4mg) of B.R.C.
25 ml (33 g) of dichloromethane
7.5 ml (7.9 g) of GE RTV 118 (Silicon)

Mixing directions: Mix the B.R.C. to the dichloromethane, then add the GE RTV 118

### PtOEP - Based

Ingredients: 1/3 level scoops (4mg) of PtOEP
25 ml (33 g) of dichloromethane
7.5 ml (7.9 g) of GE RTV 118 (Silicon)

Mixing directions: Mix the PtOEP to the dichloromethane, then add the GE RTV 118

### PtTFPP - Based

Ingredients: 1/3 level scoops (4mg) of PtTFPP
25 ml (33 g) of dichloromethane
7.5 ml (7.9 g) of GE RTV 118 (Silicon)

Mixing directions: Mix the PtTFPP to the dichloromethane, then add the GE RTV 118

# Appendix C

## *EL-Foils Specifications*

The EL-foils used for the measurements were provided by:

Lumitec AG,
GZS Strahlholz,
9056 Gais,
Switzerland.

Further informations can be found under www.lumitec.ch. The used/investigated EL-foils are summarized in Tab. C.1.

| | EL-foil type | Datasheet |
|---|---|---|
| 1 | Lumitec 1655 | see Fig. C.1 |
| 2 | Lumitec 1659 | see Fig. C.2 |
| 3 | Lumitec 1659 with filter | see Fig. C.3 |
| 4 | Lumitec 2007 | n.a. |

Table C.1: Investigated EL-foils.

**LUMITEC AG**
El-Leuchtsysteme
GZS Strahlholz
CH-9056 Gais
Telefon 071/791 07 37
Telefax 071/793 14 23

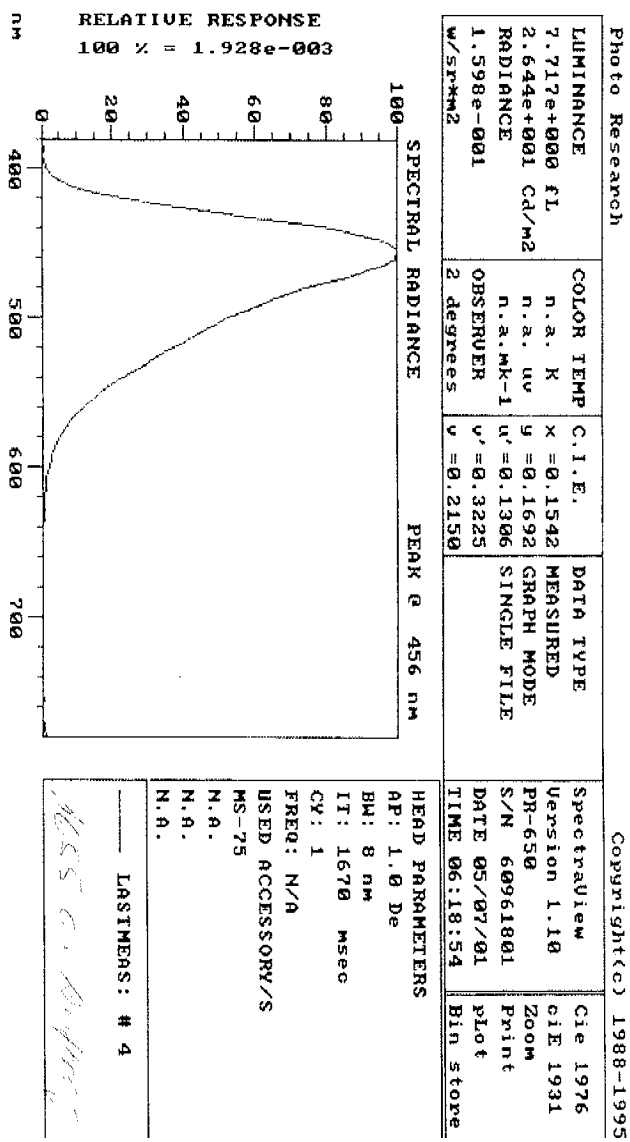


Figure C.1: Lumitec 1655

**LUMITEC AG**
El-Leuchtsysteme

GZS Strahltholz
CH-9056 Gais
Telefon 071/791 07 37
Telefax 071/793 14 23

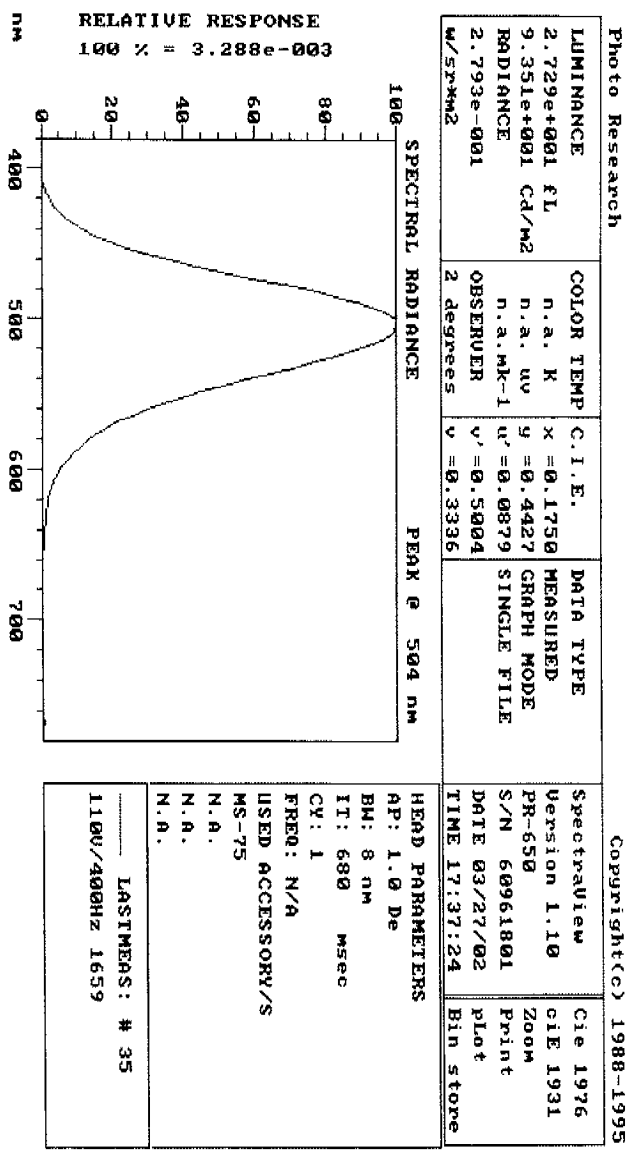


Figure C.2: Lumitec 1659

**LUMITEC AG**
EL-Leuchtsysteme
GZS Strahlholz
CH-9056 Gais
Telefon 071/791 07 37
Telefax 071/793 14 23

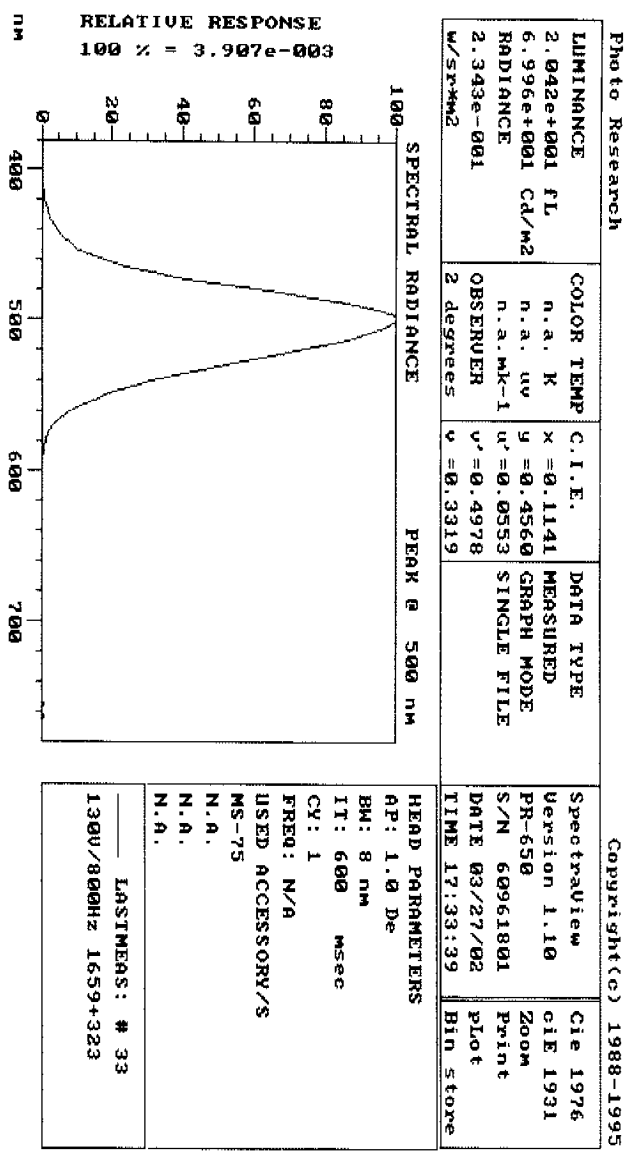


Figure C.3: Lumitec 1659 with filter

# Appendix D

## *Filter transmission curves*

A list of the used filters is given in Tab. D.1

| No. | | Type | Transmission curve |
|---|---|---|---|
| 1 | Andover Corporation | 400 FS70-50 | Fig. D.1 |
| 2 | Andover Corporation | 470 FS10-50 | Fig. D.2 |
| 3 | Andover Corporation | 500 FS40-50 | Fig. D.3 |
| 4 | Andover Corporation | 600 FS10-50 | Fig. D.4 |
| 5 | Schott Filters | OG 570 | Fig. D.5 |
| 6 | Schott Filters | OG 590 | Fig. D.6 |
| 7 | Schott Filters | RG 610 | Fig. D.7 |
| 8 | Schott Filters | RG 630 | Fig. D.8 |

Table D.1: Filters list

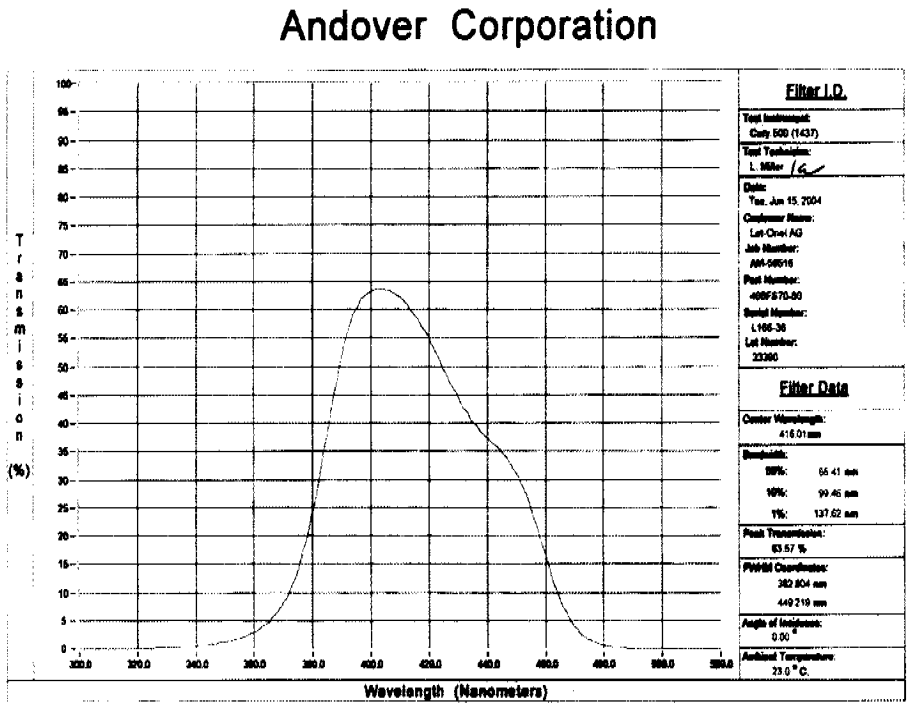


Figure D.1: Transmission curve 400FS70-50

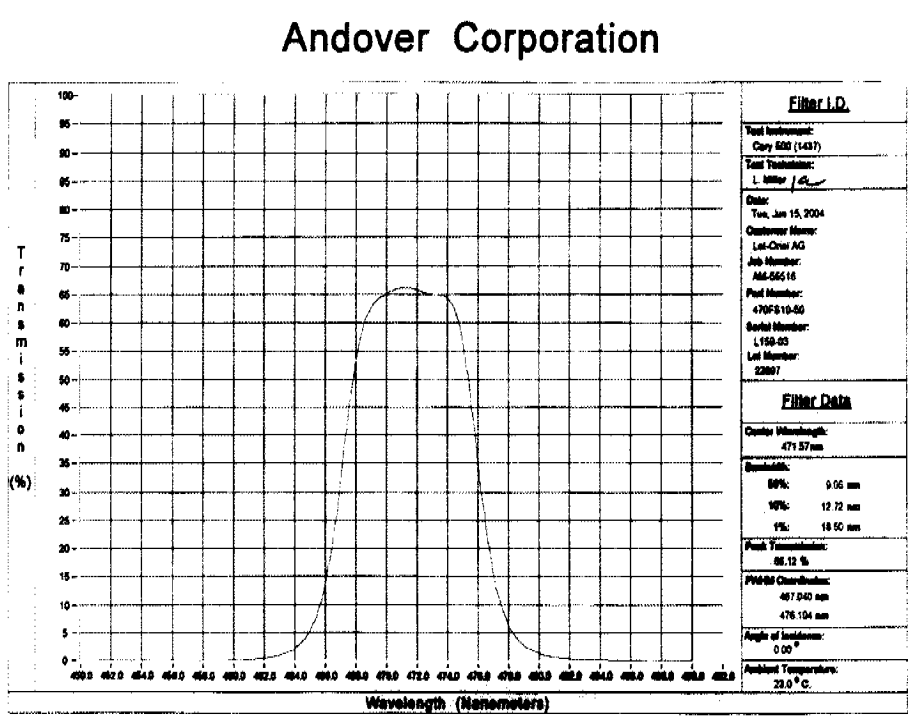


Figure D.2: Transmission curve 470FS10-50

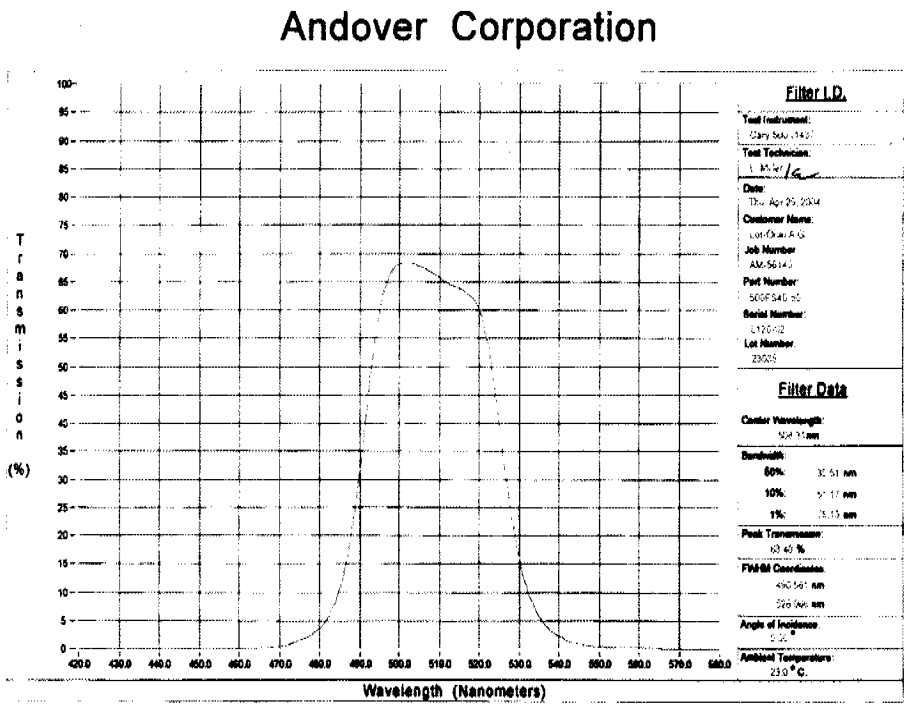


Figure D.3: Transmission curve 500FS40-50

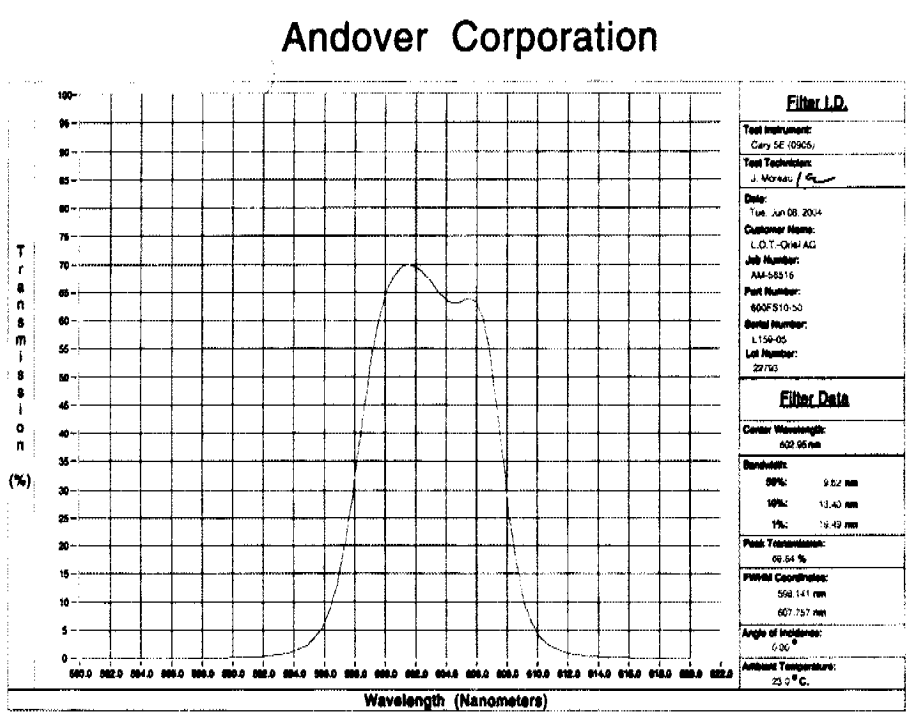


Figure D.4: Transmission curve 600FS10-50

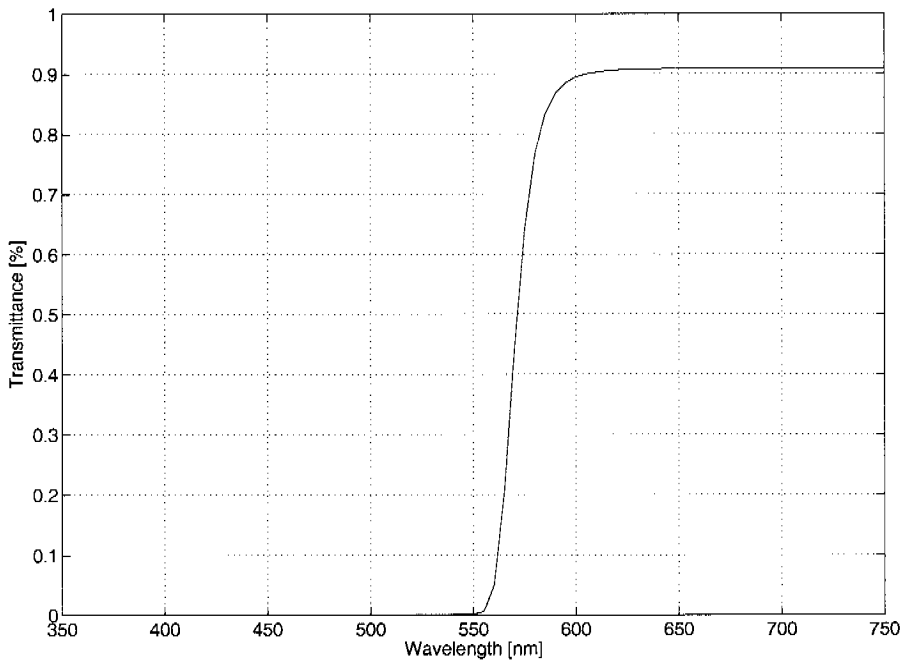


Figure D.5: Transmission curve OG570

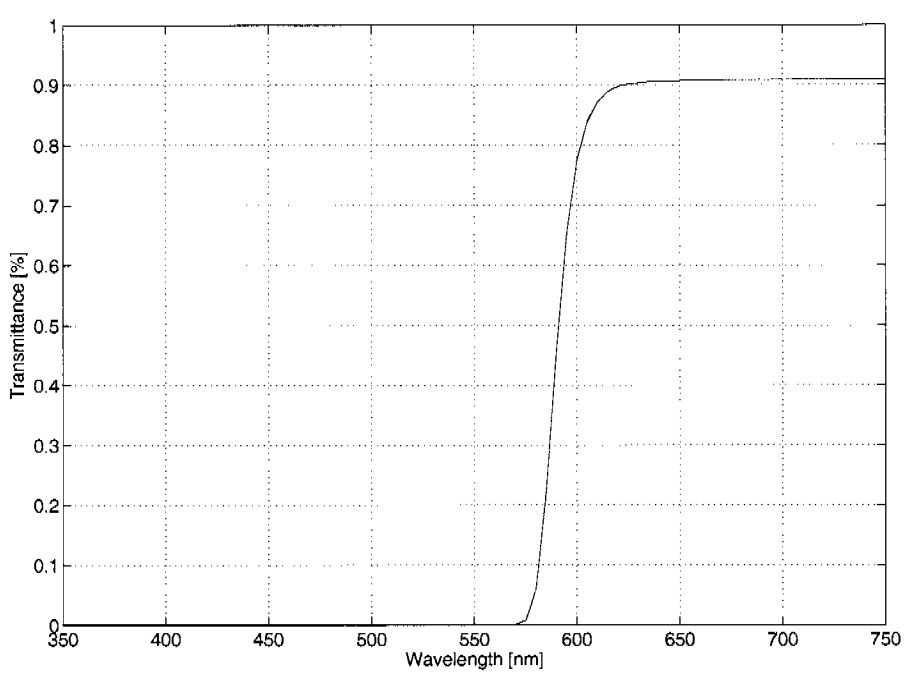


Figure D.6: Transmission curve OG590

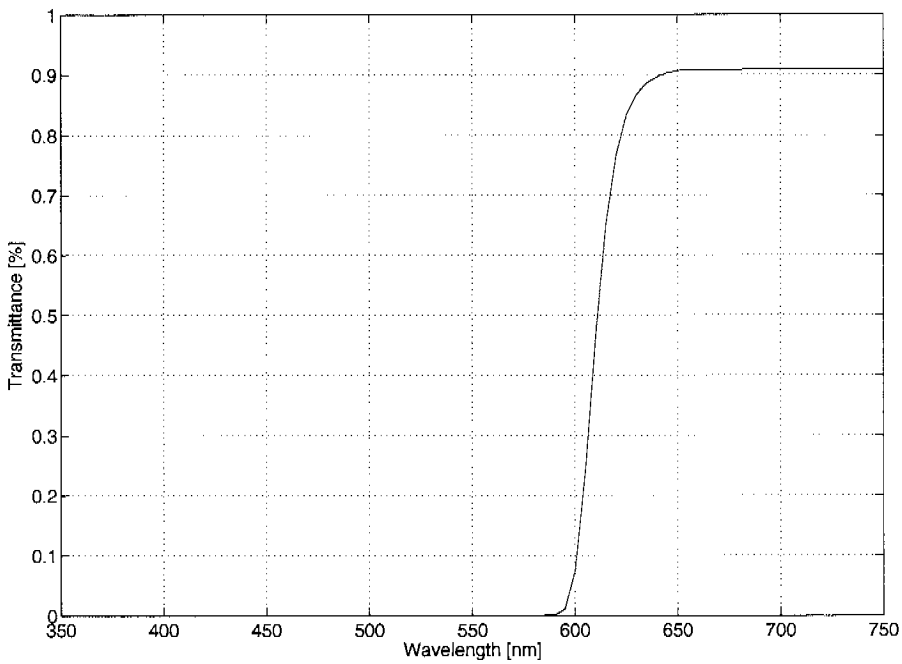


Figure D.7: Transmission curve RG610

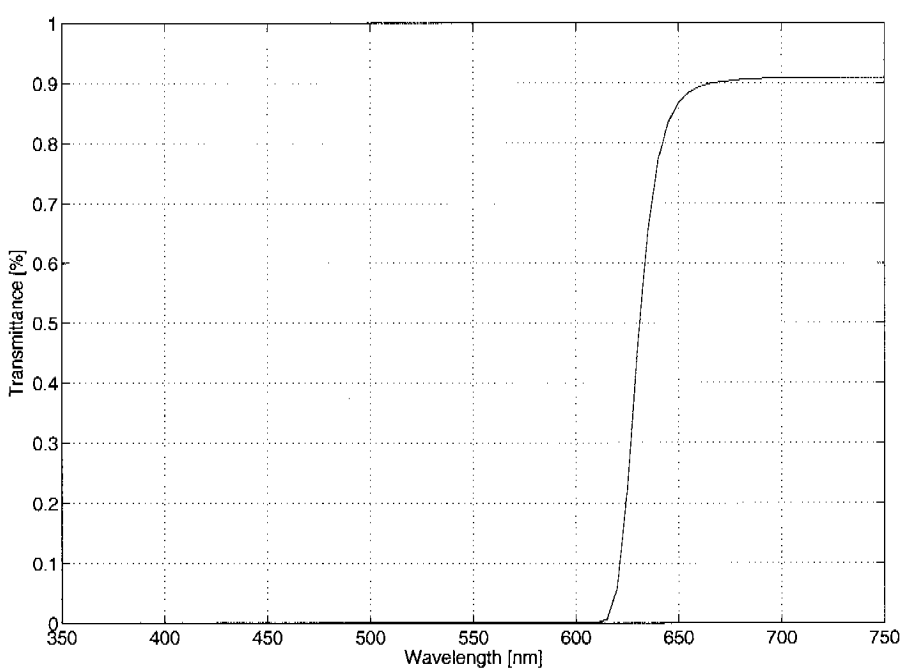


Figure D.8: Transmission curve RG630

# Appendix E

## *Performed Measurements*

All the measurements performed in the TC as research purpose or calibration are given in App. E.1. The measurements of the RUAG Aerospace and IFD wind tunnel test campaign are summarized in App. E.2 and E.3.

# E.1 TC Measurements/Calibrations

| | Target | | Illumination | | Power supply | | Optics | | Pressure | | Calibration | | Measurement | | | |
|---|---|---|---|---|---|---|---|---|---|---|---|---|---|---|---|---|
| # | Paint ID | Type | Type | [V] | Lens | Camera Filter | Pmin | Pmax | Tmin | Tmax | Frames avg. | Meas. Name | Comments |
| 1 | 2 | EL-foil 2007 | EL-driver (3) | max | Nikon 60mm | - | atm | - | atm | - | 1 | t01.mat | Ref. Image: ref01.mat |
| 2 | 2 | EL-foil 2007 | EL-driver (1) | 12.8 | Nikon 60mm | - | atm | - | atm | - | 1 | t02.mat | Ref. Image: ref01.mat |
| 3 | 2 | EL-foil 2007 | EL-driver (2) | 31.8 | Nikon 60mm | - | atm | - | atm | - | 1 | t03.mat | Ref. Image: ref01.mat |
| 4 | - | EL-foil 2007 | EL-driver (2) | 31.8 | Nikon 60mm | - | atm | - | atm | - | 1 | t04.mat | |
| 5 | 2 | EL-foil 2007 | EL-driver (3) | max | Nikon 60mm | EO 45064 | atm | - | atm | - | 1 | t05.mat | |
| 6 | 2 | EL-foil 2007 | EL-driver (1) | 12.8 | Nikon 60mm | EO 45064 | atm | - | atm | - | 1 | t06.mat | |
| 7 | 2 | EL-foil 2007 | EL-driver (2) | 31.8 | Nikon 60mm | EO 45064 | atm | - | atm | - | 1 | t07.mat | |
| 8 | - | EL-foil 2007 | EL-driver (2) | 31.8 | Nikon 60mm | EO 45064 | atm | - | atm | - | 1 | t08.mat | |
| 9 | - | Blue LED | External | 15.3 | Nikon 60mm | EO 45064 | atm | - | atm | - | 1 | t09.mat | |
| 10 | - | Blue LED | External | 15.3 | Nikon 60mm | - | atm | - | atm | - | 1 | t10.mat | |
| 11 | 2 | Blue LED | External | 15.3 | Nikon 60mm | - | atm | - | atm | - | 1 | t11.mat | |
| 12 | - | Blue LED | External | 14.8 | Nikon 60mm | - | atm | - | atm | - | 1 | t12.mat | |
| 13 | 2 | Blue LED | External | 14.8 | Nikon 60mm | - | atm | - | atm | - | 1 | t13.mat | |
| 14 | - | Blue LED | External | 14.4 | Nikon 60mm | - | atm | - | atm | - | 1 | t14.mat | |
| 15 | 2 | Blue LED | External | 14.4 | Nikon 60mm | - | atm | - | atm | - | 1 | t15.mat | |
| 16 | 2 | EL-foil 2007 | EL-driver (2) | 31.8 | Nikon 60mm | - | atm | - | atm | - | 1 | t16.mat | With source filter EO 46432 |
| 17 | 2 | EL-foil 2007 | EL-driver (2) | 31.8 | Nikon 60mm | - | atm | - | atm | - | 1 | t17.mat | With source filter EO 46432 |
| 18 | 2 | EL-foil 2007 | EL-driver (2) | 31.8 | Nikon 60mm | EO 45064 | 0 | 2 | atm | - | 1 | ref18.mat | Ref. Image ref18.mat |
| 19 | 2 | EL-foil 2007 | EL-driver (2) | 16.6 | Nikon 60mm | EO 45064 | 0 | 2 | atm | - | 1 | ref19.mat | Ref. Image ref19.mat |
| 20 | - | White light | External | - | Nikon 60mm | - | atm | - | atm | - | 1 | t20.mat | White light spectrum (reference) |
| 21 | 3 | White light | External | - | Nikon 60mm | - | atm | - | atm | - | 1 | t21.mat | |
| 22 | - | White light | External | - | Nikon 60mm | - | atm | - | atm | - | 1 | t22.mat | White light spectrum (reference) |
| 23 | 2 | White light | External | - | Nikon 60mm | - | atm | - | atm | - | 1 | t23.mat | |
| 24 | - | Blue LED | External | 21 | Nikon 60mm | - | atm | - | atm | - | 1 | t24.mat | |
| 25 | 3 | Blue LED | External | 21 | Nikon 60mm | - | atm | - | atm | - | 1 | t25.mat | |
| 26 | 3 | EL-foil 2007 | EL-driver (2) | 31.8 | Nikon 60mm | - | atm | - | atm | - | 1 | t26.mat | |
| 27 | - | EL-foil 2007 | EL-driver (2) | 31.8 | Nikon 60mm | - | atm | - | atm | - | 1 | t27.mat | |
| 28 | - | White light | External | - | Nikon 60mm | - | atm | - | atm | - | 1 | t28.mat | White light spectrum (reference) |
| 29 | 4 | White light | External | - | Nikon 60mm | - | atm | - | atm | - | 1 | t29.mat | |
| 30 | 4 | Blue LED | External | 21.0 | Nikon 60mm | EO 45064 | atm | - | atm | | 1 | t30.mat | Ref. Image: t30ref |
| 31 | 4 | EL-foil 2007 | EL-driver (2) | 31.8 | Nikon 60mm | EO 45064 | atm | - | atm | - | 1 | t31.mat | Ref. Image: t31ref |
| 32 | 2 | EL-foil 2007 | EL-driver (2) | 32.0 | Nikon 60mm | - | 0 | 2 | atm | - | 1 | t32dark.mat | Ref. Image: t32dark.mat |
| 33 | - | EL-foil 1659 | EL-driver (3) | max | Nikon 60mm | - | atm | - | atm | - | 1 | foil1659.mat | |
| 34 | - | EL-foil 2007 | EL-driver (2) | 32.0 | Nikon 60mm | - | 0 | 2 | 10 | 40 | 1 | TEST01 | |
| 35 | - | EL-foil 1659 | EL-driver (2) | 32.0 | Nikon 60mm | - | 0 | 2 | 10 | 40 | 1 | TEST02 | |
| 36 | - | EL-foil 1659 (F) | EL-driver (2) | 32.0 | Nikon 60mm | Specim | 0 | 2 | 10 | 40 | 1 | TEST03 | |

TC measurements list (1 of 3)

TC measurements list (2 of 3)

| | Target | Illumination | Power supply | | Optics | | Pressure | | Temperature | | | Measurements | |
|---|---|---|---|---|---|---|---|---|---|---|---|---|---|
| # | Paint ID | Type | Type | [V] | Lens | Camera Filter | Pmin | Pmax | Tmin | Tmax | Frames avg. | Meas. Name | Comments |
| 37 | 5 | EL-foil 1659 | EL-driver (2) | 32 | Nikon 60mm | Schott 590 | 0 | 2 | 10 | 40 | 1 | TEST04 | --- TC test ---- |
| 38 | 5 | EL-foil 1659 (F) | EL-driver (2) | 32 | Nikon 60mm | Specim | 0 | 2 | 0 | 40 | 1 | TEST05 | |
| 39 | 5 | EL-foil 1659 (F) | EL-driver (2) | 32 | Nikon 60mm | Schott 590 | 0 | 2 | 0 | 40 | 1 | TEST06 | |
| 40 | 5 | Blue LED | External | n.a. | Nikon 60mm | Schott 590 | 0 | 2 | 0 | 40 | 1 | TEST07 | |
| 41 | 5 | EL-foil 1659 (F) | EL-driver (2) | 32 | Nikkor 80mm 1:1.4 +sd | Schott 590 | 0 | 2 | 0 | 40 | 1 | TEST08 | |
| 42 | 5 | EL-foil 1659 (F) | EL-driver (2) | 32 | Nikkor 80mm 1:1.4 +sd | Specim | 0 | 2 | 0 | 40 | 1 | TEST09 | |
| 43 | | | | | | | | | | | - | Test10 | Software test |
| 44 | 5 | EL-foil 2007 | EL-driver (2) | 32 | Nikkor 80mm 1:1.4 +sd | Specim | 0 | 2 | atm | - | - | TEST11 | Problem with CH2 |
| 45 | 5 | EL-foil 2007 | EL-driver (2) | 32 | Nikkor 80mm 1:1.4 +sd | Specim | 0 | 2 | atm | - | - | TEST12 | Problem with CH2 |
| 46 | 5 | EL-foil 2007 | EL-driver (2) | 32 | Nikkor 80mm 1:1.4 +sd | Schott 590 | 0 | 2 | atm | - | - | TEST13 | Problem with CH2 |
| 47 | 5 | EL-foil 2007 | EL-driver (2) | 32 | Nikkor 80mm 1:1.4 +sd | Schott 590 | 0 | 2 | atm | - | - | TEST14 | Problem with CH2 |
| 48 | 5 | EL-foil 1659 | EL-driver (2) | 32 | Nikkor 80mm 1:1.4 +sd | Specim | 0 | 2 | 0 | 40 | 1 | TEST15 | |
| 49 | 5 | EL-foil 1659 | EL-driver (2) | 32 | Nikkor 80mm 1:1.4 +sd | Specim | 0 | 2 | 0 | 40 | 30 | TEST16 | |
| 50 | 5 | EL-foil 1659 | EL-driver (2) | 32 | Nikkor 80mm 1:1.4 +sd | - | 0 | 2 | 0 | 40 | - | TEST17 | Problem with CH2 and CH1 |
| 51 | - | EL-foil 1659 (F) | EL-driver (2) | 32 | Nikkor 80mm 1:1.4 +sd | - | 0 | 2 | 0 | 40 | - | TEST18 | |
| 52 | 5 | EL-foil 1659 | EL-driver (2) | 32 | Nikkor 80mm 1:1.4 +sd | Specim | 0 | 1 | 10 | 30 | 20 | TEST19 | 20 frames averaged |
| 53 | - | - | - | - | - | - | - | - | - | - | - | TEST20 | |
| 54 | - | - | - | - | - | - | 0 | 1 | 10 | 30 | - | TEST21 | Test new software (T and p control) |
| 55 | 5 | EL-foil 1659 | EL-driver (2) | 32 | Nikkor 80mm 1:1.4 +sd | Schott 570 | -0.5 | 1.5 | 10 | 30 | 5 | TEST22 | |
| 56 | 6 | EL-foil 1659 | EL-driver (2) | 32 | Nikkor 80mm 1:1.4 +sd | Schott 570 | -0.8 | 1.2 | 10 | 30 | 5 | meas01 | |
| 57 | 6 | EL-foil 1659 | EL-driver (2) | 32 | Nikkor 80mm 1:1.4 +sd | Schott 590 | -0.8 | 1.2 | 10 | 30 | 5 | meas02 | |
| 58 | 6 | EL-foil 1659 | EL-driver (2) | 32 | Nikkor 80mm 1:1.4 +sd | Schott 610 | -0.8 | 1.2 | 10 | 30 | 5 | meas03 | |
| 59 | 6 | Blue LED | External | 19 | Nikkor 80mm 1:1.4 +sd | Schott 570 | -0.8 | 1.2 | 10 | 30 | 5 | meas04 | |
| 60 | 6 | Blue LED | External | 19 | Nikkor 80mm 1:1.4 +sd | Schott 590 | -0.8 | 1.2 | 10 | 30 | 5 | meas05 | |
| 61 | 6 | Blue LED | External | 19 | Nikkor 80mm 1:1.4 +sd | Schott 610 | -0.8 | 1.2 | 10 | 30 | 5 | meas06 | |
| 62 | 6 | Blue LED | External | 19 | Nikkor 80mm 1:1.4 +sd | Specim | -0.8 | 1.2 | 10 | 30 | 5 | meas08 | |
| 63 | 6 | EL-foil 1659 | EL-driver (2) | 32 | Nikkor 80mm 1:1.4 +sd | Specim | -0.8 | 1.2 | 10 | 30 | 5 | meas07 | |
| 64 | 10 | EL-foil 1655 | EL-driver (2) | 32 | Nikkor 105mm 1:28 +sd | Specim | -0.8 | 1.2 | 20 | 30 | 10 | Lab01 | |
| 65 | 10 | EL-foil 1655 | EL-driver (2) | 32 | Nikkor 105mm 1:28 +sd | Schott 610 | -0.8 | 1.2 | 20 | 30 | 10 | Lab02 | |
| 66 | 10 | EL-foil 1655 | EL-driver (2) | 32 | Nikkor 105mm 1:28 +sd | Schott 630 | -0.8 | 1.2 | 20 | 30 | 10 | Lab03 | |
| 67 | 10 | Blue LED | External | 15 | Nikkor 105mm 1:28 +sd | Schott 610 | -0.8 | 1.2 | 20 | 30 | 10 | Lab00 | |
| 68 | 10 | Blue LED | External | 15 | Nikkor 85mm 1:1.4 +sd | Schott 610 | -0.8 | 1.2 | 20 | 30 | 10 | Lab04 | |
| 69 | 10 | Blue LED | External | 15 | Nikkor 105mm 1:28 +sd | Schott 610 | -0.8 | 1.2 | 20 | 30 | 10 | Lab05 | |
| 70 | 10 | EL-foil 1659 | EL-driver (2) | 32 | Nikkor 105mm 1:28 +sd | Schott 610 | -0.8 | 1.2 | 20 | 30 | 10 | Lab06 | |
| 71 | 10 | Blue LED | External | 15 | Nikkor 105mm 1:28 +sd | Schott 610 | -0.8 | 1.2 | 20 | 30 | 10 | Lab07 | |
| 72 | 12 | EL-foil 1659 | EL-driver (2) | 32 | Nikkor 105mm 1:28 +sd | Schott 610 | -0.8 | 1.2 | 20 | 30 | 20 | PtOEP1 | |

| | Paint | | Power supply | | Optics | | Pressure | | Timeline | | | Measurement | |
|---|---|---|---|---|---|---|---|---|---|---|---|---|---|
| # | Paint ID | Type | Type | [V] | Lens | Camera Filter | Pmin | Pmax | Tmin | Tmax | Frames avg. | Meas. Name | Comments |
| 73 | 12 | EL-foil 1659 | EL-driver (2) | 32 | Nikkor 105mm 1:28 +sd | Schott 630 | -0.8 | 1.2 | 20 | 30 | 20 | PtOEP2 | |
| 74 | 12 | EL-foil 1655 | EL-driver (2) | 32 | Nikkor 105mm 1:28 +sd | Schott 630 | -0.8 | 1.2 | 20 | 30 | 20 | PtOEP3 | |
| 75 | 12 | EL-foil 1655 | EL-driver (2) | 32 | Nikkor 105mm 1:28 +sd | Schott 610 | -0.8 | 1.2 | 20 | 30 | 20 | PtOEP4 | |
| 76 | 13 | EL-foil 1655 | EL-driver (2) | 32 | Nikkor 105mm 1:28 +sd | Multifilter | -0.8 | 1.2 | 20 | 30 | 10 | Multifilter1 | |
| 77 | 13 | EL-foil 1659 | EL-driver (2) | 32 | Nikkor 105mm 1:28 +sd | Multifilter | -0.8 | 1.2 | 20 | 30 | 10 | Multifilter2 | |
| 78 | 17 | EL-foil 1655 | EL-driver (2) | 32 | Nikkor 60mm | Multifilter | -0.5 | 0.5 | 25 | 35 | 40 | Multifilter3 | |

TC measurements list (3 of 3)

## E.2 RUAG Measurement Campaign

| No. | V [m/s] | α [°] | β [°] | Avg. frames # | Illumination | Filter | Shutter | Comments |
|---|---|---|---|---|---|---|---|---|
| 161 | 70 | 10 | 0 | 20 | EL foil green | OG 590 | - | |
| 162 | 70 | 10 | 0 | 20 | EL foil green | OG 610 | G:2.8 IT:A | |
| 163 | 70 | 10 | 0 | 20 | EL foil green | OG 570 | - | |
| 164 | 70 | 10 | 0 | 20 | LED (green) | OG 570 | | |
| 165 | 70 | 10 | 0 | 20 | LED (green) | OG 590 | | |
| 166 | 70 | 10 | 0 | 20 | LED (green) | OG 610 | | |
| 167 | 70 | 10 | 0 | 60 | LED (green) | OG 610 | | |
| 168 | 70 | 10 | 0 | 60 | EL foil green | OG 610 | G:2.8 IT:A | |
| 169 | 70 | 10 | 0 | 180 | EL foil green | OG 610 | G:2.8 IT:A | |
| 170 | 70 | 10 | 0 | 20 | EL foil blue | OG 610 | G:2.8 IT:B | |
| 171 | 70 | 10 | 0 | 20 | EL foil blue | OG 590 | G:0.0 IT:B | |
| 172 | 70 | 10 | 0 | 20 | EL foil blue | OG 570 | G:2.8 IT:A | |
| 173 | 70 | 10 | 0 | 180 | EL foil blue | OG 610 | G:2.8 IT:A | |
| 174 | 70 | 10 | 0 | 20 | LED (blue) | OG 610 | G:5.0 IT:A | |
| 175 | 70 | 10 | 0 | 180 | LED (blue) | OG 610 | G:5.0 IT:A | |
| 177 | 70 | 0 | 0 | 180 | EL foil green | OG 610 | G:3.5 IT:A | |
| 178 | 70 | 0 | 0 | 180 | LED (green) | OG 610 | G:5.8 IT:A | |
| 179 | 70 | -10 | 0 | 180 | EL foil green | OG 610 | G:3.5 IT:A | |
| 180 | 70 | -10 | 0 | 180 | LED (green) | OG 610 | G:5.8 IT:A | |
| 181 | 70 | 5 | 0 | 180 | EL foil green | OG 610 | G:3.5 IT:A | |
| 182 | 70 | 5 | 0 | 180 | LED (green) | OG 610 | G:5.8 IT:A | |
| 183 | 70 | 5 | 0 | 180 | EL foil (green) | OG 610 | G:3.5 IT:A | w.o. PSP |
| 184 | 70 | 5 | 0 | 300 | EL foil (green) | - | G:0.0 IT:6 | w.o. PSP |
| 185 | 70 | 10 | 0 | 300 | EL foil (green) | - | G:0.0 IT:6 | w.o. PSP |
| 186 | 70 | 0 | 0 | 300 | EL foil (green) | - | G:0.0 IT:6 | w.o. PSP |

Performed test - RUAG Aerospace

## E.3 NACA 0012 Wind Tunnel Tests

| No. | Illumination | T | ρ dyn. | Max ρ | $\rho_{tot}$ | α | File name |
|---|---|---|---|---|---|---|---|
| | | [°C] | [mmH$_2$O] | [%] | [mmH$_2$O] | [°] | |
| 1 | EL-Foil blue | 25.5 | 204.5 | 91.09 | 250.4 | 10 | Wt_01 |
| 2 | LED (on blue EL-foil) | 28.5 | 202.5 | 91.09 | 250 | 10 | Wt_02 |
| 3 | EL-Foil blue | 28.6 | 202 | 91.09 | 250.5 | 10 | Wt_03 |
| 4 | LED (on blue EL-foil) | 29 | 202.3 | 91.09 | 249.8 | 10 | Wt_04 |
| 5 | EL-Foil blue | 29 | 200.3 | 91.09 | 248.9 | -10 | Wt_05 |
| 6 | LED (on blue EL-foil) | 30 | 200.3 | 91.09 | 248 | -10 | Wt_06 |
| 7 | EL-Foil blue | 31 | 201.4 | 91.09 | 249.7 | 5 | Wt_07 |
| 8 | LED (on blue EL-foil) | 31 | 201 | 91.09 | 249 | 5 | Wt_08 |
| 9 | EL-Foil blue | 31 | 147.2 | 78.5 | 249.2 | 18 | Wt_09 |
| 10 | LED (on blue EL-foil) | 30.5 | 146.7 | 78.5 | 248.6 | 18 | Wt_10 |
| 11 | EL-Foil green | 28.3 | 202.9 | 91.09 | 248.5 | 10 | Wt_11 |
| 12 | LED (on green EL-foil) | 28.5 | 202.4 | 91.09 | 250 | 10 | Wt_12 |
| 13 | EL-Foil green | 28.9 | 200.4 | 91.09 | 247.8 | -10 | Wt_13 |
| 14 | LED (on green EL-foil) | 28.8 | 200.5 | 91.09 | 249.9 | -10 | Wt_14 |
| 15 | EL-Foil green | 30.2 | 201 | 91.09 | 249.9 | 5 | Wt_15 |
| 16 | LED (on green EL-foil) | 29.8 | 201.3 | 91.09 | 249.3 | 5 | Wt_16 |
| 17 | EL-Foil green | 29.8 | 144.9 | 78.5 | 249.3 | 18 | Wt_17 |
| 18 | LED (on green EL-foil) | 29.4 | 145.3 | 78.5 | 248.2 | 18 | Wt_18 |

IFD wind tunnel measurements

# *Bibliography*


[1] Allison, S., Cates, M. R., and Beshears, D. L. A survey of thermally sensitive phosphors for pressure sensitive paint applications. Isa technical paper, ISA, 2000.

[2] Allison, S. W., Garvey, D., Cates, M. R., Goedeke, S. M., Gillies, G. T., and Hollerman, W. A. On the use of phosphors for flow measurements. In *11TH International Symposium on Flow Visualization* (Notre Dame, Indiana, USA, 2004), University of Notre Dame.

[3] Bencic, T. J. Pressure-sensitive paint measurements on surfaces with non-uniform temperature. In *45th International Instrumentation Symposium* (Albuquerque, NM, 1999), Instrument Society of America.

[4] Carrol, B., Hubner, J., Schanze, K. S., and Bedlek-Anslow, J. Principal component analysis of dual-luminophore pressure/temperature sensitive paints. *Journal of Visualization 4*, 2 (2001), 121–129.

[5] Demas, J. N., and DeGraff, B. A. Luminescent-based sensors: microhcterogeneous and temperature effects. *Sensors and Actuators 11* (1993), 35–41.

[6] Engler, R. H., Fey, U., Henne, U., Klein, C., and Sachs, W. E. Quantitative wind tunnel studies using pressure- and temperature sensitive paints. *Journal of Visualization 8*, 3 (2005).

[7] Gouterman, M., Callis, J., Dalton, L., Khalil, G., Mébarki, Y., Cooper, K. R., and Grenier, M. Dual luminophore pressure-sensitive paint: Iii. application to automotive model testing. *Meas. Sci. Technol.*, 15 (2004), 1986–1994.

[8] Gouterman, M., J.Callis, Burns, D., Kavandi, J., Gallery, J., Khalil, G., Green, E., McLachlan, B., and Crowder, J. Luminescence imaging for aerodynamic testing. In: Sullivan jp, holmes b proc. of the onr/nasa workshop on quantitative flow visualization, Purdue University, IN, USA, 1990.

[9] GUILLE, M. Luminescent paint measurement systems for aerodynamics applications. Master's thesis, School of Aeronautics and Astronautics, Purdue University, May 2000.

[10] HARRY, J., GOETT, J., AND BULLIVANT, W. K. Test of n.a.c.a. 0009, 0012, and 0018 airfoils in the full-scale tunnel. Report no. 647, national advisory committee for aeronautics, Langley Memorial Aeronautical Laboratory, Langley Fiels, Va., 1938.

[11] HYVÄRINEN, A., KARHUNEN, J., AND OJA, E. *Indipendent component analysis.* Wiley-Interscience Publication, 2001.

[12] JR., L. K. L., AND COHEN, K. S. Aerodynamic characteristics of a number of modified naca four-digit-series airfoil sections. Report no. 1591, national advisory committee for aeronautics, Langley Memorial Aeronautical Laboratory, Langley Fiels, Va., 1948.

[13] JR., L. K. L., AND SMITH, H. A. Aerodynamic characteristics of 15 naca airfoil sections at seven reynolds numbers from 0.7 x $10^6$ to 9.0 x $10^6$. Technical note 1945, national advisory committee for aeronautics, Langley Memorial Aeronautical Laboratory, Langley Fiels, Va., 1949.

[14] KAVANDI, J., CALLIS, J., GOUTERMAN, M., KAHLIL, G., D. WRIGHT, E. G., BURNS, D., AND MCLACHLAN, B. Luminescent barometry in wind tunnels. *Rev. Sci. Instrum. 61* (1990), 3340–3347.

[15] KÖSE, M. E., CARROLL, B. F., AND SCHANZE, K. S. Preparation and spectroscopic properties of multiluminophore luminescent oxygen and temperature sensor films. *Langmuir*, 21 (2005), 9121–9129.

[16] LIU, T., CAMPBELL, B. T., BURNS, S. P., AND SULLIVAN, J. P. Temperature- and pressure-sensitive luminescent paints in aerodynamics. *Appl Mech Rev 50*, 4 (April 1997).

[17] LIU, T., AND SULLIVAN, J. P. *Pressure and Sensitive Paints.* Springer-Verlag, 2005.

[18] MCLACHLAN, B. G., AND BELL, J. H. Pressure-sensitive paint in aerodynamic testing. *Experimental Thermal and Fluid Science* (1995), 470–485.

[19] MEBARKI, Y. Peintures sensible a la prcssion: application en soufflerie aerodynamique. Notc tcchnique, Onera, 1998.

[20] MÉBARKI, Y. *Peintures sensibles à la pression: application en soufflerie aérodynamique.* PhD thesis, Onera, UniversitLille, 1998.

[21] MEIER, A. Multispektrale auswertung der signalc drucksensitiver farben. Semcsterarbeit ws03/04, internal report, Institute of Fluid Dynamics, ETH Zürich, 2004.

[22] PARKER, C. A. *Photoluminescence of Solutions.* Elsevier Publishing Company, 1968.

[23] PERVUSHIN, G., AND NEVSKY, L. Composition for indicating coating (in russian). patent of ussr-su 1065452, 1981.

[24] PETERSON, J. I., AND FITZGERALD, R. V. New technique of surface flow visualization based on oxygen quenching of fluorescence. *Rev. Sci. Instrum. 51* (1980), 670–671.

[25] RABEK, J. F. *Mechanisms of Photophysical Processes and Photochemical Reactions in Polymers, Theory and Applications.* John Wiley & Sons Ltd., 1987.

[26] ROESGEN, T., AND TOTARO, R. A statistical calibration for thermochromic liquid crystals. *Experiments in Fluids 33* (2002), 732–734.

[27] RÖSGEN, T. Quantitative flow visualization. Vorlesungsskript, Institute of Fluid Dynamics, ETH Zürich, 1999.

[28] SANT, T. L., AND MÉRIENNE, M.-C. Surface pressure measurements by using pressure-sensitive paints. *Aerospace Science and Technology 9* (2005), 285 299.

[29] SCHANZE, K. S., CARROLL, B. F., AND KOROTKEVITCH, S. Temperature dependence of pressure sensitive paints. *AIAA Journal 35*, 2 (1997).

[30] SONG, L., AND FAYER, M. D. Temperature dependent intersystem crossing and triplet-triplet absorption of rubrene in solid solution. *Journal of Luminescence 50* (1991), 75–81.

[31] WALDER, M. Temperatur- und druckmessungen mit druckempfindlichen farben. Semesterarbeit ss2004, internal report, Institute of Fluid Dynamics, ETH Zürich, 2004.

[32] WOODMANSEE, M. A., AND DUTTON, J. C. Treating temperature-sensitivity effects of pressure-sensitive paint. *Experiments in Fluids*, 24 (1998), 163–174.

# *List of Figures*

# *List of Tables*

Seite Leer /
Blank leaf

# *Curriculum Vitæ*

## Personal Information

| | |
|---|---|
| Firstname | Stefano Angelo |
| Lastname | Airaghi |
| Birth date | January 10, 1975 |
| Nationality | Swiss, Brusino Arsizio (TI) |
| | Italian, Campione d'Italia |

## Education

**PhD Fluid Dynamics** (Dr. sc. techn.), Swiss Federal Institute of Technology (ETHZ), Zürich, Switzerland, March 2006

PhD Thesis: *Self-Illuminating Pressure Sensitive Paints Using Electroluminescent Foils*

**MS Fluid Dynamics** (Dipl. Masch.-Ing. ETH), Swiss Federal Institute of Technology (ETHZ), Zürich, Switzerland, 1994-2000

MS in Fluid Dynamics and Material Science
Diploma thesis: *Optimization Algorithms based on Models of Bacterial Chemotaxis*

Liceo (high school), Mendrisio, TI, Maturità tipo C (scientific curriculum), 1990-1994.

## Publications

- S.Airaghi, T.Rösgen and M.Guille *Electroluminescent Foils as Illumination Source for Pressure Sensitive Paint*, 11th International Symposium on Flow Visualization, ISFV11 CDRom Proceedings, 2004.

- Sibylle D. Müller, Jarno Marchetto, Stefano Airaghi, Petros Koumoutsakos *Optimization based on bacterial chemotaxis*, IEEE Trans. Evolutionary Computation, 6(1), 16-29 (2002)
- S. Mueller, S. Airaghi, J. Marchetto, P. Koumoutsakos *Optimization Algorithms based on a Model of Bacterial Chemotaxis*, Sixth International Conference on Simulation of Adaptive Behavior: From Animals to Animats, SAB 2000 Proceedings Supplement, International Society for Adaptive Behavior, 2000